The Dehydrogenation Reactions between LiH and Organic Amines for Solid State Hydrogen Storage Systems

Thesis submitted to the University of Glasgow for the Degree of Doctor of Philosophy

Tina Yu-Ting Su

School of Chemistry

College of Science and Engineering

University of Glasgow

October 2016

Abstract

Hydrogen is considered as an appealing alternative to fossil fuels in the pursuit of sustainable, secure and prosperous growth in the UK and abroad. However there exists a persisting bottleneck in the effective storage of hydrogen for mobile applications in order to facilitate a wide implementation of hydrogen fuel cells in the fossil fuel dependent transportation industry. To address this issue, new means of solid state chemical hydrogen storage are proposed in this thesis. This involves the coupling of LiH with three different organic amines: melamine, urea and dicyandiamide. In principle, thermodynamically favourable hydrogen release from these systems proceeds *via* the deprotonation of the protic N-H moieties by the hydridic metal hydride. Simultaneously hydrogen kinetics is expected to be enhanced over heavier hydrides by incorporating lithium ions in the proposed binary hydrogen storage systems. Whilst the concept has been successfully demonstrated by the results obtained in this work, it was observed that optimising the ball milling conditions is central in promoting hydrogen desorption in the proposed systems.

The theoretical amount of 6.97 wt% by dry mass of hydrogen was released when heating a ball milled mixture of LiH and melamine (6:1 stoichiometry) to 320 °C. It was observed that ball milling introduces a disruption in the intermolecular hydrogen bonding network that exists in pristine melamine. This effect extends to a molecular level electron redistribution observed as a function of shifting IR bands. It was postulated that stable phases form during the first stages of dehydrogenation which contain the triazine skeleton. Dehydrogenation of this system yields a solid product Li_2NCN, which has been rehydrogenated back to melamine *via* hydrolysis under weak acidic conditions.

On the other hand, the LiH and urea system (4:1 stoichiometry) desorbed approximately 5.8 wt% of hydrogen, from the theoretical capacity of 8.78 wt% (dry mass), by 270 °C accompanied by undesirable ammonia and trace amount of water release. The thermal dehydrogenation proceeds *via* the formation of $Li(HN(CO)NH_2)$ at 104.5 °C; which then decomposes to LiOCN and unidentified phases containing C-N moieties by 230 °C. The final products are Li_2NCN and Li_2O (270 °C) with LiCN and Li_2CO_3 also detected under certain conditions. It was observed that ball milling can effectively supress ammonia formation. Furthermore results obtained from energetic ball milling experiments have indicated that the barrier to full dehydrogenation between LiH and urea is principally kinetic.

Finally the dehydrogenation reaction between LiH and dicyandiamide system (4:1 stoichiometry) occurs through two distinct pathways dependent on the ball milling conditions. When ball milled at 450 RPM for 1 h, dehydrogenation proceeds alongside dicyandiamide condensation by 400 °C whilst at a slower milling speed of 400 RPM for 6h, decomposition occurs *via* a rapid gas desorption (H_2

and NH_3) at 85 °C accompanied by sample foaming. The reactant dicyandiamide can be generated by hydrolysis using the product Li_2NCN.

Table of contents

List of Figures and Schematics

List of tables

Acknowledgement

Professor Duncan Gregory has been the source of inspiration and the enduring presence throughout these past four years as I explored the world of chemistry. I am eternally grateful for opportunities I have been given to learn. I am in awe for the countless hours he has generously spent reviewing abstracts, proposals and the seemingly endless task that was this thesis. Beyond the formalities he is a kind and compassionate mentor, meticulous and approachable.

Dr. Tuan Hoang and Dr. Sina Saremi-Yarahmadi were my daily role models on both personal and professional levels. Always willing to help; always willing to laugh together. Without the pioneering work on melamine by Dr. Hoang this thesis would have never come to be.

It has been an honour to work with the extensive technical support in Chemistry, namely Jim G, Jim T, Andy, Claire, Michael and Stuart. I would especially like to thank Ted for the power tools, and Karen for various deliveries.

Kirsten, Angus, Akiko and Zhe have provided the most insightful discussions for which ideas were bounced, binned and begotten. I thank Kirsten, Angus and Hallam especially, for casting their eyes over the various versions of drafts. Members of the Gregory group have grounded me throughout the most memorable four years of my life as we fixed, tidied, debated, photographed and dined our days together.

To the other fantastic company in my life, Valters, Max, Emily, Irene, Kirsty, Bo, Steph, Mr. Baron, Finn and Rowan, thank you.

Thank you dad and mum, for my life and the many years supporting my education.

Finally, I thank God for guiding me through my days and nights in this foreign land, for the joy of the Lord is my strength.

To my grandmother, whom in her late sixties learned how to read and write, and to this day continues to practices her Chinese characters two hours every day so she doesn't forget

1.0 Introduction

Energy has driven human progress since the industrial revolution.[1-5] From the widely recognised contribution of the steam engine patented by Glasgow's James Watt in 1871, the quest to convert natural energy sources, for example, coal to work has proved highly challenging as we begin to phase out the use of finite fossil fuel sources.[1-5] Europe alone has observed a significant 10% decrease in the use of solid fuels from 1990 to 2013, followed by 4.2% in petroleum products and 1.9% in natural gas, whilst renewable sources increased by 7.2% followed by 5.4% in nuclear heat sources (figure 1-1).[6]

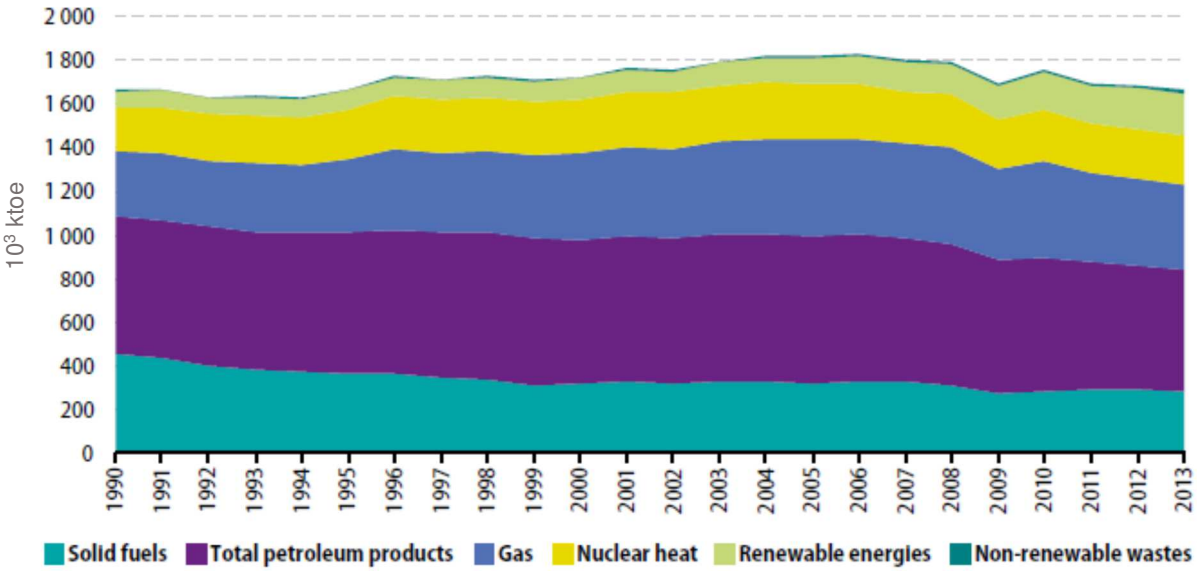

Figure 1-1. Total energy consumption in Europe between 1990 and 2013, by fuel type[6]

More locally, the UK has observed an increase of 1.7% in its total energy consumption in 2015, with 40% contributing to a largely fossil fuel dependent transportation industry, equivalent to 5.754 PJ (one kilo tonne of oil equivalent, ktoe, is approximately 41.87 GJ, figure 1-2).[7] These consumptions by the transportation industry can be further subdivided into road (74%), flight (23%), rail (1.9%) and water (1.2%).[7]

Energy is not only a commodity but a strategic resource, with prices fluctuating dependent on international situations and the value of the pound. Upon an overall energy dependency of 46.4% on imports, and also a 39.8% import on total petroleum products in 2013,[6] the UK stands in a vulnerable position, open to exploitation from energy producing countries. Therefore, developing alternative transportation fuel sources is essential for the continuous progress of the UK as a whole.

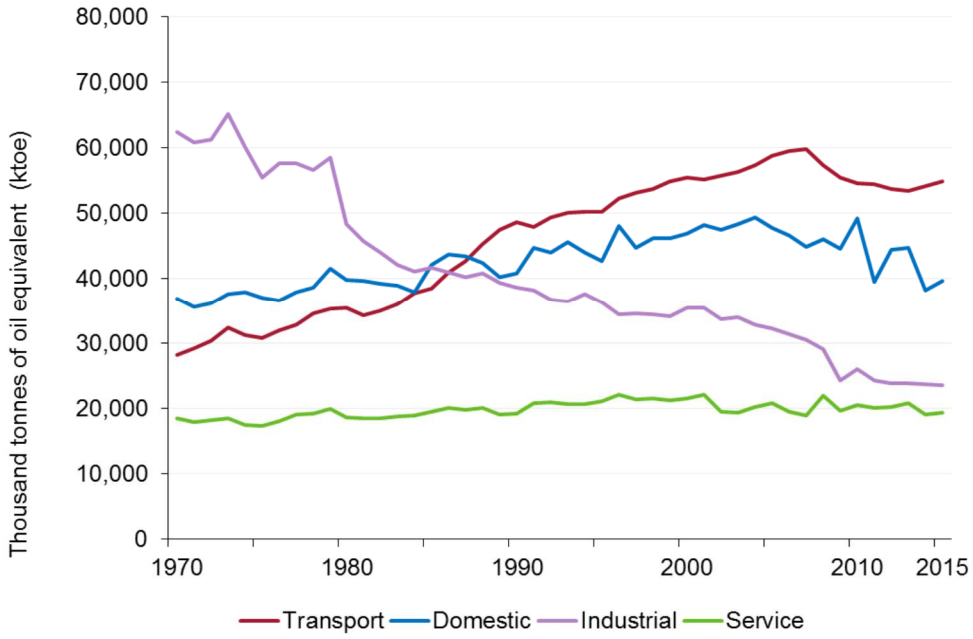

Figure 1-2. 2015-2016 UK energy consumption by sector[7]

Hydrogen is proposed as a sustainable energy vector to replace fossil fuels.[2-5] It is the most abundant element in the universe and can be used as an energy store necessary to buffer the intermittent nature of renewable energy sources such as solar and wind.[8] Hydrogen can be directly combusted with oxygen in an internal combustion engine to form water and converted into electricity in fuel cells with high efficiency (equation 1).[4, 9]

$$H_2 + ½\ O_2 \rightarrow H_2O \qquad (E° = 1.2291\ V) \quad (1\text{-}1)$$

Fuel cell technologies have flourished since Grove's first iron-copper fuel cell in 1838 to sophisticated apparatus that operate across a wide range of conditions.[9-13] A vivid distinction of applicability based on operating conditions can be drawn between the conventional polymer electrolyte membrane fuel cells (PEMFC, Figure 1-3) with solid oxide fuel cells (SOFC) as an example. SOFC is a high performance system operating between 500 – 1000 °C yet it would be inappropriate for a start-and-stop nature mobile applications compared to PEMFC with a lower 50 – 100 °C operating temperature.[10, 12, 14]

Sustainability of a hydrogen energy cycle proves contingent on an effective hydrogen source.[4, 16] There is a need to move away from the current industrial hydrogen production by methane steam reform which is counterintuitively fossil fuel dependent.[17] The rationale is to split the product water (equation 1-1) back into hydrogen and oxygen *via* electrolysis but this is only practical in large scale, stationary facilities where the low volumetric power density of hydrogen and high

materials costs can be offset by the quantity produced.[1] Under standard conditions hydrogen gas has a low power density and is in fact a largely inefficient form to store energy when considering it as a replacement for the fossil fuel reliant transportation industry. To address this power density issue for mobile applications, three other forms of hydrogen have been identified: compressed hydrogen, liquid hydrogen and condensed phase hydrogen.

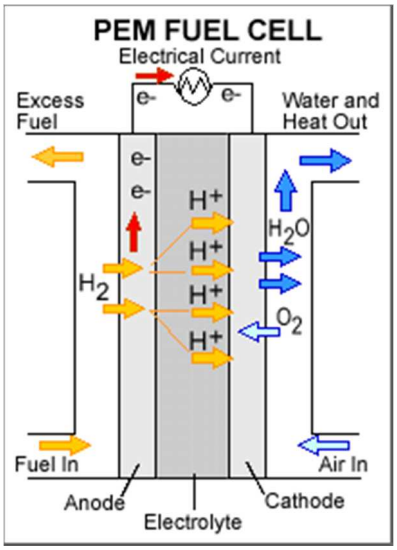

Figure 1-3. Schematic of a PEMFC for automobiles[15]

Compressed hydrogen at 700 bar is the current industry standard[18] which tethers vehicles to specialist fuelling stations requiring mass scale infrastructure upgrades with high capital costs.[19] This limits the prospects of hydrogen replacing fossil fuel in mobile applications. While liquid hydrogen has the potential energy to propel rockets,[20] to retain its high energy density state it must be cooled to 20.28 K under atmospheric pressure which limits commercial applications. In the condensed phase, a high density of hydrogen can be stored in solids by binding hydrogen either physically or chemically.

Physical hydrogen storage relies on physisorption of molecular hydrogen onto the surfaces of porous solids such as carbon nano-materials [21-23] or metal organic frameworks, MOF, materials.[24-26] The efficacy of these materials are a function of their surface areas (>2000 $m^2 g^{-1}$) and hydrogen binding energies (20 kJ mol^{-1}).[27] Typical high surface area materials include nanoporous carbon formed with a zeolite template (≈3200 $m^2 g^{-1}$), MOFs (1000 – 6000 $m^2 g^{-1}$) and high porosity polymers.[27-29] Hydrogen adsorption on high surface area carbon materials is only effective under particular conditions such as high pressure and low temperatures,[23, 30-31] whereas their metal modified equivalents operate closer to ambient conditions.[32] MOFs with various ligands are also able to operate in the binding energy range of electrostatic, inductive and even covalent charge transfer levels to enhance hydrogen uptake.[33] Despite achieving remarkable storage capacities,

practical energy densities can only be achieved with high pressure and low temperatures which is not practical in transportation applications.

Chemical hydrogen storage materials on the other hand capitalises on hydrogen's affinity to compounds with the majority of elements on the periodic table; participating in chemical and biological processes *via* interactions from Van der Waals to ionic bonding.[4, 8, 34] Molecular hydrogen gas is therefore not a prerequisite when devising regeneration strategies as other hydrogen rich compounds such as water and ammonia can be used as hydrogen source. The vanguards of current research efforts are metal hydrides, complex hydride, and multi-component systems.[5, 16] Metal hydrides are ionic compounds consisting of one or more metallic elements with hydrogen such as light metal hydrides (LiH, NaH, MgH_2)[8, 35] and ternary metal hydrides ($NaMgH_3$).[36] Complex hydrides are ultrahigh energy density storage materials, commonly group I and II salts of $[AlH_4]^-$, $[NH_2]^-$ and $[BH_4]^-$ where hydrogens are covalently bonded to a central main group element to form an anion (except for alanates).[37-40] Direct thermolysis of complex hydrides produces hydrogen with often unwanted side products such as ammonia, with high decomposition temperatures and with sluggish kinetics. Finally, multi-component systems involve either tailoring of the thermodynamics of a hydrogen rich host compound by introducing a destabilising agent to release the bonded hydrogen (e.g. $LiBH_4 + MgH_2$); or a redox of protic $H^{\delta+}$ and hydridic $H^{\delta-}$-containing moieties often in two compounds (e.g. $LiH + LiNH_2$).[27, 41-42] With a seemingly endless array of potential hydrides it is the purpose of this introduction to navigate briefly through the literature starting from a well-understood hydride, LiH, in order to identify some of the key components of an appropriate hydrogen store.

Any suitable solid storage product should address the environmental, social and economic impacts of the prospects of successively replacing fossil fuel with hydrogen, against a realistic timeline. With this agenda, the United States Department of Energy launched an exhaustive investigation on performance metrics necessary for a hydrogen economy through an industry, government and academic partnership.[16] By 2003 a preliminary set of specifications was published for hydrogen storage materials which is revised frequently to incorporate technological advances. The current list of specifications (table 1) focuses on the energy density, costs, operability, kinetics and environmental health and safety.[43]

In light of this concise list of specifications for performances, this chapter will continue to discuss chemical hydrogen storage materials in terms of reaction mechanisms in conjunction with system performance to arrive at the proposal for this thesis: hydrogen storage systems consisting of LiH paired with organic amine compounds.

Table 1-1. Technical system target of hydrogen storage systems for light duty fuel cell vehicles [43]

Parameter	2020 (Ultimate target)	Units
System gravimetric capacity	5.5 (7.5)	Dry weight % H_2
System volumetric capacity	4 (7)	Volume % H_2
Storage system cost	6.20 (4.95)	£ GBP per kWh net
Min / Max delivery temperature	-0.5	°C
Operation cycle life	1500	Cycles
'Well' to power plant efficiency	60	%
System fill time for 5 kg H_2	3.3 (2.5)	Min
Environmental health and safety	Meets or exceeds industrial standards (e.g. SAE J2579)	

1.1 Properties of LiH

Lithium hydride is the lightest ionic compound known. It crystallises in the rock salt $Fm\bar{3}m$ lattice where the hydride ions occupy the octahedral sites in the face centred cubic array of lithium ions (figure 1-4).[44] With a unit cell parameter a = 4.0752Å, the bonding in solid state LiH is 87.8% ionic[8, 45] with covalent H…H characteristics along the [001] direction.[46]

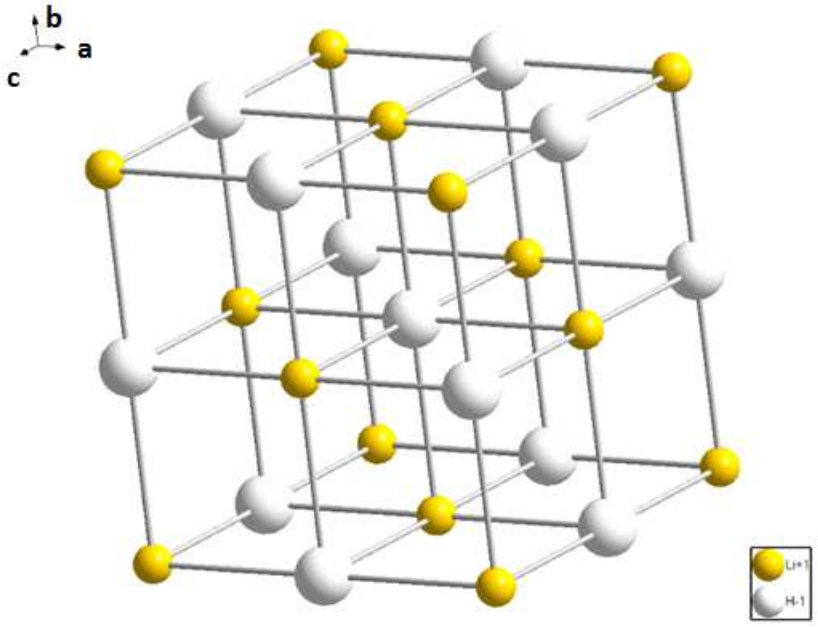

Figure 1-4. Unit cell of LiH

LiH has a gravimetric and volumetric hydrogen density of 12.6 wt% and 9.82 vol% respectively, higher than the target listed in table 1-1. It is formed by the exothermic hydrogenation of metallic lithium under hydrogen pressure. The material has very little mechanical integrity with an average Mohr hardness of 3.5.[47] LiH reacts readily in air with water and carbon dioxide to form Li_2O and Li_2CO_3. In fact it is highly pyrophoric and would auto ignite with moist air. LiH is a well-known Lewis base which liberates hydrogen with acids, ammonia, and primary and secondary amines. Most organic compounds contain functional groups that react with LiH with the exception of ethers, fully saturated hydrocarbons and saturated aromatics. The activity of LiH is dependent on the impurity content. Most commonly Li_2O and LiOH form on the surface of the hydride as a diffusion barrier.[47]

LiH melts at 692 °C, and decomposes fully by 720 °C. The gas phase thermal decomposition of LiH was described by Grochala *et al.* to proceed through a first order reaction process where the Li-H bond elongates and weakens, followed by the energetically favoured H-H pairing in equation (1-2) leading to a final Li-H bond dissociation at ≈718 °C.[8, 48]

$$2\ H^- \rightarrow H_2 + 2\ e^- \ (\Delta H° = -3.02\ eV) \qquad (1\text{-}2)$$

Despite having a high gravimetric and volumetric content, LiH is often classified as an unsuitable storage medium due to its high decomposition temperature, which would be unsuitable for PEMFCs.[5] One method to access the hydrogen has been identified as coupling the hydridic hydride with protic hydrogen ligands such as amides *via* equation C(1-3):[27, 41]

$$H^- + H^+ \rightarrow H_2 \qquad (\Delta H° = -7.37\ eV) \ (1\text{-}3)$$

This approach opens up gateways to tailoring the system thermodynamics while maintaining hydrogen content using a vast variety of possible pairing compounds.[34, 49 - 50] The following section will review some of the notable LiH-coupled hydrogen storage systems developed since the seminal report on the Li-N-H system by Chen *et al.* in 2002.[41]

1.2 Li-N-H systems

The thermally activated phase transition of lithium nitride under hydrogen, namely hexagonal Li_3N to face centred cubic Li_2NH, and then body centred tetragonal $LiNH_2$ was identified as a reversible hydrogen storage system (equation (1-4)). The theoretical gravimetric capacity is 11.5 wt% of hydrogen, however only *ca.* 10 % can be reversibly attained at temperatures above 300 °C.[41]

$$Li_3N + 2\ H_2 \leftrightarrow Li_2NH + LiH + H_2 \leftrightarrow LiNH_2 + 2\ LiH \qquad (1\text{-}4)$$

Dehydrogenation between LiH and $LiNH_2$ operates at a lower temperature (onset *ca.* 150 °C) which qualifies as an appropriate hydrogen storage candidate for practical use with its 6.5 wt% theoretical capacity. The enthalpy of reaction between LiH and $LiNH_2$ was measured using van't Hoff's method to be -66 kJ mol^{-1} and using calorimetry to be -67 kJ mol^{-1}.[51-52] Since the inception of the Li-N-H system, extensive efforts experimentally and using computational modelling have been dedicated to establish the nature of the interaction between lithium amide and lithium hydride. In simple terms, dehydrogenation is thought to prevail through Li^+, H^- and H^+ Frenkel pair migration[38] in the solids involved to facilitate either a solid-solid cooperative redox of $NH^{\delta+}\cdots H^{\delta-}Li$[53-56] or a solid-gas ammonia mediated mechanism.[38, 57] These mechanisms were proposed based on various structural models derived from diffraction, spectroscopy, thermal analysis, physical characterisation and isotopic labelling experiments (summarised in the following sections, including methods to improve performance are also described including mechanical activation, catalysis and nano-confinement).

1.2.1 Properties of Li-N-H materials

To gain insights into the possible dehydrogenation scheme, it is worthwhile to consider first the structural transition due to hydrogenation of Li_3N *via* Li_2NH and $LiNH_2$ as reported by Würthwein *et al.*[58] It is unsurprising that the Li-N bonds were found to be significantly more ionic than the N-H bonds due to the presence of electropositive lithium.[59] Li charge repels neighbouring positive charge which in turn contributes to the preferred planar geometries of these Li-N-H materials. A sequential lengthening of the N-H bond was also observed with as lithium replaces hydrogen (table 1-2). Consequently proton affinity increases with the increasing number of lithium atoms due to lithium's ability to stabilise positive charge around the central nitrogen.[58]

Table 1-2: N-H bond, calculated proton affinity based on Mulliken population analysis [58]

Species	N-H (overlap populations)	Proton affinity* (kJ mol^{-1})
NH_3	0.673	–949.3
$LiNH_2$	0.612	–1190.8
Li_2NH	0.538	–1343.1
Li_3N	-	–1388.3

*Calculation optimised by analytic force evaluation routines and split valence set 3-21G [58]

Two Li_3N phases exists and have both been reported in the context of potential hydrogen stores. The polymorphs are α-Li_3N (P6/mmm) and high pressure β-Li_3N ($P6_3/mmc$) [41, 60-61] (figure (1-5)). α-

Li_3N exists in an ABAB hexagonal structure with an alternating lithium layer (A) and $[Li_2N]$ layer (B). The nitrogen is coordinated by six lithiums in the *ab* plane and with two lithiums in the *c* direction to complete a hexagonal bi-pyramidal geometry.[39] On the other hand the β-Li_3N retains the hexagonal lithium A layer whilst the B layer, [LiN] is staggered in the *c*-direction into a close-pack motif.[60-61]

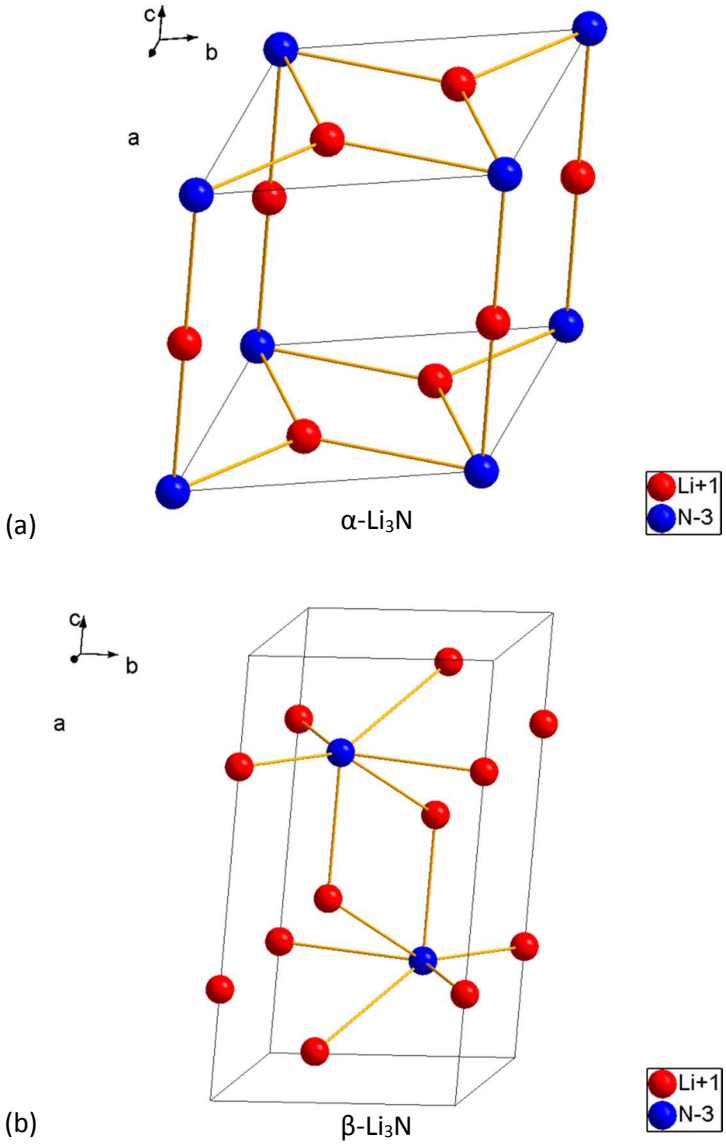

Figure 1-5. Unit cells of (a) α-Li_3N and (b) β-Li_3N.

Hydrogen uptake of α-Li_3N was reported by Chen *et al.* to begin at 100 °C under 3 bar of H_2 to form the stable phase, Li_2NH.[41] Despite considerable efforts the exact structure of the mono-hydrogenated imide has not yet been confirmed.[62] Whilst neutron and X-ray diffraction data were used to refined antifluorite structures in cubic space groups $F\bar{4}3m$ and $Fm\bar{3}m$ respectively (figures 1-6 (a) and (b)),[63-64] ^{1}H solid state MAS NMR spectra showed a peak at –4.6 ppm suggesting a highly disordered lithium conformation.[62] The discrepancy lies in the hydrogen positions where in

the $F\bar{4}3m$ model hydrogen occupies ¼ of the 16e Wyckoff sites, whilst in the $Fm\bar{3}m$ model $^{1}/_{12}$ of the 48h sites are occupied. The fully hydrogenated lithium amide has a well characterised tetragonal $I\bar{4}$ symmetry with lithium occupying the tetrahedral sites (figure 1-6 (c)).

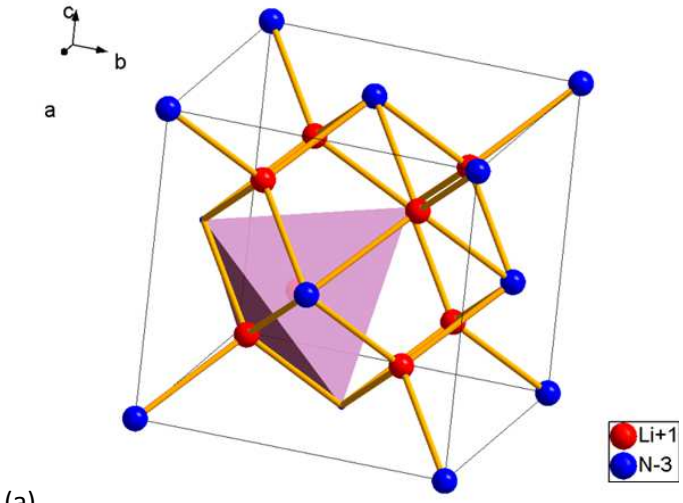

(a) Li_2NH $(Fm\bar{3}m)$

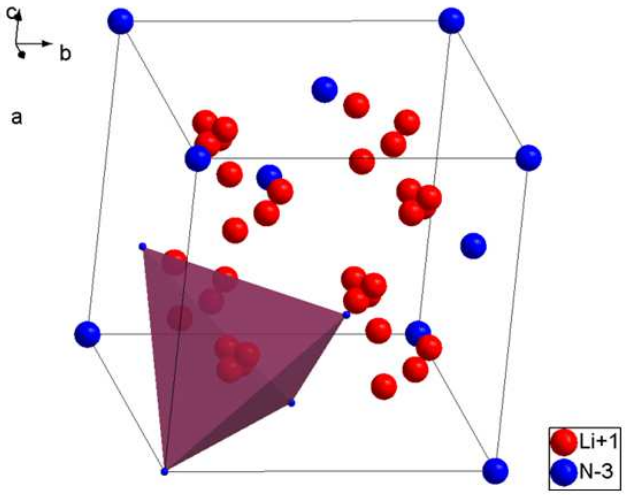

(b) Li_2NH $(F\bar{4}3m)$

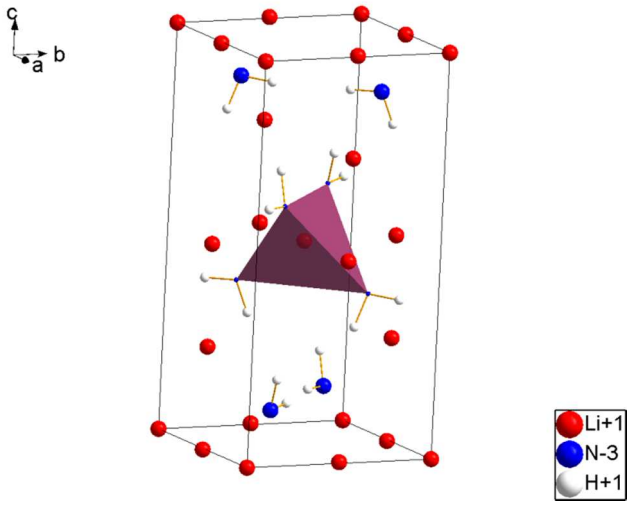

(c) $LiNH_2$

Figure 1-6. Unit cells of Li_2NH without hydrogen positions (a) $Fm\bar{3}m$, (b) $F\bar{4}3m$ and (c) $LiNH_2$

1.2.2 Ionic diffusion and Frenkel pair formation in LiH and Li-N-H materials

Crystal structures is closely correlated with a variety of physical mechanisms key to dehydrogenation. Ionic diffusion, as an example, was identified as the rate determining step for both the solid-solid and solid-gas dehydrogenation schemes.[55] Ionic diffusion in a material can be quantified by measuring the macroscopic lithium ion conductivity, however the transport mechanism may not be as forthcoming. For LiH, the first approximation of ionic diffusion was measured by solid state NMR between 250 and 500 °C and the diffusion coefficients for hydrogen and lithium were calculated to be $D_H = 1.91 \times 10^{-8}$ m^2 s^{-1} and $D_{Li} = 1.27 \times 10^{-9}$ m^2 s^{-1} respectively.[65] Using molecular dynamics simulations the diffusion constant was calculated with respect to deuterium exchange to be $D_{LiH} = 1.49 \times 10^{-9}$ $m^2 s^{-1}$ with an activation energy of $\Delta E_{LiH} \approx 0.66$ eV $atom^{-1}$ by point defect mechanism.[66] Ionic conductance of α-Li_3N perpendicular to the *c*-axis was measured to be 5.77×10^{-4} S cm^{-1}, for Li_2NH at 2.54×10^{-4} S cm^{-1} while $LiNH_2$ is barely ionic conductive.[68] The high conductivity measured for α-Li_3N can be rationalised in terms of the layers of Li atoms perpendicular to the *c*-axis. On the other hand, the high ionic conductivity found in Li_2NH arises from the favourable Frenkel defect formation (formation energy = 0.948 kJ mol^{-1}) involving the displacement of a lattice lithium atom from a tetrahedral to an octahedral interstitial site. As for $LiNH_2$ crystals, Frenkel defects formation is unfavourable (formation energy between –623.3 to –611.7 kJ mol^{-1}) which is reflected in the absence of ionic conductivity at room temperature.[68] Similarly, the diffusivity of lithium ions in Li-N-H materials without the presence of pre-existing vacancies was modelled using molecular dynamics simulation based on DFT principles.[69] From theory, diffusivity ranks in the order of Li_2NH > Li_3N > $LiNH_2$. It was construed that in Li_3N, lithium ion diffusion is directly correlated to lithium hopping between equilibrium lithium sites along the direction perpendicular to the *c*-axis. Whilst the lithium ion diffusion in Li_2NH is assisted by rotation of the partially positively charged H in the $[NH]^{2-}$ moieties to minimise repulsion from neighbouring lithium ions above 400 K. In contrast, the amide anions are more restrained in rotational freedom and hence hinder lithium diffusion, even at higher temperatures. It was concluded that the introduction of lattice defects greatly enhances the lithium diffusion for all three compounds.[69]

1.2.3 Thermolysis and cycling of Li-N-H materials

Another crucial physical property to characterise when studying dehydrogenation is a material's thermal response. The decomposition of Li-N-H materials was found to depend on hydrogen and ammonia partial pressures.[53, 70-71] It was first reported that the equilibrium pressure when hydrogenating lithium imide to amide at 240 °C was 10 kPa H_2.[70] Furthermore Pinkerton *et al.*

reported that that hydrogen and ammonia are competitively desorbed by $LiNH_2$ during hydrogenation of Li_3N. At as low as 175 °C, $LiNH_2$ is formed upon exposing Li_3N to 0.13 MPa of H_2 however as the amide concentration increases the subsequent ammonia desorption prevails. It was observed that in larger samples, local ammonia concentration mitigates further decomposition until higher temperatures.[71] In essence, pristine $LiNH_2$ decomposes to Li_2NH and ammonia (36% mass loss between 200 and 350 °C [53]) whilst the addition of LiH as previously stated promotes hydrogen desorption.[53, 72-73] Ammonia desorption is undesirable as not only does it readily poison PEMFCs by reducing the proton conductivity in the Nafion membrane and the anode catalyst ionomer layer,[74] but also reduces storage capacity significantly upon cycling Li_3N in hydrogen.[75-76] Chien *et al.* reported a loss in hydrogen storage capacity observed during extended cycling of Li_3N under 10.25 and 0.86 bar H_2 at 255 °C. Phase evolution during cycling by powder X-ray diffraction (PXD) revealed the formation of Li_2O impurity as a by-product of cycling and LiH content in excess of the stoichiometric amount.[75] Lamb *et al.* proposed the reduction of hydrogen storage capacity as a function of nitrogen loss from the system during cycling. It was observed that bleeding in trace amounts of N_2 in the inlet H_2 stream has a significant effect on reinstating the hydrogen capacity in a Sieverts type apparatus. A Li-N-H phase diagram was constructed using CALPHAD simulations for the phase distribution at 528 K and two bar H_2 (figure 1-7). By tracing the changes in lithium, nitrogen and hydrogen mass fraction on the phase diagram it can be deduced that at low hydrogen content liquid lithium is the thermodynamically favoured phase. Li_3N is formed from liquid lithium with low concentration of nitrogen in the inlet stream which contributes to mitigating the overall hydrogen capacity loss during cycling. The capacity improvement could also arise from the direct formation of the imide and amide when a 20% N_2 in H_2 is used.[76]

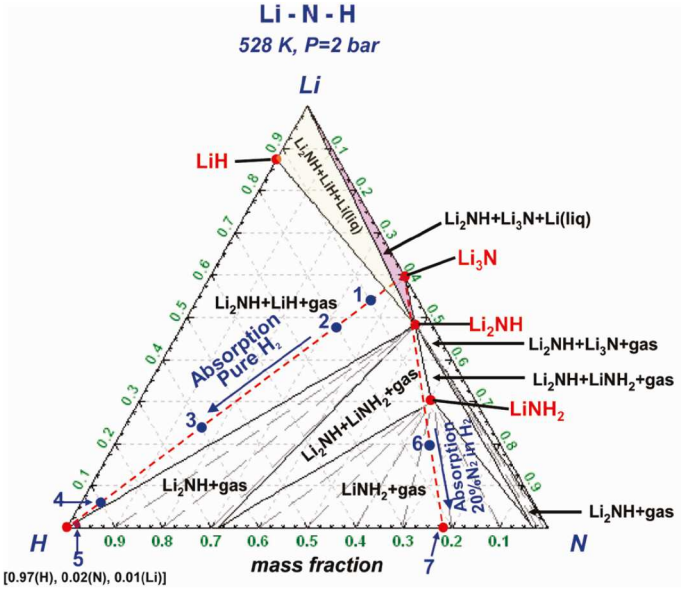

Figure 1-7. Li-N-H ternary phase diagram by CALPHAD simulations; positions of Li_3N, Li_2NH, $LiNH_2$ and LiH are marked in red.[76]

1.2.4 Proposed reaction mechanisms

1.2.4.1 Direct acid-base mechanism

The solid-solid direct acid-base mechanism involves a Columbic attraction and recombination between hydridic LiH with protic N-H moieties in the system through the formation of lithium and hydrogen Frenkel pairs (figure 1-8). It was first proposed by Chen *et al.* to rationalise a significantly lower hydrogen desorption temperature between ball milled LiH and $LiNH_2$ compared with the decomposition temperature of each individual reactant.[53]

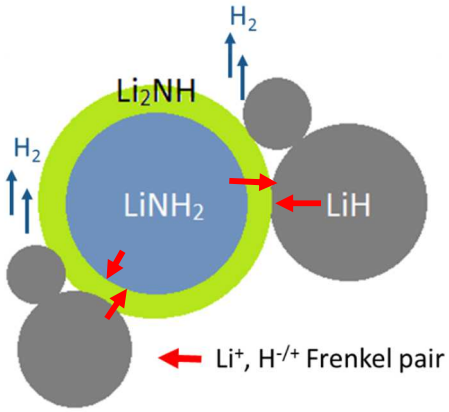

Figure 1-8. Simplified schematic of the direct redox dehydrogenation mechanism between $LiNH_2$ (blue) and LiH (grey) with product Li_2NH (green) forming around an $LiNH_2$ particle.

In instances where lithium ion mobility in lithium amide is dramatically improved by the introduction of defect concentration (ball milling) or catalysis, surface dehydrogenation was found in preference to ammonia formation through the interaction between $LiNH_2$ Frenkel pair migration and LiH Schottky defects in LiH.[54-56] The theory evolves from an important physical principle that in insulating, large band gap materials such as lithium amide, native point defects are expected to exist in the charged state, with coexisting defects in the opposite charge to maintain local and global charge neutrality. Through computation it was found that lithium cations and their corresponding charged vacancies in the amide are highly mobile even at room temperature; which suggest that lithium related defects readily achieve equilibrium concentration at temperatures of interest for practical applications. Hydrogen related defect pairs on the other hand have higher binding energy and therefore lithium amide is prone to Frenkel disorder on the lithium sub-lattice. High energy ball milling would create large defect concentration beyond the equilibrium and therefore the activation energy would be lowered; as energy required to create the defect threshold is removed leaving the ionic migration barrier to be the limiting step.[56] Experimentally, through introducing 'cage' like Br ionic diffusion barriers by doping Br into the

$LiNH_2$ lattice, an ammonia mediate dehydrogenation can be instigated with LiH. An experimental activation energy of 162.1 kJ mol^{-1} was recorded for ball milled Li_2NH_2Br whereas 177 kJ mol^{-1} was reported for the Li_2NH_2Br + 2 LiH system. Kinetic analysis of neat $LiNH_2$·LiH on the other hand showed a lower activation barrier of 83.3 kJ mol^{-1} upon inclusion of LiH (133 kJ mol^{-1} for pristine $LiNH_2$). It should be noted that the marked difference in activation energy measured for pristine $LiNH_2$ and $LiNH_2$ + LiH is often argued as evidence against the ammonia mediated dehydrogenation mechanism.[72] It was proposed that ionic diffusion driven by a concentration gradient across the reactant and product interface facilitated solid-solid dehydrogenation; whilst at higher temperature ammonia diffusion dominates.[72] Furthermore, Zhang *et al.* recently reported a direct visualisation of a $TiCl_3$ catalysed LiH + $LiNH_2$ powder mixture *in situ* by TEM during hydrogen cycling. During hydrogenation, LiH particles form on the surface of lithium amide and these shrink and disappear during dehydrogenation to form a Li_2NH layer.[54]

1.2.4.2 Ammonia mediated mechanism

The ammonia mediated route (figure 1-9) was proposed based on an ammonia partial pressure detected during the thermal decomposition of the Li-N-H systems by mass spectrometry and NMR spectroscopy.[57, 77] Hu *et al.* demonstrated this mechanism directly by layering LiH with $LiNH_2$ and observed that 99.7% of ammonia desorbed by $LiNH_2$ can be absorbed by LiH within 2.4 ms.[57] The ammonia mediated mechanism was further affirmed by Isobe *et al.* using an isotopic labelling study by decomposing two ball milled samples of $LiNH_2$·2LiD and $LiND_2$·2LiH. It was found that the desorbed gas ratio and mass loss followed the ammonia mediated model.[78]

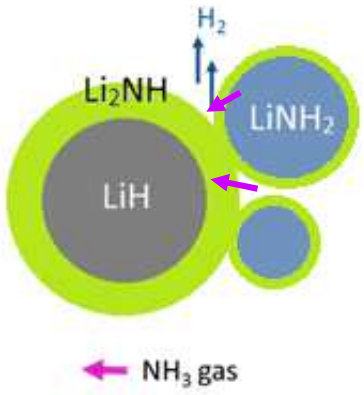

Figure 1-9. Simplified schematic of the ammonia mediated dehydrogenation mechanism between $LiNH_2$ (blue) and LiH (grey) to form Li_2NH (green) around a LiH particle.

Ex situ synchrotron experiment conducted by David *et al.* revealed non-stoichiometric intermediates $Li_{1+x}NH_{2-x}$ during cycling of the Li-N-H system.[38] The formation of $Li_{1+x}NH_{2-x}$ phases was attributed to a superionic transition of antifluorite imide product at elevated temperatures caused by thermally activated Frenkel defect pairs hopping in vacancies of the lithium sublattice. It was proposed that the cationic migration of lithium into neighbouring tetrahedral or octahedral sites (equation (1-5)) could promote the formation of H^+ ions from charged intermediates such as $[LiLiNH_2]^+$ (equation (1-6)). H^+ ion would then be attracted to nearby $[\square NH_2]^-$ species to form NH_3 (equation (1-7)).

$$LiNH_2 + LiNH_2 \rightarrow [LiLiNH_2]^+ + [\square NH_2]^- \qquad (1\text{-}5)$$

$$[LiLiNH_2]^+ \rightarrow Li_2NH + H^+ \qquad (1\text{-}6)$$

$$[\square NH_2]^- + H^+ \rightarrow NH_3 \qquad (1\text{-}7)$$

The process would continue until natural delamination occurs and ammonia is released at the surface. At this point the ammonia can either react with LiH in the near vicinity or dissipate into the purge stream.[38] David's theory was visualised in a DFT based computer simulation which assessed the activation energies involved with Frenkel pair induced deammoniation in lithium amide and imides. The diffusion constants were calculated for all relevant ionic species, namely NH_2^- and Li^+, and the product, NH_3 in the form of H^+ hopping between neighbouring NH_2^- groups. It was concluded that the formation of ammonia on surfaces is favourable over that in bulk, where the amide core shrinks due to imide shell formation.[79] Kinetics model fitting by Shaw *et al.* on cycling the Li-N-H system revealed that diffusion of ammonia through a porous lithium imide layer was the rate limiting step. It was found that the sample retained its nano-scale average particle size during cycling when examined by both surface area and diffraction techniques. A physical model was proposed drawing analogy to the corrosion process, where the unit cell volume of a core metal is compared with that of its expected shell metal oxide by a so-called Pilling-Bedworth ratio. When the ratio is smaller than 1, the oxide layer will not have the integrity to hold an intact shell, and therefore breaks and further oxidation occurs. In the case of Li-N-H system, a Pilling-Bedworth ratio of 0.5 is calculated using $LiNH_2$ as core to a shell Li_2NH, which can be deduced as porous adherent layers of Li_2NH around $LiNH_2$ cores that allow NH_3 gas to escape freely. The physical mechanism is perceived as deammoniation to create a porous shell of lithium imide around the amide core. Simultaneously, dehydrogenation occurs by a natural 'flaking' of the product imide from the hydride core exposing new surfaces.[80]

1.2.5 Means to enhance dehydrogenation between LiH and $LiNH_2$

Several means to improve the performance of the Li-N-H system have been proposed based on two broad categories: chemical catalysis and surface to bulk ratio enhancement.

1.2.5.1 Ti catalysts

$TiCl_3$ was identified as an effective catalyst for the Li-N-H system by Ichikawa *et al.* which narrows the decomposition temperature window from 150 - 400 °C to 150 - 250 °C by means of enhancing ammonia diffusion kinetics.[81-82] The catalytic activity of $TiCl_3$, nanosized TiO_2 and Ti-metal was probed by XANES to show that the Ti atoms reside in an intermediate valence between 3^+ and 4^+ when ball milled with $LiNH_2$.[83] More recently, Zhang *et al.* identified from *in situ* TEM studies that the catalytic intermediate $LiTi_2O_4$ phase forms alongside Li_2O impurities (figure 1-10). The catalytic intermediate functions as a "lithium pump" for the formation of lithium imide during dehydrogenation by sustaining a Li^+ flow as in the amide lattice Li^+ diffusion is normally slow.[54]

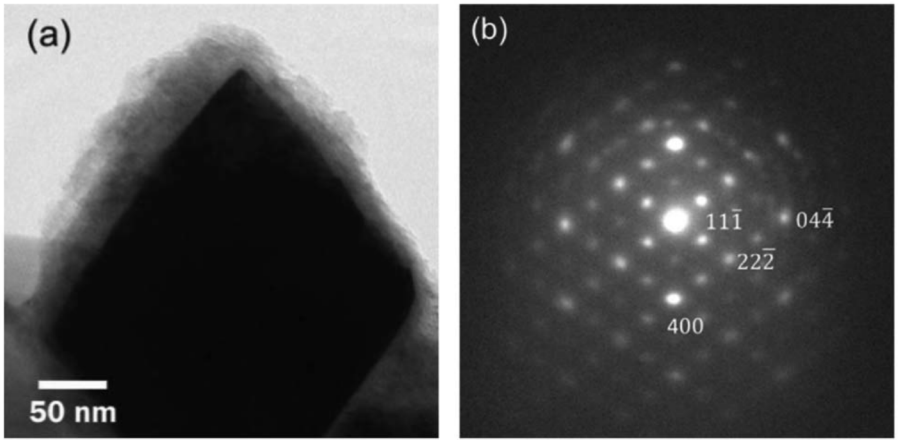

Figure 1-10. TEM images of $LiTi_2O_4$ post hydrogenation: (a) bright field image showing the particle and (b) selected area electron diffraction of particle showing $LiTi_2O_4$ phase.[54]

1.2.5.2 Other catalysts

BN was found to be a catalyst reducing the dehydrogenation window to 200-300 °C and increasing the kinetics by close to three fold. The compound was reported to be lightly Li^+ adsorbent which facilitates Li^+ ion diffusion as the main mode of catalysis. Whilst the main reaction occurs through a direct LiH-$LiNH_2$ reaction with Li^+ diffusion, the side reaction of H^- nucleophile attack on the nitrogen is also likely to occur. An ammonia mediated step was found to be unlikely in the presence of BN as a catalyst.[53]

Metal halides have also been reported to catalyse the Li-N-H system by improving the lithium cation conductivity at room temperature. Whilst the dehydrogenation temperature window

remains unaltered, ammonia release is significantly suppressed. It was postulated that the effect is derived from a topotactic mechanism within the crystal without the involvement of ammonia.[84] Other common catalysts used in solid hydrogen storage systems are Si,[85] graphite,[86] transition metals[55, 82] and metal hydroxides[87] which have achieved limited improvement to the thermodynamics or kinetics of the Li-N-H systems.

1.2.5.3 Ball milling

Ball milling LiH with $LiNH_2$ was first reported by Ichikawa et al. to reduce the dehydrogenation peak temperature effectively by approximately 80 °C and to suppress deammoniation at higher temperatures.[81-82] The technique is extensively used as a prerequisite for creating a homogeneous mixture crucial in multi-component solid state reactions.[52, 55, 71-73, 77-78, 80, 83, 85-87] Several studies have focused on the effect of ball milling on the decomposition of the Li-N-H system. First to be noted is the study of ball milled lithium amide by Markmaitree *et al.* using SEM, PXD and BET to investigate particle morphology post ball milling. It was found that crystallite size was reduced by close to 20 fold while the effective surface area increased 15 fold.[88] The relatively lower surface to bulk ratio was attributed to solid agglomerate formation as a result of milling, hence each amide particle is suggested to contain many crystallites. When ball milled lithium amide was decomposed thermally, hydrogen and nitrogen were released alongside ammonia, which was speculated to result from partial ammonia cracking occurring at elevated temperatures. Moreover, a 175 °C decrease in decomposition temperature with a 10 % weight loss was recorded for the ball milled sample. A marked decrease in activation energy was also observed as a function of the extent of ball milling. It is proposed that this change in activation energy correlates to a change in reaction mechanism or in energy states of the reactants, rather than a surface area or a particle size effect. During ball milling, defects such as dislocations can be introduced which increases the potential energy of the material. In theory, atoms in a defect site have higher free energies than those located at perfect crystal sites, which contributes to a decrease in activation energy.[88]

1.2.5.4 Confinement

Li_3N was confined in mesoporous carbon by liquid filtration with lithium azide, LiN_3 followed by calcination which leads to a potentially explosive transformation with a 73% weight loss due to N_2 formation at 220 °C.[61] The high pressure β-Li_3N phase is formed, which nearly fully hydrogenates at 200 °C under 100 bar of H_2 in less than half an hour. Dehydrogenation occurs in one step at 300 °C without apparently undergoing the previously described imide intermediate route. The

high pressure beta phase remains upon cycling. Drastic improvement of reaction enthalpy from the commonly reported 115 to 60 kJ mol^{-1} was measured. It appears that the carbon host structure survives cycling and no reactions occur between the host and guest components. Storage capacity reduces to 1.8 wt% as a result of the presence of the host material, and the mechanisms of kinetic and thermodynamic improvements are yet to be fully understood.[61]

1.3 LiH·B-N compounds

Boron nitrides are another class of materials widely reported to dehydrogenate readily with LiH. Their boron and nitrogen centres are lightweight main group elements capable of bonding with multiple hydrogens at a time. B-H and N-H moieties tend to be hydridic and protic respectively which allows facile tunability with respect to physical properties such as melting and decomposition temperature.[89] In a comprehensive review, Hamilton *et al.* recognised that the key characteristics for a successful B-N hydrogen store were: multiple hydrogen equivalents associated with each main group element; a good match between the number of protic and hydridic hydrogens and the stability to attain safety on-board vehicles.[90] The sections below describe the hydrogen desorption reactions between LiH and two B-N compounds, ammonia borane (NH_3BH_3, AB) and hydrazine borane ($N_2H_4{\cdot}BH_3$, HB).

1.3.1 LiH·AB

AB is a colourless solid stable at room temperature and soluble in relatively polar co-ordinated solvents.[91] The crystal structure of the material was determined by single crystal neutron diffraction at 298 K as orthorhombic $Pmn2_1$ with cell parameter a = 5.395(2), b = 4.887(2), and c = 4.986(2) Å (figure 1-11).[92] AB exhibits unusual physical properties such as being a solid at room temperature in comparison to its isoelectronic counterpart ethane which is a gas at the same temperature. This is due to the polarity between boron and nitrogen, resulting in an extensive network of dihydrogen bonding formed between the protic N-H and hydridic B-H groups.[91] The N-H···H-B distance was characterised to be 2.02 Å which falls into the regime of conventional hydrogen bonding as this is shorter than the sum of the Van der Waal's radius between the two hydrogen ions (2.4 Å).

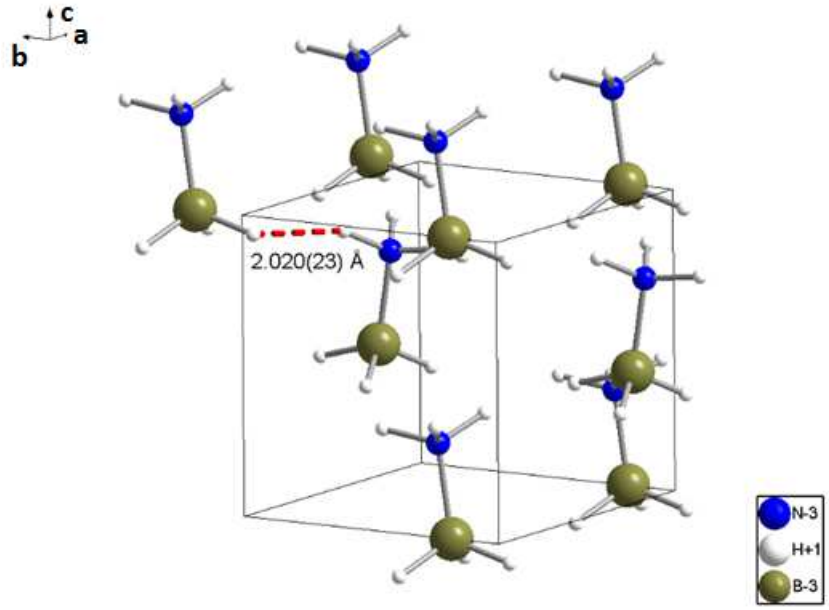

Figure 1-11. Unit cell of NH_3BH_3

1.3.1.1 Thermolysis of AB

Stephen *et al.* summarised that the thermolysis of AB is strongly dependent on reaction conditions such as pressure and heating rates.[91] At equilibrium heating rates for example, AB dehydrogenates from around 97 °C following melting to form diammoniate of diborane $[BH_2(NH_3)_2][BH_4]$; whereas at higher heating rates, volatile species such as borazine and diborane can be released. The dehydrogenation of AB is known to adopt a bimolecular mechanism leading to the elimination of H_2 by the redox of intermolecular protic N-H and hydric B-H.[90-91] Indeed despite comprising of both protic and hydridic moieties, AB is unable to dehydrogenate through intramolecular interactions. This is further evident by gas phase calculations that show that the intramolecular deprotonation energy barrier is *ca.* 25.5 kJ mol^{-1} higher than that of the dissociation energy of the B-N bond.[93] Further dehydrogenation occurs over a broad temperature range with the maximum rate found at 150 °C yielding a variety of oligomeric products by ^{11}B NMR.[90-91]

1.3.1.2 Lithium amidoborane

Xiong *et al.* first reported that LiH and AB released 10.9 wt% of H_2 at 92 °C without toxic side-products *via* the formation of intermediate lithium amidoborane (LiAB). LiAB was found when ball milling stoichiometric amount of LiH and AB, resulting in the elimination of one molecular H_2 during the milling process (equation 1-8):[94-95]

$$NH_3BH_{3\,(s)} + LiH_{\,(s)} \rightarrow LiNH_2BH_{3\,(s)} + H_{2\,(g)} \qquad (1\text{-}8)$$

The crystal structure of LiAB is orthorhombic *Pbca* with a Li-N distance of 2.063 Å and a Li-B distance between 2.5-2.69 Å. The amidoborane ions form a tetrahedral coordination around the lithium atom. When compared with AB, Li-substitution in LiAB results in the B-N bond shortening from 1.58 Å to 1.547 Å (figure 1-12).[96]

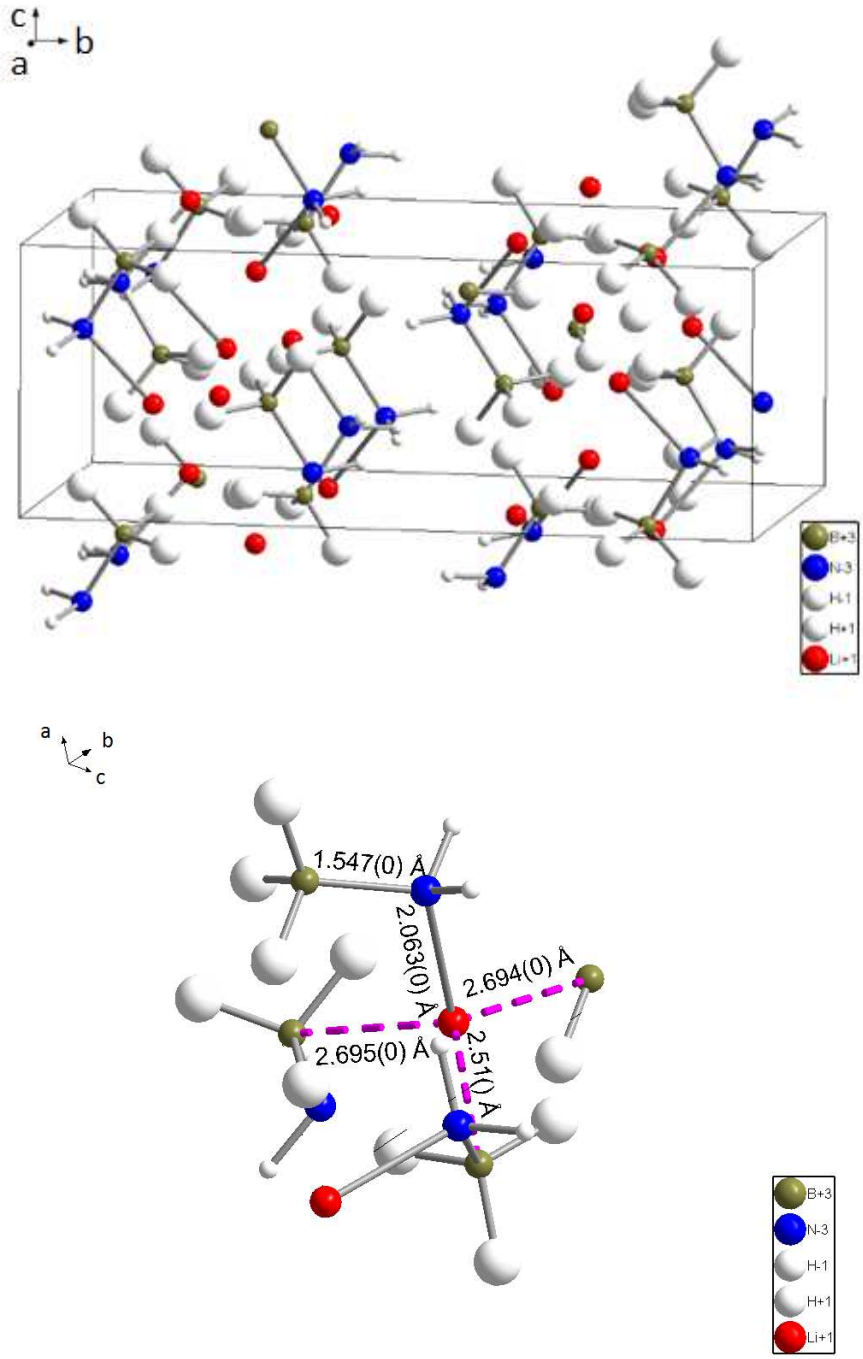

Figure 1-12. Unit cell of $LiNH_2BH_3$ and the local lithium geometry

1.3.1.3 The formation of LiAB

Osborn *et al.* calculated the Gibbs free energy for the reaction between LiH and AB to form LiAB to be zero at –46 °C by DFT. This indicates that the reaction is spontaneous at room temperature

if no kinetic barrier is present.[98] Indeed LiAB forms readily between LiH and AB upon physical mixing in both liquid and solid states.

By mixing equimolar AB and LiH in THF and heating in a stirred tank, 14.3 wt% of H_2 was desorbed.[99] The dehydrogenation proceeds in two steps under constant temperature measurements, with the activation energy for the first step measured to be 46.6 kJ mol^{-1} following first order kinetics. The second step is zero order and hence the rate is independent of reactant concentration, with an activation energy of 83.2 kJ mol^{-1}. It was observed that LiAB was formed in competition with the expected lithium substituted ring amidoborane (BCDB, product of pristine AB decomposing in THF) during the induction period of step 1. Furthermore, the THF insoluble LiH appeared to have been completely consumed as the solution after step 1 is translucent. At this stage, evaporating the THF would yield solid LiAB (by PXD), hypothesised to be the result from a redox between protic N-H with hydridic LiH. The product after the second dehydrogenation was not incontrovertibly identified but it was postulated to contain the terminal BH_3 group characteristic of a partially dimerised LiAB as the ^{11}B NMR signal for monomeric LiAB decreases gradually during dehydrogenation. Gravimetric studies indicated a mass loss of 1.8 equivalents of H_2 during the intermolecular second step whilst ^{11}B NMR revealed the major species taking a planar $B(N_2H)$ environment in addition to residual BH_3 and BH_4^+ species in secondary products. No borazine formation was detected.[99]

Xiong and Kang reported that LiAB forms readily when ball milled at room temperature.[94-95] Osborne *et al.* attempted to cryomill LiH with AB at –196 °C and successfully retained the integrity of LiH and AB while reducing particle size and increasing contact; however the milled sample degases upon warming to room temperature. In the decomposition of RT milled samples traces of monomeric aminoborane, borazine and aminodiborane was found in the gas stream besides the dominating H_2.[98]

1.3.1.4 Thermolysis of LiAB

As stated previously, thermal decomposition of LiAB commences at 92 °C liberating hydrogen vigorously. The dehydrogenation enthalpy was measured at –3 kJ mol^{-1}, while the system kinetics at 91 °C is measured to be 75% of H_2 is release within an hour.[94] In a separate experiment, Kang *et al.* reported a decrease in the activation energy of dehydrogenation to 75 kJ mol^{-1} for LiAB as compared to 183 kJ mol^{-1} for pristine AB. The reaction enthalpy however increased from the measured for AB itself by 13 kJ mol^{-1} to –8 kJ mol^{-1}.[95]

Both Xiong and Kang reported an up-field shift of ^{11}B MAS NMR signal of LiAB, –19.7[94] and –22 ppm[95] compared to –22.8 ppm of AB, as a result of a stronger donor complex between the metal amido group and the borane. Wu *et al.* confirmed the product composition at 200 °C to be

$LiBNH_{1.32}$ using neutron prompt-ϒ activation analysis on the reaction product which has a ^{11}B NMR signal of 29.8 ppm ascribed to internal B=N or $B=NH_2$ units.[96] Hydrogen retention in the product is not surprising as the lithium substituted AB has an imbalance of $H^{\delta+}$ / $H^{\delta-}$ species where hydridic B-H hydrogen is expected to remain in excess without a suitable redox pair.[96] However the nature of the non-stoichiometric hydrogen desorption was not discussed, neither were there any indications to the proportionality of the residual hydrogen with respect to B-H and N-H connectivity.

1.3.1.5 Dehydrogenation mechanism of LiAB

Xiong *et al.* proposed the following reaction scheme based on the product ^{11}B NMR shift at 29.8 ppm, which was attributed to a trigonal planar N-BH-N environment for boron as found in borazine or borazine like polymers (equation 1-9).[94]

$$n\ LiNH_2BH_{3\ (s)} \rightarrow (LiNBH)_{n\ (s)} + 2n\ H_{2\ (g)} \qquad (1\text{-}9)$$

Through *ab initio* calculations by Kim *et al.*, the lowest energy hydrogen desorption pathway was predicted as a LiH mediated pathway, where the rate limiting step is the transfer of a hydride from $NH_2BH_3^-$ to Li^+ followed by the formation of a triangular Li_2H moiety between two LiAB molecules (Scheme 1-1).[100-101] This occurs simultaneously with the formation of intermolecular B-N bond between two LiAB molecules. Two H_2 can be liberated *via* the redox between the new hydridic LiH and protic N-H moieties in the structure; resulting in further structural stabilisation through LiN bonds hence lowering the activation energy barrier. It was recognised by the authors that the key dehydrogenation process relies on Li^+ and $H^{+/-}$ mobility, similar to that in the $LiH{\cdot}LiNH_2$ systems.[100] Luedtke *et al.* validated this bimolecular reaction mechanism from the observed changes in reactivity upon varying the metal cation species; as well as deuterium isotopic labelling experiments on B-H and N-H groups.[101] The reactivity of metal amidoboranes (MAB, M= Li, Na and K) was observed to increase with increased ionicity as the energy barrier to scissor N-M bonds decreases. Furthermore, only $LiNH_2BD_3$ demonstrated a kinetic isotope effect confirming that BH_3 scission is the other rate limiting step. Overall, the role of the metal ion was postulated to assist hydride transfer as well as to increase the ionic character of the molecule which increases the dative characteristic of the B-N bond and weakening of the B-H bonds. A monomolecular (intramolecular) mechanism similar to that observed for AB would involve N-H…H-B interactions to form tetrahedral BH_2 moiety which were absent in ^{11}B NMR spectra. From a crystallographic point of view, the AB dihydrogen network is inconspicuous in LiAB where the H_2 distances are in the range of 2.249 Å in comparison to the 2.023 Å in AB. The reaction product was proposed to be $MNHBH{=}NMBH_3$ based on NMR for when M=Li, Na.[101]

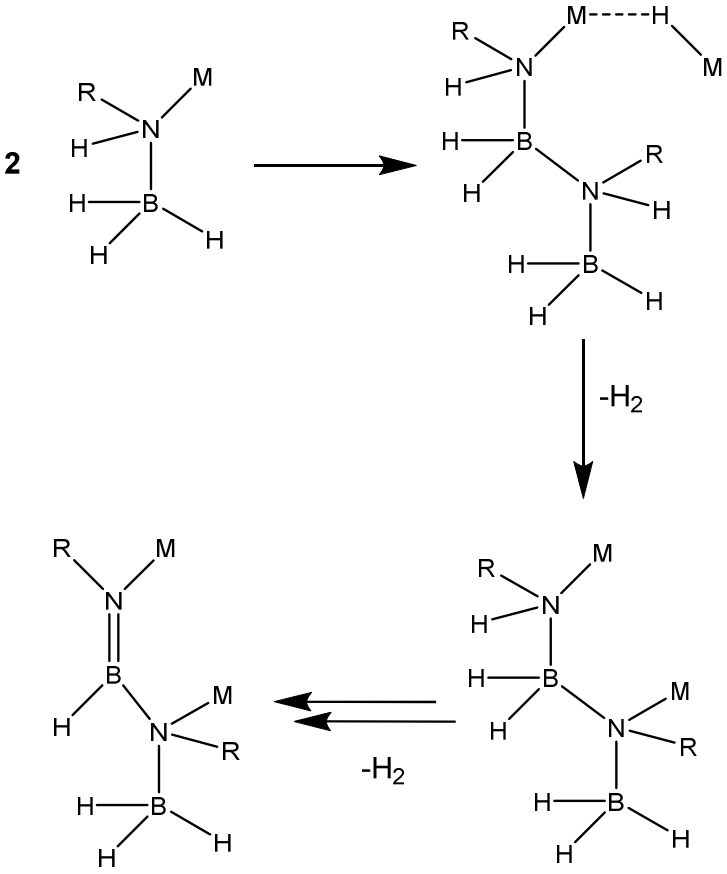

Scheme 1-1: Bimolecular dehydrogenation mechanism of $MNHRBH_3$, M= Li, Na, K; R= H, Me, Bu.[101]

1.3.1.6 LiAB regeneration

Two accounts of LiAB regeneration have been reported to date by the same research team. In 2012, Tang *et al.* reported that LiAB can be regenerated from its dehydrogenated product using hydrazine in liquid ammonia, similar to the regeneration of AB spent fuel by Sutton *et al.*[102-104] Dehydrogenated LiAB (150 mg, heated to 200 °C) was dispersed in liquid ammonia (30 ml) at –77 °C followed by injecting N_2H_4 (200 mg) using a syringe. The vessel was sealed and heated to 40 °C for 3 days, after which the solution was poured into a Schlenk flask and all volatiles removed under reduced pressure. It was found that the regenerated material consists of LiAB, and a mono-ammonia LiAB adduct by-product which spontaneously dehydrogenates at 40 °C. A typical yield of 63% was achieved due to the impurity. Lowering the reaction temperature is detrimental to the yield while raising the reaction temperature prompts faster decomposition of the $LiAB.NH_3$ adduct. The authors further examined the regeneration of LiAB *via* the synthesis of AB from LiAB dehydrogenation product $LiNBH_n$.[102] Through a series of solvent treatments, boron was extracted from the products in the form of $B(OCH_3)_3$ which is initially reacted with NH_4Cl then with $LiAlH_4$ in THF to form AB. Precious lithium in the form of $LiOCH_3$ was indicated to be recoverable by electrolysis in a reducing environment. Neither of the processes appears completely satisfactory

as the liquid ammonia + hydrazine method lacks satisfactory yield and the AB route involves pyrophoric reactants ($LiAlH_4$) and lacks overall energy efficiency (≈46 %).[104]

1.3.2 LiH·HB

Hydrazine borane (HB) is closely related to AB and contains 15.37 wt% of H_2 with four protic N-H and three hydridic B-H moieties. It can be synthesised from dihydrazine sulfate $(N_2H_5)_2SO_4$ with $NaBH_4$ in cyclic ethers such as dioxane (equation 1-10).[105]

$$(N_2H_5)_2SO_{4\,(s)} + 2\ NaBH_{4\,(s)} \rightarrow 2\ N_2H_4BH_{3\,(s)} + Na_2SO_{4\,(s)} + 2\ H_{2\,(g)} \qquad (1\text{-}10)$$

The crystal structure of HB was confirmed by Moury *et al.* using single crystal XRD to be orthorhombic *Pbcn* with unit cell parameters *a* = 12.9788(5) Å, *b* = 5.0616(2) Å, and *c* = 9.5087(4) Å (figure 1-13). Similar to AB, HB crystallises to form an extensive dihydrogen network in a 'head-tail' formation of neighbouring HB molecules, where the B-H···H-N intermolecular bond distances are around 2.246 Å. Note this is larger than the sum of the Van der Waals radius for dihydrogen (2.4 Å) and the intramolecular B-H···H-N distance of 2.426 Å. The "excess" N-H moiety is not bonded with any B-H moiety but rather forms a N-H...N bond with neighbouring HB molecule at a bond distance of 2.114 Å. As depicted in figure 1-13, the HB crystal structure therefore adopts a 'head-tail' formation between two HB molecules in alternating orientation along the *a*-axis to accommodate for the N-H…N hydrogen bond.[105]

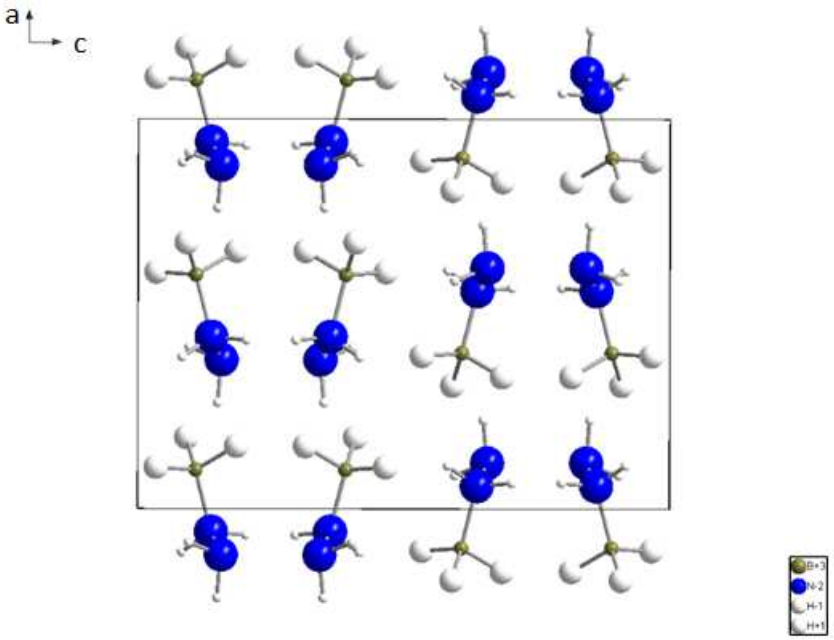

Figure 1-13. Unit cell of $N_2H_4BH_3$

1.3.2.1 Thermolysis of HB

Thermal decomposition of HB occurs with melting at around 60 °C.[105-106] Under a constant heating rate of 5 °C min^{-1}, the TG, DTA and DSC data were recorded by Moury *et al.* to show three exothermic weight losses corresponding to a 1.2 wt% loss between 60 and 95 °C, followed by 28.7 wt% between 105 and 160 °C and finally 4.3 wt% between 250 and 275 °C. This is accompanied by a physical observation of HB melting, foaming (forming a solid at *ca*. 160 °C) coupled with further degassing. In a separate isothermal experiment at 140°C, H_2, N_2H_4 and NH_3 were detected by a μGC-MS to account for 8.3% of weight loss.[105] This corroborates the observations of H_2 and N_2H_4 evolved during the pyrolysis of HB by Goubeau and Ricker in 1961.[107]

1.3.2.2 Formation of lithium hydrazine borane

LiH was reacted with HB with the incentive that a metal hydrazine borane would form as an intermediate similar to LiAB. Lithium hydrazine borane (LiHB) would have equal portions of protic N-H and hydridic B-H moieties which was predicted to allow complete dehydrogenation assisted by redox pair recombination. Whilst the system H_2 content is 14.8 wt%, a hand mixed sample of stoichiometric LiH and HB released a maximum of 11.9 wt% of H_2 at 150 °C within 4.5 hours.[105] Wu *et al.* reported the formation of phase pure α-LiHB by ball milling stoichiometric LiH with HB for 3 hours (equation 1-11).[108]

$$LiH_{(s)} + N_2H_4BH_{3\,(s)} \rightarrow \alpha\text{-}LiN_2H_3BH_{3\,(s)} + H_{2\,(g)} \qquad (1\text{-}11)$$

α-LiHB crystallises in a monoclinic $P2_1/c$ unit cell with cell parameters a = 5.8521 Å, b = 7.4655 Å, c = 8.8973 Å, and β = 122.381 ° (figure 1-14a). Using first principles MD simulations, LiH was found to deprotonate the bridging N-H group instead of the terminal N-H group. This results in Li^+ forming an ionic interaction (2.105 Å) with the same bridging N which retains its tetrahedral sp^3 hybridisation. The Li^+ is also coordinated tetrahedrally by interacting with the lone pair on the terminal N, and two other BH_3 units from three neighbouring $LiN_2H_3BH_4$ molecules (figure 1-14b). Further increase of LiH reactant did not result in further Li^+ uptake into the HB molecule. Similar to that in LiAB, Li substitution results in a shortening of B-N bond from 1.596 Å in HB to 1.550 Å in α-LiHB as Li donates electrons to N, increasing the dative characteristic of the B-N bond. Whilst the 0.015 Å increase in N-N bond is likely due to the coordination of terminal N with Li^+ through its lone pair. In contrast to a disruption of the intermolecular dihydrogen bonding network when doping AB with Li, α-LiHB has comparable intermolecular B-H···H-N distances (2.003 – 2.102 Å) with HB (2.010 Å). [105-108]

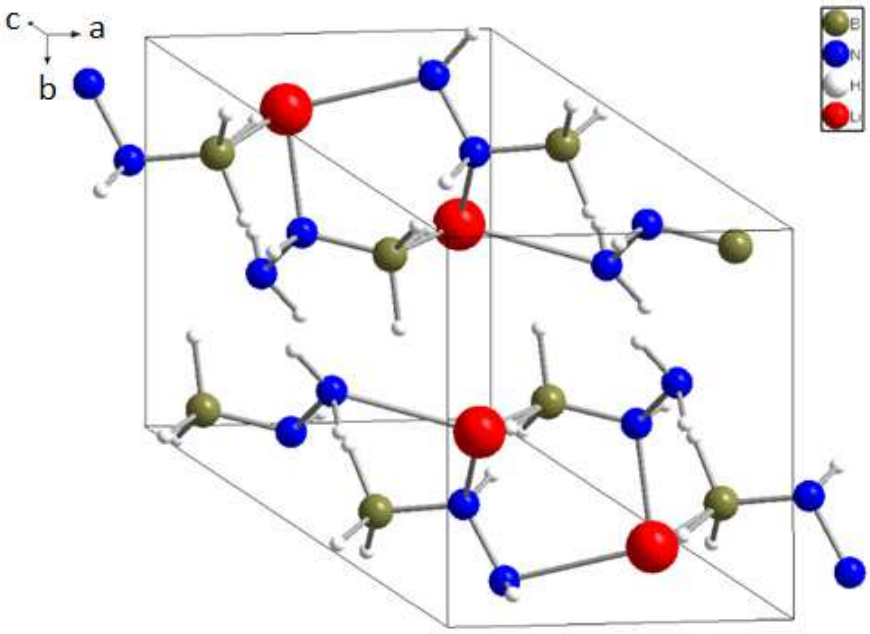

Figure 1-14. (a) Unit cell of α-$LiN_2H_3BH_3$.

1.3.2.3 Dehydrogenation of α-LiHB

With a lower net hydrogen content of 11.7 wt% than the 15.3 wt% of pristine HB, α-LiHB desorbs 9.5 wt% of H_2 and a minor amount of N_2 (0.7 wt%) by 150 °C. No hydrazine or ammonia was observed in the evolved gas stream up to this point. It is kinetically superior to HB, and an LiH·HB mixture; releasing 9.3 wt% of H_2 at 130 °C compared with 4.8 and 7.9 wt% for HB and LiH·HB respectively.[108] Preferential hydrogen release in α-LiHB instead of hydrazine as found in HB was attributed to the increase of polarity in the B-H moieties due to the presence of the Li-N bond evident in the downfield ^{11}B NMR shift detected for α-LiHB compared to HB.[109] As the ionic compound underwent dehydrogenation, species containing terminal NBH_3 and tricoordinated sp^2 N_2BH_2 form in transiently at 135 °C, whilst tetracoordinated N_2BH is the only specie found in the product. The authors hypothesised that α-LiHB is subjected to a similar dehydrogenation mechanism as found for LiAB where multiple molecules of α-LiHB interact and deprotonate *via* the formation of transient Li_xH at terminal BH_3 and NH_2 moieties (*c.f.* Scheme 1).[109] The final decomposition product is likely of polymeric nature due to a broad FTIR spectrum in the ν(NH) region.[106]

1.2.3.4 The formation of β-LiHB

Moury *et al.* reported the discovery of a room temperature polymorph, β-LiHB with an orthorhombic unit cell *Pbca* and cell parameters *a* = 10.2518 Å, *b* = 8.4785 Å and *c* = 7.4689 Å. Li substitution in β-LiHB occurs also on the bridging N with a Li-N distance of 2.086 Å.[110] The lithium again is tetrahedrally coordinated by a terminal NH_2 and two BH_3 moieties. However a 'head-tail' cluster formation was found in β-LiHB with a neighbouring LiHB unit through the terminal NH_2 units, where the two lithiums are separated by a distance of 3.49 Å.[110] Note that the synthesis of the two polymorphs differ by the milling procedure where β-LiHB appears to form when substantial cooling time is allowed.[108, 110] β-LiHB displayed a smaller extent of intermolecular dihydrogen bonding in comparison to HB with a smaller number of ν(NH) bands. The influence of Li substitution on the N-N and N-B bonds are red and blue shifts respectively indicating a weaker N-N bond and a stronger N-B bond. β-LiHB transforms to α-LiHB at 91 °C *via* the loss of H_2 and N_2 by a total of 1.2 wt%.[110-111] This indicates that β-LiHB contains excess N and H compared to α-LiHB, potentially an ball mill intermediate with metastable Li-H…H-N connectivity. The authors estimated 11.6 wt% of H_2 was released by β-LiHB up to 400 °C to yield a product characterised by ^{11}B MAS NMR to be bis(lithium hydrazide) diborane $[(LiN_2H_3)_2BH_2]^+[BH_4]^-$, analogous to the diammoniate of diborane $[(NH_3)_2BH_2]^+[BH_4]^-$ found in the decomposition of AB.[110] It is finally important to note that both α and β-LiHB appear to dehydrogenate in the solid state, which is favourable in terms of containment and the safety of the material in practical applications.[111]

1.4 Summary and project objectives

From the above examples, the role of LiH in dehydrogenation reactions can be summarised to invoking initial deprotonation of molecular or inorganic species with protic N-H moieties, and to provide lithium ions which has a profound influence on the charge distribution and geometry of Li-N-H and BN materials. The decomposition of these materials is consequently altered where lithium contributes to crucial mass transport mechanisms deduced. It should be noted that other main group hydrides and hydroxides have been paired with LiH with limited success; namely the LiH·LiOH system,[112-113] LiH·H_2O steam hydrolysis[114-117] and LiH·CH_4 system.[118] With the exception of the LiH·CH_4 system, all reported LiH based hydrogen storage systems have focused on inorganic hydrides despite a wealth of documented organic hydrides able to deprotonate in the presence of bases. In the search for new candidates for hydrogen storage we have identified three organic amines: melamine ($C_3N_6H_6$), 2-cyanoguanidine ($C_2N_4H_4$) and urea ($CO(NH_2)_2$) to form potential dehydrogenation reaction pairs with LiH (figure 1-15). Melamine and urea have been previously

reported as potential hydrogen stores when combined with $LiBH_4$ whilst 2-cyanoguaindine, a lower derivative of melamine is introduced for the first time as a potential hydrogen storage material.

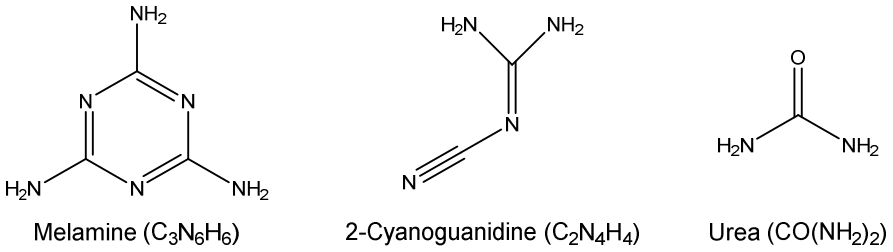

Figure 1-15. Compounds identified as dehydrogenation pairs with LiH.

Liu *et al.* reported the formation of a stable complex hydride, $3LiBH_4{\cdot}C_3N_6H_6$ upon ball milling at 150 RPM for two hours.[119] The monoclinic complex releases 7.83 wt%, of the theoretical 9.4 wt% H_2 in three steps (exo-endo-exo) between 100 and 340 °C. Through mechanistic studies using PXD, ^{11}B NMR and FTIR during thermal decomposition, the system is argued as a demonstration of B-$H^{\delta-}\cdots H^{\delta+}$-N based systems where hydrogen is released *via* electrostatic recombination of the $H^{\delta-}\cdots H^{\delta+}$ pair and the thermodynamically favourable formation of B-N bonds. However the nature of the interaction between $LiBH_4$ and NH_2 in melamine restricts the dihydrogen combination to six equivalent hydrogen pairs, hence the final 1.5 equivalent at 300 °C measured should be assigned to the self-decomposition of the remaining B-H molecule as reported for the decomposition of $LiBH_4$.[119] A deviation from the general rule of thumb, in which redox pair operative systems should have equivalent protic and hydridic hydrogens, is the leading cause to unwanted hydrogen retention in the system.[91] No crystalline intermediates were present throughout decomposition in this system and Li_2NCN was characterised as the sole crystalline residue; whereas spectroscopic characterisation revealed the presence of BN_3 and BN_2H post decomposition. FTIR further confirmed the aromatic triazine skeleton breaks down during the endothermic second decomposition step at 205 °C. The system was reported to be irreversible.[118]

Following on from this, Liu *et al.* reported a $LiBH_4{\cdot}CO(NH_2)_2$ complex hydride which crystallises in a monoclinic unit cell with cell constants *a* = 14.7645 Å, *b* = 5.9158 Å, *c* = 13.6484 Å and β = 115.237°.[120] By first principle calculations, the B-H···H-N pair are separated by 2.136 - 2.351 Å which qualifies for dihydrogen interaction. 8.13 out of 9.7 wt% of H_2 was released from the complex from 120 °C in multiple steps. Dehydrogenation was determined to be exothermic accompanied by likely melting of the complex at 131.5 °C. The product is non-crystalline with ^{11}B MAS NMR signals suggesting a variety of possible boron bonding states including BH_4^-, tricoordinated B^{III}, tetracoordinated BN_3 or NBH_2, BO_2 or BO_4 and trivalent HN-B=N species.

Rehydrogenation was not attempted, but the authors recognised the difficulties in reintroducing hydrogen to exothermically formed B-N bonds.[120]

By replacing $LiBH_4$ with LiH the complexity of hydrogen desorption is expected to reduce as amorphous boron complexes are removed; at the same time retaining high hydrogen capacity and lithium ion incorporation which have a clear role in facilitating hydrogen kinetics in binary systems.

The objectives of this thesis are hence unambiguously:

1. To examine the hydrogen desorption reactions between LiH paired with melamine, urea and 2-cyanoguanidine in the solid state, and
2. To develop regeneration strategies for the main solid product common to all three reaction pairs, lithium cyanamide (Li_2NCN)

1.5 References

1. Chu, S.; Majumdar, A. *Nature* **2012***, 488*, 294-303
2. Bockris, J. O. M. *Science* **1972**, *176*, 1323
3. Dawson, J. K. *Nature* **1974**, *249*, 724-726
4. Schlapbach, L.; Züttel, A. *Nature* **2001**, *414*, 353-358
5. Mandal, T.K.; Gregory, D. H. *Annu. Rep. Prog. Chem., Sect. A* **2009**, *105*, 21-54
6. *Energy, transport and environment indicators 2015 Edition*; Eurostat Statistic Books, Luxembourg, 2015.
7. *Energy consumption in the UK (2016)*; Department for Business, Energy & Industrial Strategy, London, 2016
8. Grochala, W.; Edwards, P. P. *Chem. Rev.* **2004,** *104,* 1283-1315
9. Winter, M.; Brodd, R. *J. Chem. Rev.* **2004,** *104*, 4245-4269
10. Steele, B. C.; Heinzel, A. *Nature* **2001**, *414*, 345-352
11. Li, Q.; He, R.; Jensen, J. O.; Bjerrum, N. J. *Chem. Mater.* **2003,** *15*, 4896-4915
12. Wang, Y.; Chen, K. S.; Mishler, J.; Cho, S. C.; Adroher, X. C. *Applied Energy* **2011**, *88*, 981-1007
13. Debe, M. K. *Nature* **2012**, *486,* 43-51
14. Minh, N. Q. *J. Am. Ceram. Soc.* **1993**, *76*, 563-588
15. US Department of Energy Fuel Cells Homepage. http://energy.gov/eere/fuelcells/fuel-cells (Accessed 14th July 2016)
16. Executive Summaries for the Hydrogen Storage Materials Centers of Excellence; US Department of Energy, Government Printing, **2012**
17. Holladay, J. D.; Hu, J.; King, D. L.; Wang, Y. *Catalysis Today* **2009,** *139*, 244-260
18. Toyota Mirai Fuel Cell Vehicle Homepage. https://ssl.toyota.com/mirai/fcv.html (Accessed 14th July 2016)
19. US Department of Hydrogen pipeline Homepage. http://energy.gov/eere/fuelcells/hydrogen-pipelines (Accessed 14th July 2016)

20. Granath, B. *Liquid Hydrogen--the Fuel of Choice for Space Exploration* [Online] http://www.nasa.gov/content/liquid-hydrogen-the-fuel-of-choice-for-space-exploration (Accessed 14th July 2016)
21. Liu, C.; Fan, Y. Y.; Liu, M.; Cong, H. T.; Cheng, H. M.; Dresselhaus, M. S. *Science* **1999**, *286*, 1127-1129
22. Baughman, R. H.; Zakhidov, A. A.; de Heer, W. A. *Science* **2002**, *297*, 787-792
23. Dai, L.; Chang, D. W.; Baek, J.; Lu, W. *Small* **2012**, *8*, 1130-1166
24. Rosi, N. L.; Eckert, J.; Eddaoudi, M.; Vodak, D. T.; Kim, J.; O'Keeffe, M.; Yaghi, O. M. *Science* **2003**, *300*, 1127-1129
25. Morris, R. E.; Wheatley, P. S. *Angew. Chem. Int. Ed.* **2008***, 47*, 4966-4981
26. Li, J.; Kuppler, R. J.; Zhou, H. *Chem. Soc. Rev.* **2009,** *38*, 1477-1504
27. Liu, C.; Li, F.; Ma, L.; Cheng, H. *Adv. Mater.* **2010**, *22*, 28-62
28. Yang, Z.; Xia, Y.; Mokaya, R. *J. Am. Chem. Soc.* **2007**, *129*, 1673-1679
29. Dinca, M.; Long, J. R. *Angew. Chem. Int. Ed.* **2008**, *47*, 6766-6779
30. Dillon, A. C.; Jones, K. M.; Bekkdahl, T. A.; Kiang, C. H.; Bethune, D. S.; Heben, M. J. *Nature* **1997**, *386*, 377-379
31. Aricò, A. S.; Bruce, P.; Scrosati, B.; Tarascon, J.; Schalkwijk, W. V. *Nature Mater.* **2005**, *4*, 366-376
32. Chen, P.; Wu, X.; Lin, J.; Tan, K. L. *Science* **1999**, *285*, 91-93
33. Lochan, R. C.; Head-Gordon, M. *Phys. Chem. Chem. Phys.* **2006**, *8*, 1357-1370
34. Breternitz, J.; Gregory, D. H. *Crystals* **2015**, *5*, 617-633
35. Xiao, X.; Liu, Z.; Saremi-Yarahmadi, S.; Gregory, D. H. *Phys. Chem. Chem. Phys.* **2016**, *18*, 10492-10498
36. Reardon, H.; Mazur, N.; Gregory, D. H. *Prog. Natur. Sci. Mater. Int.* **2013**, *23*, 343-350
37. Orimo, S.; Nakamori, Y.; Eliseo, J. R.; Züttel, A.; Jensen, C. M. *Chem. Rev.* **2007,** 107, 4111-4132
38. David, W. I. F.; Jones, M. O.; Gregory, D. H.; Jewell, C. M.; Johnson, S. R.; Walton, A.; Edwards, P. P. *J. Am. Chem. Soc.* **2007**, *129*, 1594-1601
39. Gregory, D. H. *J. Mater. Chem.* **2008**, *18*, 2321-2330
40. Mao, J.; Gregory, D. H*. Energies* **2015**, *8*, 430-453
41. Chen, P.; Xiong, Z.; Luo, J.; Lin, J.; Tan, K. L. *Nature* **2002**, *420*, 302-304
42. Mao, J.; Gu, Q.; Gregory, D. H. *Materials* **2015**, *8*, 2191-2203
43. DOE TARGETS FOR ONBOARD HYDROGEN STORAGE SYSTEMS FOR LIGHT-DUTY VEHICLES. [Online] http://energy.gov/eere/fuelcells/downloads/doe-targets-onboard-hydrogen-storage-systems-light-duty-vehicles (Accessed 14th July 2016)
44. Wolstenholme, D.J.; Dobson, J. L.; McGrady, G. S. *Dalton Trans. **2015**, 44,* 9718–9731
45. Calder, R. S.; Cochran, W.; Griffths, D.; Lowde, R. D. *J. Phys. Solids.* **1962**, *23*, 621-632
46. Yamamura, S.; Kasahara, S.; Takata, M.; Sugawara, Y.; Sakata, M. *J. Phys. Chem. Solids* 1999, *60*, 1721-1724
47. Montgomery, C. D. *Nuc. Eng. Des.* **1973**, *25,* 309-314
48. Wolstenholme, D. J.; Roy, M. M. D.; Thomas, M. E.; McGrady, G. S. *Chem. Commun.* **2014**, *50*, 3820-3823
49. Alapati, S. V.; Johnson, J. K.; Sholl, D. S. J. *Phys. Chem. B*. **2006**, *110*, 8769-8776
50. Cho, Y. W.; Shim, J.; Lee, B. *CALPHAD* **2006**, *30*, 65-69
51. Kojima, Y.; Kawai, Y. *J. Alloy. Compounds.* **2005**, *395,* 236-239
52. Isobe, S.; Ichikawa, T.; Tokoyoda, K.; Hanada, N.; Leng, H.; Fujii, H.; Kojima, Y. *Thermochimica Acta* **2008,** *468*, 35-38
53. Chen, P.; Xiong, Z.; Luo, J.; Tan, K. L. *J. Phys. Chem. B* **2003**, *107*, 10967-10970
54. Zhang, T.; Isobe, S.; Wang, Y.; Hashimoto, N.; Ohnuki, S. *RSC Adv.* **2013**, *3*, 6311-6314
55. Aguey-Zinsou, K.; Yao, J.; Guo, Z. X. *J. Phys. Chem. B* **2007**, *111*, 12531-12536
56. Hoang, K.; Janotti, A.; Van de Walle, C. G. *Angew. Chem. Int. Ed.* **2011**, *50*, 10170-10173
57. Hu, Y. H.; Ruckenstein, E. *J. Phys. Chem. A* **2003**, *107*, 9737-9739
58. Würthwein, E.; Sen, K. D.; Pople, J. A.; von Ragué Schleyer, P. *Inorganic Chemistry* **1983,** *22*, 496-503
59. Miwa, K.; Ohba, N. Towata, S. *Phys. Rev. B* **2005**, *71*, 195109

60. Huq, A.; Richardson, J. W.; Maxey, E. R.; Chandra, D.; Chien, W. *J. Alloy. Compounds.* **2007**, *436*, 256-260
61. Demir-Cakan, R.; Tang, W. S.; Darwiche, A.; Janot, R. *Energy Environ. Sci.* **2011**, *4*, 3625-3631
62. Ludueña, G. A.; Wegner, M.; Bjålie, L.; Sebastiani, D. *Chem. Phys. Chem.* **2010**, *11*, 2353-2360
63. Ohoyama, K.; Nakamori, Y.; Orimo, S.; Yamada, K. *J. Phys. Soc. Jpn.* **2005**, *74*, 483-487
64. Noritake, T.; Nozaki, H.; Aoki, M.; Towata, S.; Kitahara, G.; Nakamori, Y.; Orimo, S. *J. Alloy. Compounds.* **2005**, *393*, 264-268
65. Funke, V. K.; Richtering, H. *Ber. Bunsenges. Phys. Chem.* **1968**, *72*, 619-623
66. Ramzan, M.; Ahuja, R. *J. Appl. Phys.* 2009, *106*, 016104
67. Alpen, U. *J. Solid State Chem.* **1979**, *29*, 379-392
68. Li, W.; Wu, G.; Xiong, Z.; Feng, Y. P.; Chen, P. *Phys. Chem. Chem. Phys.* **2012**, *14*, 1596-1606
69. Blomqvist, A.; Araújo, C. M.; Scheicher, R. H.; Srepusharawoot, P.; Li, W.; Chen, P,.; Ahuja, R. *Phys. Rev. B.* **2010**, *82*, 024304
70. Meisner, G. P.; Pinkerton, F. E.; Meyer, M. S.; Balogh, M. P.; Kundrat, M. D. *J. Alloy. Compounds.* **2005**, *404-406*, 24-26
71. Pinkerton, F. E. *J. Alloy. Compounds.* **2005**, *400*, 76-82
72. Cao, H.; Wang, H.; He, T.; Wu, G.; Xiong, Z.; Qiu, J.; Chen, P. *RSC Adv.* **2014**, *4*, 32555-32561
73. Shaw, L. L.; Ren, R.; Markmaitree, T.; Osborn, W. *J. Alloy. Compounds.* **2008**, *448*, 263-271
74. Cheng, X.; Shi, Z.; Glass, N.; Zhang, Lu.; Zhang, J.; Song, D.; Liu, Z.; Wang, H.; Shen, *J. Power Sources* **2007**, *165,* 739-756
75. Chien, W.; Chandra, D.; Lamb, J. H. *JCPDS-International Centre for Diffraction Data* **2008**, 190-195
76. Lamb, J. H.; Chandra, D.; Chien, W. *J. Phys. Chem. C* **2011**, *115*, 14386-14391
77. Lu, Chun.; Hu, J.; Kwak, J. H.; Yang, Z.; Ren, R.; Markmaitree, T.; Shaw. L. L. *J. Power Sources* **2007**, *170,* 419-424
78. Isobe, S.; Ichikawa, T.; Hino, S.; Fujii, H. *J. Phys. Chem. B* **2005**, *109,* 14855-14858
79. Miceli, G.; Cucinotta, C. S.; Bernasconi, M.; Parrinello, M. *J. Phys. Chem. C* **2010**, *114,* 15174-15183
80. Shaw, L. L.; Osborn, W.; Markmaitree, T.; Wan, X. *J. Power Sources* **2008**, *177*, 500-505
81. Ichikawa, T.; Isobe, S.; Hanada, N.; Fujii, H. *J. Alloy. Compounds.* **2004**, *365*, 271-276
82. Ichikawa, T.; Hanada, N.; Isobe, S.; Leng, H.; Fujii, H. *J. Phys. Chem. B* **2004**, *108,* 7887-7892
83. Isobe, S.; Ichikawa, T.; Kojima, Y.; Fujii, H. *J. Alloy. Compounds.* **2007**, *446-447*, 360-362
84. Anderson, P. A.; Chater, P. A.; Hewett, D. R.; Slater, P. R. *Faraday Discuss.* **2011**, *151*, 271-284
85. Palade, P.; Lungu, G. A.; Husanu, A. M. *J. Alloy. Compounds.* **2010**, *505*, 343-347
86. Varin, R. A.; Jang, M. *J. Alloy. Compounds.* **2011**, *509*, 7143-7151
87. Dong, B.; Ge, J.; Teng, Y.; Gao, J.; Song, L. *J. Mater. Chem. A* **2015**, *3*, 905-912
88. Markmaitree, T.; Ren, R.; Shaw, L. L. *J. Phys. Chem. B* **2006,** *110,* 20710-20718
89. Nöth, H.; Beyer, H. *Chem. Ber.* **1960***, 93*, 2251-2263
90. Hamilton, C. W.; Baker, R. T.; Staubitz, A.; Manners, I. *Chem. Soc. Rev.* **2009**, *38*, 279-293
91. Stephen, F. H.; Pons, V.; Baker, R. T. *Dalton Trans.* **2007**, 2613-2626
92. Klooster, W. T.; Loetzle, T. F.; Siegbahn, P. E. M.; Richardson, T. B.; Crabtree, R. H. *J. Am. Chem. Soc.* **1999,** *121*, 9337-9344
93. Nguyen, M. T.; Nguyen, V. S.; Matus, M. H.; Gopakumar, G. Dixon, D. A. *J. Phys. Chem. A* **2007,** *111,* 679-690
94. Xiong, Z.; Yong, C. K.; Wu, G.; Chen, P.; Shaw, W.; Karkamar, A.; Autrey, T.; Jones, M. O.; Johnson, S. R.; Edwards, P. P.; David, W. I. F. *Nature Materials* **2007**, *7*, 138-141
95. Kang, X.; Fang, Z.; Long, L.; Cheng, H.; Yao, X.; Lu, G.; Wang, P. *Adv. Mater*. **2008**, *20*, 2756-2759
96. Wu, H.; Zhou, W.; Yildirim, T. J. Am. Chem. Soc. **2008**, *130*, 14834-14839
97. Kang, X.; Fang, Z.; Long, L.; Cheng, H.; Yao, X.; Lu, G.; Wang, P. *Adv. Mater*. **2008**, *20*, 2756-2759
98. Osborn, W.; Sadowski, T.; Shaw, L. L. *Scripta Materialia* **2011,** *64*, 737-740
99. Xiong, Z.; Chua, Y. S.; Wu, G.; Xu, W.; Chen, P.; Shaw, W.; Karkamkar, A.; Linehan, J.; Smurthwaite, T.; Autrey, T. *Chem. Commun.* **2008**, 5595–5597

100. Kim, D. Y.; Singh, N. J.; Lee, H. M.; Kim, K. S. *Chem. Eur. J.* **2009**, *15*, 5598-5604
101. Luedtke, A. T.; Autrey, T. *Inorganic Chemistry* **2010**, *49*, 3905-3910
102. Sutton, A.; Burrell, A. K.; Dixon, D. A.; Garner III, E. B.; Gordon, J. C.; Nakagawa, T.; Ott, K. C.; Robinson, J. P.; Vasiliu, M. *Science* **2011**, *311*, 1426-1430
103. Tang, Z.; Tan, Y.; Chen, X.; Yu, X. *Chem. Commun*. **2012**, *48*, 9296-9298
104. Tang, Z.; Zhang, L.; Wan, L.; Huang, Z.; Liu, H.; Guo, Z.; Yu, X. *Int. J. Hydrogen Energy* **2016**, *41,* 407-412Osborne11
105. Moury, R.; Moussa, G.; Demirci, U.; Hannauer, J.; Bernard, S.; Petit, E.; van der Lee, A.; Miele, P. *Chem. Chem. Phys.* **2012**, *14*, 1768-1777
106. Hügle, T.; Kühnel, M. F.; Lentz, D. *J. Am. Chem. Soc.* **2009**, *131*, 7444-7446
107. Goubeau, V. J.; Ricker, E. *Z. Anorg. Allg. Chem.* **1961**, *310*, 123-142
108. Wu, H.; Zhou, W.; Pinkerton, F. E.; Udovic, T. J.; Yildirim, T.; Rush, J. J. *Energy Environ. Sci*. **2012**, *5*, 7531-7535
109. Chua, Y. S.; Pei, Q.; Ju, X.; Zhou, W.; Udovic, T.; Wu, G.; Xiong, Z.; Chen, P.; Wu, H. *J. Phys. Chem. C* **2014**, *118*, 11244-11251
110. Moury, R.; Demirci, U.; Ban, V.; Filinchuk, Y.; Ichikawa, T.; Zheng, L.; Goshome, K.; Miele, P. *Chem. Mater*. **2014**, *26*, 3249-3255
111. Moury, R.; Robeyn, K.; Filinchuk, Y.; Miele, P.; Demirci, U. B.; *J. Alloy. Compounds* **2016**, *659*, 210-216
112. Vajo, J. J.; Skeith, S. L.; Mertens, F.; Jorgensen, S. W. *J. Alloy. Compounds* **2005,** *390*, 55-61
113. Lu, J.; Fang, Z.; Sohn, H. Y. *J. Power Sources* **2007,** *172*, 853-858
114. Haertling, C. L.; Hanrahan, R. J.; Tesmer, J. R. *J. Phys. Chem. C* **2007,** *111,* 1716-1724
115. Prosini, P. P.; Cento, C.; Gislon, P. *Int. J. Green Energy* **2010**, *7,* 103-115,
116. Gilson, P.; Prosini, P. P. *Int. J. Hydrogen Energy* **2011**, *36*, 240-246
117. Aiello, R.; Sharp, J. H.; Matthews, M. A. *Int. J. Hydrogen Energy* **1999,** *24,* 1123-1130
118. Miyaoka, H.; Ichikawa, T.; Fujii, H.; Kojima, Y. *J. Phys. Chem. C* **2010,** *114,* 8668–8674
119. Liu, L.; Hu, D.; He, T.; Zhang, Y.; Wu, G.; Chu, H.; Wang, P.; Xiong, Z.; Chen, P. *J. Alloy. Compounds* **2013,** *552*, 98-101
120. Liu, L.; Wu, G.; Xiong, Z.; He, T.; Chen, P. *Int. J. Hydrogen Energy* **2015,** *40,* 429-434

2.0 Experimental

In attempt to address the objectives proposed in section 1.3, a series of practical experiments were conducted to optimise the hydrogen release from the three systems. Accordingly the results and mechanistic deductions presented in chapters 3 (LiH-melamine), 4 (LiH-urea) and 5 (LiH-2-cyanoguanidine) are derivatives of the sample handling, preparation and analytical techniques used, which form the topics of this chapter.

A control of substance hazardous to health form and risk assessment were completed and signed by lab managers before the start of each new procedures; and any waste materials disposed of according to the guidelines provided by the corresponding materials safety data sheet.

2.1 Sample handling

Handling and long term storage of air sensitive materials such as LiH were conducted in high purity argon (B.O.C. 99.9% pure) filled UniLab and UniStar gloveboxes supplied by MBraun. The atmosphere in the gloveboxes are maintained at O_2 < 0.5 ppm and H_2O < 0.1 by a continuous circulation through a built in filter unit containing copper catalyst supported on aluminium substrate which removes oxygen and molecular sieve which removes moisture. A breach of the specified oxygen and moisture level could result in uncontrolled degradation of the air sensitive materials used and hence requires the glovebox to be purged with the high purity argon supply until the atmosphere returns to acceptable levels. Moreover it is vital to ensure any tools, equipment or non-air sensitive reactants introduced into the gloveboxes are thoroughly dried before transporting through the box antechambers. The antechambers are evacuated fully and refilled with argon three times to ensure oxygen is completely removed.

Once prepared, samples are stored in standard 7 or 10 ml glass vials and sealed with parafilm. Sealed sample vials can adequately keep out moisture and oxygen to allow transportation outside the gloveboxes for short periods of time.

2.2 Sample preparation

2.2.1 Planetary ball milling

Mechanical milling of particles through Coriolis forces in the planetary Retsch P100 ball mill is crucial to facilitate the dehydrogenation between LiH and the organic amines described in this thesis. As reviewed in the previous chapter, ball milling is an effective means to reduce particle size, provides intimate mixing in multi-component solid state experiments and introduce defects which have an impact on reaction pathway.[1-7] Through vigorous experimentation, a specific milling 'recipe' is often developed for each hydrogen storage system which can be broken down into milling energy, duration and milling sequence. Milling energy is accumulated over the duration of the experiment by two variables: milling speed and the ball to powder ratio. Whilst milling sequence is used to allow cooling for highly reactive systems in which reaction can be initiated by friction heat.

50 ml stainless steel milling jars were utilised in all of the ball milling preparations described in this thesis. Air sensitive samples were sealed with a specialist bracket in the gloveboxes described previously allowing the samples to be milled under argon (figure 2-1). Milling is conducted with ten 10 mm diameter stainless steel balls each weighing approximately 4 g unless otherwise specified. In order to account for the gradual wear and tear of these milling balls, the ball to powder ratio of every experiment was calculated according to the weight of 10 balls combined.

Figure 2-1. Air sensitive clamp and the 50 ml stainless steel milling jars

The respective reactants were weighed and loaded into the milling jar with the milling balls and locked in place by the spider clamp in the planetary mill (figure 2-2). Hereto the milling speed, time and the milling programme can be determined *via* the digital control interface on the Retsch

PM100. For the 50 ml milling jar, the degree of milling can be loosely defined as a function of milling speed, where speeds lower than and equal to 150 RPM is defined as the critical mixing stage,[8-9] otherwise termed as intimate mixing; and speeds above 450 RPM are known as high energy milling as the milling balls moves in a chaotic manner inside the milling jar colliding not only with the powder against the milling jar but also between one another.

Figure 2-2. The Retsch PM 100 planetary mill with the spider clamp

2.2.2 Pressure monitored ball milling

Energetic ball milling is known to induce dehydrogenation.[4-5] To monitor the milling conditions as a function of pressure increase in the milling jar, the PM GrindControl accessory from Retsch can be used with the 250 ml stainless steel jar. Changes in pressure are measured with respect to grinding time by the built in pressure sensor that can operate to 500 kPa, *via* a wireless transmitter to a computer.

2.2.3 Furnaces

For preliminary tests and bulk heat treatment of samples the bench furnaces were employed with a Eurotherm 3612 temperature controller. 12 mm diameter quartz tubes with 2 mm wall thickness were used and an argon or nitrogen purge can be used with a rubber septum.

2.3 Analysis and characterisation techniques

The hydrogen desorption mechanism and performances of the proposed LiH-organic amines systems were characterised by a variety of techniques centred around crystallography, spectroscopy and thermal analysis. The fundamental principles of these techniques are described in the following sections. The experimental outputs are also detailed and how these relate to mechanistic deductions and system performance pertaining to hydrogen storage is discussed. Protocols adopted during data collection and analysis are also provided.

2.3.1 Crystallography and diffraction

Crystallography concerns the laws governing crystalline solids in terms of their periodic atomic arrangement in three-dimensional space. By identifying the repeating patterns in a crystal, otherwise known as unit cell (figure 2-3), the chemical bonding of a crystalline material can be determined which dictates a vast array of physical and chemical properties such as melting point, mechanical strength and ionic conductivity. In the domain of hydrogen storage materials, crystal structure can be used to postulate the diffusion mechanism of ions during hydrogen cycling as demonstrated in section 1.2 using the example of Li-N-H materials. Moreover, the crystallographic studies of LiH.B-N compounds described in section 1.3, elucidated the effect of Li^+ in invoking initial deprotonation of protic N-H groups and define lithium's role in mass transport of LiAB and LiHB during dehydrogenation. In a similar manner, the study of crystals will form an important basis for the mechanistic studies described in this thesis.

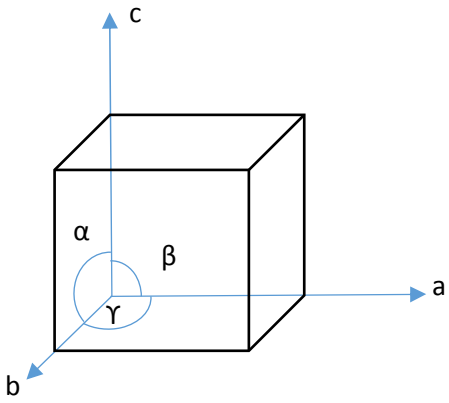

Figure 2-3. A crystal unit cell, the smallest group of atoms defined by a space group and unit cell parameters

The crystal structure of a crystalline solid is studied using diffraction, by which the unit cell parameters and space group (crystal symmetry) are derived through mathematical modelling and refinement. Diffraction experiments use beams of radiation, often X-ray or neutron radiation, with a wavelength comparable to that of common chemical bonds (between 1 and 2 Å) on either powder or single crystal samples. During a diffraction experiment a coherent monochromatic beam of radiation (**a** and **b**) is irradiated on a sample (figure 2-4). If the sample is crystalline, a diffraction pattern is observed according to Braggs law:[10]

$$n\lambda = 2d_{hkl}\sin\Theta \qquad (2\text{-}1)$$

where n is the integral multiple of the incident wavelength, λ; d_{hkl} is the spacing between oriented crystal lattice planes denoted by Miller indices hkl; and Θ is the scattering angle at which the radiation reflected by the lattice planes interfere constructively. The diffracted wavelength is in phase when **xyz** is zero or an integral multiple, n, of the incident wavelength, λ, hence:

$$\mathbf{xyz} = n\lambda \qquad (2\text{-}2)$$

Since the space group and unit cell dimensions are often unique to a particular material, diffraction patterns can be employed as a fingerprint to identify and even differentiate distinct between phases in a sample.

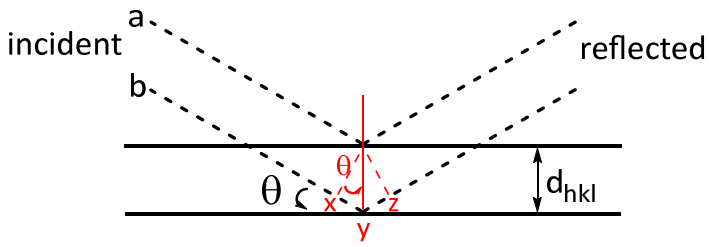

Figure 2-4. Diffraction of a radiation by a crystal

In the case of ball milled powder samples used in this thesis, the Debye-Scherrer method of powder diffraction is utilised, which assumes that crystallites are randomly oriented in fine a powder.[11-12] The resulting diffracted radiation from a plane (*hkl*) with each reflections of d_{hkl} hence yield discrete continuous cones of intensity with cone angles of 2Θ, rather than single narrow intensities as found in single crystal diffraction experiments (figure 2-5). A cross-section of these cones will produce a two dimensional diffraction pattern, where intensities, or Bragg peaks can be found at certain values of 2Θ for each d_{hkl} in the crystal obeying Bagg's law.

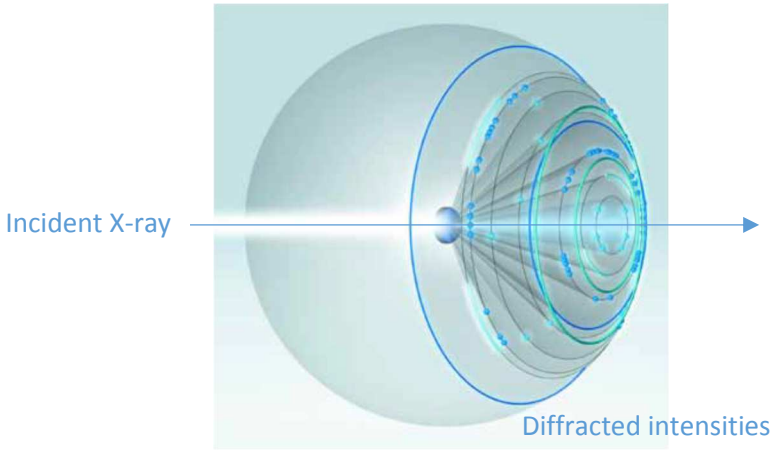

Figure 2-5. Debye-Scherrer cone diffraction from a powder sample[13]

The d_{hkl}-spacing, intensity and peak form are the main contributing factors for determining the crystal structure as they relate directly to the positions of atoms and size of a unit cell. The presence or absence of certain reflections is determined by the space group and in total, there are 230 space groups. Each space group is a unique 3D pattern which expresses the crystal symmetry in terms of the hierarchy of 7 crystal systems, 14 Bravais lattices and 32 point groups as summarised in table 2-1. The crystal system is derived from the d_{hkl}-spacing to describe the geometry of the unit cell, the Bravais lattices to describe the crystal configuration and point group to define the symmetry operating within the unit cell. Details of each space group can be accessed from the International Tables of X-Ray Crystallography.[14] Mathematical modelling of diffraction patterns through algorithms such as the Rietveld method can extract useful information such as the precise crystal structure and the composition of known phases within a sample.

Diffraction techniques based on different radiation sources are often used to complement one another. For example, while X-ray diffraction is the widely adopted laboratory-based technique, the electromagnetic radiation interacts with the electron cloud around an atom resulting in poor scattering lengths in lighter elements. Moreover laboratory sources are often weaker in power and thus requiring a longer time to acquire signal intensity per data point leading to potential timing issues for *in situ* experiments. Neutron based experiments on the other hand utilise a beam of neutrons which interacts with the nucleus of elements. Scattering of neutrons by a nucleus is dependent on its scattering length, *b*, which is characteristic to a particular isotope of an element. Neutron diffraction is particularly useful in the determination of hydrogen positions in hydrogen storage materials by isotopic labelling of hydrogen by deuterium as isotopes have neutron coherent scattering lengths of -3.741 and 6.671 fm respectively. Neutron diffraction allows the atomic position in 3D space to be effectively located with respect to its neutron position, providing structural information that complements X-ray diffraction which probes the

electron density distribution (form factor). However each neutron experiment requires authorisation from the respective national facilities which can take up to 6 months in the application process, with a possibility of not being granted time on the beamlines. The diffraction experiments employed in this thesis are described in the following subsections.

Table 2-1. Space group table based on crystal system[11-12]

Crystal System	Unit Cell Parameters	Bravais Notation	Point Groups	d_{hkl}
Triclinic	$\alpha \neq \beta \neq \gamma \neq 90°$ $a \neq b \neq c$	P	$1, \bar{1}$	$\frac{1}{d_{hkl}} = 1/V^2 \{h^2b^2c^2\sin^2\beta + k^2a^2c^2\sin^2\beta + l^2a^2\sin^2\beta + l^2a^2b^2\sin^2\gamma + 2hkabc^2(\cos\alpha\cos\beta - \cos\gamma) + 2kla^2bc(\cos\beta\cos\gamma - \cos\alpha) + 2hlab^2c(\cos\alpha\cos\gamma - \cos\beta)\}$ $V = abc\sqrt{(1 - \cos2\gamma - \cos2\beta - \cos2\gamma + 2\cos\alpha\cos\beta\cos\gamma)}$
Monoclinic	$\alpha = \gamma = 90°$ $\beta \neq 90°$ $a \neq b \neq c$	P, C	$2, m, 2/m$	$\frac{1}{d_{hkl}} = \frac{1}{\sin^2\beta}\left(\frac{h^2}{a^2} + \frac{k^2\sin^2\beta}{b^2} + \frac{l^2}{c^2} + \frac{2hcos\beta}{ac}\right)$
Orthorhombic	$\alpha = \beta = \gamma = 90°$ $a \neq b \neq c$	P, C, I, F	$222, mm2, mmm$	$\frac{1}{d_{hkl}} = \frac{h^2 + k^2 + l^2}{a^2}$
Tetragonal	$\alpha = \beta = \gamma = 90°$ $a = b \neq c$	P, I	$4, \bar{4}, 4/m, 422, 4mm, \bar{4}2m, 4/mmm$	$\frac{1}{d_{hkl}} = \frac{h^2 + k^2}{a^2} + \frac{l^2}{c^2}$
Trigonal (Rhombohedral)	$\alpha = \beta = \gamma \neq 90°$ $a = b = c$	R	$3, \bar{3}, 32, 3m, \bar{3}m$	$\frac{1}{d_{hkl}} = \frac{3}{4}\left(\frac{h^2 + k^2 + l^2}{a^2}\right) + \frac{l^2}{c^2}$
Hexagonal	$\alpha = \beta = 90°$ $\gamma = 120°$ $a = b \neq c$	P	$6, \bar{6}, 6/m, 622, 6mm, \bar{6}m2, 6/mmm$	
Cubic	$\alpha = \beta = \gamma = 90°$ $a = b = c$	P, I, F	$23, m3, 432, \bar{4}3m, m3m$	$\frac{1}{d_{hkl}} = \frac{h^2 + k^2 + l^2}{a^2}$

2.3.1.1 Powder X-ray Diffraction

Laboratory powder X-ray diffraction (PXD) employs a monochromatic X-ray tube generating Cu or Mo K_α radiation of 1.5148 and 0.7107 Å respectively. The X-ray irradiated onto a sample interacts with the electron density within the material. While the majority of the radiation would be transmitted through the sample, radiation can also be elastic reflected, photoabsorbed, and Rayleigh and Compton scattered (figure 2-6). Diffraction patterns for crystallography are extracted from the Rayleigh (elastic) scattered radiations.

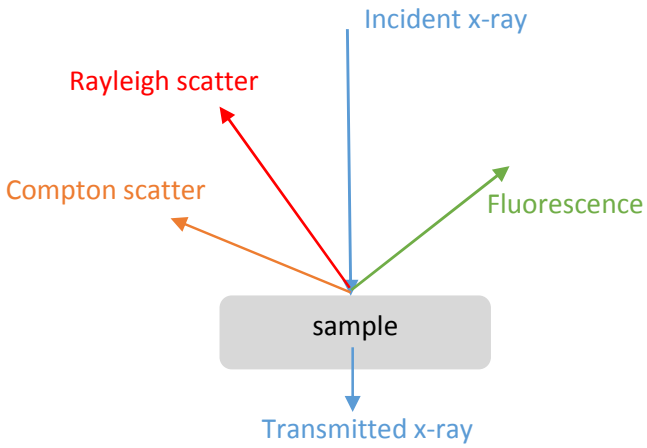

Figure 2-6. X-ray interaction with matter

A typical laboratory diffractometer consists of three major elements: the X-ray source, a sample holder and a detector (figure 2-7).[12] Whilst the X-ray source is commonly fixed in position, the sample holder and detector are independent revolving parts precisely aligned to the ω and 2Θ axes respectively. The detector is placed a fixed distance from the 2Θ axis on the Rowland (focusing) circle, whereas the sample holder usually has some degree of freedom around the ω axis for reflective flat plate holders (Bragg-Brentano geometry), and complete rotational freedom for transmission capillaries (Debye-Scherrer) (figure 2-8). The X-ray source is focused to the ω axis and can be filtered by a slit according to the size of sample stage used to reduce angular dispersion and improve spatial resolution. During the experiment, the detector revolves around the sample collecting diffracted intensities in designated increments of 2Θ.

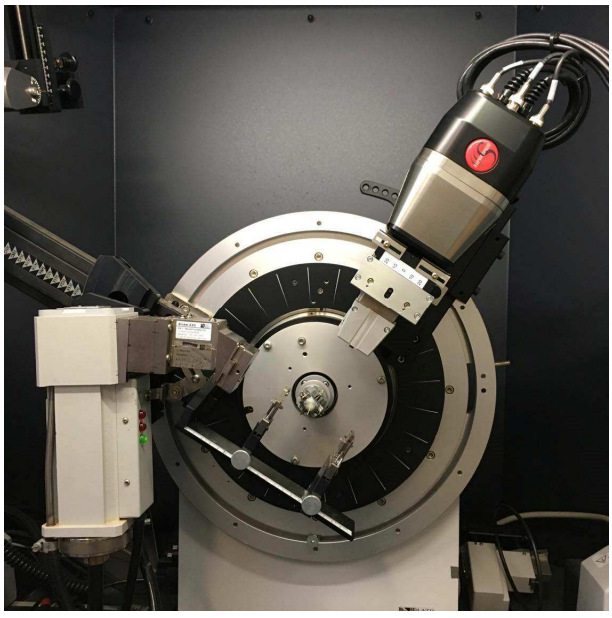

Figure 2-7. The Bruker D8 powder diffractometer set up

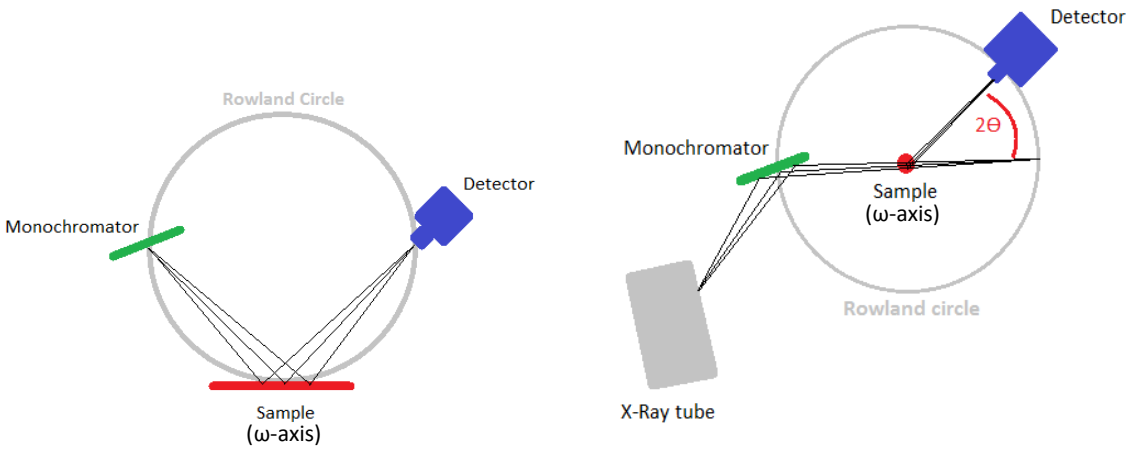

Figure 2-8. The flat plate (reflection, left) and capillary (transmission, right) sample geometries

Two diffractometers were used for data collection for the work described in this thesis: the Bruker D8 Advance for transmission capillary experiments and the PANalytical X'pert Pro for flat plate experiments. Sample preparation and data collection specific to the two instruments are described below.

The first step for preparing a powder sample is grinding the sample in a mortar and pestle to produce a well dispersed powder mixture of randomly oriented crystallites of dimensions of the order of microns. Air sensitive samples are examined using sealed silica glass capillaries supplied by Hilgenberg of 0.5 and 0.7 mm in diameter on the D8, or the air sensitive flat plate stage for the X'pert instrument. The spinning flat plate on the X'pert can also be used for non-air sensitive samples.

The capillary filling procedure involves first sitting the fine glass capillary tube in a larger, standard laboratory capillary sleeve for easier manoeuvring. Utilising the larger opening of the capillary, the powder is allowed to fall into the capillary by gentling rubbing the ridged surface of a pair of tweezers against the sleeve capillary. Once over an inch of the capillary has been filled the fine glass capillary is sealed with high vacuum silica grease and brought outside the glovebox *via* the antechamber. The fine glass capillary is then fixed onto the edge of a lab bench using blue-tak and sealed by flame.

The sealed capillary is transported to the D8 instrument and mounted on a goniometer using beeswax (figure 2-9). The capillary is aligned to the ω axis of the diffractometer and loaded onto the diffractometer. For the 0.7 mm capillary a 2 mm divergence slit is used, whereas for the 0.5 mm capillary a 1 mm or smaller slit is preferred.

On the other hand, the air sensitive flat plate for the X'pert is prepared by filling the circular cavity of the flat plate sample holder. The powder is packed tightly into the cavity using a glass slide while ensuring a flat surface level to the sample holder. This is crucial as the X-ray is aligned to the ω axis of the diffractometer which is positioned about the centre of the circular cavity of the filled sample holder. The flat plate is then mounted onto the goniometer stage and covered by the air sensitive bracket with an air-tight polymer window (Figure 2-10). The holder is then transported outside of the glovebox through the antechamber and mounted onto the diffractometer for data collection. A 10 mm divergence slit is used for all flat plate experiments.

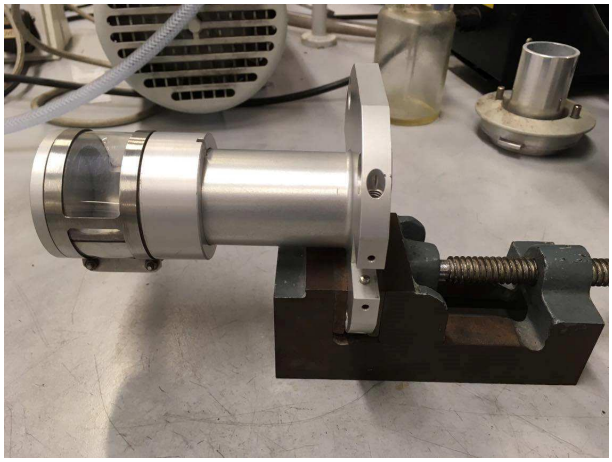

Figure 2-10. Air sensitive bracket for the PANalytical X'pert diffractometer

Phase identification experiments could vary from 20 minutes to 1 hr depending on the quality of the sample and the rate of sample degradation (for example, H_2NCN in air). A standard

experiment examines the intensities between 5 and 85° 2Θ at a step size of 0.0167° on both Bruker and PANalytical instruments. The data collection is extended to *ca.* 13 h with a smaller step size of 0.008° when further analysis, such as structural indexing and refinement are intended.

Phase identification was conducted using the PANalytical High Score software suite and the PowderCell package supported by the International Centre for Diffraction data Powder Diffraction File database (ICDD PDF) and the Inorganic Crystal Structure Database (ICSD) respectively.

For visualising diffraction data, the Winplotr package developed as an extension to the FullProf suite has a wide range of functionalities including viewing multiple experimental patterns on one set of axes and can accommodate the different experiment output files generated by the D8 (.raw) and the X'pert (.xrdml). The PowDLL software package is used to convert diffraction data between various formats.

2.3.1.2 Powder Neutron Diffraction

Neutron radiation is conventionally generated by either a nuclear reactor or a spallation source. Different to X-ray, the neutron radiation is a particle beam with wave characteristics. The wavelength of a neutron, λ, is governed by the de Broglie equation:

$$\lambda = h / mv \qquad (2\text{-}3)$$

where h is the Plank constant, m is the mass of the neutron and v its velocity.

Apart from the aforementioned sensitivity to light elements, neutrons can be used to distinguish elements with similar valence electron configurations such as those adjacent to one another on the periodic table. Due to low adsorption and weak scattering it has a high penetration depth therefore high acquisition rates and good temporal resolution. Neutron radiation also contains a substantial magnetic moment which can probe the magnetic structure of a material.[15]

The powder neutron diffraction (PND) experiment for the purpose of this thesis was conducted at the constant wavelength nuclear reactor source at ILL facility in Grenoble, France. This high-flux fission reactor uses highly enriched ^{235}U source to produce, at a steady state, 1.5 x 10^{15} $s^{-1}cm^{-2}$ of moderated neutrons at a maximum thermal power of 58.3 MW. D_2O is employed as both coolant and moderator.[15]

The thermal beamline H11 is divided into two parallel beams, the high intensity D20 which was used for varying temperature *in situ* measurements, and the high flux D2B which was used for *ex situ* experiments to investigate the dehydrogenation mechanism between LiH and melamine, detailed in chapter 3 of this thesis.

The experimental set up of the D20 is depicted in figure 2-11. The neutron beam is first filtered by one of several reflective Germanium monochromators into the desired wavelengths by rotating the crystal monochromator.[16] (120 ° take-off angle for a λ = 1.36 and 1.87 Å) The beam is then shielded by one of its five take-off ports for a designated instrument resolution and irradiates the sample residing in an argon flowing quartz tube inside a furnace. The diffracted radiation is simultaneously detected by a large microstrip multidetector, at which the intensities are accumulated for a set period of time, for example 10 minutes, to produce a well-defined diffraction pattern along the 2Θ axis. A more in depth description of the instrument can be found on the D20 homepage on the ILL website listed in the reference.

Approximately 2 g of samples were measured for each *in situ* experiment which were loaded into quartz tubes inside an argon glovebox immediately prior to measurement. Experiments on D20 were conducted under the supervision of beamline scientist Dr. Thomas Hansen.

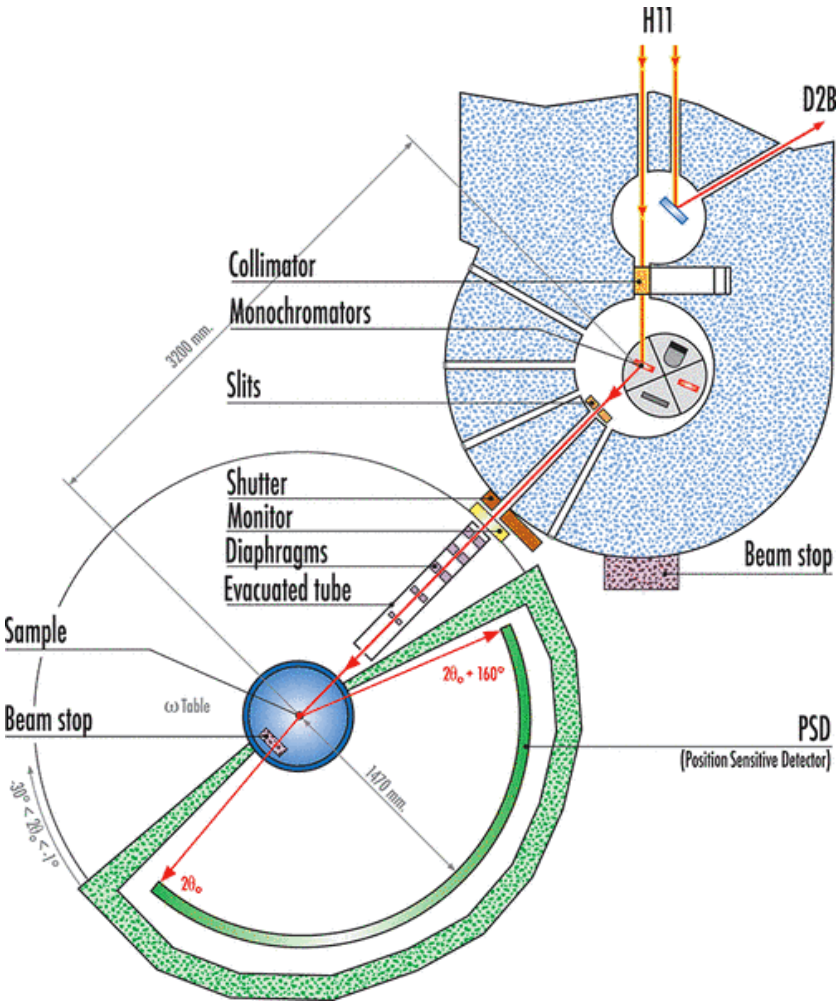

Figure 2-11. Schematic of the D20 Neutron Beamline[16]

Ex situ room temperature experiments were conducted on the D2B instrument (figure 2-12). The shared polychromatic neutron beam is diffracted by a Ge monochromator at a take-off angle of 135° for ultra-high resolution (λ = 1.59 Å). This wavelength can be easily adjusted by rotating the Ge monochaomator crystal to different orientations. Vanadium cells were employed as sample cans sealed with indium wire for the air sensitive samples investigated. 128 He^3 detector blocks are spaced out at 1.25° 2Θ at which a complete diffraction pattern can be revealed in 25 steps of 0.05° over 30 minutes.[17] 2 g of powder per sample is loaded and sealed into the vanadium sample cans provided by ILL inside an argon glovebox before sending to the ILL facility. Experiments on this beamline were conducted with Dr. Clemens Ritter whom also provided valuable discussions for the analysis of PND data.[17]

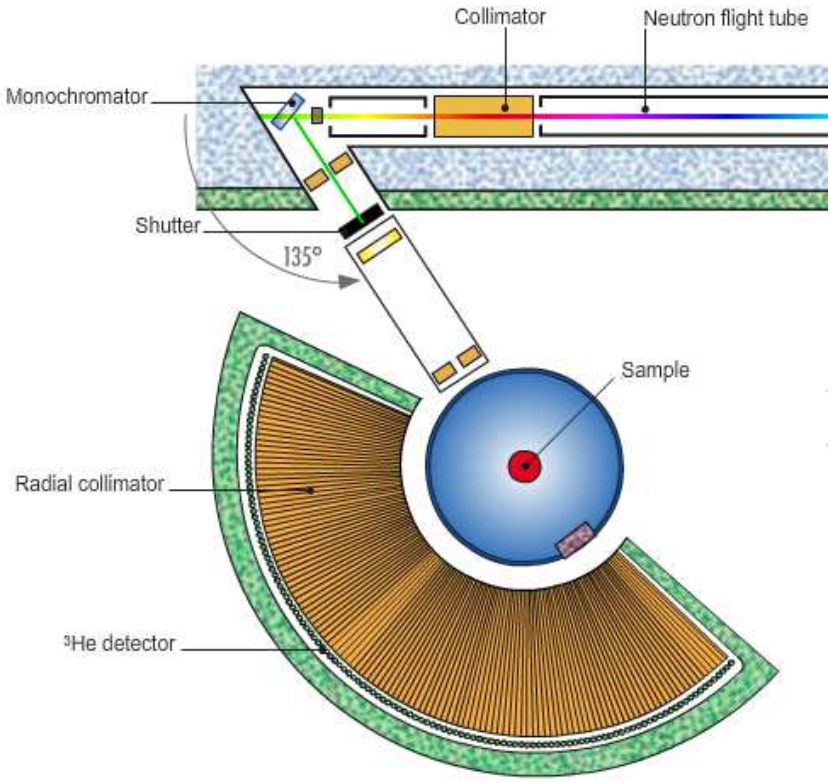

Figure 2-12. Schematic of the D2B Neutron Beamline[17]

2.3.1.3 Rietveld Refinement

Diffraction data can be used on the most fundamental level to identify phase present in a sample. However further data analysis is often desired for either characterising unknown structures or to estimate the composition of known phases in the sample as a function of temperature or to clarify the course of a reaction. The Rietveld method was developed to interpret the structural information from a powder diffraction pattern by using peak shape parameters. The least square algorithm *M*, is a product of the sum of all the independent observations with respect to i^{th} steps,

Σ_i, and a calculated intensity y_{oi}, for any specific Bragg reflection, y_{ci}. This is scaled by the statistical weighting factor, w_i for either PND or PXD data (equation (2-4)).[18]

$$M = \Sigma_i w_i (y_{oi} - y_{ci})^2 \qquad (2\text{-}4)$$

The calculated intensity y_{ci} represents the peak shape function for the specific Bragg reflection denoted by its Miller indicies, *k*, which is proportional to the scale factor, s, the structure factor, F_k, L_k which consists of multiplicity, the Lorentz and the polarisation factors, the reflection profile function, φ, the preferred orientation factor, P_k, and the absorption function, A. The sample background function, y_{bi} also contributes to every data point (equation (2-5))

$$y_{ci} = s \Sigma_k L_k |F_k|^2 \phi (2\Theta_i - 2\Theta_j) P_k A + y_{bi} \qquad (2\text{-}5)$$

It should be noted that the Lorentz and polarisation factors are dependent on instrument configurations, which are characterised individually for each diffractometer (geometry, detector and beam), as well as sample factors (sample volume and geometry).

Rietveld refinement is conditional on an initial structural model being in place. For samples with known phases, .cif or .cel files (which contains cell and atomic information) can be obtained from various crystal structure databases such as the ICSD. If a new structural solution is required, a first approximation can be made, for example, with the graphical unit cell refinement package CELREF. In either instance the initial structural model must consist of a space group and the approximate unit cell parameter for calculating the first set of y_{ci}. Refinements for this thesis were performed using the General Structural Analysis System package (GSAS) developed for the US Department of Energy.[19] Through the EXP graphical users interface (EXPGUI), the atomic and profile parameters described in equation (2-5) can be refined against the initial structural model with the aid of visual and statistical tools to evaluate a 'best fit' profile for the target sample. The statistical fit is described by reliability values $R_{profile(p)}$, $R_{expected(exp)}$ and $R_{weighted\ profile(wp)}$, and X^2, that is the goodness of fit. The R-value series is defined in equations (6) to (8), where N is the number of observations, C is the number of constraints and P is the number of refinable parameters:

$$R_p = \frac{\sum_i (y_i^{obs} - y_i^{calc})}{\sum_i y_i^{obs}} \qquad (2\text{-}6)$$

$$R_{exp} = \sqrt{\frac{(N-C+P)}{\sum_i w_i (y_i^{obs})^2}} \qquad (2\text{-}7)$$

$$R_{wp} = \sqrt{\frac{\sum_i w_i (y_i^{obs} - y_i^{calc})^2}{\sum_i w_i (y_i^{obs})^2}} \qquad (2\text{-}8)$$

of which R_{wp} is the most mathematically significant as it measures directly the extent of convergence. R-values are then used to calculate the X^2 value:

$$X^2 = (\frac{R_{wp}}{R_{exp}})^2 \qquad (2\text{-}9)$$

In practice, X^2 should be close to 1 respectively to signify a good fit with a small R_{wp} value. It is important to note that this best fit profile is only the mathematical solution and therefore must be carefully verified against real physical parameters such as bond length and bond angles for the proposed crystal structure to have credible physical meaning.[20]

Once the measurement file, in the .gsas format, the structural model and the instrument file, in .prm format are defined in GSAS, Rietveld refinement according to equation (5) is launched. The first parameter to be refined is the scale factor, s, followed by fitting the background function y_{bi}, either by one of the eight predefined polynomial functions, or manually using the built-in graphical interface. The refinement should readily converge, which indicate that the fluctuation of the mathematical model for each refined parameter compared to its associated error (shift/esd) is smaller than 0.1. This is succeeded by the precise refinement of the observed Bragg reflections against the lattice parameters and zero-point correction. The reflection profile function is next refined based on the pseudo-Voigt approximation, pV (equation (2-10)):

$$pV = \eta L + (1 - \eta)G \qquad (2\text{-}10)$$

where η is the mixing factor as a linear function of 2Θ (equation (2-11)), L is the Lorentzian function (equation (2-12)) and G is the Gaussian function (equation (2-13)) in terms of the total full width half maximum (FWHM), H_k, denoted to a particular Miller indices, *k*.

$$\eta = N_A + N_B (2\Theta) \qquad (2\text{-}11)$$

$$L = \frac{2}{\pi H_k} \frac{1}{[1+4\frac{(2\theta_i - 2\theta_k)^2}{H_k^2}]} \qquad (2\text{-}12)$$

$$G = \frac{\sqrt{4\ln 2}}{H_k\sqrt{\pi}} \exp(\frac{-4\ln 2(2\theta_i - 2\theta_k)^2}{H_k^2}) \qquad (2\text{-}13)$$

The atomic positions are refined followed by the thermal displacement parameters described of the atoms' thermal motion. These can be refined either isotropically or anisotripiclly, as appropriate. The refinement is complete when all of the refining parameters are calculated together and the fit converges.

2.3.2 Other spectroscopy techniques

Spectroscopy concerns the absorption and emission of electromagnetic radiation and particle beams by matter.[21] Each branch of spectroscopy represents a specific material characteristic as a function of the probing wavelength. Three segments in the broad field of spectroscopy, namely Fourier transform Infrared (FTIR) in optical spectrometry, nuclear magnetic spectroscopy (NMR) and mass spectrometry (MS) that are used in this thesis will be reviewed in the subsequent sections.

2.3.2.1 IR spectroscopy

The field of optical spectroscopy refers to all techniques that utilises non-ionising energies.[21] From ultra-violet (UV) to IR, the physical principles of optical spectroscopy dwell in the absorption of light by matter, which induces a transition from the ground state to a particular excited state. The energy absorbed, E, is described by the substituted Maxwell equation:

$$E = hc\tilde{\nu} \qquad (2\text{-}14)$$

where h is the Plank constant, c is the speed of light in vacuum and $\tilde{\nu}$ is the wavenumber, that is the inverse of wavelength, λ. This energy is also the sum of energies associated with molecular vibration and rotation as a result of light absorption:

$$E = E_{ele} + E_{vib} + E_{rot} \qquad (2\text{-}15)$$

In the condensed phases, only E_{vib} is relevant for the IR region, while E_{ele} and E_{rot} are considered for UV and microwave wavelengths.

The fundamental IR region extends from the wavenumbers of 4000 to 400 cm^{-1} in terms of percentage transmittance. An IR spectrum represents molecule specific harmonics from atomic bonds that change their dipole moments upon infrared induced vibrations. Absorption peaks within the spectrum express bond movements such as stretching, bending, twisting, rocking and wagging modes. These modes can be further divided with respect to the symmetry of the vibration.

Features such as peak position, number of peaks, shape and their relative intensities are unique to each molecule. For compounds with known IR spectrum the technique is rapid, sensitive, and can be used quantitatively to estimate the concentration in a mixture by the Beer-Lambert law. Whilst evaluating the spectrum of a new compound can be complicated by issues such as overtones, coupling, and anharmonicity. However certain band locations and to some extent their intensities can indicate the possibility of certain bonds present in a material.

IR spectroscopy is used in hydrogen storage material research as a complementary technique to PXD, to probe bonding in structures which may not be crystalline or that have poor crystallinity due to preparations such as ball milling. It is also sensitive to phases at low concentrations and is effective at verifying isotopic labelling of hydrogen by deuterium.[3, 22-23]

In this work, a Shimazdu Fourier Transform IR (FTIR) 8400s spectrometer was employed with a diamond attenuated total reflectance (ATR) stage. Central to the spectrometer is the Michelson interferometer with a high brightness ceramic light source, which consists of a Ge-coated KBr beam splitter, and two flat mirrors, one fixed and the other movable by a precisely controlled electromagnetic drive (figure 2-13). The resolution of an interferometer is a function of the maximum path difference between the two flat mirrors, which is controlled by a He-Ne laser source (λ = 632.8 nm) at 0.85 cm^{-1}.

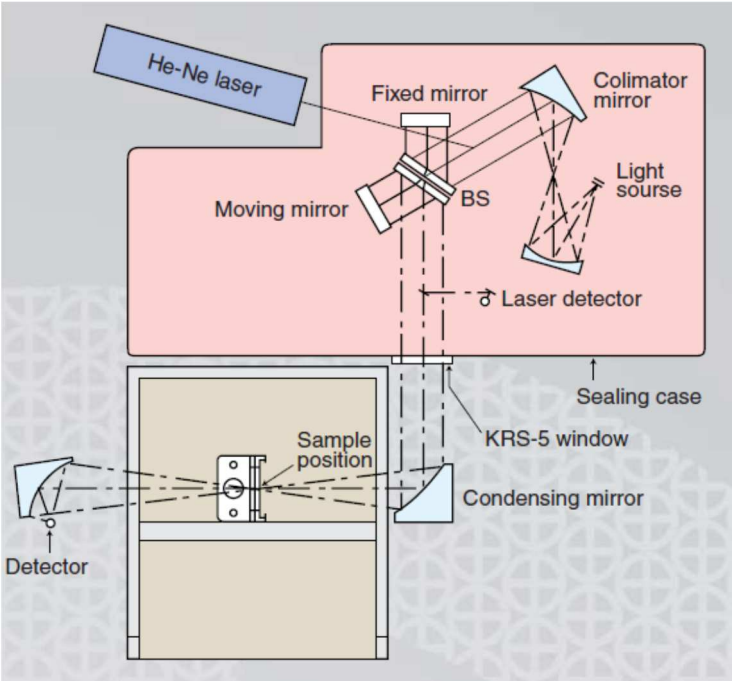

Figure 2-13. The Michelson interferometer inside the Shimazdu FTIR 8400s[24]

A temperature controlled high sensitivity Deuterated Lanthanum α Alanine doped Triglycine Sulphate detector completes the acquisition loop which sends an IR interferogram to the IRSolution software package connected to the instrument. The interferogram contains signal intensity over time, which can then be Fourier transformed into an IR spectrum which is in the frequency domain. This is then subtracted by a background function measured immediately before sample acquisition with an empty stage to form the final instrument independent transmittance spectrum.[24]

The reflective ATR stage requires minimum preparation for powder and liquid samples as the evanescent field will extend beyond the sample crystal between 0.5 to 5 µm. A powder sample is deposited in a cone-shape holder over the diamond ATR prism and packed down using a compression rod, whilst liquid samples are dispensed directly over the prism.

A standard acquisition accumulates 20 scans from 4000 to 600 cm^{-1} with a 4 cm^{-1} resolution. The Happ-Genzel apodization function is used to remove rippling from the measured signal without significantly compromising the resolution (equation (2-16)).

$$A(x) = 0.54 + 0.46 \cos\left(\frac{\pi x}{L}\right) \qquad (2\text{-}16)$$

where A(x) is the apodization function, x is the optical path difference and L is the integration range.

2.3.2.2 Solid state NMR

Nuclear magnetic resonance (NMR) spectroscopy is a technique which probes the magnetic resonance of a nucleus. In the core of this technique is a spinning nucleus, *j*, with a magnetic moment, µ, as a function of its mass, charge and angular momentum. The magnetic momentum vector of such a nucleus can be described by quantum mechanics in terms of its nuclear spin quantum number, I_j, the Plank constant, *h*, and the gyromagnetic ratio, Υ_j, that is a ratio of the magnetic moment and angular momentum of the nucleus (equation (2-17))[21]

$$\mu_j = \frac{\Upsilon_j I_j h}{2\pi} \qquad (2\text{-}17)$$

In the presence of a strong static magnetic field, B_0, the directional µ can be aligned, and its resonance under radiofrequency (RF) radiation characterised.[24] For each spinning nucleus, the isotope specific RF, the Larmor precession frequency v_0, is defined for the magnetic field applied by the Larmor correlation (equation (2-18)):

$$v_0 = \frac{|\Upsilon_j B_0|}{2\pi} \qquad (2\text{-}18)$$

It is at its Larmor frequency that the given nuclei would resonate hence its electromagnetic spectrum can be measured.[21] As an example, ^{15}N NMR used in the characterisation of LiH-melamine hydrogen storage system was measured on a 9.4T magnet, with a ϒ of -27.126 x 10^6 rad s^{-1} T^{-1}, the Larmor frequency is calculated to - 40.582 MHz.

The energy transmitted to the nuclei during resonance is the sum of contributions from the interaction between RF radiation and the spinning nuclei (E_{RF}), the potential energy of the nuclei magnet in the applied field (Zeeman energy, E_Z), electron shielding which modifies the Zeeman

effect (E_S), and spin coupling effects in terms of the indirect (E_J), dipolar (E_D) and quadropolar (E_Q) coupling (equation (2-19)).[25]

$$E_{NMR} = E_{RF} + E_Z + E_S + E_J + E_D + E_Q \qquad (2\text{-}19)$$

Of these six components, the Zeeman energy, E_Z, has the largest contribution, which can be expressed as:

$$E_Z = \frac{\Upsilon_j h I_j B_0}{2\pi} \qquad (2\text{-}20)$$

The final four terms, E_S, E_J, E_D and E_Q are orientation dependent internal interactions (coupling) within a molecule which are more complex than the equivalent in solution. The contributions of these four terms in the solid state are discussed below.

The first shielding term corresponds to the physical phenomenon where the magnetism of the nuclei is shielded by electrons, giving rise to an observed chemical shift, δ. As electrons are usually not spherically distributed around a given nucleus, shielding is anisotropic with an associated tensor, σ. Shielding modifies the Larmor frequency of the nucleus by the expression:

$$\nu = \frac{-\Upsilon B_0(1-\sigma)}{2\pi} = \nu_0 - \nu_{cs} \qquad (2\text{-}21)$$

which can be converted to a chemical shift, in the unit of ppm, with a given reference, ν_{ref} by:

$$\delta = \frac{\nu-\nu_{ref}}{\nu_{ref}} \times 10^6 \qquad (2\text{-}22)$$

In solution, due to the random tumbling of molecules, shielding is averaged into an isotropic scalar, δ_{iso} which can be used to determine the chemical environment of the nuclei. However for solid powder samples a broadened shielding powder pattern is observed which requires extensive modelling to interpret.

Indirect coupling, otherwise known as J-coupling describes the through bond spin-spin interactions. It provides clues to the macromolecular bonding network and therefore the conformation of a molecule. In solution it is one of the key component for identifying the extended structure of a molecule however in the solid state the interaction becomes insignificant in magnitude.

Dipole couple is derived from the nuclear magnetic fields interacting between the magnetic moments of distinct nuclei. The interaction can be homonuclear or heteronuclear to give rise to the characteristic 'Pake doublet' in powder samples, which is a mirror image to the shielding pattern (figure (2-14)). Note that at Θ = 54.756° with respect to the direction of the magnetic field B_0, the dipole interaction is zero (figure 2-15).

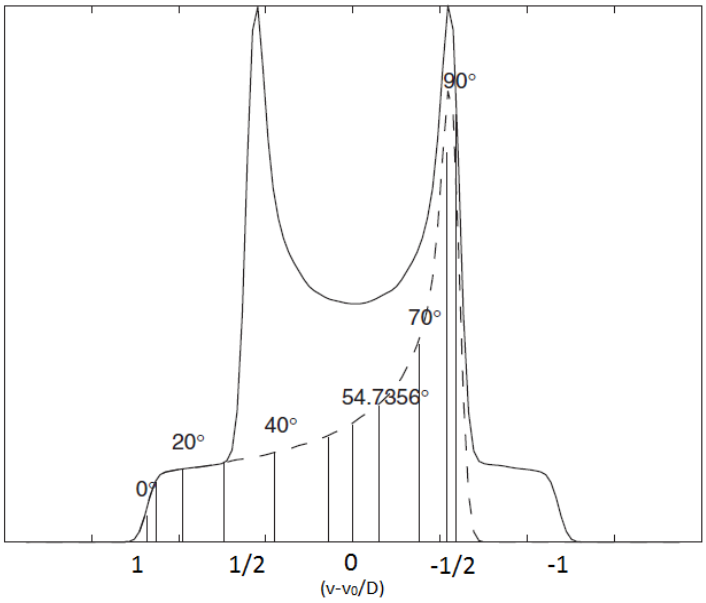

Figure 2-14. Typical heteronuclear Pake doublet for the A spin of an AX spin system. The dashed line shows the subspectra with the resonance frequency at an angle Θ with respect to the magnetic field B_0.[25]

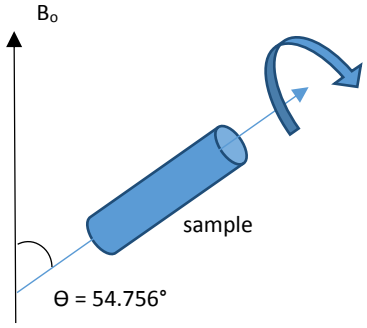

Figure 2-15. Sample geometry with respect to the magnetic field of the spectrometer B_0 during a MAS spinning experiment.

For nuclei with spin, $I_j > 1/2$ (e.g. $^2H = 1$, $^7Li = 3/2$), a non-spherical charge distribution around the nuclei tends to interact with a nearby electric field gradient. Otherwise termed as the nuclear quadrupole moment, the interaction may have energy contributions comparable to that of the Zeeman potential. It often dominates the appearance of a powder spectrum and can be a useful addendum to resonance assignment and electronic structure interpretation.

Band broadening of powder samples results from the shielding and internal coupling in the sample. This complicates the interpretation of the target nuclei when more than one chemical environment exists as broad bands would overlap. A method has been developed to decouple the spectrum based on two observations: that the interactions are averaged in solution as the

molecules tumble rapidly, and that the dipolar and quadrupolar coupling are zero at a common angle of 54.7356° from the direction of the magnetic field B_0. By revolving the solid sample around the axis of this 'magic angle' at a speed greater than that of the static line width of the nuclei in question, it is possible to obtain a 'solution like' spectrum with a central δ_{iso}. The technique is known as magic angle spinning (MAS) which effectively averages the anisotropic contributions from the shielding and coupling interactions.

The versatility of NMR spectroscopy lies in the fact that non-zero nuclear spins exist for one or more isotopes of most known elements in the periodic table. By measuring the NMR spectrum of a specified nuclei, characteristics on its bonding, local electronic structure and local site dynamics can be revealed. It has been the overriding technique used to characterise the reaction products of B-N based hydrogen storage materials summarised in section 1.3 as many of the intermediates and products do not have long range order and therefore the local structure invisible to diffraction techniques. Moreover, solid state NMR has been used to differentiate *in situ* the release of hydrogen and ammonia during the thermal decomposition of Li-N-H materials reviewed in section 1.2.[26-29]

In this thesis two spectrometers at the Solid State NMR services in Durham University were used: the Varian VNMRS spectrometer and a Bruker Advance III HD spectrometer, both operating with 9.4 T magnets. The MAS NMR spectrometer is often set up so that the sample is loaded in a spinning probe placed inside the spectrometer cavity lined with RF transmitting coils. The probe is equipped with a RF receiver coil which records the free induction decay (FID) of the total magnetisation from all nuclei present in the sample. This signal, which is of the order of one hundred MHz in frequency, is then amplified in magnitude and scaled down in frequency to the order of 1 MHz. Data processing then involves smoothing the FID function, Fourier transforming into the frequency domain, phasing the data into real (in phase) and imaginary (out of phase) components and finally setting the zero point against the reference sample for the chemical shift axis.[21, 30]

Each measurement requires approximately 250 mg of powder which is inside a sealed 10 ml glass vial. At Durham, the sample is loaded into the designated MAS probes inside a nitrogen filled glovebox by the service scientists and measured accordingly. The local contact at Durham University is Dr. David Apperley at the NMR services.

2.3.3 Scanning Electron Microscopy

The scanning electron microscope (SEM) is an imaging instrument with an electron source. The electron beam, often from a tungsten filament or a field emission gun source, is focused on the

surface of a sample and the resulting interactions of the electrons with the sample recorded. The sample chamber of a SEM is often maintained at a high vacuum to allow a clear path from the electron lens to the sample. The SEM utilises many of the interactions between an electron beam and a sample (figure (2-16)).

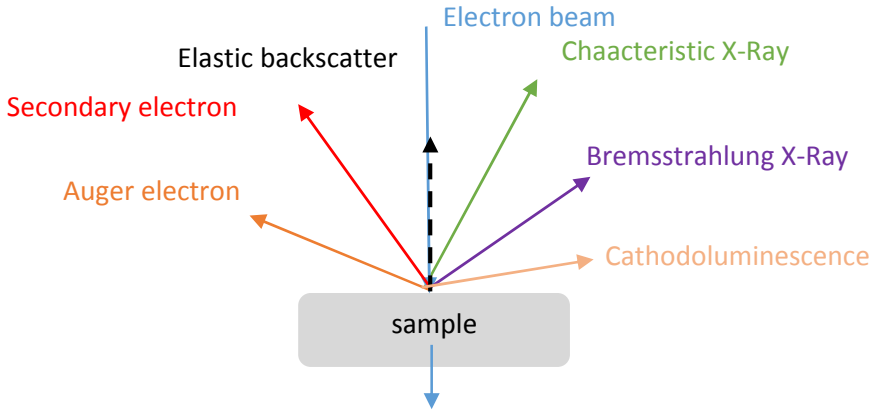

Figure 2-16. Electron beam interaction with matter

For imaging purposes, secondary electrons collected by an angled Faraday cage detector are the most widely used as the image produced has good depth of focus. The back scattered electrons can also be used, with the advantages of high electron intensities, however the images tend to be more 'flat' and locations where heavier elements congregate would reflect more electrons which can be mistaken as morphological features. As X-rays can also be emitted when electrons interact with matter, site-specific elemental analysis is an appealing addendum when using the SEM. An energy dispersive detector (EDS) or a wavelength dispersive detector (WDS) can be used for either point analysis or imaging over a large surface.

Electron microscopy can often provide physical parameters such as particle size which are crucial for solid hydrogen storage systems, as well as the physical microstructure post dehydrogenation which complements mechanistic derivations.

The Philips XL 30 SEM with a tungsten electron source was used for the micrographs imaged for this work. Samples are dispersed on the sample stub over sticky carbon tape, and then coated with a thin layer of gold by a PVD apparatus under He before transferring to the SEM chamber. The conductive coating and the carbon tape lining is crucial for draining electron charge from the sample surface, without which electrons would accumulate and distort the images obtained. This procedure is especially important for non-electron-conducting materials such as the ionic and organic compounds used in this work. Contact with air is minimised during transportation, and for very air sensitive samples argon is blown over the sample *via* a flexible tube with a dispersing

nozzle for the transportation process. Once the SEM chamber is evacuated to high vacuum, secondary electrons were used to image the samples in this work at 5 kV.

2.3.4 Thermal Analysis

Thermal analysis refers to the group of techniques whereby certain physical or chemical properties of a material are measured as a function of temperature. Such techniques are related to intrinsic materials properties by classical thermodynamics principles, characterised by the Gibbs free energy, G, in the expression:

$$G = H - TS \qquad (2\text{-}23)$$

where H is enthalpy, T is temperature and S is entropy. For a reaction at constant temperature,

$$\Delta G^0 = \Delta H^0 - T\,\Delta S^0 \qquad (2\text{-}24)$$

at which the reaction would proceed spontaneously in the direction of decreasing standard Gibbs energy. Standard enthalpy and entropy can be readily obtained for a given sample using quantitative differential thermal analysis (DTA) and differential scanning calorimetry (DSC) by:[31]

$$\Delta H^0 = C_P\,\Delta T \qquad (2\text{-}25)$$

$$\Delta S = \int \frac{C_P}{T}\,dT \qquad (2\text{-}26)$$

Likewise, thermal analysis methods (thermal gravimetry (TG), DTA, DSC) are the corner stone for the kinetics evaluation of a system. Kinetic parameters including activation energy, E_a, the frequency factor, A, and the reaction kinetic model *f(α)* (in terms of the extent of reaction, α), are characterised by constant heating rate and isothermal experiments.[32] The activation energy and the frequency factor are given by the Arrhenius equation:

$$k(T) = A \exp\left(\frac{E_a}{RT}\right) \qquad (2\text{-}27)$$

where *k*(T) is the reaction rate and R is the Universal gas constant. Using the Kissinger-Akahira-Sunose expression:

$$ln\left(\frac{\beta_i}{T_{\alpha,i}^2}\right) = \text{constant} - \frac{E_a}{RT_\alpha} \qquad (2\text{-}28)$$

where β_i is i^{th} heating rate, it is possible to evaluate E_a by measuring thermal analysis data at different heating rates and plotting $ln\left(\frac{\beta_i}{T_{\alpha,i}^2}\right)$ versus $\frac{1}{T_\alpha}$.

The reaction model and frequency requires model fitting against a plot of the extent of reaction, α, over time at a constant temperature which is described by the encyclopaedic recommendations of kinetic analysis by the International Confederation of Thermal Analysis and Calorimetry.[32]

Thermal analysis is centre to the majority of hydrogen storage materials research as thermal induced dehydrogenation is the preferred gas release mechanism. A thermally induced hydrogen fuel would be technologically and economically straightforward to implement and manage. The Instrument employed for this project is the Netzsch simultaneous thermal analyser (STA) coupled with a Hiden HPR 20 MS. It is capable of measuring TG and DTA simultaneously with the MS sampling the gas composition in real time (figure (2-17)). The instrument is located inside an argon glovebox and purged also in argon to enable air sensitive materials analysis with high accuracy (different atmospheric and purge gases can cause inaccuracy for the balance). Typical purge gas flow rate is set at 60 ml min^{-1}. TG is recorded by the microbalance with an electromagnetic load compensator, in percentage weight loss. Simultaneously DTA is evaluated by recording the difference in heat flux (by a calibrated thermometer) between two ceramic crucibles, one empty and the other filled with sample, in mW mg^{-1}. The heating profile is also recorded so that the data has dual time and temperature dependence.

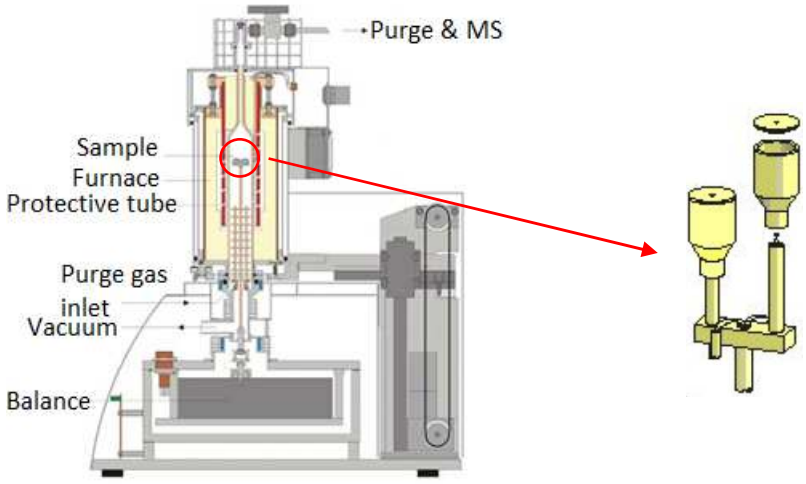

Figure 2-17. Schematic of the Netzsch STA 409 PC unit and ceramic crucible sample holder

2.3.4.1 Data collection

Prior to testing the desired sample on the STA it is advisory to carry out a safety run using a standard bench furnace at the desired temperature programme. This is to prevent damage to the sensitive instrument as gas releasing reactions can be accompanied by foaming and samples becoming air-borne.

To account for the natural deviation of the balance and thermocouple over time, a periodic background profile function, termed 'correction file' is measured by heating two empty sample crucibles at the desired heating rate. The instrument is also calibrated annually using manufacture specified standards.

Powder samples are brought into the glovebox *via* an antechamber. At this point the MS is started on a pre-run acquisition, usually in the Faraday mode (see below), tracing the desired *m/z* specie, water and argon. The pre-run is designed to eliminate vapour condensation in the ionisation chamber during idle. Two empty crucibles are first of all weighed and tared as the flux reaches – 1 mV as displayed on the STA 409 PC software under the view signals function. Approximately 20 mg of sample is loaded into the sampling crucible and the furnace assembly closed. Once the flux is again stabilised, the experiment is programmed to start simultaneously with the experiment-run on the MS. Data collected can be viewed and analysed using the Proteus software supplied by Netzsch.

2.3.4.2 Mass Spectrometry

Mass spectrometry is a technique for analysing gaseous free ions by using magnetic and electric fields in high vacuum.[21] The magnetic and or electric field applies a force onto the ionised molecule which causes a certain acceleration as a function of its mass and charge. Hence characterising the ionised molecule by its mass-to-charge ratio (*m/z*). The Hiden HPR 20 QIC MS (figure (2-18)) is set to operate at a vacuum of 1 x 10^{-6} torr which can be tuned by varying the inlet bypass valve VR1 to balance the contribution from the main turbo drag pump (P1) and the bypass scroll pump (P2). The pressure is measured by a Penning gauge at location G1 and displayed on the front digital panel of the instrument.[33]

The QIC (quartz insert capillary) inlet typically operates at 160 °C to eliminate condensation with lining materials carefully selected to prevent memory effect caused by molecules adhering to the capillary walls. Central to the HPR module is the MS assembly equipped with an electron impact ionisation source tuneable to the desired *m/z* range (up to 200 amu), a triple filtered quadrupole mass analyser and dual Faraday cup and secondary electron multiplier (SEM) detector (Figure 2-19). Quadrupole mass analysers are mass filters operating at combined direct current (DC) and RF potentials. Ions of designated *m/z* ratio are allowed through to the detector whereas the others collide on the quadrupole rods in the pre-filter stage.[21, 33] Finally at the detector stage, the ions collide on either the Faraday cup which records the charge compensation as the ions are neutralised on the cup metal surface; or the SEM which causes a secondary electron emission which avalanches is multiplied in the charged dynode multiplier. The signal measured by the

Faraday detector has quantitative significance to concentration of the respective molecular species in the inlet gas stream. The overall MS assembly has a detection limit of 5 ppb.

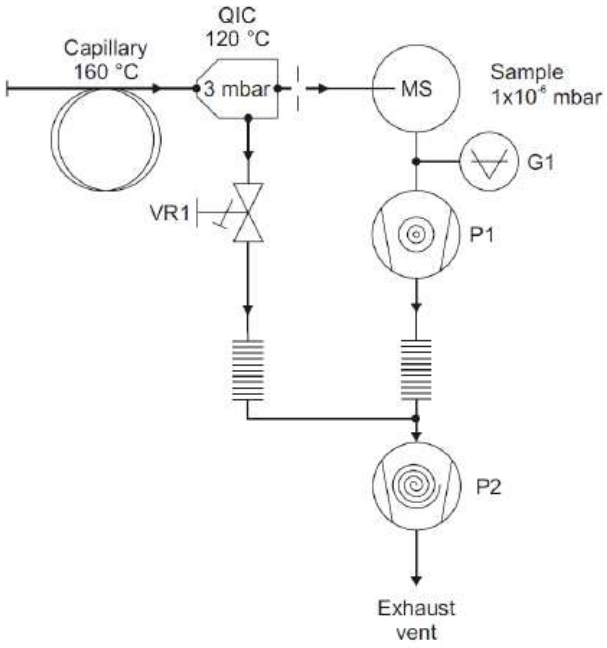

Figure 2-18. Schematic of the Hiden HPR 20 QIC system

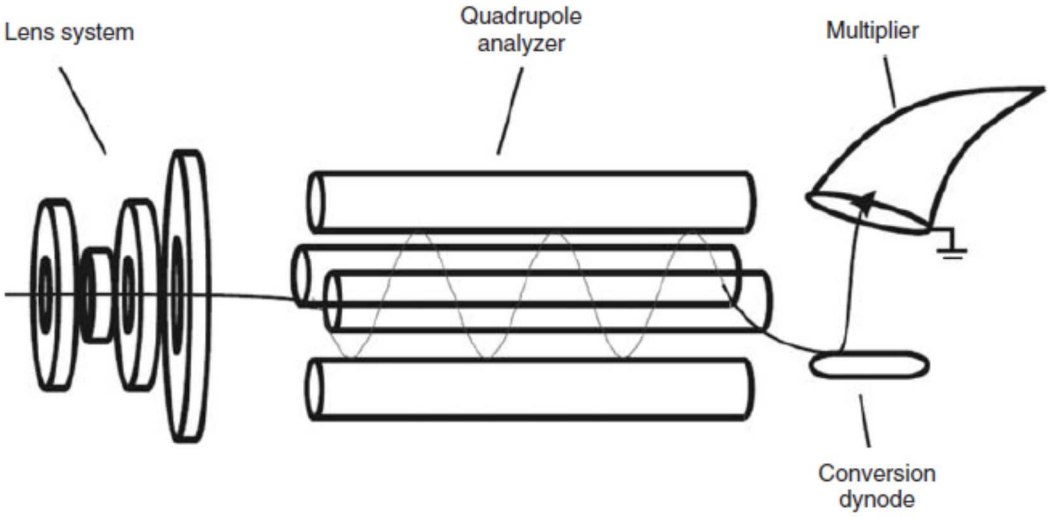

Figure 2-19. A typical quadrupole analyser, reproduced from the handbook of Spectroscopy[33]

Data acquisition on the HPR 20 is controlled by the Hiden MassSoft package which allows the desired measurement mode to be selected: sweeping scans across a designated *m/z* range used for identifying ion species, or tracking of known species with known *m/z* ratio, such as hydrogen at 2. The mass spectrum is measured over the experiment time, which can be correlated to the experimental temperature by the heating profile recorded on the STA.

2.4 References

1. Chen, P.; Xiong, Z.; Luo, J.; Tan, K. L. *J. Phys. Chem. B* **2003**, *107*, 10967-10970
2. Zhang, T.; Isobe, S.; Wang, Y.; Hashimoto, N.; Ohnuki, S. *RSC Adv.* **2013**, *3*, 6311-6314
3. Isobe, S.; Ichikawa, T.; Hino, S.; Fujii, H. *J. Phys. Chem. B* **2005**, *109,* 14855-14858
4. Hoang, K.; Janotti, A.; Van de Walle, C. G. *Angew. Chem. Int. Ed.* **2011**, *50*, 10170-10173
5. Xiong, Z.; Yong, C. K.; Wu, G.; Chen, P.; Shaw, W.; Karkamar, A.; Autrey, T.; Jones, M. O.; Johnson, S. R.; Edwards, P. P.; David, W. I. F. *Nature Materials* **2007**, *7*, 138-141
6. Kang, X.; Fang, Z.; Long, L.; Cheng, H.; Yao, X.; Lu, G.; Wang, P. *Adv. Mater*. **2008**, *20*, 2756-2759
7. Liu, L.; Hu, D.; He, T.; Zhang, Y.; Wu, G.; Chu, H.; Wang, P.; Xiong, Z.; Chen, P. *J. Alloy. Compounds* **2013,** *552*, 98-101
8. Watanabe, H. *Powder Technology* **1999**, *104*, 95-99
9. Sahoo, A., Roy, K. *Asia Pacific Journal of Chemical Engineering* **2008***, 3*, 230-235
10. Bragg, W. H.; Bragg, W. L. *Proc. R. Soc. Lond*. *A* **1913**, *88*, 428-438
11. Borchardt-Ott, W. *Crystallography. An introduction,* 3rd edition, Springer-Verlag Berlin Heidelberg, 2011
12. Waseda, Y.; Matsubara, E.; Shinoda, K. *X-Ray Diffraction Crystallography. Introduction, Examples and Solved Problems*, Springer-Verlag Berlin Heidelberg, 2011
13. Reiss, H.; Bruegemann, L. *Good Diffraction Practice Webinar Series, Powder XRD Instrumentation and Data Quality* [Online] https://www.bruker.com/fileadmin/user_upload/8-PDF-Docs/X-rayDiffraction_ElementalAnalysis/XRD/Webinars/Bruker_AXS_Good_Diffraction_Practice_III_-_Powder_XRD.pdf (Accessed 19th September 2016)
14. International Tables for Crystallography [Online] http://it.iucr.org/ (Accessed 19th September 2016)
15. Neutron scattering length [Online] https://www.ncnr.nist.gov/resources/n-lengths/
16. ILL D20 Homepage [Online] https://www.ill.eu/instruments-support/instruments-groups/instruments/d20/description/instrument-layout/ (Accessed 19th September 2016)
17. ILL D2B Homepage [Online] https://www.ill.eu/instruments-support/instruments-groups/instruments/d2b/description/instrument-layout/ (Accessed 19th September 2016)
18. Rietveld, H. M. *J. Appl. Cryst.* **1969**, *2*, 65-71
19. Larson, A. C.; von Dreele, R. B. *General Structure Analysis (GSAS)*, Los Alamos National Laboratory Report LAUR 86-748 (2004).
20. McCusker, L. B.; Von Dreele, R. B.; Cox, D. E.; Louër, D.; Scardi, P. *J. Appl. Cryst.* **1999**, *32*, 36-50
21. Gauglitz, G.; Moore, D. S. *Handbook of Spectroscopy*, 2nd Edition, Wiley VCH, 2014
22. Chua, Y. S.; Pei, Q.; Ju, X.; Zhou, W.; Udovic, T.; Wu, G.; Xiong, Z.; Chen, P.; Wu, H. *J. Phys. Chem. C* **2014**, *118*, 11244-11251
23. Tang, Z.; Zhang, L.; Wan, L.; Huang, Z.; Liu, H.; Guo, Z.; Yu, X. *Int. J. Hydrogen Energy* **2016**, *41,* 407-412Osborne11
24. Shimadzu FTIR 8400s Feature Sheet [Online] http://www.antteknik.com/documents/catalogs/FTIR-8400S.pdf (Accessed 19th September 2016)
25. Apperley, D. C.; Harris, R. K.; Hodgkinson, P. *Solid State NMR: Basic Principles and Practice*, Momentum, New York, N.Y., 2012.
26. Luduena, G. A.; Wegner, M.; Bjalie, L.; Sebastiani, D. *Chem. Phys. Chem.* **2010**, *11*, 2353-2360
27. Hu, Y. H.; Ruckenstein, E. *J. Phys. Chem. A* **2003**, *107*, 9737-9739
28. Hamilton, C. W.; Baker, R. T.; Staubitz, A.; Manners, I. *Chem. Soc. Rev.* **2009**, *38*, 279-293
29. Stephen, F. H.; Pons, V.; Baker, R. T. *Dalton Trans.* **2007**, 2613-2626
30. Sasaki, A. *Further Development in Solid-State NMR of Half-Integer Quadrupolar Nuclei*, PhD Thesis, University of Glasgow, 2016

31. Atkins, P.; Paula, J. *Atkins's Physical Chemistry*, 8th Edition, W. H. Freeman and Compan, NY, 2006
32. Vyazovkin, S.; Burnham, A. K.; Criado, J. M.; Pérez-Maqueda. L. A.; Popescu, C.; Sbirrazzuoli, N. *Thermochimica Acta* **2011***, 520*, 1-19
33. Hiden HPR 20 QIC specifications [Online] http://www.hidenanalytical.com/en/docman/presentations/825-hpr-20-qic-r-d

3.0 Dehydrogenation reaction between LiH and melamine

3.1 Introduction

An understanding of mechanism can be crucial to the control and tailoring of any chemical system. By deducing the step by step sequence of the elementary reactions by which an overall chemical change occurs, it is possible to influence the rate or path by which the process takes place. Solid state systems have the added complexity of the constituents being fixed in specific positions, in often dense materials, where the reactivity is largely dependent on diffusive transport within solids and between interfaces, as well as heterogeneous reactions on surfaces.[1-2] This chapter aims to investigate the reaction mechanism for hydrogen desorption derived in chapter 1.3, in the potential hydrogen storage system of lithium hydride and melamine. The relevant dehydrogenation is based on equation (3-1):

$$6\ LiH + C_3N_6H_6 \rightarrow 3\ Li_2NCN + 6\ H_2 \qquad (3\text{-}1)$$

$$6.97\ wt\%\ H_2 \qquad \Delta H^o_r = -468.62\ KJ.mol^{-1}$$

The following sections will briefly review the chemical and physical properties of melamine in conjunction with the properties of LiH described in chapter 1.1, that will form the basis of the experimental investigation of the reaction pathway behind equation (3-1).

3.1.1 Properties of melamine

Melamine (1, 3, 5-triazine-2, 4, 6-triamine, figure 3-1) is an organic trimer of cyanamide which is industrially produced and used as a thermosetting resin to improve the hardness of wood,[3] and as a fire retardant, since it releases nitrogen gas when combusted.[4] Melamine is also a synthetically important precursor used to construct supramolecular structures based on the aromatic triazine ring.[5-6] For example, graphitic carbon nitrides (*g-C_3N_4* materials) formed by controlled calcination of melamine are a class of non-metallic semiconductors which display significant chemical and photo-catalytic activity in a wide range of applications.[7-8] Melamine can be formed by polymerisation of cyanamide either by direct heating or through KOH promoted thermal condensation in solution.[9-10] Industrially melamine is synthesised from urea, as described in equation (3-2), either *via* catalysed gas-phase or high pressure liquid-base reactions; with China as the largest global producer.[11] The gas products from reaction 2 are recycled for the synthesis of urea and these processes are often complementary to the production of ammonia *via* the Haber-Bosch process.[12]

$$6\ CO(NH_2)_2 \rightarrow C_3N_6H_6 + 6\ NH_3 + 3\ CO_2 \qquad (2)$$

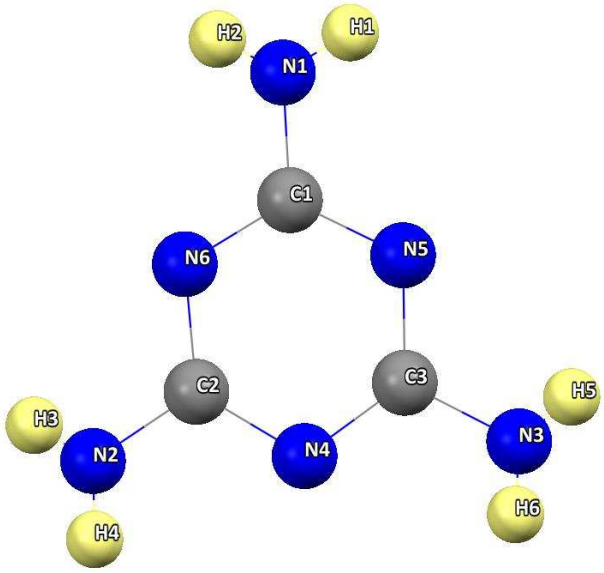

Figure 3-1. The molecular structure of melamine with numbering scheme according to Hughes in 1941. Carbon is shown in grey, nitrogen in blue and hydrogen in yelllow[13]

The free melamine molecule has three equivalent amino groups exocyclic to the triazine ring and a molecular symmetry of *D3h*.[14] Gas phase FTIR and NMR in DMSO have confirmed that the molecule is structurally and magnetically symmetrical.[15-16] Chemically, melamine behaves as an imide-like triazine triamine where the triazine nitrogen exhibits a greater degree of basicity than the amino nitrogen. The amino lone pair electrons are predominantly delocalised into the aromatic ring, whilst the lone pairs of the triazine nitrogens remain localised on the nitrogen atoms. Thus, the amino groups contribute acidic character to the molecule, with gas phase acidity comparable to that of urea at 1508.3 kJ mol^{-1}. The proton affinity of the endocyclic nitrogen was calculated to be 945.2 kJ mol^{-1} and the overall molecular basicity in the gas phase is 913.8 kJ mol^{-1}.[17] Polarity associated with the nitrogens contributes to melamine's most notable chemistry in self-assembly; the formation of supramolecular compounds *via* extensive hydrogen bonding networks, with the likes of formaldehyde, [4, 18] phosphoric acid [19] and cyanuric acid.[20]

Solid melamine was one of the first molecular structures to be refined using the least squares method by Hughes in 1941.[13] It has since been characterised using various X-ray and neutron diffraction techniques. Melamine crystallises in monoclinic spacegroup $P2_1/a$, with cell parameters a= 10.433 (1) Å, b=7.458 (1) Å, c=7.238 (1) Å, β=113.30(2)° and Z=4 (figure 3-2).[14, 21-22] The triazine ring lies approximately planar whilst the exocyclic amino groups experience positive dipole and quadrupole distortion at the non-bonding sites closely associated with the delocalised ring-NH_2 π-electrons.[21] ^{15}N NMR confirmed a sp^2-hybridised carbon orbital in the triazine ring with moderate

participation of the amino group in the π ring system.[16, 23] Intermolecular hydrogen bonding in the unit cell further distorts the molecular geometry from ideal D_{3h} symmetry, as the C3-N3 bond distance is elongated slightly compared to the other two chemically equivalent C-N bonds. Consequently the C3-N4 and C3-N5 bonds are shorter than the remaining equivalent ring C-N distances. N-H bonds that do not participate in intermolecular hydrogen bonding, N2-H3 and N3-H6 interactions are therefore unequivocally shorter.[13, 21] A single crystal neutron diffraction study carried out at 14 K by Cousson *et al.* in 2005 confirmed the hydrogen positions, validating the molecular symmetry in solid state as C_s. The N3 amine group was found to have a trigonal pyramidal geometry while the N1 and N2 amines were close to trigonal planar. This difference in geometry and the asymmetric packing in the unit cell is directly associated with the intermolecular hydrogen bonding. This is also reflected in the out of plane hydrogens positions H1 and H4, with torsion angles observed to be larger than 10°.[22]

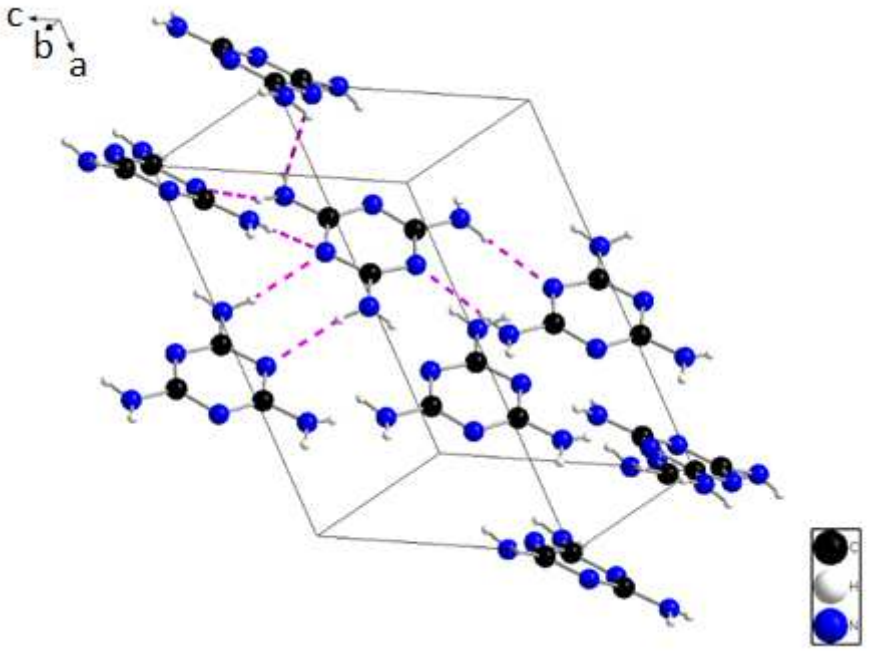

Figure 3-2. Solid state crystal structure of melamine showing the unit cell with carbon, nitrogen and hydrogen atoms as black, blue and white spheres respectively showing hydrogen bonding[22]

3.1.2 Thermolysis of melamine

Thermal decomposition studies of melamine have been surrounded by controversy, due to the ambiguity of the reaction processes which leads to the formation of the important tri-*s*-triazine (C_6N_7) building blocks for higher order "carbon nitrides".[7] Much of the debate in the literature focusses on the tendency of melamine to self-assemble with its many reaction products, forming enigmatic intermediates and a high selectivity of products based on the ammonia partial pressure.[16,

[23-24] Scheme 3-1 outlines the pyrolysis pathway of melamine. Upon heating, melamine **1** can either condense into melam **2**, melem **3** or melon **4**, or depolymerise under an ammonia atmosphere into dicyandiamide **5** or cyanamide **6;** under the specified temperatures and pressures. [16, 23-25]

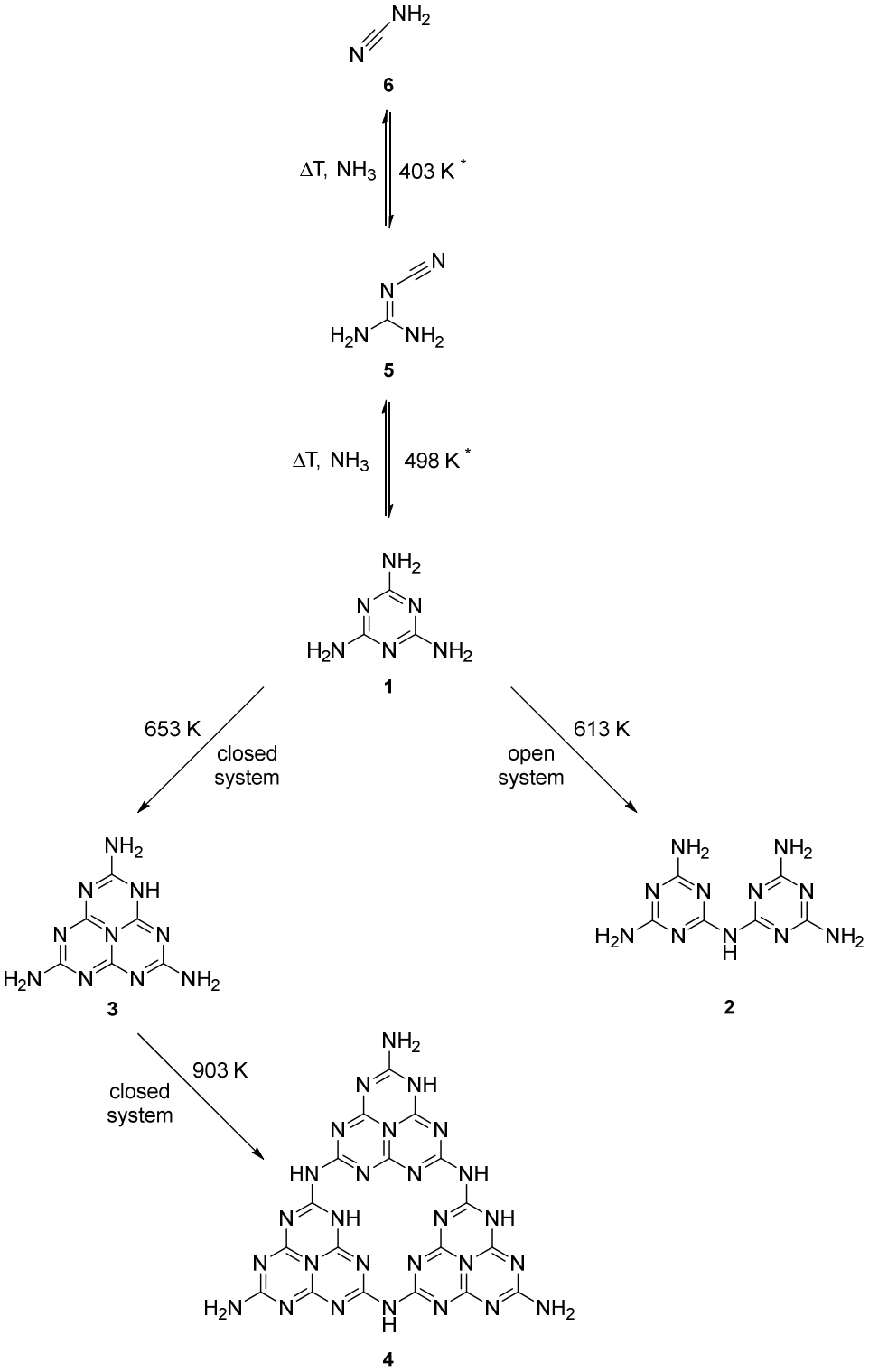

Scheme 3-1. Schematic of melamine pyrolysis. * marks results obtained using commercial H_2NCN (Sigma Aldrich, 99%)[16, 23-25]

3.1.2 Melamine in hydrogen storage

Melamine, cyanamide and dicyandiamine all have the generic formula $(H_2NCN)_n$ with an overall hydrogen content of 4.76 wt%. Whilst higher melamine derivatives, listed in scheme 3-1, have higher chemical and thermal stability and significantly less hydrogen density (melam at 3.86, melem at 3.22 and melon at 1.99 wt%). A series of preliminary studies in the Gregory group combined LiH with all three molecules.[26] Cyanamide was found to be inappropriate as a hydrogen storage material as it reacted violently upon contact with the metal hydride, even under inert conditions. Melamine was the most successful releasing the theoretical hydrogen content of 6.98 wt% by 320 °C with six equivalent of LiH. Whereas the study of the LiH – dicyandiamine system is still in its infancy and the preliminary results are reported in chapter 5.

Full hydrogen desorption was achieved using a 6:1 ratio of LiH to melamine to release hydrogen and solid dilithium carbidiamide (Li_2NCN). It was observed that high energy ball milling provided a reproducible means for controlling particle size and achieving homogeneous mixing of the two compounds to induce a three step exothermic dehydrogenation by 320 °C. A study of the relationship between dehydrogenation and the extent of ball milling by PXD, FTIR and STA-MS concluded that it was possible to mechanically disrupt the long range hydrogen bonding network whilst preserving the intramolecular structure in solid melamine; which subsequently facilitates dehydrogenation without melamine sublimation. Hoang *et al.* proposed that the dehydrogenation mechanism, at least in the initial steps, is governed by intermolecular $H^{\delta+} \ldots H^{\delta-}$ interaction between LiH and protic NH_2 groups, which are facilitated by high energy ball milling.[26]

This chapter presents a systematic study of the dehydrogenation in the LiH-melamine system with the aim of elucidating the reaction mechanism using FTIR, *in situ* powder neutron diffraction, solid state NMR and isotopic labelling experiments. In an attempt to close the energy cycle, the reaction product, Li_2NCN was rehydrogenated using a series of chemical treatments back to the starting material melamine.

3.2 Experimental

3.2.1 Materials

Commercially available LiH (95%), LiD (98 atomic%) and melamine (99%) were sourced from Sigma Aldrich for the experiments described in this chapter.

Deuterated melamine was synthesized in the laboratory by ball milling CaNCN in D_2O at 300 RPM with a ball to powder to liquid ratio of 40:1:10 continuously for 20 minutes. The filtrate was then treated with 5% D_2SO_4 in D_2O (99.5 atom% D, 96-98 wt% in D_2O) to form deuterated cyanamide

D_2NCN, and Ca_2SO_4 as an impurity. [9] The dried mixture was then washed with ethanol to precipitate out the sulphate. The highly hygroscopic cyanamide was then heated in an open vessel in a fume hood as the polymerisation releases ammonia rapidly, first to 90 °C to form dicyandiamine and then 260 °C to form $C_3N_6D_6$ (figure 3-3).

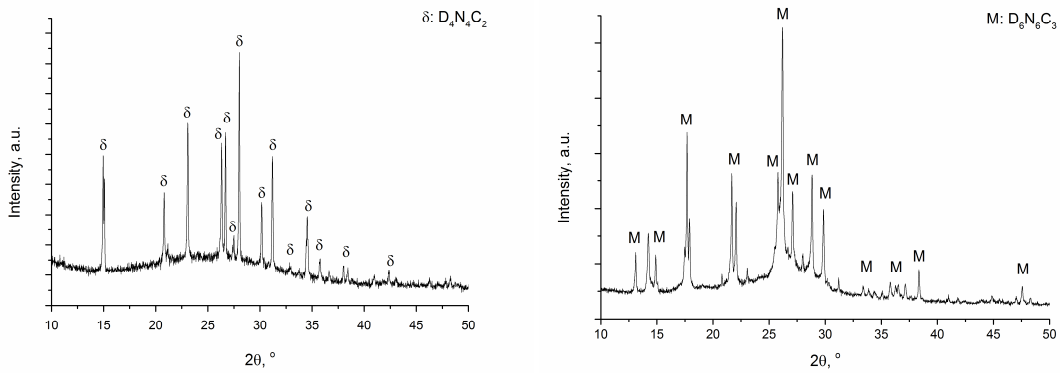

Figure 3-3. PXD of deuterated dicyandiamine (left) and melamine (right) synthesised in the laboratory

3.2.2 Sample preparation

3.2.2.1 Ball milling

Standard procedures described in chapter 2.2.1 were followed for all ball milling experiments and will otherwise not be reproduced here. The specific milling conditions used were as follows: five 10 mm stainless steel balls, 450RPM for 12 hours at 35:1 ball to powder weight ratio and a milling frequency of 5 min with 30 sec rest periods. A list of samples used in this chapter is compiled in table 3-1.

Table 3-1. Samples used to investigate the dehydrogenation between 6 LiH : $H_6N_6C_3$

Sample	Content	RPM	Ball : powder	Milling time	Programme	# Balls
M-01	6 LiH : $H_6N_6C_3$	450	35:1	12 h	5 m rest 1 m	5
M-02	6 LiH : $H_6N_6C_3$	450	35:1	12 h	5 m rest 1 m	10
M-03	6 LiD : $D_6N_6C_3$	450	35:1	12 h	5 m rest 1 m	5
M-04	$CuCl_2$ doped $H_6N_6C_3$	450	35:1	12 h	5 m rest 1 m	5
M-05	6 LiH : $CuCl_2$ doped $H_6N_6C_3$	450	35:1	12 h	5 m rest 1 m	5
M-06	6 LiD :$H_6N_6C_3$	450	35:1	12 h	5 m rest 1 m	5
M-07	6 LiD :$H_6N_6C_3$	Hand ground	-	10 m	-	-

3.2.3 Characterisation techniques

Standard procedures described in chapter 2.3 for thermal analysis using STA/MS, and material characterisation using PXD and FTIR were used for the work described in this chapter. Procedures followed for powder neutron diffraction (PND) and solid state NMR experiments are described in the following sections.

3.2.3.1 Powder Neutron Diffraction

In situ and *ex situ* measurements were conducted on the D20 and D2B beamlines at ILL neutron source in Grenoble.

The *in situ* experiments were measured for two batches of as-milled 6LiD : $D_6N_6C_3$ samples loaded in an argon glove box into quartz tubes to be used with a supply of flowing argon. Samples were heated from RT to 400 °C. Diffraction data were collected for the samples at wavelength λ = 1.36 and 1.87 Å for approximately 10 h each. The λ = 1.87 Å experiment was conducted using a step-wise heating programme first from RT to 150 °C, followed by 5 °C increments and holding isothermally for 10 min scans. For the λ = 1.36 Å experiment, statistics were counted at RT, 150 °C and then in a dynamic manner over 3 °C increments every 10 mins.

Ex situ measurements were conducted on the D2B beamline, scanning 4 samples, (as milled, 180, 285 and 400 °C) loaded into vanadium cells with indium seal in an argon glove box. The samples were measured for 2 h each at λ = 1.59 Å.

3.2.3.2 Solid state NMR

3.2.3.2.1 $CuCl_2$ doping

For ^{15}N NMR experiments, melamine was doped with paramagnetic $CuCl_2$ by lyophilising from aqueous solution in order to reduce relaxation time for efficient cross polarisation (CP) data collection *via* ^{1}H in the solid state (0.01%).[20]

3.2.3.2.2 ^{2}H and ^{15}N MAS NMR measurements

^{2}H and ^{15}N solid state MAS NMR were measured at RT at the EPSRC National NMR service at University of Durham on a Bruker Advance III HD spectrometer and a Varian VNMRS spectrometer respectively; both with a 9.4 T magnet. Samples were loaded into 4 mm (^{2}H) and 6mm (^{15}N) diameter probes in a nitrogen filled glovebox.

The spinning frequency for all ^{2}H experiments was set to 10 kHz, whereas those used for the ^{15}N experiments were 2.925, 6 and 3 kHz for melamine, 12 h ball milled melamine and 12 h ball milled LiH with melamine samples respectively. The signals were referenced to tetramethylsilane for deuterium and nitromethane for nitrogen. ^{2}H spectra were determined using deuterated samples from the neutron diffraction experiments in section 3.3.2 for consistency. ^{15}N natural abundance measurements were made on non-deuterated samples *via* ramped cross polarisation through the ^{1}H nuclei in the samples. Contact time was 10 ms and a two-pulse phase-modulated (TPPM) sequence was applied for broadband proton decoupling. For the pristine melamine and ball milled sample with LiH, dipolar dephasing (interrupted decoupling) measurements were made to differentiate protonated and ternary nitrogen at 200 μs intervals; as this frequency suppresses the NMR signal in the protonated sites.

3.3 Dehydrogenation mechanism between LiH and melamine

3.3.1 System reproducibility

Reproducibility of the ball milling conditions reported by Hoang *et al*. was examined.[26] Six equivalents of LiH were ball milled with melamine at 450 RPM with 5 balls at 35:1 ball to powder ratio for 12 h (**M-01**). The milling programme was to mill 5 for min with 30 sec rest intervals. The resulting powder was characterised by PXD (figure 3-4 (a)) then decomposed in the STA-MS at 5 °C min^{-1} to 400 °C under flowing argon. Figure 3-5 shows that using the ball milling procedure it is possible to reproduce the three-step decomposition onset at 96.7, 203.8 and 293.1 °C reported by Hoang *et al*. Li_2NCN (Figure 3-6) was found to be the sole solid product at 400 °C by PXD (figure 3-4 (b)).

However there is a discrepancy of about 0.5 wt% in total between the TG recorded for **M-01** compared to that reported by Hoang *et al*. Further investigations into the effect of ball milling on the LiH-melamine system with respect to mass loss revealed that for any given milling product, as the number of balls increases, the final mass loss decreases. Figure 3-7 is a comparison between the TG of powder milled with 5 and 10 (**M-02**) 10 mm stainless steel balls respectively showing a final mass loss difference of 2 wt%. Accordingly, under the severe milling conditions prescribed by Hoang *et al*., any variations in the mass of the starting balls used would result in slight fluctuation of the final mass loss measured (for examples by means of wear and tear, as new balls have a mass of around 4 g whereas the balls weighed for this experiment are on average 3.9 g each).

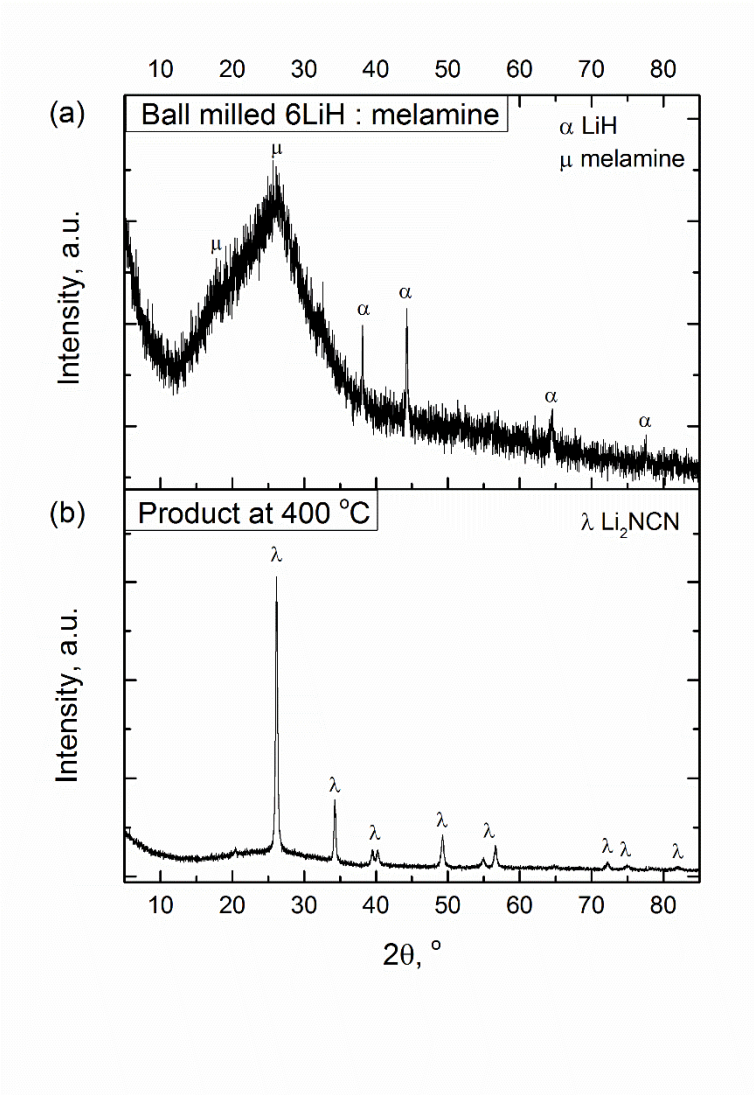

Figure 3-4. PXD patterns of (a) **M-01** (b) the decomposition product following heating to 400 °C under Ar

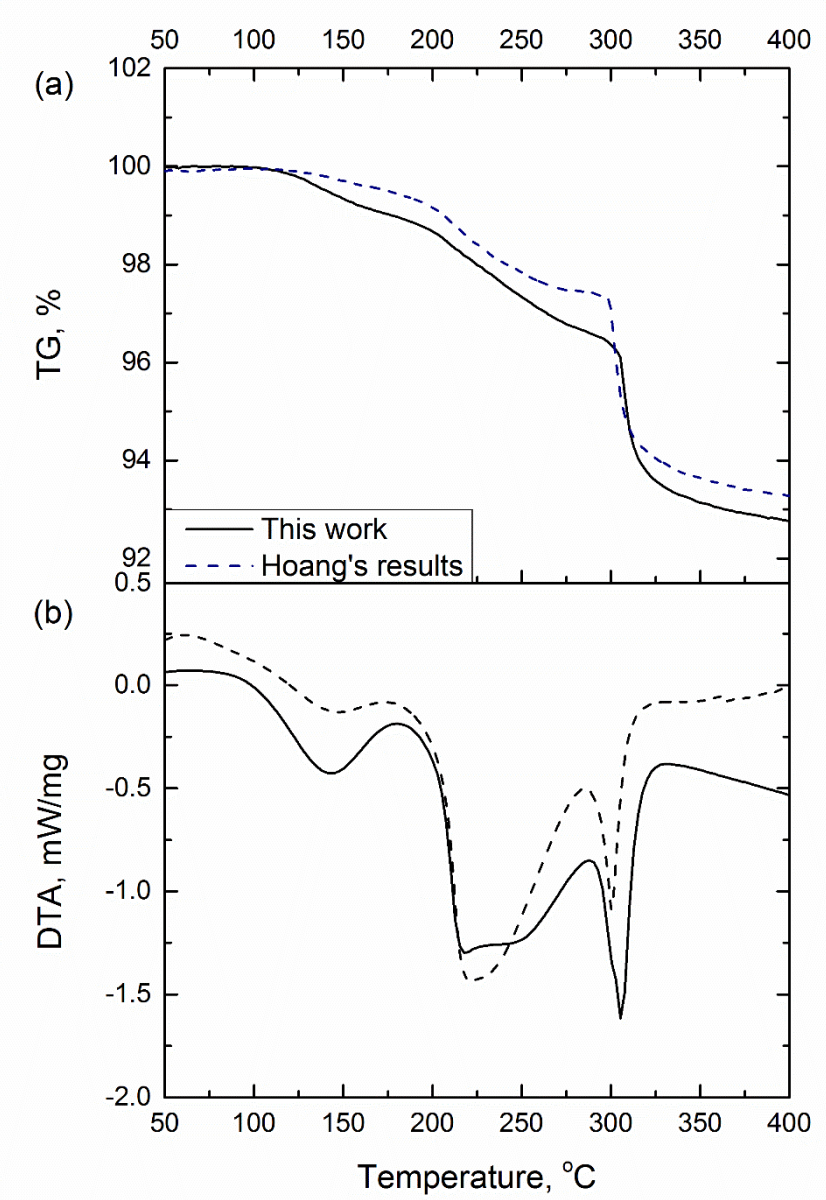

Figure 3-5. Experimental TG/DTA data of sample **M-01**; solid line for the present experiment and dotted line from Hoang's previous results[26]

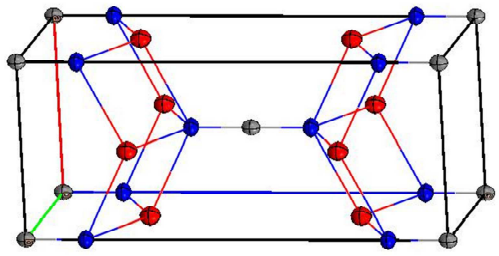

Figure 3-6. Crystal structure of Li_2NCN, lithium atoms are represented in by red spheres, nitrogen in blue and carbons in grey[27]

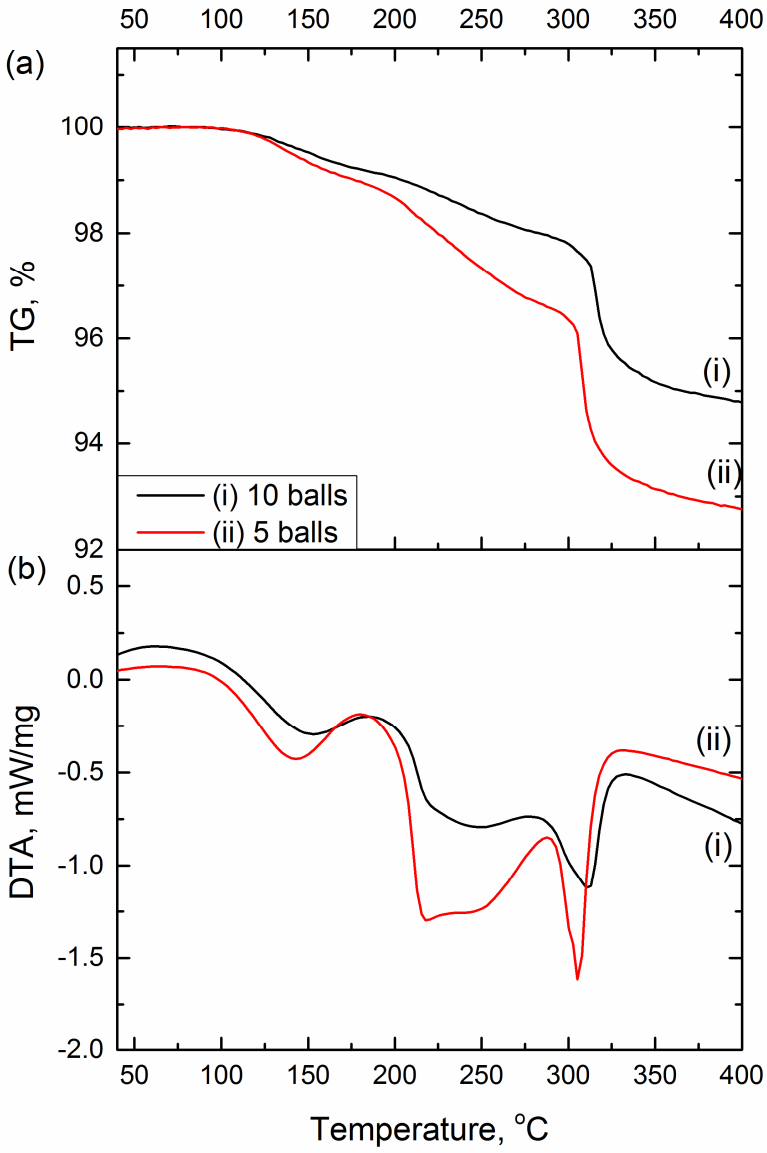

Figure 3-7. (a) TG and (b) DTA of ball milled 6 LiH with melamine using (i) 10 and (ii) 5 milling balls

Measured FTIR spectra were in good agreement with Hoang's analysis for both starting materials, LiH and melamine, for **M-01**,[26] and its decomposition products at 200, 305 and 400 °C (figure 3-8). The observed frequencies are tabulated and assigned (table 3-2). A number of observations can be made with regards to the effect of ball milling on the amino group on melamine, and the effect of heat on various bonds present in ball milled LiH-melamine.

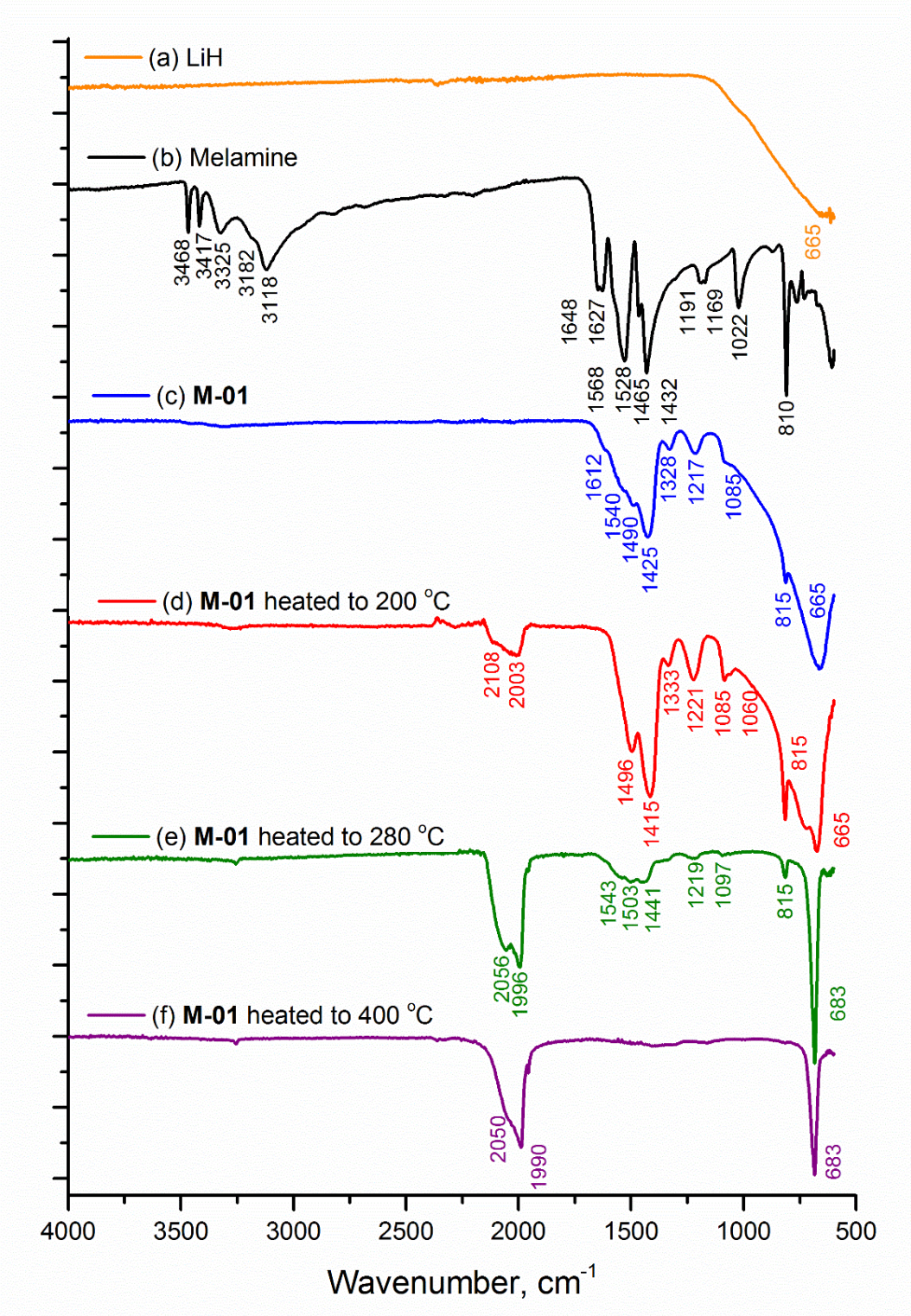

Figure 3-8. FTIR of (a) pristine LiH, (b) pristine melamine, (c) ball milled sample **M-01**, *ex situ* samples taken after heating **M-01** to (d) 200 °C, (e) 280 °C and (f) 400 °C

Table 3-2 Previously reported and experimental FTIR data for melamine and **M-01**[15, 31-32]

Melamine				*Experimental*			
Experimental	**Gas [15]**	**Solid [30]**	**Assignment [15, 30-31]**	**Ball Milled 12H 6LiH:Melamine**	**200 °C**	**280 °C**	**400 °C**
810 vs	824 (833)	810 (822)	Ring out of plane def	815 vs	815 s	815 w	
1022 m	1000 (981)	1022 (1027)	Ring breathing	1085 m	1060 m	1097 vw	
1169 w		1170 (1170)	ρ(NH2)		1085 m		
1191 w		1194	ρ(NH2)	1217 m	1221 m	1219 vw	
				1328 w	1333 w		
1432 vs	1440 (1410)	1432 (1432)	$\nu_s(CNH_2)$	1425 s	1415 s	1441 w	
1465 s		1465 (1449)	Ring breathing (CNH_2)				
1528 vs	1556 (1544)	1526 (1579)	$\nu_a(CNH_2)$	1490 s		1503 w	
1568 s		1567 (1565)	ring stretching	1540 s	1496 s	1543 w	
1627 s	1598 (1577)	1626 (1624)	$\delta(NH_2)$	1612 m			
1648 s		1646	$\delta(NH_2)$ coupled $\nu(CNH_2)$				
					2003 vw	1996 s	1990 s
					2108 vw	2056 s	2050 s
3118 s	3453 (3465)	3123	ν_s(NH2)				
3182 m		3178					
3325 m		3323					
3417 m	3571 (3584)	3417	ν_a(NH2)				
3468 m		3468					

Hoang *et al.* have previously attributed the absence of symmetric and asymmetric NH_2 vibrations in the ball milled mixture to the breakdown of intermolecular hydrogen bonding within the melamine lattice; which is also reflected in the lack of long range order observed by PXD.[26] In the work presented herein a collective red shift is observed for all triazine skeletal symmetric and asymmetric C-NH_2 stretching as well as side chain-ring breathing modes between 1650 and 1000 cm^{-1}. Intensities of the NH_2 bending modes at 1600 cm^{-1} are also noticeably reduced compared to pristine melamine. A contrasting blue shift for the ring deformation coupled with amine rocking modes was found between 1200 and 1000 cm^{-1} signifying the bond has contracted. The simultaneous red shift of the NH stretching modes and blue shift of the out of plane bending modes has been empirically correlated linearly with hydrogen bond energies in hydrogen bonded organic and inorganic complexes.[28] The characteristic triazine ring out-of-plane bending mode blue-shifted 5 cm^{-1} is a consequence of the redistribution of π-electrons as a result of increasing C-NH distances. The absorption band at 1328 cm^{-1} is a feature more frequently associated with cross-linking between higher order triazine polymers such as melam (1338 cm^{-1})[23] and melem (1304 cm^{-1}).[16] However formation of melam or melem from melamine, as described in scheme 3-1, requires high temperature and is accompanied by elimination of ammonia, which, in the presence of intimate ball milled LiH, should readily form $LiNH_2$ (ν(NH_2) at 3259 and 3312 cm^{-1}).[29-30, 33] $LiNH_2$ however is absent from the system by FTIR and PXD.

Upon heating to 200 °C, the FTIR spectrum does not change significantly except for a further 10 cm^{-1} red shift on the symmetric C-NH_2 stretching mode at 1415 cm^{-1} and the complete disappearance of the NH_2 bending modes in the 1600 cm^{-1} region. Signals at 2003 and 2108 cm^{-1} can be attributed to the formation of linear C=N bonds. This feature red shifts and becomes more prominent at 280 °C as the majority of melamine and LiH features diminish, with the exception of small signals relating to the triazine sextant bend at 815 cm^{-1}. By 400 °C, the only features that remain (at 2050, 1990 and 683 cm^{-1}) are those reported for Li_2NCN, and can be assigned to NCN stretching and bending modes.[27]

The sequential red shifts in the C-NH_2 breathing modes after ball milling and heating to 200 °C are accordingly proposed to result from direct and increasing ionic interactions between the exocyclic nitrogen and lithium ion. It can be argued that the observed exocyclic C-N elongation is indeed a result of hydrogen desorption as indicated by the evolved gas mass spectrum in figure 3-9. If amine deprotonation alone is considered, the charge on the anionic nitrogen would donate into the π-electron system shortening the C-N bond, yet the opposite is observed. It is therefore likely that the redistribution of electron density, in the presence of Li^+ favours electron localisation at the exocyclic nitrogen after deprotonation as a complex ion.

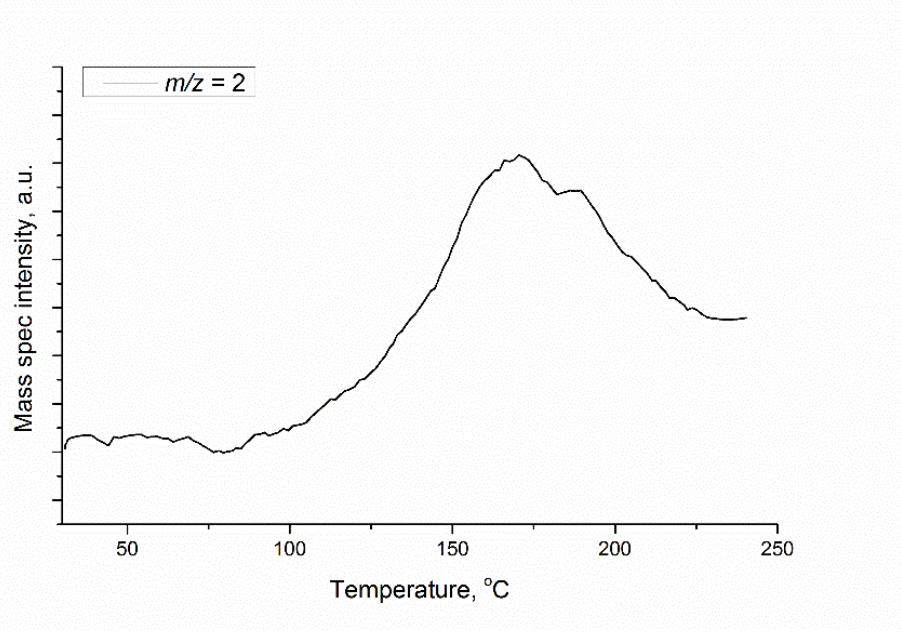

Figure 3-9. MS of BM LiH : melamine to 230 °C for *m/z* = 2

Although the triazine skeleton (sextant bend at 810 cm^{-1}) still exists at 280 °C it is only in trace amount, and Li_2NCN constitutes the majority of the sample at this stage of the reaction. However, as the FTIR measurement was made *ex situ* it should be pointed out that heat released during this exothermic third step could easily carry the experiment to completion and the bonding configuration immediately before the final hydrogen release at 293.1 °C could be misconstrued.

3.3.2 Powder neutron experiments

To interrogate the dehydrogenation mechanism of the 6LiH : $C_3N_6H_6$ system, further *in situ* and *ex situ* neutron diffraction experiments were conducted on the D20 and D2B beamlines at the ILL facility Grenoble, France. The main purpose of investigation was to examine whether intermediate phases could be identified *in situ* and determine whether the breakdown of the triazine ring at 290 °C occurs prior to or simultaneous to hydrogen release.

Data obtained from *in situ* experiments on D20 with λ = 1.87 and 1.36 Å are compiled in the contour profile plot shown in Appendix A with peak intensity represented by the colour bar (height) to the right of the plots. Figure 3-10 (a) and (b) shows the room temperature (blue) and final (red) diffraction patterns for the λ = 1.87 and 1.36 Å experiments respectively. Both room temperature measurements showed no features of the expected starting materials LiD and $melamine_d$ (**M-03**), but instead rather broad reflections of the product Li_2NCN. It is evident that ball milling had provided sufficient energy to react **M-03** partially in the milling jar *in situ*. Nonetheless two peaks

were identified to have d-spacing of 2.93 and 2.76 Å, which match no known Li-N-C-H phases (marked by black arrows in Figure 3-10). This suggests a potential intermediate phase. However, these two peaks are insufficient for identifying unknown phases so non-diffraction based techniques are required for further investigation. At *ca.* 450 K (λ = 1.87 Å) and 430 K (λ = 1.36 Å) the broad reflections intensified, alongside all weaker reflections of phase pure Li_2NCN. This transition is characteristic of a sintering or crystallisation.

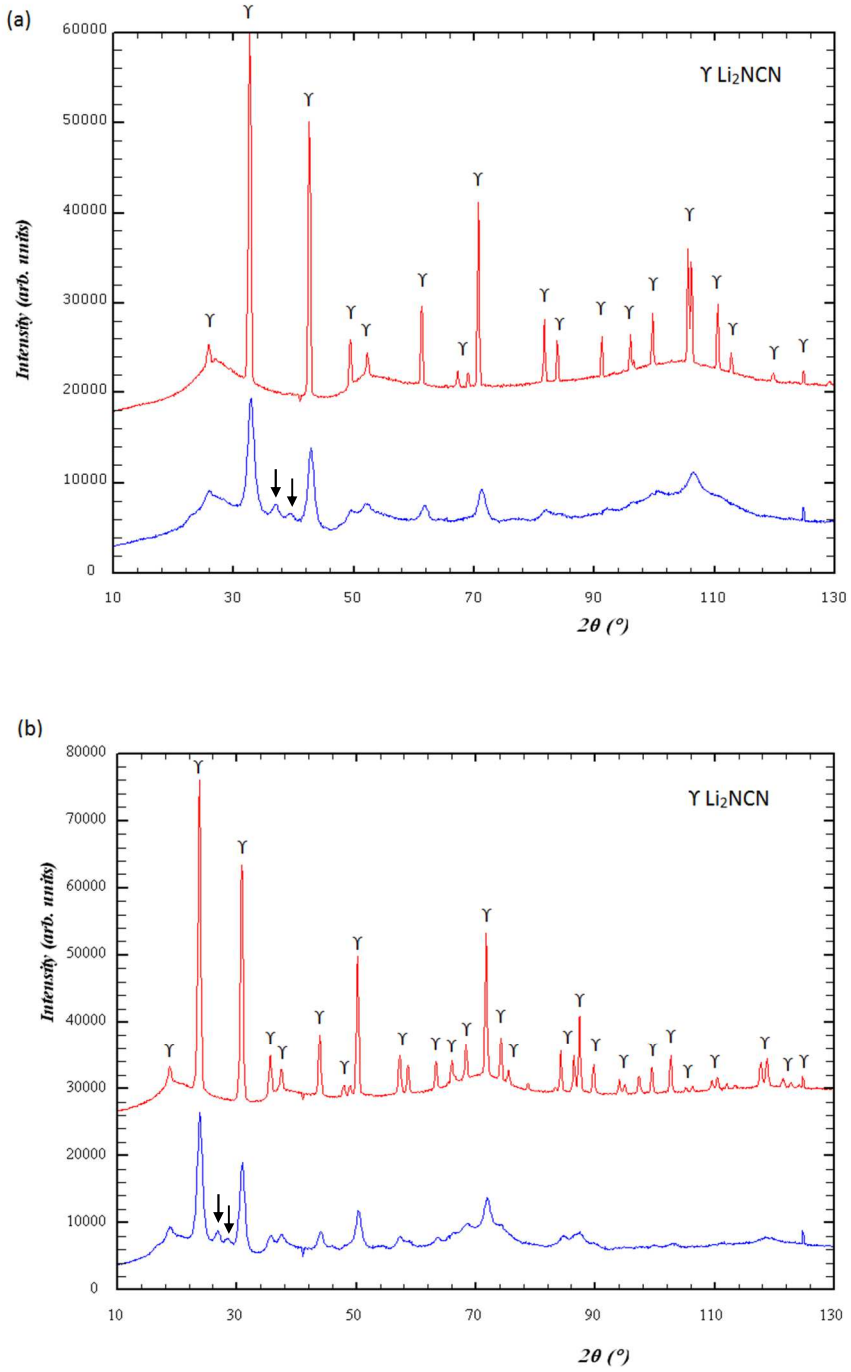

Figure 3-10. Room temperature (blue) and final (red) neutron diffraction patterns (a) λ = 1.87 Å and (b) λ = 1.36 Å collected for the ball milled **M-03**. The black arrows point to two unidentified peaks while the remainder can be assigned to Li_2NCN

The results of the e*x situ* measurements on D2B are displayed in figure 3-11 for the four temperature points; RT as milled, 180, 285 and 400 °C. The RT diffraction pattern exhibits broad melamine reflections due to sample amorphorisation, microstrain and nano-crystallisation of the sample. The most intense melamine reflections, {011}, {210} and {201}, can be identified. However LiD remains crystalline and the reflections are intense. At 180 °C, melamine reflections diminish and Li_2NCN peaks begin to form. An unidentifiable reflection at d= 2.12 Å (44.04° 2Θ) is present (marked by the red arrow) which suggests that there could be crystalline intermediate phases at this temperature. Again the single reflection is insufficient to provide conclusive evidence of any specific phase. By 285 °C the sample is predominately Li_2NCN with a small amount of LiCN impurity which has not been previously observed by Hoang *et al*.[26] It is possible that LiCN had formed as a result of a different sample preparation since 2 g of **M-03** powder was heated to 285 °C inside a quartz tube with Ar flowing by a bench furnace instead of the standard procedure using 20 mg in the STA. Non-stoichiometric product formation is not uncommon in solid state reactions as observed by David *et al.* in the study of Li-N-H hydrogen storage system in bulk.[29] The extent of impurity LiCN formation as a function of bulk is of great importance as it indicates unaccountable nitrogen loss, likely in the form of NH_3 gas in the proposed system, however it is beyond the scope of this current investigation. Finally, there was no obvious difference between the 285 and 400 °C diffraction patterns to suggest the presence of a crystalline intermediate product during this phase of the reaction.

Through the series of *in situ* and *ex situ* PND experiments we were unable to draw definitive conclusions regarding the identity of the crystalline intermediate phases during dehydrogenation between LiD and $D_6N_6C_3$. This is due to the sample preparation required to fully dehydrogenate lithium hydride and melamine, which produces diffraction patterns that tend to contain broad peaks hiding details such as phases present in trace quantities. Hence it was considered that other solid state characterisation techniques that do not rely on sample crystallinity, such as NMR spectrometry may provide beneficial insights into the dehydrogenation mechanism between LiH and melamine and these experiments are discussed in the section below.

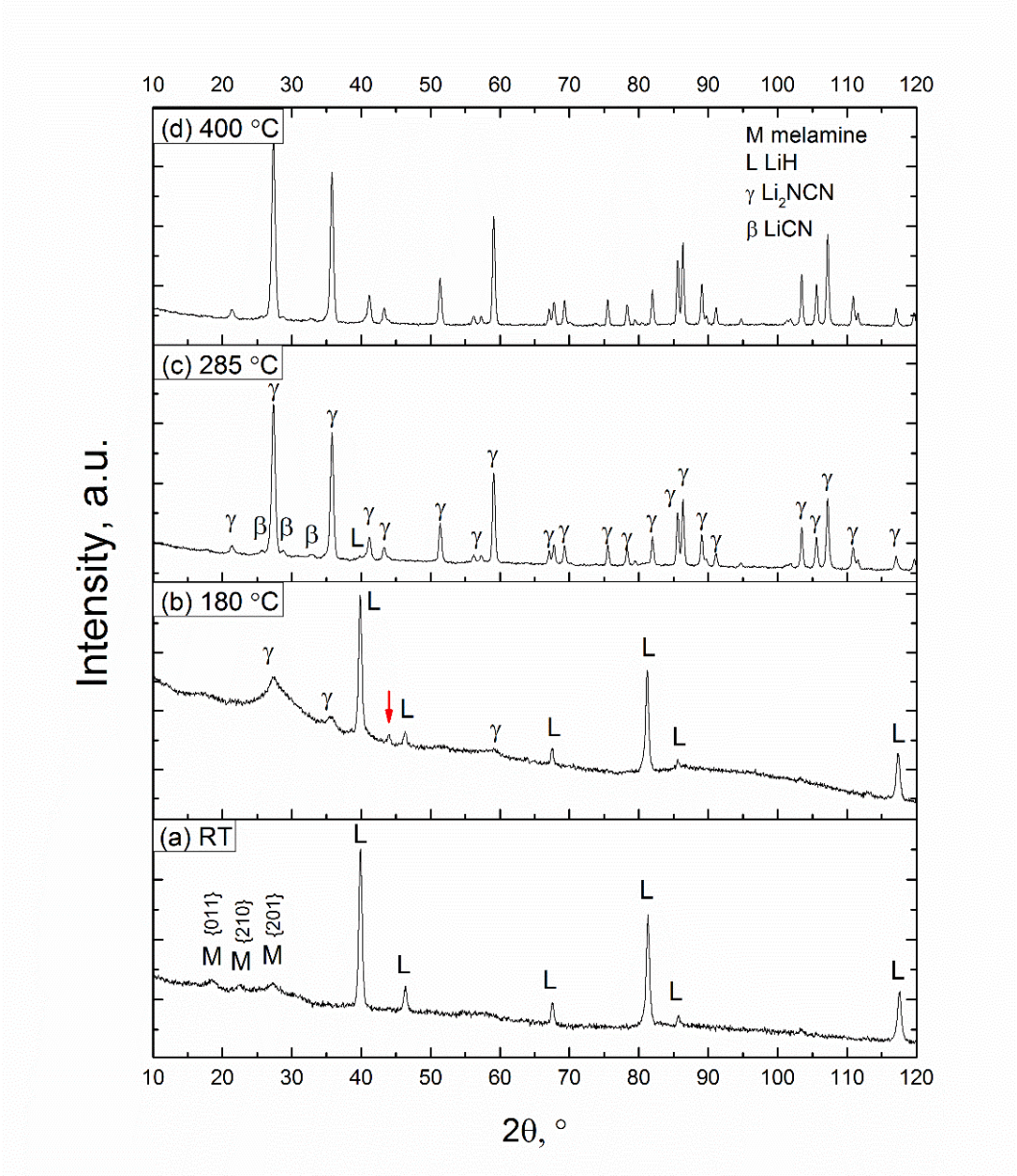

Figure 3-11. *Ex situ* neutron diffraction patterns for **M-03** (a) at room temperature, heated to (b) 180, (c) 285 and (d) 400 °C

3.3.3 Solid state NMR experiments

Solid state NMR has been the essential technique for unravelling the complicated array of thermolysis products from melamine described in section 3.1.2. ^{15}N NMR in the solid state has proven especially beneficial in establishing the positions of nitrogen in the structure and their relative proton environment in conjunction with crystallographic data [16, 23, 25]. We have demonstrated by FTIR studies in section 3.3.1 that whilst the triazine skeleton of melamine remains intact during milling, there is persuasive evidence that LiH has interacted with the exocyclic amino group in sample **M-01**. The absorption band at 1328 cm^{-1} also indicates that possible cross-linking

had occurred as a result of ball milling. However it was not possible to identify the exact change in structures by either PXD or PND as ball milling introduces defects and strains that disrupt the long-range periodicity and render the resulting diffraction patterns imperceptible. ^{2}H and ^{15}N NMR was therefore employed to study the chemical environment around the various hydrogen and nitrogen positions in samples **M-03**, a ball milled $CuCl_2$ doped $C_3N_6H_6$ (**M-04**), ball milled 6 LiH : $CuCl_2$ doped $C_3N_6H_6$ mixture (**M-05**) and **M-05** heated to 200 °C, to elucidate these possible interactions further.

In the ^{2}H NMR spectrum (figure 3-12 (a)) the broad peaks between 3.7 and 9.1 ppm of pristine $C_3N_6D_6$ are comparable to data reported by Damodaran *et al*.[20]

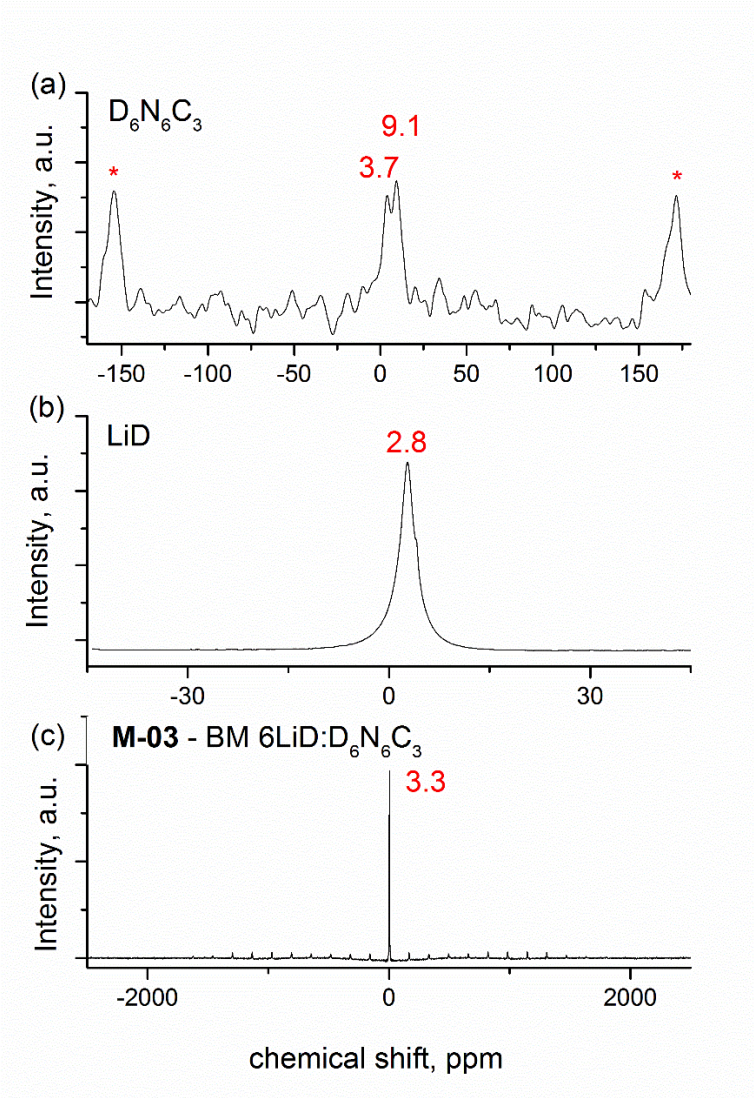

Figure 3-12. ^{2}H MAS NMR spectra of (a) synthesised deuterated melamine, (b) pristine LiD and (c) **M-03** BM 6 LiD : $melamine_d$

The stronger 9.1 ppm signal represents immobile deuterium in the system due to the associated spinning sidebands observed (marked by the red asterix). On the other hand, the smaller peak at 3.7 ppm without any spinning sidebands represents deuterium with a higher relative mobility. Although such information is scarce in literature, the signal at 2.8 ppm without any sidebands for

LiD in Figure 3-12 (b) is characteristic of highly mobile deuterium ions. Sample **M-03** shows an intense single peak at 3.3 ppm with little or no associated sideband intensity to this signal (Figure 3-12 (c)). The narrowness and an absence of associated sidebands are consistent with a high mobility species. This peak position deviates from both deuterated melamine and LiD. Moreover, a manifold of sidebands centred to 9 ppm was identified in **M-03** as a non-mobile species similar to that found in melamine. Deuterium in the ball milled samples are hence present in two chemical environments: one in which it is highly mobile and different to that found in either $D_6N_6C_3$ or LiD; and a second, rigid environment in which its mobility is highly limited.

The ^{15}N NMR spectrum of $CuCl_2$ doped melamine (figure 3-13 (a)) shows good agreement with data recorded by Jürgen and Damodaran.[16, 20] The proton decoupled ^{15}N NMR experiment, highlighted and overlaid in red, affirmed that the two peaks at -207.85 and -210.015 ppm result from endocyclic tertiary nitrogens; whilst the three peaks at -290.667, -294.337 and -297.819 ppm belong to the exocyclic amino nitrogens. Ball milling the same melamine on its own (Figure 3-13 (b)) has very little influence on the position of its NMR spectrum compared to that of the pristine melamine. Once LiH is included in the milling procedure (Figure 3-13 (c)), the spectrum changes dramatically. Two broad peaks were recorded with maxima at -218.998 and -256.83 ppm, indicating a lack of long-range order. Once the proton signal has been decoupled, shown in red, the peak at -218.998 ppm can be confirmed as non-protonated ternary nitrogen whereas the suppressed -256.83 ppm peak has one proton associated with the nitrogen. It is possible that the immobile deuterium signal recorded in figure 3-12 (c) is associated with the NH peak here at -256.83 ppm, however, a 2D experiment would be necessary to confirm this association. Moreover, amine peaks in the -250 ppm region are often associated with a secondary connectivity in the triazine system; as reported for melam at -252 (melam bridge) and -254.8 ppm (intermolecular NH)[23] and melamine orthophosphate at -258 ppm (Figure 3-14 (a) and (b) respectively).[19] The data in figure 3-13 (c) show a broad linewidth and a complicated peak shape which disguise the true origin of the proposed imine connectivity. It should be also noted that the tertiary nitrogen is shifted *ca.* -8 ppm, with respect to pristine melamine. This upfield shift indicates that the ternary nitrogen becomes more electronegative due to either an increase in hydrogen bonding or a deshielding effect caused by the presence of basic LiH. The latter is more likely as FTIR suggested that ball milling with LiH had disrupted the intermolecular hydrogen bonding network in melamine.

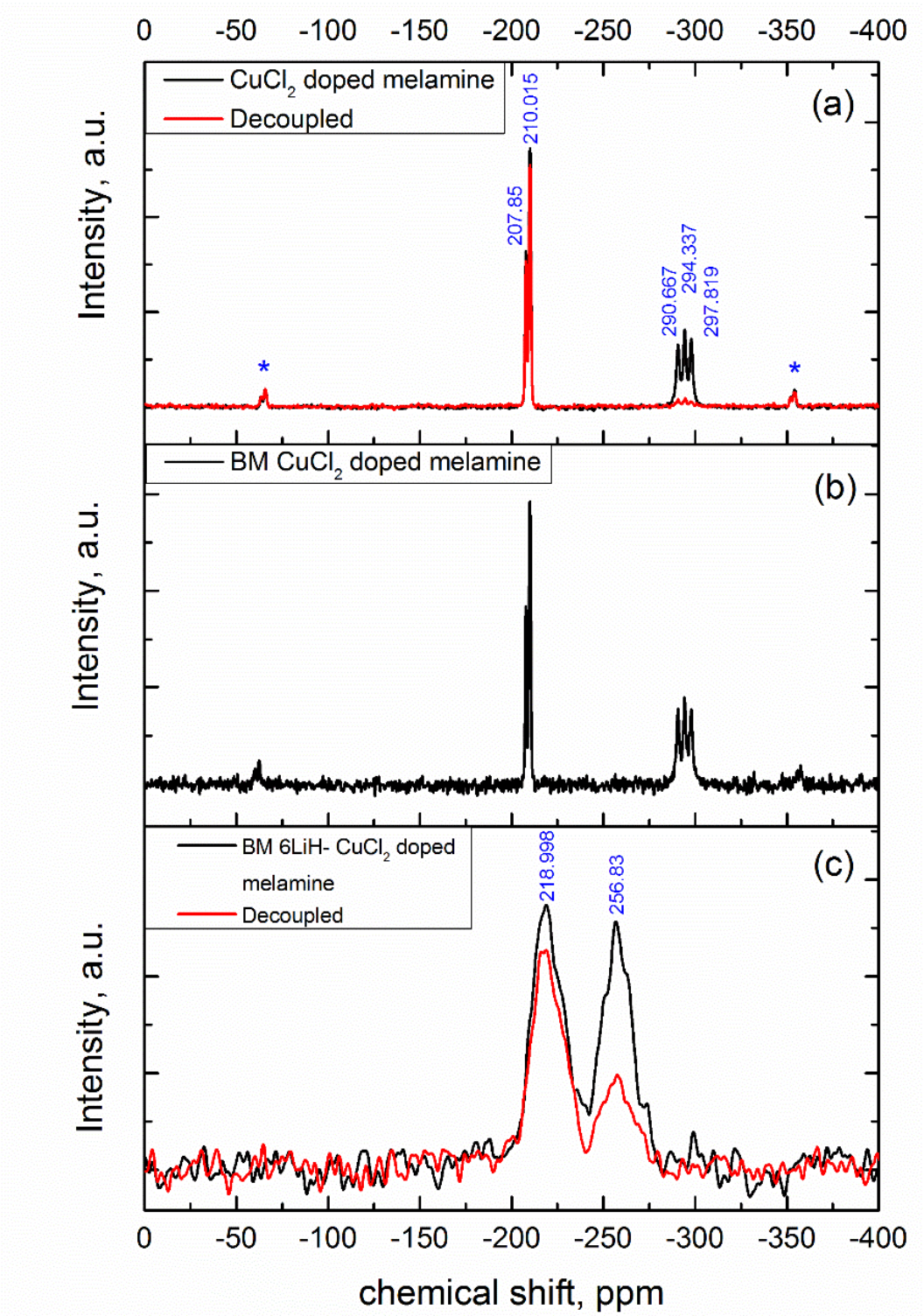

Figure 3-13. ^{15}N MAS NMR spectra on (a) $CuCl_2$ doped melamine, (b) ball milled $CuCl_2$ doped melamine and (c) **M-05** (ball milled 6LiH : $CuCl_2$ doped melamine)

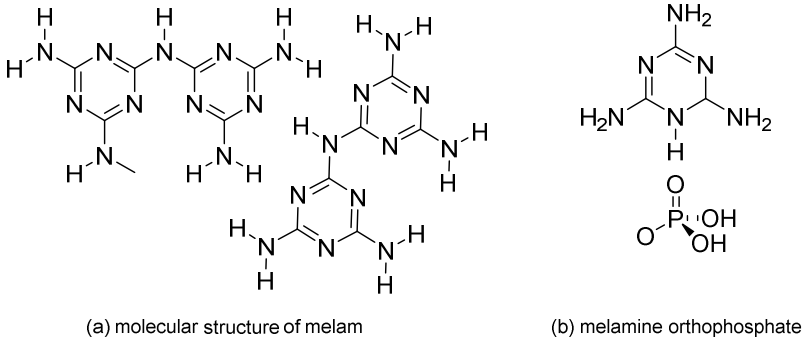

Figure 3-14. Molecular structures of (a) melam and (b) melamine orthophosphate

The ^{15}N NMR spectrum of sample **M-05** heated *ex situ* to 200 °C (Figure 3-15) shows a combination of peaks in the primary (three peaks at -297.504, -293.644 and -290.838 ppm), secondary (-251.483 ppm) and two ternary positions, one in the usual melamine endocyclic position (-209.87 ppm) and the other in the centre of three triazine rings as found in melem (-234.167 ppm).[16] This gives an indication that melamine condensation occurred during dehydrogenation, the exact sequence of which will be determined by further *in situ* NMR experiments following this project using ^{15}N labelled reactants to improve temporal resolution.

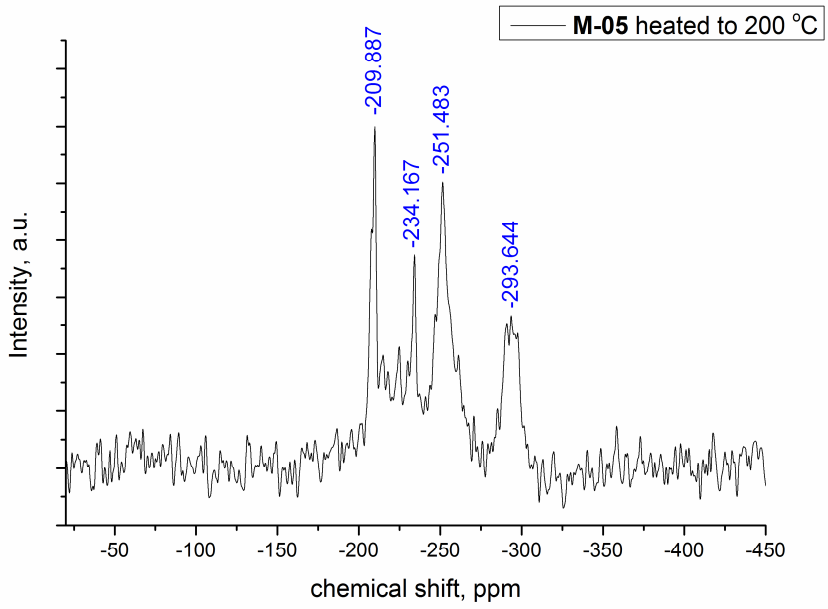

Figure 3-15. ^{15}N MAS NMR spectrum of **M-05** (ball milled 6LiH : $CuCl_2$ doped melamine) heated to 200 °C

3.3.4 Isotopic labelling experiments

Positive identification of structural changes induced following the ball milling of LiH with melamine elicited further examination of the interactions and reactions that might result from the dynamic mechanochemical process. Isotopic labelling with deuterium is an effective way to probe the ball milled system as the extent of the $NH^{\delta+}$ ...$MH^{\delta-}$ interaction can be readily detected by FTIR and the decomposition mechanism can be resolved by studying the ratio of the desorbed H_2:HD:D_2 using mass spectrometry as has been suggested for dehydrogenation in other hydride systems.[33-35]

Six equivalents of LiD were ball milled with commercial melamine under the same conditions described in section 3.3.1 (**M-06**). The same stoichiometry mixture was also prepared by hand grinding in a mortar and pestle for ten minutes in the glovebox (**M-07**). FTIR and PXD data for the two deuterated samples are compiled along with those for **M-01** in figures 3-16 and 3-17. Firstly, a comparison is drawn between the room temperature FTIR spectra of pristine melamine (a), **M-01** (b) and **M-06** (d) in figure 3-16. It was previously established that ball milling LiH with melamine interrupts the intermolecular hydrogen bonding network within the melamine lattice and elongates the intramolecular bond between the triazine ring and the exocyclic amino groups. The isotopically substituted spectrum (d) shows a similar trend between the 1600 and 1400 cm^{-1} region, although a smaller overall shift is exhibited. Each individual band is better defined, conceivably due to the random introduction of deuterium during milling which breaks local NH_2 group symmetry and suppresses the local resonances interactions between individual NH bonds.[28] The reduced extent of the C-NH_2 red shift and the triazine out of plane blue shift are both consequences of the presence of deuterium.[36] LiD is known to form more stable hydrogen bonds than those formed with LiH, hence would lengthen the N-H bond, in turn reducing the extent of the C-N stretch. The more unusual features found in the region from 3500 to 3100 and 2500 to 2000 cm^{-1} can be assigned to primary and secondary N-H and N-D stretching modes respectively. In contrast to that observed in sample **M-01** (spectrum (b)), the primary and secondary amine interactions at 3475, 3330 and 3145 cm^{-1} are more prominent in **M-06**. This is mirrored by the deuterated amine peaks at 2522, 2362, 2154, 2013 and 1969 cm^{-1}. Although no pure-phase data is available for deuterated melamine, the N-D assignment here is based on a combination of FTIR study on deuterated melaminium nitrate (ND2 at 2564, 2490 and 2468 cm^{-1})[37], cytosine (2532 and 2332 cm^{-1})[28] and similar isotopic labelling experiments, using LiD to replace LiH in the LiH-$MgNH_2$ system.[35, 35] The observed isotopic exchange reported by Isobe *et al.* and Chen *et al.* were correlated to ball milling and the effect ascribed to bimolecular or trimolecular transition states through columbic $LiD^{\delta-}$… $^{\delta+}$HN attractions.[33, 35] The exchange was suggested to be facilitated by the bombardment of LiD on melamine within the chaotic ball milling environment. In the present experiment, the effect of ball milling on isotopic H/D exchange is evident by the IR spectrum of **M-07**, (c) which resembles that of pristine melamine.

This confirms, as might be expected that the $LiD^{\delta-}$… $^{\delta+}HN$ interaction is activated by the mere energetic process of ball milling.

Heating **M-06** yielded similar trends to its LiH analogue (**M-01**). However at 280 °C (spectrum (f)) the deuterated sample shows a higher proportion of features in the 1400 cm^{-1} region that can be attributed to melamine.

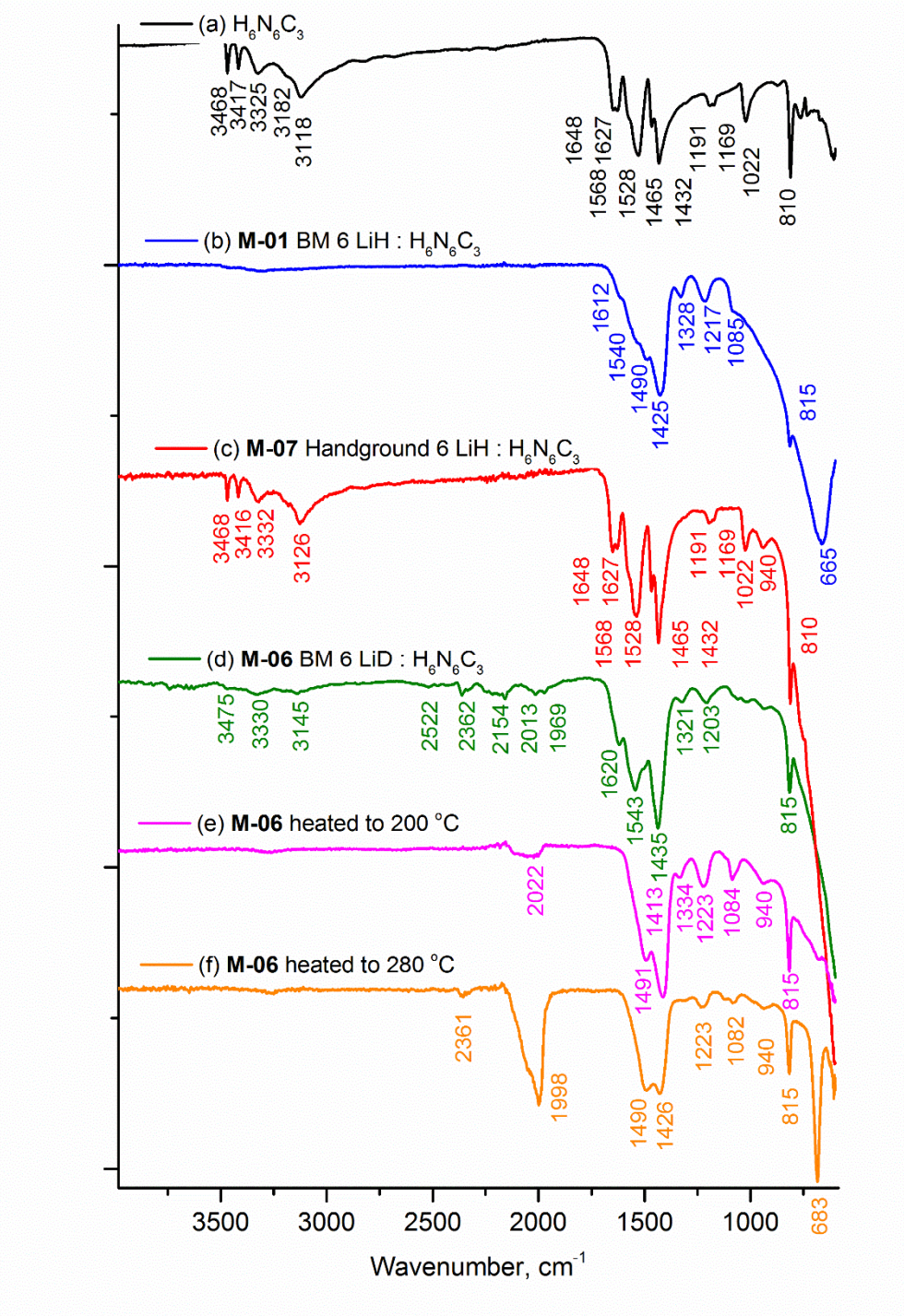

Figure 3-16. FTIR spectra comparing the results from the isotopic labelling experiment with (a) melamine, (b) **M-01** BM 6LiH:melamine (c) **M-07** Handground 6LiD:melamine (d) **M-06** BM 6LiD:melamine, (e) **M-06** heated to 200 °C and (f) **M-06** heated to 280 °C

Ball milled LiD : melamine yielded a similar diffraction pattern to its protonated analogue, as shown in figure 3-17. With the exception of LiH reflections, the samples exhibit poor crystallinity and the patterns show some indications of the melamine starting materials and more compelling evidence of LiH(D). The hand ground sample, as expected, displays sharper narrow peaks indicative of higher crystallinity.

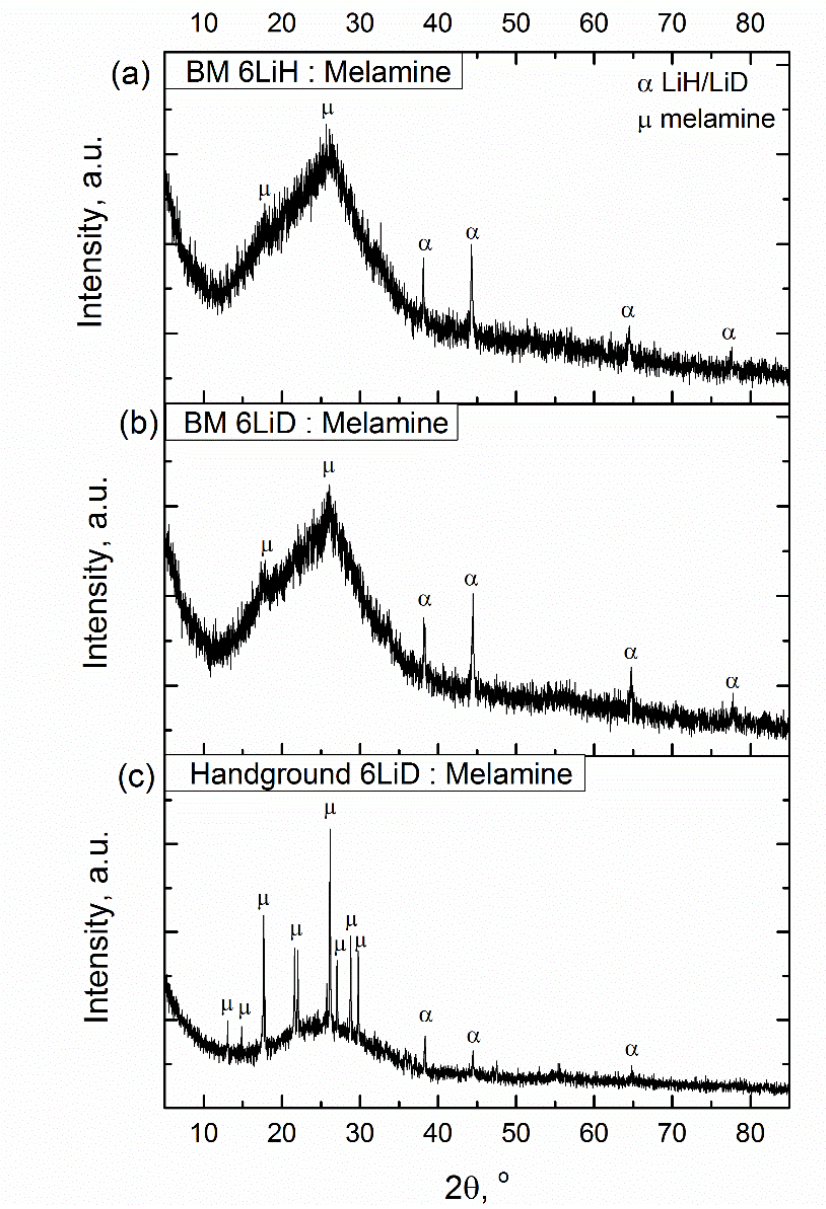

Figure 3-17. PXD of isotopic labelling experiment with LiD, (a) BM LiH : melamine, (b) BM LiD : melamine and (c) hand ground LiD : melamine

Thermal analysis of the decomposition of samples **M-01** and **M-06** are presented below in three figures; figure 3-18 shows the TG and DTA profiles, figure 3-19 the hydrogen and deuterium mass spectra and figure 3-20 the ammonia mass spectra.

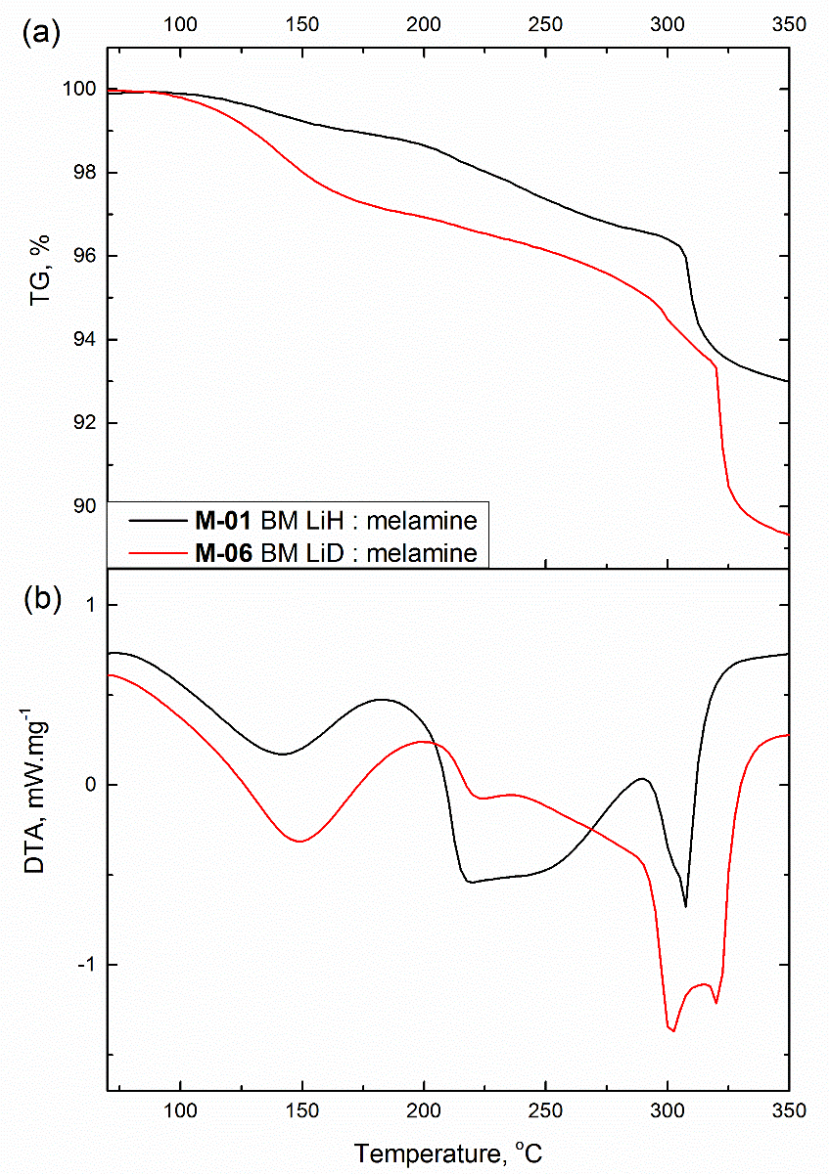

Figure 3-18. TG (a) and DTA (b) profiles resulting from the isotopic labelling experiment with LiD (**M-06**: red, handground: blue) compared with LiH (**M-01**: black)

The mass loss of **M-06** amounted to 10.7 wt% at 350 °C (figure 3-18 (a)), which is slightly higher than the theoretical 10.01 wt%. The DTA recorded four exotherms with peak values 141.7, 220.6, 301.3 and 321.3 °C; corresponding to 2.4, 2.66, 1.59 and 4.06 % mass loss in the TG. By using the second derivative of the DTA trace, it is possible to determine the end point of the final exothermic peak to be 330 °C. This corresponds to a mass loss of 10 wt%, equivalent to the theoretical system H/D content of 10.02wt%. Both ball milled samples lose approximately half of their theoretical H/D content by the end of the second step, and the remaining half after 300 °C.

In a similar manner to its protonated analogue, decomposition of **M-06** features two gradual TG steps followed by two much sharper weight losses. The corresponding DTA peaks also culminate at

the same temperatures yet it should be noted that only one peak is observed during the second step for the deuterated sample; whilst the protonated sample (**M-01**) produced a broader, compounded profile. The final two exotherms of **M-06** are further apart and the relative peak intensities reversed in comparison to **M-01**. It is suspected that kinetic isotope effect is likely to be responsible for the wider split DTA peaks which can be aggravated by the unquantifiable extent of isotopic scrambling from ball milling.

The mass spectrum of the gas evolved during thermal decomposition for **M-06** is shown in figure 3-19 (b). A mixture of H_2 : HD : D_2 was recorded during the first two steps followed by an overwhelming HD concentration during the final two steps at an onset of 300 °C. Here the observed H_2 and D_2 can be rationalised as a consequence of isotopic H/D scrambling during ball milling as described previously by the FTIR study. The formation of N-D must be accompanied by the formation of LiH, thus randomly distributed N-D could interact with LiD to form D_2, and likewise N-H to interact with LiH to form H_2.

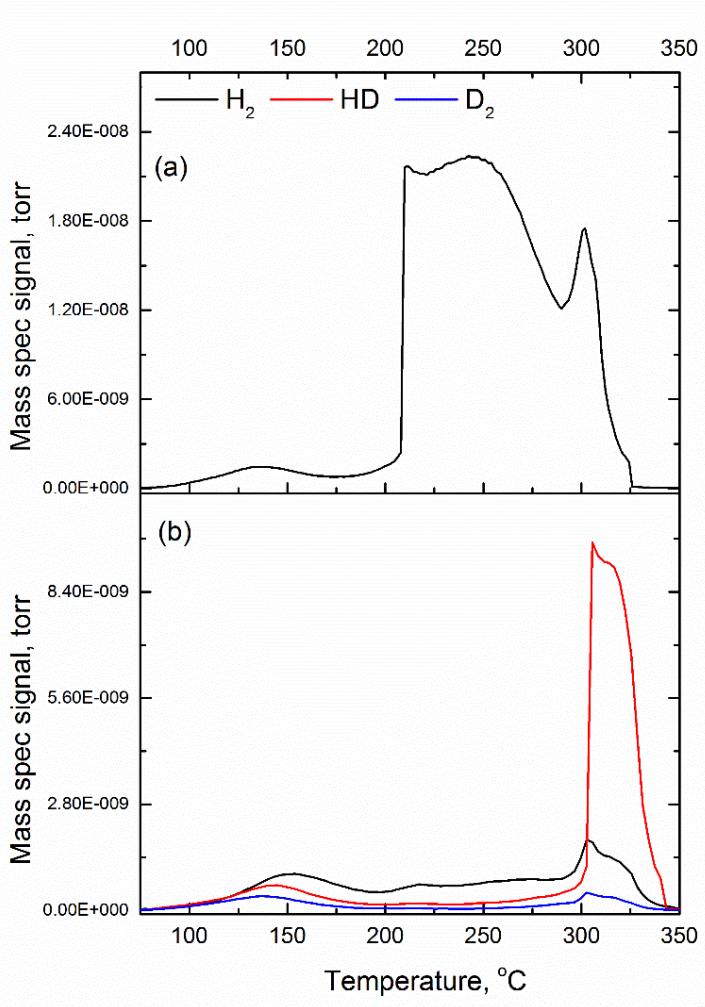

Figure 3-19. Evolved gas mass spectrum for (a) **M-01** and (b) **M-06** heated to 350 °C in the STA. *m/z* = 2 (black), 3, (red) and 4 (green)

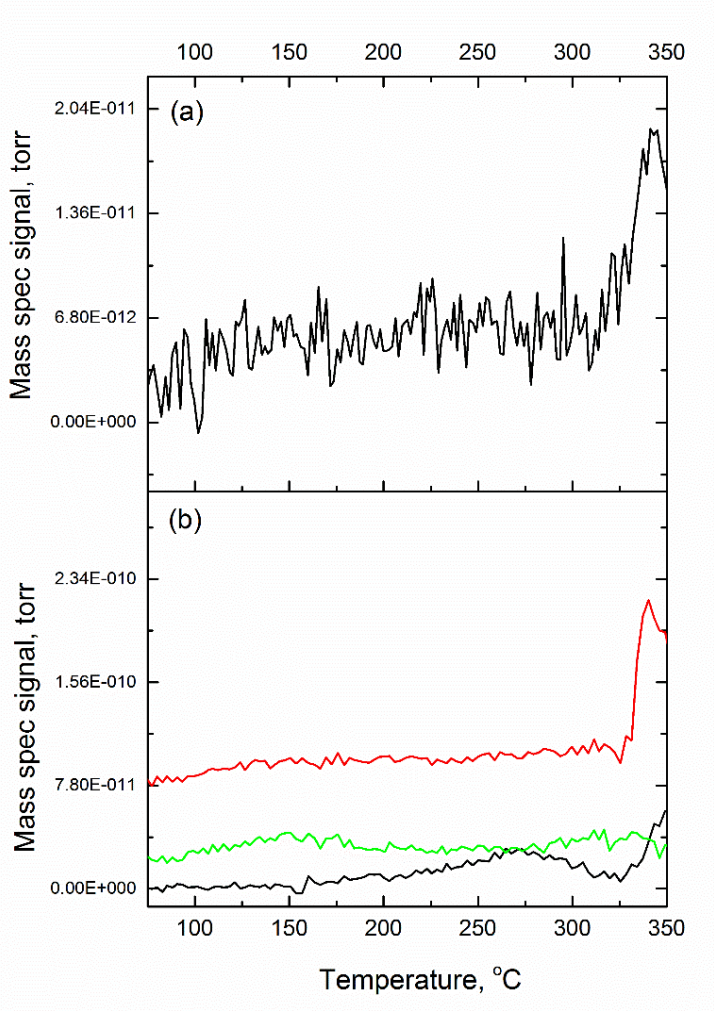

Figure 3-20. Evolved gas MS of (a) **M-01** (b) **M-06** heated to 350 °C in the STA. *m/z* = 16 (black), 18, (red) and 19 (green)

It is not unusual to observe mixed species by evolved gas MS during isotopic labelling experiments such as depicted in figure 3-19.[33, 35] A possible mechanism contributing to the mixed species was recently proposed as homopolar recombination by Wolstenholme *et al.*[38] In this comprehensive review on hydrogen storage systems the author highlighted the role of this non-conventional dihydrogen interaction in dehydrogenation; ranging from systems such as simple binary LiH to more complex systems such as ammonia borane. Hydrogen desorption is proposed to occur *via* a spectrum of processes varying in energy pathways. For ammonia borane in the gas phase for example, these processes range from columbic recombination calculated at 26.78 kJ mol^{-1} to homopolar hydrogen formation calculated at 201.25 kJ mol^{-1}. It was predicted that in the solid state, the range of processes possible for hydrogen release is less diverse as atoms are fixed in 3D space and dehydrogenation tends to depend on crystal structure.[38] In the case of ball milled LiH and

melamine, as the exact structural model post ball milling has not yet been resolved the extent of contribution towards H_2 and D_2 formation by homopolar hydrogen formation cannot be quantified.

Even without a firm mechanism for the release of H_2 and D_2, it is evident that HD formation between LiD and melamine is the dominant pathway at *ca.* 300 °C with a H_2 : HD : D_2 ratio of 3.75 : 20 : 1 calculated from the highest peak positions at 305 °C. At a temperature nearing its sublimation, the rigid N-H in melamine is likely to exhibit higher vibrational mobility to interact with LiD. A near vertical TG profile reflects fast kinetics for the thermodynamically favourable formation of HD and Li_2NCN at this temperature. This suggests strongly that hydrogen release is predominantly $N\text{-}H^{\delta+}\ldots{}^{\delta-}HLi$ by nature.

Negligible ammonia was detected during dehydrogenation of all three samples between 100 - 320 °C as indicated in figure 3-20. Trace amounts were recorded for both ball milled samples above 330 °C, corresponding to the slight and gradual mass loss in the TG profile.

Closer examination of the decomposition experiment as a whole reveals excellent agreement between the MS and TG profiles recorded. Figure 3-21 compiles the cumulative hydrogen MS (sum of *m/z* = 2, 3 and 4) as recorded and integrated against the TG profile. The broadly similar profiles reinforces the direct association between mass loss and hydrogen release.

Finally, PXD of the reaction product between Ball milled LiD : melamine, shown in figure 3-22 confirmed the solid product Li_2NCN was produced to stoichiometry.

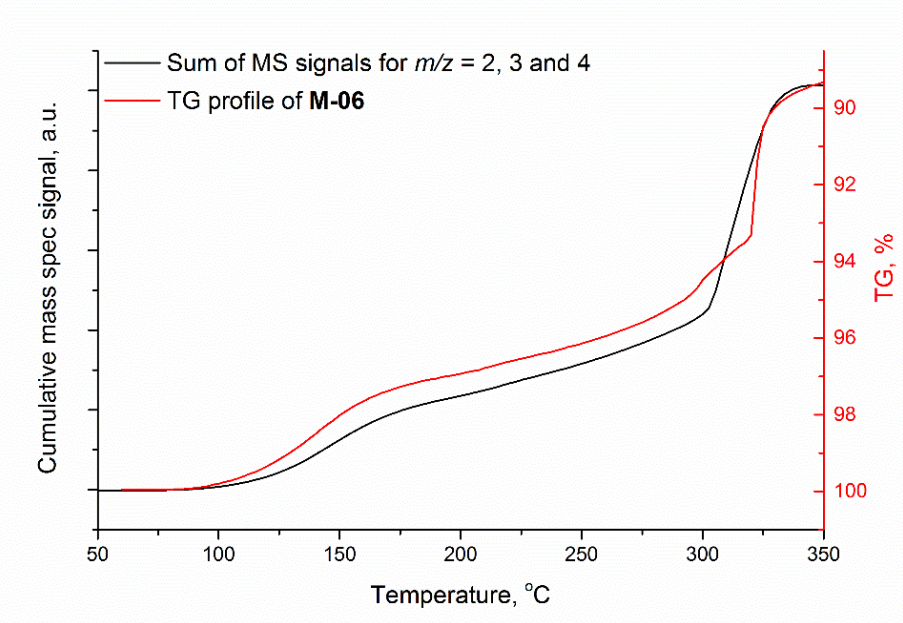

Figure 3-21. TG and MS of BM 6LiD : melamine decomposed to 350 °C in the STA

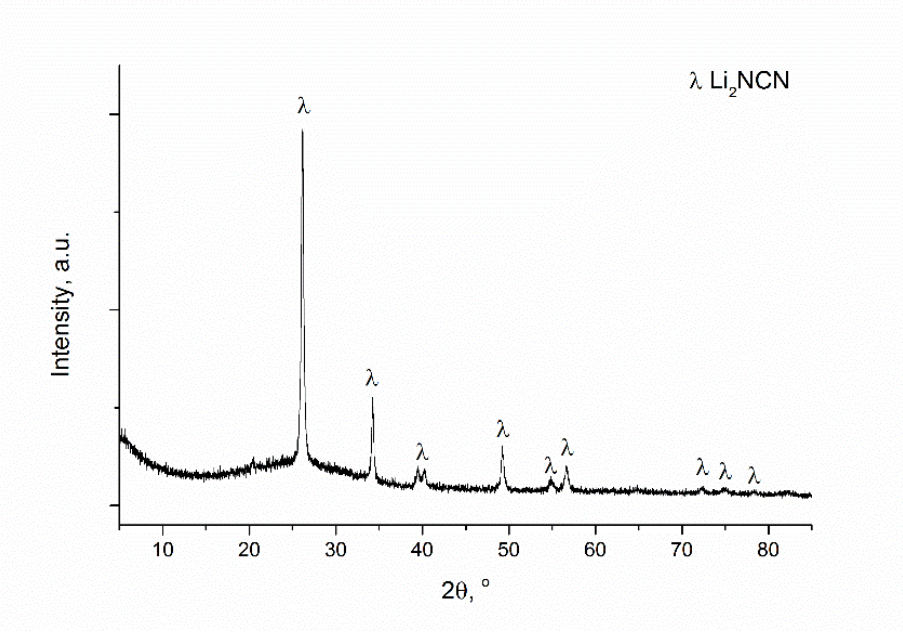

Figure 3-22. PXD pf 6LiD : melamine decomposed to 350 °C in the STA

In summary, isotopic labelling using LiD further confirmed the structural changes induced by ball milling proposed previously in section 3.3.1. FTIR revealed similar, though smaller, red shifts to the ring-NH_2 stretching vibrations in the 1400 cm^{-1} region. A plausible explanation is in that LiD is subtly superior in stabilising hydrogen bonds hence the NH_2 groups further lengthens, in turn causing a smaller elongation on the C-NH_2 bond. Isotopic scrambling was observed with the presence of N-D vibration modes as a result of milling. This implies that the LiD…HN distance was brought close to that of conventional hydrogen bonds during ball milling. H/D exchange in this case could occur through a transient hydrogen bond, or bombardment of LiD with melamine on impact in the ball mill. Hand grinding LiD with melamine yielded neither of the interactions described above confirming that the structural change and isotopic exchange is actuated through mechanical means.

The decomposition of ball milled LiD : melamine is comparable to that of its hydrogenated counterpart by 330 °C. The crystalline decomposition products were identical between the hydrogenated and deuterated analogues by XRD. A mixture of H_2, HD and D_2 is detected by the MS during heating with a H_2 : HD : D_2 ratio of 3.75 : 20 : 1 at 305 °C. The dominating formation of HD suggests $LiD^{\delta-}\ldots^{\delta+}H$-N type interaction indeed facilitate dehydrogenation during the final stages of desorption. It was however not possible to pinpoint the dehydrogenation mechanism throughout the entire dehydrogenation process as H/D scrambling was introduced during ball milling. Trace amounts of ammonia were observed only after dehydrogenation was completed at above 320 °C. TG and MS profiles showed excellent cohesion, which confirms a direct association between mass loss and hydrogen desorption.

3.4 Discussion

3.3.5.1 Structural changes to facilitate hydrogen desorption

The results presented thus far indicated that a structural change had occurred upon ball milling which facilitated the hydrogen desorption observed between LiH and melamine. The various experimental evidence can be summarised as follows:

- PND and PXD of post milled samples exhibited reflections from LiH(LiD) but presented no evidence of Bragg diffraction from crystalline melamine. The broad peak between 10 and 40 ° 2Θ indicates amorphous material.
- FTIR indicated the loss of intermolecular N-H interactions after milling the two reactants and the spectra red shifted with respect to the ring-NH_2 stretching and bending modes. H/D scrambling was found when ball milling LiD with melamine. Upon heating to 200 °C the ring-NH_2 continues to red shift, while the bending modes disappear. Linear C=N stretching modes appear at this point.
- ^{15}N NMR of the ball milled sample revealed the absence of any primary NH_2 moiety with only secondary and tertiary nitrogen remaining in system. Upon heating to 200 °C the spectrum shows a combination of primary, secondary and two types of tertiary nitrogen (triazine endocyclic N and tri-s-triazine central N) connectivities present in the sample. On the other hand ^{2}H NMR detected an immobile deuterium specie similar to that found in pristine melamine, and a highly mobile deuterium specie found to belong to neither deuterated melamine nor LiD.

It is worthy to note that both diffraction and NMR techniques are known to probe deep within the volume of powder samples, indicating the above observations permeate the sample bulk.

Beyond doubt melamine experiences substantial structural modification when ball milled with LiH. Here, the lack of crystallinity in melamine should not be perceived as originating from conventional nano-sizing or crystal defects introduced during milling, but from a complete rearrangements in its extended structure, as spectrometry suggested an absence of intermolecular hydrogen bonding. The exocyclic amino species also transitioned from primary to secondary while the triazine skeleton remained intact. Considering melamine's renowned characteristic to self-assemble with polar molecules,[18-20] it can be hypothesised that the melamine crystal network broke down during milling to interact with ionic LiH. Such an interaction, is supported by the ^{2}H NMR shift from 2.8 ppm for pristine LiD to 3.3 ppm for the ball milled sample.

H/D scrambling during isotopic labelling also implies interactions between the reactants, rather than reaction, as full theoretical amount of hydrogen was desorbed to form Li_2NCN in subsequent thermal analysis.

3.3.5.2 Dehydrogenation scheme

To formulate the decomposition mechanism between LiH and melamine, it is useful to first consider how a free melamine molecule would react with six equivalents of LiH. Molecular symmetry in free melamine dictates that the three equivalent exocyclic amino groups have the same reactivity in the presence of LiH as shown in scheme 3-2 **A**. The elimination of the first hydrogen molecule results in an $Li^+...N^-$ interaction which forms an anion from the melamine. Sequential dehydrogenation on the same nitrogen is unfavourable as it is now more electronegative, due to the loss of one hydrogen, consequently the remaining hydrogen becomes less acidic. Simultaneous deprotonation on all three primary amines is also improbable as the increase in negative charge from the first deprotonation also contributes to the π-electron configuration to further stabilise the triazine ring. Electron repulsion therefore raises the thermodynamic barrier for the 2nd and 3rd primary amine deprotonations. This agrees well with the observed TG observations that approximately 1 equivalent of H_2 is liberated in the first step with an onset temperature of 96.7 °C, followed by the release of another 2 equivalents of H_2 at 203.8 °C. The deprotonation of the first primary amine will result in resonance structures **B1** and **B2** as the intermediate. From experimental results by FTIR at 200°C, it appears that the aromaticity of the triazine ring is broken here to form a C=N bond in resonance **B2**. The breakdown in aromaticity would also facilitate the C-NH_2 elongation observed. In similar manner, the second and third equivalents of hydrogen forms via **C** to intermediate **D**.

Further deprotonation would occur *via* the mechanism depicted by **E**. The loss of another equivalent of hydrogen renders electron rearrangement of an already highly electronegative triazine ring which results in ring rupture as shown in **F**. Further breakdown of the molecule would yield the product Li_2NCN, **G** releasing the final 2 equivalents of hydrogen. This is the most compelling scenario based on theoretical deductions as well as the TG results from the isotopic labelling experiment in Figure 3-17. The final stages of dehydrogenation described from **E** to **G** are potentially analogous to the depolymerisation of melamine to cyanamide under ammonia pressure with a guanidine intermediate.[24]

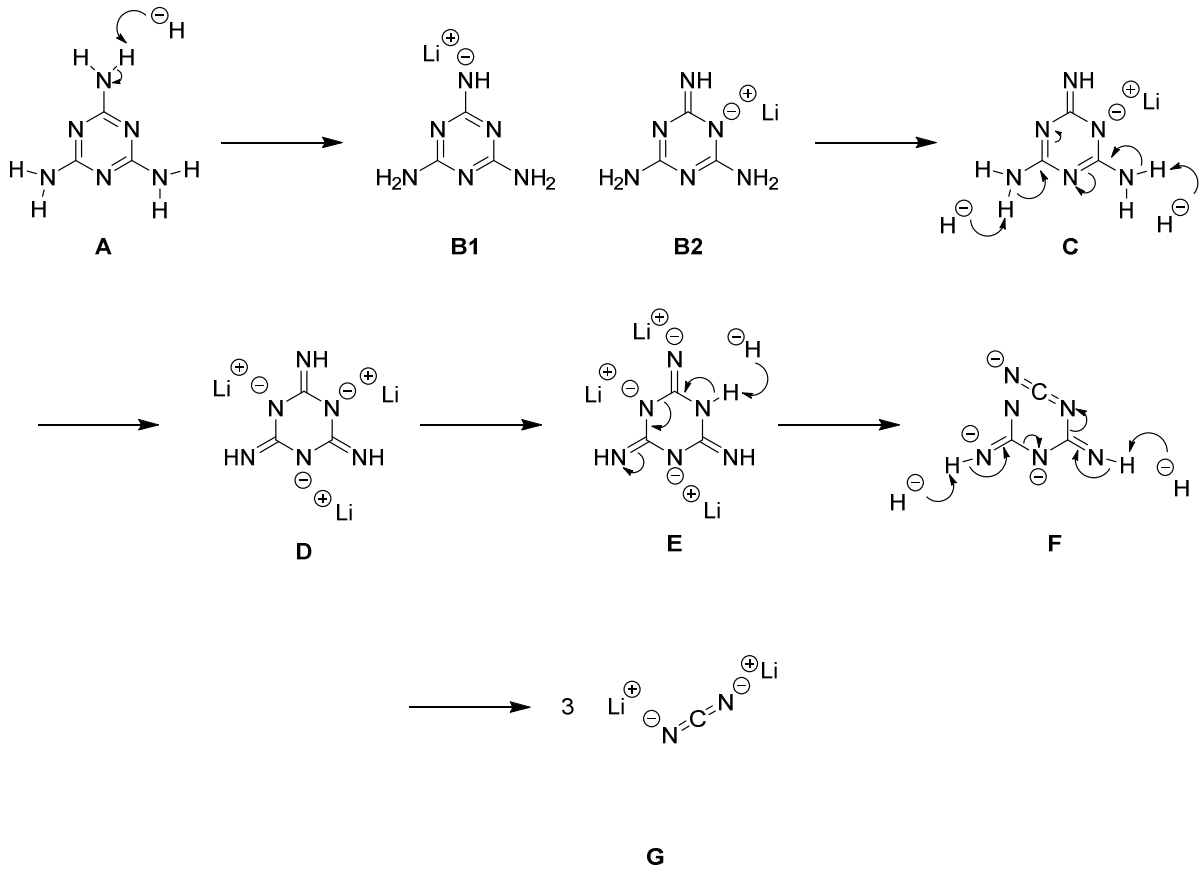

Scheme 3-2. Schematic of free melamine reacting with LiH

If we then apply solid state restrictions to the system it is immediately apparent that melamine is not symmetrical in its crystal lattice. The exocyclic N3 amine group resides 3.6 ° out of plane in the pyramidal position with respect to the triazine ring with a C-N bond of 1.3618 Å.[22] This deviation from ideal renders N3 a fraction more electron dense as the lone pair electron participates less in the triazine π-electron field in this configuration. Consequentially H5 and H6 have slightly higher $H^{\delta+}$ charge than H1-4. With a stronger positive charge, hydrogens on N3 are likely form a more significant interaction with $LiH^{\delta-}$ by Columbic attraction hence the preferential site for the release of the first equivalent of hydrogen. Pyramidal N1 and N2, on the other hand are 1.68 and 1.34 ° from the triazine plane and hence their lone pair elections would participate in the triazine π-system. This further correlates with the observed equivalents of mass lost due to hydrogen release after the first (96.7 °C) and second (203.8 °C) TG step.

While this scheme is theoretically sound, there is evidence that the starting ball milled sample in fact contains secondary amine moieties rather than primary amines as usually found in melamine. Moreover, after the first deprotonation tertiary nitrogen bonding environment that is usually found central in tri-s-triazine structures such as melem is observed alongside primary, secondary and tertiary endocyclic amine connectivity. This suggests potential ring condensation sequential to the

first equivalent of hydrogen desorption. The full dehydrogenation scheme cannot be wholly rationalised with the present set of data and further *in situ* NMR spectrometry work using ^{15}N labelled reactants is being proposed to gain better insights into the interactions between LiH and melamine during dehydrogenation.

3.4 Regeneration of Li_2NCN

To achieve a fully sustainable hydrogen storage system, hydrogen will need to be reinstated in the reaction product of equation (3-1), Li_2NCN. However Li_2NCN remains stable under a maximum hydrogen pressure of 150 bar up at temperatures to 360 °C in a Sieverts type apparatus. This is to be expected as Li_2NCN is a thermally stable compound ($\Delta H°_f$ estimated to be at least 359.5 kJ mol^{-1})[39] that can be formed by the solid state reactions between Li_2CO_3 and urea at 800 °C,[40] Li_2C_2 and Li_3N at 600 °C[39], or by dilithium acetylide and Li_3N in liquid lithium 530 °C[27]. It was reported, however that the dilithium salt is highly hygroscopic[27] which introduces alternative routes to rehydrogenate Li_2NCN.

The process to form $[NCN]^-$ compounds by the hydrolysis of calcium cyanamide salts is well documented dating back to the late 19th century.[41] In the presence of water, hydrogen cyanamide can be prepared from calcium cyanamide with sulfuric acid,[41] the starting material can also be replaced by sodium cyanamide.[42] Hydrogen cyanamide can then be polymerised into 2-cyanoguanidine and subsequently melamine by direct thermal condensation in schematic 3-1, or KOH assisted polymerisation at a lower temperature.[44] The same synthesis has never been reported for Li_2NCN which is the topic of investigation in this section (equation 3-3 and 3-4).

$$Li_2NCN + H_2SO_4 + H_2O \rightarrow H_2NCN + Li_2SO_4 + H_2O \quad (3\text{-}3)$$

$$3\ H_2NCN \rightarrow H_2NCN + H_4N_4C_2 \rightarrow H_6N_6C_3 \quad (3\text{-}4)$$

FTIR was used to follow the reaction in each step and PXD was used to identify the solid products. As reported, Li_2NCN is hygroscopic and dissolved easily to form a colourless solution in deionised water (Figure 3-23 (a) and (b) respectively). The solution was stirred on a magnetic stirrer and 10% H_2SO_4 was added dropwise until the pH reached approximately 5. The solution was allowed to stir for another 30 minutes before drying using the Schlenk line with a liquid N_2 trap while sitting in a water bath at 40°C to yield a white solid (figure 3-23 (c)). This was then dissolved in ethanol, and the resulting precipitate (Figure 3-23 (d)), H_2SO_4)[45] was separated to afford single phase H_2NCN once the solvent was removed.

FTIR shows the transition of the *v*(NCN) absorption from 1991 and 2048 cm^{-1} for Li_2NCN,[27] to 2102 cm^{-1} for the plausible intermediate, Li (HNCN) of Li_2NCN hydrolysis (by analogy to CaNCN, equation (3-5)) to 2227 and 2255 cm^{-1} for H_2NCN.[46]

$$Li_2NCN + 2\ H_2O \rightarrow Li(HNCN) + LiOH \qquad (3\text{-}5)$$

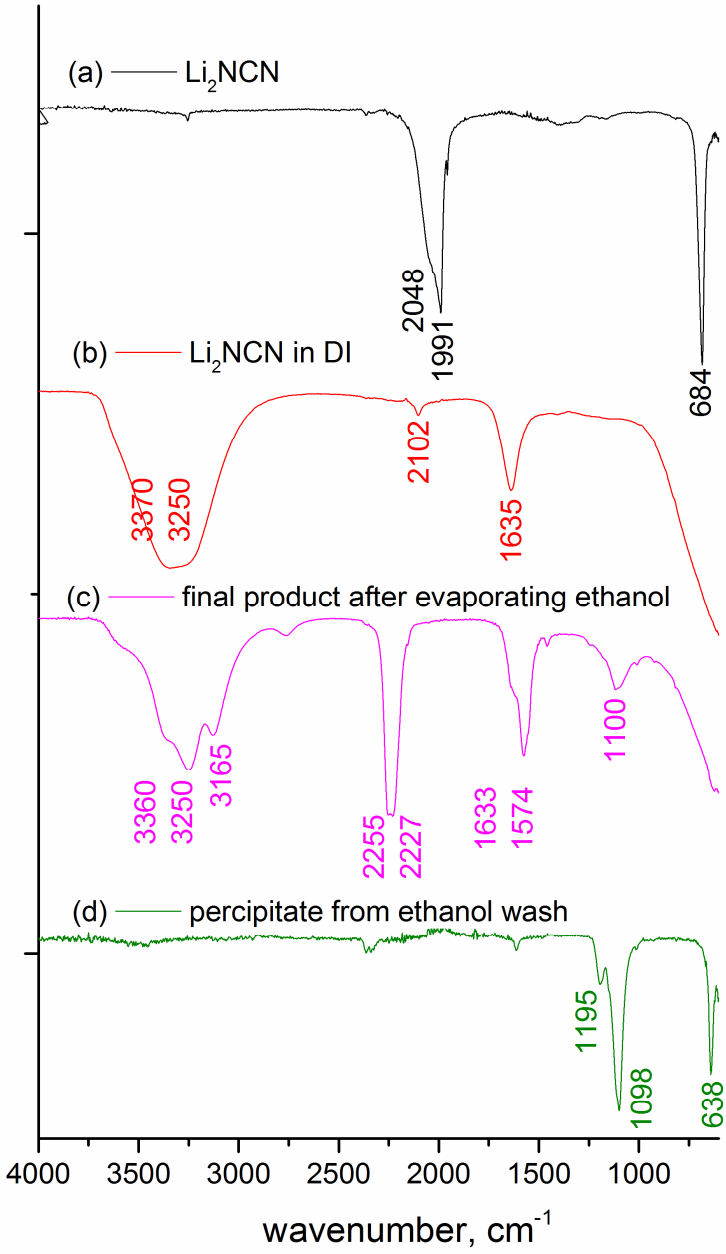

Figure 3-23. FTIR spectra of the Li_2NCN hydrolysis reaction, (a) Li_2NCN from heating **M-01** to 400 °C, (b) Li_2NCN dissolved in DI water, (c) product after solvent ethanol is evapourated and (d) precipitate formed during ethanol wash

Using the synthesized H_2NCN, pure melamine was oligomerised according to the methods described by US Patent 4069383 (PXD figure (3-24)). A 300 : 3.5 : 1 (by weight) DMSO : KOH : H_2NCN solution of was heated in an oil bath to 150 °C under static vacuum. H_2NCN recycled from Li_2NCN was dissolved in deionised water to make an 80% solution and this was added drop-wise to the DMSO solution under dynamic vacuum, maintaining a reaction temperature of 150 °C. Water was immediately distilled off, along with a small amount of DMSO. The solution was held at 150 °C for 1 h in static vacuum and cooled to 60 °C. A volume of deionised water equal to two-third of the DMSO was added to the solution. The reaction vessel was immersed in an ice bath affording crystals of melamine, which were filtered under vacuum and rinsed three times with chilled deionised water (Figure 3-24).

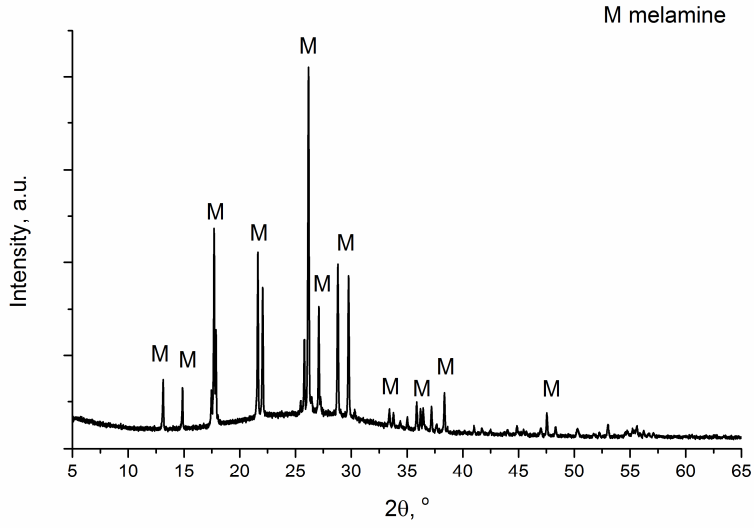

Figure 3-24. PXD of melamine obtained by polymerising H_2NCN recycled from reaction product Li_2NCN

The results shown here indicate that the product Li_2NCN can be rehydrogenated back to melamine using common chemical reagents. Lithium can also be recovered from Li_2SO_4 by electrolysis using renewable electrical generators. The processes outlined here are existing industrial procedures which propose an alternative, yet competitive operation model to the current on-board, direct rehydrogenation scheme preferred by the hydrogen storage materials community. In summary, an off-board method to rehydrogenate the 6 LiH : melamine hydrogen storage system has been identified to close the energy cycle in a sustainable manner.

3.5 Conclusions and outlook

Through the resulted presented in this chapter, it was verified that the theoretical amount of hydrogen can be released experimentally between 6 LiH and melamine. The dehydrogenation is facilitated by high energy ball milling which disrupts the intermolecular hydrogen bonding network present in solid melamine. Through FTIR, it was found that ball milling also induce a intramolecular electron redistribution resulting in a collective red shift in the triazine skeletal symmetric and asymmetric stretching modes (ν(ring-NH_2)); and a complementing blue shift on the rocking vibrations on the same bond. When the sample is heated, a sequential red shift on the same ν(ring-NH_2) modes was observed in conjunction with dehydrogenation. It is proposed that the release of hydrogen resulted in a direct and increasing ionic interaction between the exocyclic amino group and lithium ions.

Moreover, it has been identified by ^{15}N MAS NMR spectrometry that the nitrogen chemical environment of the ball milled mixture differs drastically from pristine melamine. Both PND and NMR experiments indicated that there exist stable intermediate phases during dehydrogenation from RT to 300 °C, however the present evidence is inadequate to recommend plausible structural models. *In situ* ^{15}N MAS NMR experiments would be beneficial to further characterise the reaction pathway and to verify the reaction scheme hypothesised in this chapter using ^{15}N labelled samples.

By labelling LiH with deuterium, it was possible to establish that ball milling provided sufficient energy to induce an isotopic H/D exchange with hydrogenated melamine. HD gas was identified by evolved gas MS as the dominant species during the final stages of dehydrogenation at 300 °C with fast kinetics. This suggests that hydrogen release is facilitated by enhanced $N\text{-}H^{\delta+}\ldots{}^{\delta-}HLi$ interactions.

Finally, an off-board rehydrogenation scheme is proposed where Li_2NCN is regenerated to melamine, and Li_2SO_4 by treating with sulfuric acid. Lithium could then be recovered from the lithium salt through electrolysis using renewable sources.

3.6 References

1. Schmalzried, H. *Chemical Kinetics of Solids;* VCH, Germany, 1995.
2. Rao, C. N. R.; Gopalakrishnan, J. *New Directions in Solid State Chemistry,* Edition 2*;* Cambridge University Press, 1997
3. Talbot, W. F. US Patent 2260239, Oct 21, 1941
4. Kuryla, W. C.; Papa, A. J. *Flame Retardancy of Polymeric Materials*; Dekker: New York, 1973-1979; Vols. 1-5
5. Moulton, B.; Zaworotko, M. J. *Chem. Rev.* **2001**, *101*, 1629-1658
6. Prins, L. J.; Reinhoudt, D. N.; Timmerman, P. *Angew. Chem. Int. Ed.* **2001**, *40*, 2382-2426
7. Thomas, A.; Fischer, A.; Goettmann, F.; Antonietti, M.; Müller, J.; Schlögl, R.; Carlsson, J. M. *J. Mater. Chem.* **2008**, *18*, 4893-4908
8. Wang, Y.; Wang, X.; Antonietti, M. *Angew. Chem. Int. Ed,* **2012**, *51*, 68-89
9. Hetherington, H. C.; Braham, J. M. *J. Am. Chem. Soc.* **1923**, *45*, 824-829
10. Belsky, A. J.; Li, T.; Brill, T. B. *A*
11. Merchant Research & Consulting Ltd. [Online] https://mcgroup.co.uk/news/20150312/china-major-driver-global-melamine-market.html. Accessed 5th October 2016
12. Melamine manufacturing process [Online] http://www.southernchemical.com/wp/products/melamine/melamine-manufacturing-process. Accessed 5th October 2016
13. Hughes, E. W. *J. Am. Chem. Soc.* **1941**, *63*, 1737-1752
14. Price, P. F.; Varghese, J. N.; Maslen, E. N. Acta. Cryst. **1978**, *34*, 203-216
15. Wang,Y.; Mebel, A. M.; Wu, C.; Chen, Y.; Lin, C.; Jiang, J. *J. Chem. Soc., Faraday Trans,* **1997**, *93,* 3445-3451
16. Jürgens, B.; Irran, E.; Senker, J.; Kroll, P.; Müller, H.; Schnick, W. *J. Am. Chem. Soc.* **2003**, *125,* 10288-10300
17. Mukherjee, S.; Ren, J. *J. Am. Soc. Mass Spectrom,* **2010**, *21*, 1720-1729
18. Ma, X.; Wu, Y.; Zhu, H. *J. Wood. Sci*, **2013**, *59*, 419-425
19. Brinkmann, A.; Litvinov, V. M.; Kentgens, A. P. M.; *Mag. Reson. Chem.* **2007**, *45*, 231-246
20. Damodaran, K.; Sanjayan, G. J.; Rajamohanan, P. R.; Ganapathy, S.; Ganesh, K. N. *Organic Letters,* **2001**, *3*, 1921-1924
21. Larson, A. C.; Cromer, D. T. *J. Chem. Phys.* **1974**, *60*, 185-192
22. Cousson, A.; Nicolai, B.; Fillaux, F. *Acta. Cryst.* **2005**, *61***,** 222-224
23. Lotsch, B. V.; Schnick, W. *Chem. Eur. J.* **2007**, *13*, 4956-4968
24. May, H. *J. Appl. Chem.* 1959, **9**, 340-344
25. Lotsch, B. V.; Döblinger, M.; Sehnert, J.; Seyfarth, L.; Senker, J;. Oeckler, O.; Schnick, W. *Chem. Eur. J,* **2007**, *13*, 4969-4980
26. Hoang, T. K.; Su, T. Y.; Tapia-Ruiz, N.; Xiao, X.; Gregory, D. H. *Publication submitted.*
27. Down, M. G.; Haley, M. J.; Hubberstey, P.; Pulham, R. J.; Thunder, A. E. *J. C. S. Chem. Comm.* **1978**, *2*, 52-53
28. Rozenberg, M.; Shoham, G.; Reva, I.; Fausto, R. *Spectrochemica Acta Part A,* **2004**, *60*, 463-470
29. David, W. I. F.; Jones, M. O.; Gregory, D. H.; Jewell, C. M.; Johnson, S. R.; Walton, A.; Edwards, P. P. J. Am. Chem. Soc. **2007**, *129*, 1594-1601
30. Hu, Y. H.; Ruckenstein, E. *J. Phys. Chem. A* **2003**, *107*, 9737-9739
31. Mircescu, N. E.; Oltean, M.; Chiş, V.; Leopold, N. *Vibrational Spectroscopy,* **2012**, *62*, 165-171
32. Jones, W. J.; Orville-Thomas, W. J. *Trans. Faraday Soc.*, **1959**, *55*, 203-210
33. Isobe, S.; Ichikawa, T.; Hino, S.; Fujii, H. *J. Phys. Chem. B* **2005**, *109,* 14855-14858
34. Chen, P.; Xiong, Z.; Luo, J.; Tan, K. L. J. Phys. Chem. B **2003**, *107*, 10967-10970

35. Chen, P.; Xiong, Z.; Yang, L.; Wu, G.; Luo, W. *J. Phys. Chem. B.* **2006**, *110*, 14221-14225
36. McDowell, S. A. C. *J. Comput. Chem.* **2003**, *24*, 1201-1207
37. Tanak, H.; Marchewka, M. K. *J. Mol. Struct.* **2013**, *1034*, 363-373
38. Wolstenholme, D. J.; Dobson, J. L.; McGrady, G. S.; *Dalton Trans.* **2015**, *44***,** 9718-9731
39. Down, M. G.; Haley, M. J.; Hubberstey, P.; Pulham, R. J.; Thunder, A. E. *J. C. S. Dalton Trans.* **1978**, 1407-1411
40. Pavlov, M.; Sokolov,N. A.; Dergunov, U. I.; Golov,V. G. Trudy Khinz. i khim. Tekhnol., **1973**, *2*, 27.
41. Drechsel, *J. prakt. Chem.* **1887***, 16***,** 210
42. Buchanan, G. H.; Barsky, G. *J. Am. Chem. Soc.* **1930**, *52*, 195-206
43. Pinck, L. A.; Salisbury, J. M. Cyanamide. *Inorganic Syntheses*; McGraw-Hill Book Company, Inc: New York Toronto London, 1950; Vol. 3, 39-43
44. Michaud, H.; Ortenburger, G.; Poschinger, W.; Rock, H.; Seeholzer, J. Method of preparing melamine from cyanamide and/or dicyandiamide. U.S. Patent 4,069,383, Jan 17, 1978
45. Ramondo, F.; Bencivenni, L.; Caminiti, R.; Sadun, C. *Chem. Phys.* **1991***, 151*, 179-186
46. Brik, M.; Winnewisser, M. *Chem. Phys. Letter* **1986***, 123*, 382-385

4.0 Dehydrogenation reaction between LiH and urea

4.1 Introduction

Urea is a naturally occurring hydrogen rich compound used to regulate nitrogen content in organic organisms *via* the urea cycle.[1] Known also as carbamide, urea contains two amine functionalities joined by a carbonyl moiety (Figure 4-1). It is a colourless, odourless solid soluble in non-polar solvents at standard conditions.

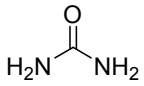

Figure 4-1. Urea

The first isolation of urea is commonly attributed to the independent discoveries in the early 1800s by Boerhaave and Rouelle respectively *via* crystallisation from urine.[2] It was the first organic compound synthesised by Wöhler in 1828 by reacting ammonia chloride with silver nitrate.[3] Industrially, urea is produced from ammonia and carbon dioxide based on the Bazarov reaction at between 170 to 220 °C (Equation 4-1) as a downstream process to Haber-Bosch ammonia production facilities (Equation 4-2).[4-5] As of 2016, global urea production exceeds 200 MT per year with over 60% produced in the Asia Pacific region.[6]

$$2\ NH_3 + CO_2 \rightarrow NH_2COONH_4 \rightarrow CO(NH_2)_2 + H_2O \qquad \Delta H^o = 11.72\ kJ\ mol^{-1} \qquad (4\text{-}1)$$

$$N_2 + 3\ H_2 \rightarrow 2\ NH_3 \qquad \Delta H^o = -45.8\ kJ\ mol^{-1} \qquad (4\text{-}2)$$

Urea is widely applied as crop fertiliser, livestock supplements and in urea-formaldehyde resins. It is an important agent in petroleum purification processes by forming clathrates with hydrocarbons.[1, 7]

Urea has been extensively studied for applications across a broad spectrum of disciplines with nearly one in four publications devoted to subjects in chemistry, amongst others such as agriculture, biochemistry, materials science and pharmacology.[8] The simple zwitterion molecule possesses unusual chemistry as a result of three potential hydrogen bonding sites at the carbonyl oxygen and two amine moieties respectively. The hydrogen bonding allows urea to blend into the tetrahedral arrangement of water seamlessly, due to a similar charge distribution despite being a significantly larger molecule.[9-10] In effect it disrupts the long range order found in pure water whilst retaining a molecular identity even at high concentrations (8 M).[11] Urea solutes function in a similar way to that of a surfactant by increasing the solubility of non-polar species such as hydrocarbons in water,[12] preventing micelle formation of ionic detergents and denaturing proteins.[10-14] This occurs

by a mechanism derived by Stumpe and Grubmüller for protein denaturing in urea solutions, where urea was observed to interact preferentially with the hydrophobic core consisting of aromatics, non-polar residues and protein backbones; whilst water solvates the hydrogen bond sites on the protein side chains.[15] Unfolding of the protein was found to be driven by enthalpically and entropically favourable solvation of the hydrophobic segments of the protein *via* urea molecules. On the other hand, Bull *et al* observed that urea increases the pH of a solution. They suggested that urea increases the ionisation of water by supressing the activity of protons.[16] Urea can also participate in coordination complexes with several metals with a wide range of coordination numbers due to is size and multiple donor sites.[17-20] In engineering urea has been adopted in the selective catalytic reduction units for heavy duty diesel vehicles.[20-23] Furthermore in organic chemistry it is thought of as a robust protecting group for aromatic and aliphatic amine groups due to resonance stability to counter nucleophilic attacks.[13, 24-25]

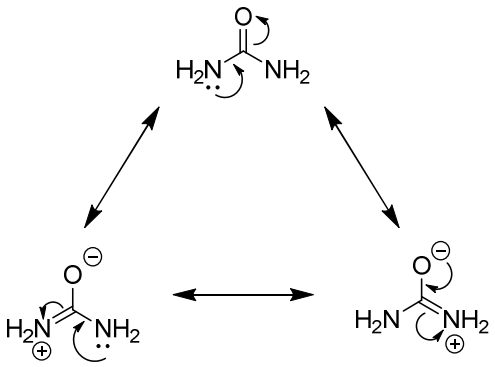

Figure 4-2. Resonance structures of urea[13]

4.1.1 The structure of urea

The properties previously mentioned are based on the electronic configuration of urea which varies according to the state of the molecule. For example, the conformation of nitrogen in solid urea is sp^2 where as in gas it is sp^3.[13] In fact, due to resonances, the lone pair electrons on nitrogen in solid urea are delocalised in the carbonyl group. Consequently, the two ionic resonance forms in Figure 4-2 are more significant in the solid state leading to a weaker C-O and stronger C-N double bond characteristic compared to the gas phase (20% sp^2 character).[13] By NMR spectroscopy, the gaseous urea monomer was observed to form a planar OCN_2 backbone with pyramidal NH_2 moieties,[26] whilst the molecule is completely flat in the solid state by FTIR, synchrotron X-ray diffraction and neutron diffraction.[27-29]

The urea crystal was amongst one of the first to be characterised by X-ray diffraction. It continuously generates interest due to its simplicity and for being a rare instance where a carbonyl

oxygen accepts four hydrogen bonds from neighbouring amine moieties.[13, 28] A tetragonal $P\bar{4}2_1m$ unit cell (a= 5.578 and c= 4.686 Å at 123 K) was confirmed by neutron diffraction. The crystal exhibits anisotropic thermal expansion and forms polymorphs under pressure (Figure 4-3).[28-30] Each unit cell in the ambient pressure structure contains two centrosymmetric C_{2v} urea molecules, which stack into orthogonal ribbons in the *ab* plane.[27-28, 31]

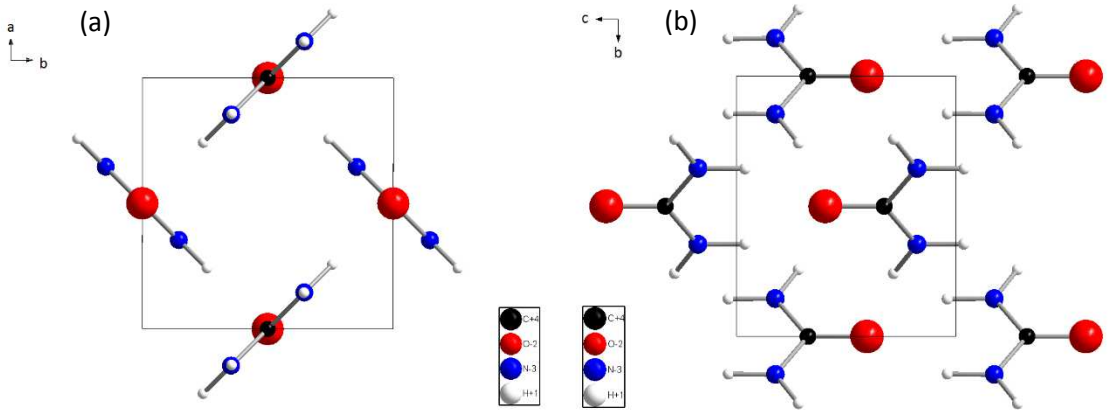

Figure 4-3. Unit cell of urea (a) along the *c*-axis (b) along the *a*-axis.

Each urea molecule features four hydrogen bonds to three neighbouring urea molecules at the carbonyl oxygen where the coplanar N-H groups are bonded to the non-bonding oxygen lone pairs, and further perpendicularly with the carbonyl pi electrons.[32] Through *ab initio* calculations, electrons near the OCN_2 backbone were found to be delocalised where the charge density of the carbonyl group indicates a σ-bond whereas a π-bond is found between C-N groups.[29] Through computational analysis Liao *et al.* found that the charge population for the oxygen non-bonding $2p_x$ (coplanar) orbital is 1.8, and of a similar strength, 1.6 for the C=O $2p_y$ (perpendicular) π-orbital. It was proposed that the nature of the hydrogen bonding in urea arise from both Coulombic interactions and donor-acceptor interactions with both oxygen lone pairs and the carbonyl π-electrons.[32] The extensive donor-acceptor hydrogen bonds between the carbonyl oxygen and amine moieties induces a dipole-dipole interaction shown in Figure 4-4 which increases the p-characteristic of the C-N bonds while the C=O and N-H bonds lengthen.[13]

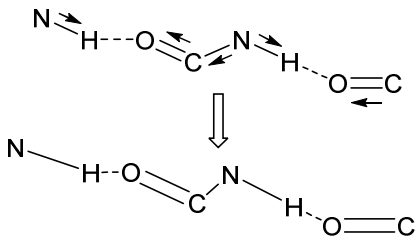

Figure 4-4. Effect of hydrogen bonding in solid urea on NH, CO and CN strength.[13]

4.1.2 Urea chemistry

The urea molecule is a neutral, active hydrogen bond donor, beyond which can be fairly chemically inert due to its resonances (resonance energy ≈ 125 – 165 kJ mol^{-1}).[33] Despite its measured proton affinity of 872.8 ± 1.5 kJ mol^{-1} (compared to NH_3 with a value of 853.6 kJ mol^{-1}),[34] urea does not participate in reactions even with strong acids but rather forms a positively charged cationic adduct, or, in the case of nitric acid, involves a proton transfer to form urea nitrate.[34] Urea is known to deprotonate in the presence of strong bases,[36-37] however reports of metal-urea salts are scarce. A possible potassium ureate (KCN_2H_3O) was reported by Franklin *et al.* in 1903 however without reliable characterisation the subject was left in abeyance.[38] Jacobson reported a monosodium ureate in 1936 as a product of metallic sodium and urea dissolved in liquid ammonia.[39] The hygroscopic dusty white powder obtained is soluble in hydroxyl based solvents and decomposes between 150 – 160 °C. Lithium ureate and dilithium ureate were synthesised by Coumbarides *et al.* in 2006 as a deprotonation agent for aryl cyclic ketones (scheme 1).[40] The synthesis involves reacting urea with stoichiometric *n*-BuLi in THF at –78 °C. The unequivocal characterisation of these products was not possible.

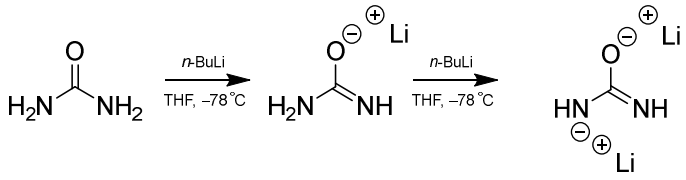

Scheme 4-1. Synthesis of lithiated urea by *n*-BuLi [40]

Sawinski *et al.* reported the synthesis of five alkali metal urea salts (ureates) for Li, Na, K, Rb and Cs in 2014.[41-42] The salts were prepared by dissolving the respective metals and urea in liquid ammonia in a steel autoclave and allowing to react at room temperature (K, Rb and Cs) or 50 °C (Li and Na) for prolonged periods of time. Pure phase materials were obtained and characterised by XRD and FTIR (Figure 4-5).

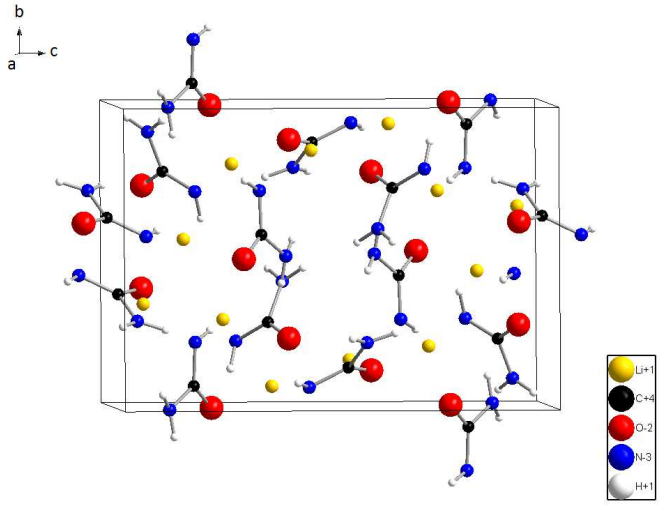

a) $LiHN(CO)NH_2$

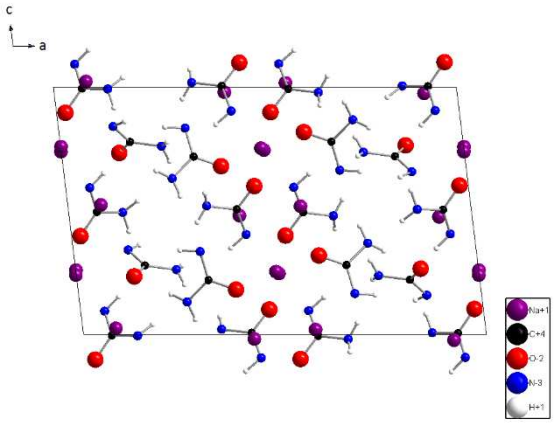

b) $NaHN(CO)NH_2$

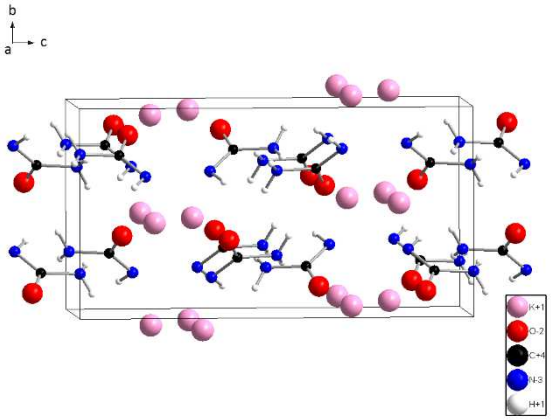

c) $KHN(CO)NH_2$

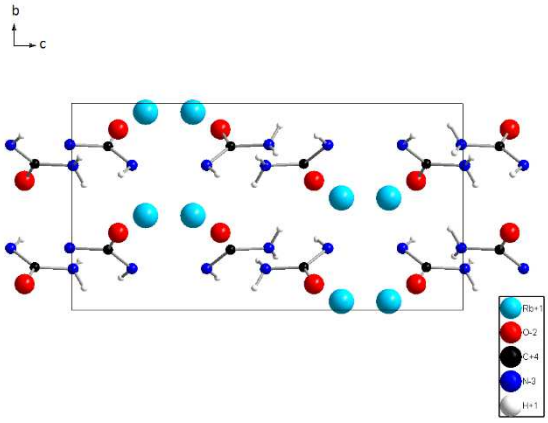

c) $RbHN(CO)NH_2$

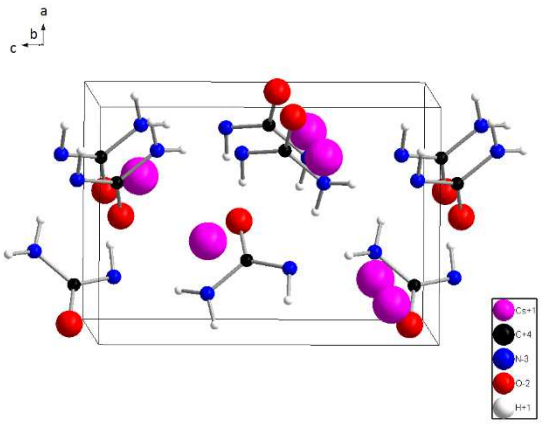

d) $CsHN(CO)NH_2$

Figure 4-5. Structures of (a) Li, (b) Na, (c) K, (d) Rb and (e) Cs ureate (black solid lines denote the respective unit cells) [41-42]

4.1.3 Decomposition of urea

4.1.3.1 Hydrolysis

Fertilisers rely on the natural hydrolysis of urea by the enzyme urease (urea amidohydrolase) produced in organic lifeforms.[24, 33, 43-44] Catalysed by the binuclear Ni (II) centre, urease hydrolyses urea into ammonia and carbamate, which decarboxylates spontaneously into more ammonia and carbon dioxide (scheme 4-2).

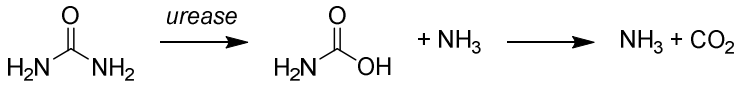

Scheme 4-2. The natural decomposition of urea by the urease protein

Mechanistically this process functions *via* the carboxyl oxygen coordinating with an Ni atom in the enzyme to facilitate nucleophilic attack by a hydroxyl ligated to the other Ni centre.[24, 33, 44-45] Synthetically equivalent catalysts based on Pd (II), lead, and tin have all shown catalytic activity for hydrolysis of urea.[46-48]

4.1.3.2 Thermolysis

Similar to AB discussed in chapter 1 and melamine in chapter 3, urea exhibits complex thermal decomposition behaviour that is influenced by heating rate, sample size, experimental geometries and reaction atmosphere.[20, 49-51] The main gaseous products are ammonia, isocyanic acid (HNCO) and carbon dioxide whilst in the condensed phase biuret ($C_2H_5N_3O_2$), cyanuric acid ($C_3N_3(OH)_3$), ammelide ($C_3N_3(OH)_2NH_2$, ammeline ($C_3N_3OH(NH_2)_2$), triuret ($H_2NC(O)NH)_2CO$) and melamine ($C_3N_6H_6$) are formed in various combinations up to 500 °C.[49-51] Controlled high temperature calcination yields graphitic carbon nitride (*g*-C_3N_4), again analogous to the thermolysis of melamine.[52-53] Urea promptly forms reaction pairs with many of its decomposition products, for example the reversible formation of biuret from isocyanic acid can be written as equation 4-3:

$$CO(NH_2)_2 + HNCO \leftrightarrow C_2H_5N_3O_2 \qquad (4\text{-}3)$$

Essentially, the decomposition of urea begins with the melting of urea at 133 °C forming isocyanic acid alongside initial urea vaporisation (Scheme 4-3). What follows is the decomposition of urea, biuret and finally cyanuric acid *via* an intricate array of intermediate products and side reactions that changes with different reaction conditions. The drastic variety in cumulative weight loss, decomposition temperature and the ratio of products in both the gaseous and condensed phases can be observed in literature.[22, 49-55]

One can only begin to deduce possible reaction schemes by comparing similar reaction conditions, as demonstrated by two comprehensive thermogravimetric studies at 10 K min^{-1} under flowing nitrogen conducted a decade apart first by Schaber *et al*. followed by Brack *et al*. (Scheme 4-3).[49-50] Accordingly, the decomposition reactions of urea, biuret and cyanuric acid proposed based on HPLC and FTIR data from the condensed and gaseous products are compiled in Table 4-1 alongside the activation energies computed by Brack *et al.*

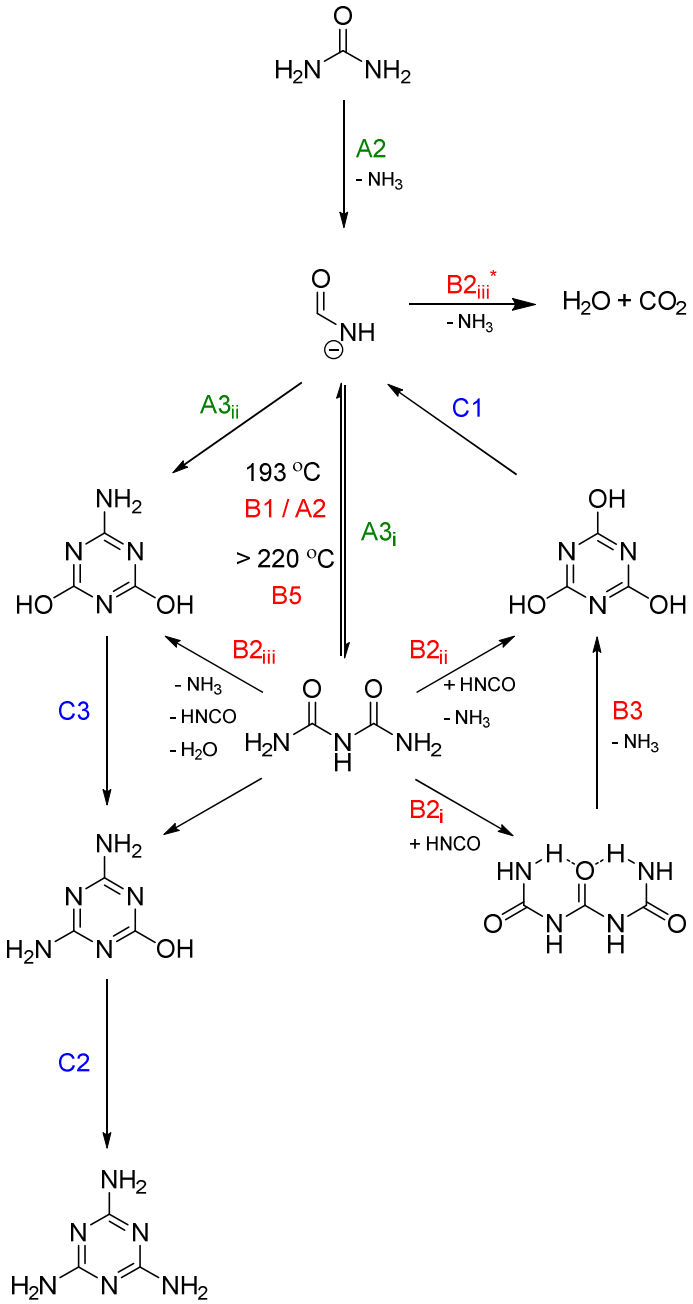

Scheme 4-3. The decomposition scheme of urea at 10 K min^{-1} under flowing nitrogen in a TGA apparatus.[22, 49-55] The deduced reactions at each step associated with each of the three mass loss steps (A, B and C) are numbered and described in full in table 4-1.

Table 4-1. The proposed reactions by which urea decomposes at 10 k min^{-1} under flowing nitrogen as computed by Schaber *et al*. and Brack *et al*.

Temperature /°C	Reaction number	Reaction	E_a, kJ mol^{-1}
133	A1	urea $_{(s)}$ → urea $_{(l)}$	160.00
	A2	urea $_{(l)}$ → HNCO $_{(l)}$ + NH_3 $_{(g)}$	74.00
140	$A3_i$	urea $_{(l)}$ + HNCO $_{(l)}$ → biuret $_{(l)}$	75.45
	$A3_{ii}$	urea $_{(l)}$ + 2 HNCO $_{(l)}$ → ammelide $_{(s)}$ + H_2O $_{(g)}$	110.40
	A*	HNCO $_{(l)}$ → HNCO $_{(g)}$	
190	A4	biuret $_{(s)}$ → biuret $_{(l)}$	122.00
	B1	biuret $_{(l)}$ → urea $_{(l)}$ + HNCO $_{(l)}$	208.23
	spontaneously	urea $_{(l)}$ → HNCO $_{(l)}$ + NH_3 $_{(g)}$	
193	$B2_i$	biuret $_{(l)}$ + HNCO $_{(g)}$ → triuret $_{(s)}$	116.97
	$B2_{ii}$	biuret $_{(l)}$ + HNCO $_{(g)}$ → cyanuric acid $_{(s)}$ + NH_3 $_{(g)}$	158.68
	$B2_{iii}$	2 biuret $_{(l)}$ → ammelide $_{(s)}$ + HNCO $_{(l)}$ + NH_3 $_{(g)}$ + H_2O $_{(g)}$	257.76
200	$B2_{iii}$*	HNCO $_{(g)}$ + H_2O $_{(g)}$ → NH_3 $_{(g)}$ + CO_2 $_{(g)}$	
220	B3	triuret $_{(s)}$ → cyanuric acid $_{(s)}$ + NH_3 $_{(g)}$	194.94
	B4	biuret $_{(l)}$ → biuret $_{(s)}$	271.50
>220	B5	biuret $_{(s)}$ → 2 HNCO $_{(g)}$ + NH_3 $_{(g)}$	266.38
270	C1	cyanuric acid $_{(s)}$ → 3 HNCO $_{(g)}$	118.42
	C2 [23, 54]	ammelide + NH_3 $_{(g)}$ → ammeline + H_2O $_{(g)}$	
	C3 [54]	ammeline + NH_3 $_{(g)}$ → melamine + H_2O $_{(g)}$	

The above scheme is merely a representation of the particular experimental conditions specified by Schaber *et al.* and Brack *et al.*; which cannot be directly extrapolated to experiments conducted under different experimental conditions.

4.1.4 Urea as a hydrogen source

Recently, urea has been identified as a renewable fuel based on two strategies: decomposition of urea to gain hydrogen, and direct urea electrolysis. Particularly in hydrogen production as the molecule has a higher volumetric hydrogen density (86 g L^{-1}) than liquid hydrogen and compressed hydrogen at 810 bar (70 and 43 g L^{-1} respectively). In the solid state it contains 6.71 wt% of hydrogen and when conjugated with water this raises by a further 3.36 wt%.

Zamfirecu *et al.* proposed a urea pyrolysis combined with an ammonia splitting procedure as an addendum to improve the efficiency and exhaust quality of existing petroleum and diesel engines.[56] The hydrogen producing module harvests ammonia from urea pyrolysis detailed previously followed by cracking catalysed by ruthenium impregnated membranes. It was estimated that the energy required to generate hydrogen is approximately 100 kJ mol^{-1} which when combusted gives 286 kJ mol^{-1}. Moreover, hydrogen production was reported using aqueous urea over Ni-Al_2O_3 catalyst in a downward flow packed-bed reactor by Rollinson *et al.* where hydrogen output peaked at approximately 600 °C.[57] The catalytic conversion was measured close to theoretical values where three moles of hydrogen was produced per mole of urea. More recently, photocatalytic electrochemical urea electrolysis was demonstrated by Wang *et al.* using TiO_2 and α-Fe_2O_3 as photoelectrodes, $Ni(OH)_2$ as the urea oxidation catalyst and Pt as the cathode (equations 4-4 to 4-8, *hv* represent light, e^- represents electrons and h^+ represents holes).[58] By careful choice of the photoelectrodes with bandgaps straddling the water reduction and urea oxidation potentials, hydrogen was produced at a self-sufficient, zero bias from both research grade urea reagents and urine.

$$\text{Cathode: } 2\,H_2O + 2\,e^- \rightarrow 2\,H_2 + 2\,OH^- \qquad E° = 0\ V \qquad (4\text{-}4)$$

$$\text{Anode: } TiO2 + hv \rightarrow TiO_2{}^* + e^- + h^+ \qquad (4\text{-}5)$$

$$Ni(OH)_2 + OH^- + h^+ \rightarrow NiOOH + H_2O \qquad (4\text{-}6)$$

$$CO(NH_2)_2 + 6\,NiOOH + H_2O \rightarrow 6\,Ni(OH)_2 + CO_2 + N_2 \qquad E° = 0.37\ V \qquad (4\text{-}7)$$

$$\text{Overall: } CO(NH_2)_2 + H_2O \xrightarrow{Ni(OH)_2} CO_2 + N_2 + 3\,H_2 \qquad E° = 0.37\ V \qquad (4\text{-}8)$$

Urea was also adopted as a fuel in an alkaline membrane fuel cell with an open circuit voltage of 1.146 V in comparison to 1.23 V in hydrogen fuel cells (equations 4-9 to 4-11).[59] Lan *et al.* reported successful electricity generation using a variety of electrode materials, C, Pt, Ni, Ag and MnO_2; and a wide selection of urea solutions from research grade reagents to commercial AdBlue solutions to human urine.[59] The authors observed that a dilute urea solution yielded the highest power and current densities likely due to diffusion of the bulky urea groups around the anode.

$$\text{Cathode: } O_2 + 2\,H_2O + 4\,e^- \rightarrow 4\,OH^- \qquad E° = 0.400\ V \qquad (4\text{-}9)$$

$$\text{Anode: } CO(NH_2)_2 + 6\,OH^- \rightarrow N_2 + CO_2 + 5\,H_2O + 6\,e^- \qquad E° = -0.746\ V \qquad (4\text{-}10)$$

$$\text{Overall: } 2\,CO(NH_2)_2 + 3\,O_2 \rightarrow 2\,N_2 + 2\,CO_2 + 4\,H_2O \qquad E° = 1.146\ V \qquad (4\text{-}11)$$

The chemistry outlined thus far strongly suggests that urea should liberate hydrogen in the presence of a strong base such as LiH. This chapter aims to continue the investigation of urea as a hydrogen source by reacting with LiH in the solid state according to equation 4-12:

$$4\ LiH + CO(NH_2)_2 \rightarrow Li_2NCN + Li_2O + 4\ H_2 \qquad \Delta H^o_r = -262.61\ KJ\ mol^{-1} \qquad (4\text{-}12)$$

which has a theoretical gravimetric density of 8.78 wt%. The focal points of this chapter are to elaborate on the interaction between LiH and urea in the solid state. The subsequent studies on reaction stoichiometry of the proposed system will elude to the role of LiH in the system and identify intermediate processes. This will be followed by a study on ball milling of the two reactants to optimise reaction conditions such as reducing diffusion distance and enhancing the activity of starting materials using ball milling.

4.2 Experimental

4.2.1 Materials

LiH (95%), LiD (98 atom%), $CO(NH_2)_2$ (99.8%) and $CO(ND_2)_2$ (98 atom%) used in this chapter were sourced from Sigma Aldrich without further purification. Commercial LiH were fine, light grey powders, while urea and deuterated urea were white powders. The as purchased LiD exhibited a wide particle size distribution (up to 5 mm in diameter) which were gently ground using a mortar and pestle into powder prior to further mechanical treatment.

As LiH and LiD degrade rapidly when in contact with O_2 and H_2O all relevant manipulations were conducted in Ar filled gloveboxes with O_2 levels < 5ppm and H_2O level < 0.1 ppm.

For clarity, preparation of the many samples discussed in this chapter are numbered and compiled in their chronological order of use (Table 4-2).

4.2.2 Ball milling

Detailed ball milling procedures are described elsewhere in section 2.2.1. It should be noted that ten 10 mm diameter steel balls were used in all of the ball milling experiments conducted in this chapter. For sample preparation, 50 ml stainless jars were used with air-tight clamps, whilst the pressure monitored high energy ball milling experiment was conducted in a 500 ml stainless steel jar with the air-tight GrindControl lid supplied by Retsch. Pressure monitoring using the Retsch GrindControl software was simultaneously started with the milling programme.

4.2.3 Characterisation techniques

Thermal analysis was conducted according to the procedures outlined in section 2.3.4 on the Ar purged Netzsch STA 409PC. Evolved gas mass spectra were collected from the purge stream of the STA and analysed on the Hiden HPR20 quadropolar MS in the Faraday mode at a resolution of 0.1 amu.

Condensed phase materials were characterised in 5 / 7 mm diameter Hilgenberg borosilicate capillary tubes by PXD using a Bruker d8 diffractometer with monochromic Cu K_α radiation (section 2.3.1.1). FTIR spectra were measured using a Shimazdu 8400s FTIR-ATR spectrometer (section 2.3.2.1) . Care was taken to minimise atmospheric exposure during measurement by transporting each sample from a sealed vial to the stage as quickly as possible. In the case of any unexpected oxidation detected, the measurement was repeated with a freshly prepared sample.

Table 4-2. List of samples used in this chapter, in chronological order of use

Sample	LiH : urea	Ball milling parameters			
		RPM	Ball : powder	Milling time	Programme
U-01	4:1	150	30:1	36m	5 m mill rest 1 m
U-02	3:1	150	30:1	36m	5 m mill rest 1 m
U-03	2:1	150	30:1	36m	5 m mill rest 1 m
U-04	1:1	150	30:1	36m	5 m mill rest 1 m
U-05	4:1	500	60:1	16H	5 m mill rest 1 m
U-06	4:1	Handground	n/a	5m	n/a
U-07	4:1	200	30:1	36m	5 m mill rest 1 m
U-08	4:1	300	30:1	36m	5 m mill rest 1 m
U-09	4:1	450	30:1	36m	5 m mill rest 1 m
U-10	4:1	600	30:1	36m	5 m mill rest 1 m
Pre3H	LiH	600	60:1	3H	5 m mill rest 1 m
PreU	urea	600	60:1	3H	5 m mill rest 1 m
U-11	4 : 1 PreU	150	30:1	36m	5 m mill rest 1 m
U-12	4 PreLiH: 1	150	30:1	36m	5 m mill rest 1 m
U-13	4 Pre3H LiD : 1	150	30:1	36m	5 m mill rest 1 m
U-14	4 Pre3H : U_D	150	30:1	36m	5 m mill rest 1 m
U-15	4 Pre3H LiD : U_D	150	30:1	36m	5 m mill rest 1 m

4.3 Results and discussion

4.3.1 Intimately mixed 4 LiH : urea

Light mechanical milling applied to 4LiH : urea (sample **U-01**) has provided reproducible intimate mixing of the two starting powders without inducing premature hydrogen release, evident by the lack of pressure build up in the milling jar. The starting materials appear discrete and crystalline post milling by PXD with no impurity phases (Figure 4-6).

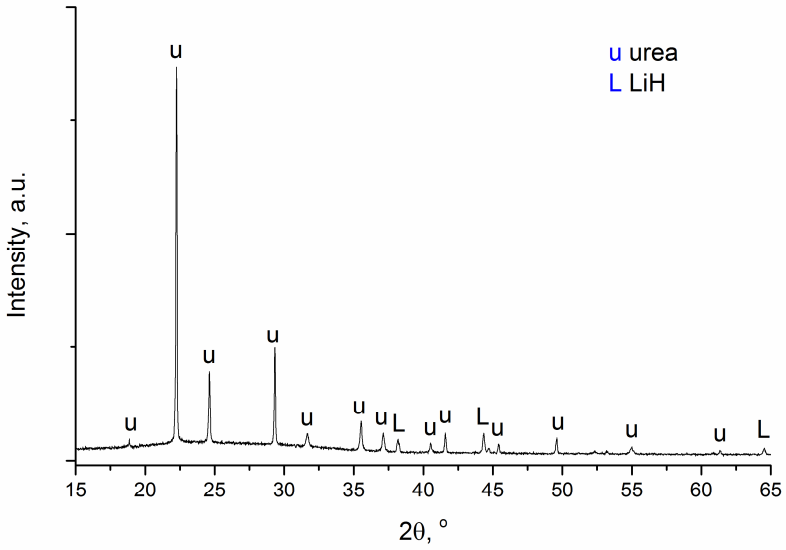

Figure 4-6. PXD of **U-01**

Sample **U-01** was exposed to controlled heating using the combined STA/MS from room temperature to 300 °C at a rate of 5 °C min^{-1}. TGA and DTA profiles show multi-step decomposition occurring at approximately 100, 170 and 260 °C releasing hydrogen and ammonia (Figure 4-7). Detailed decomposition is described for the following in terms of three temperature regions: RT to 140, 160 to 230 and finally 260 to 300 °C. Note that the temperatures and mass losses discussed in the sections below are averaged values of distinct experiments recorded, each instance with freshly prepared powder. The reaction intermediate and final products at various temperatures were probed using powder diffraction and spectroscopic techniques to formulate the preliminary reaction scheme discussed.

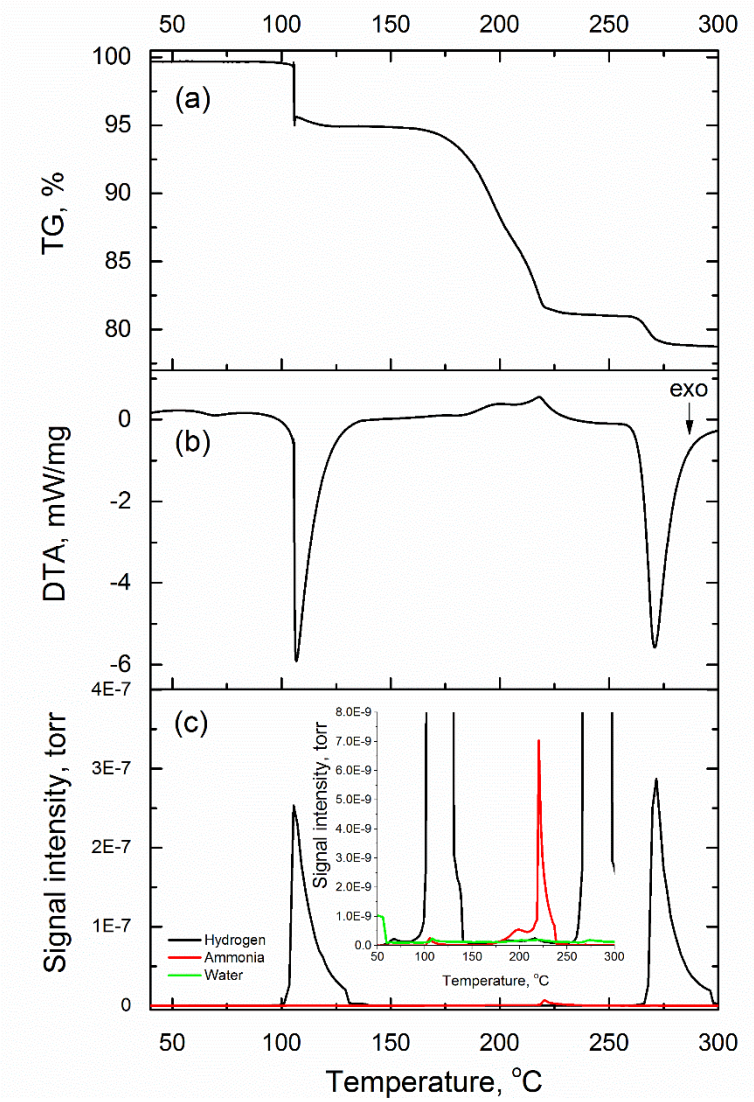

Figure 4-7. (a) TG profile, (b) DTA and (c) MS of hydrogen and ammonia released during the thermal decomposition of **U-01**

4.3.1.1 Region 1 – RT to 140 °C

DTA recorded an exothermic event at approximately 60 °C (Figure 4-7 (b)). It is accompanied by a small amount of hydrogen release detected on the MS though no apparent mass loss was recorded on the TGA profile (Figure 4-7 (c) and (a) respectively). This is followed by the main exothermic event at 104.5 °C, releasing hydrogen and traces of ammonia and water corresponding to a sharp decrease in an average weight of 5.1 wt%. A sudden drop in mass is also observed during the dehydrogenation reaction of HB (section 1.3.1.1) accompanied by the solids frothing during reaction.[60] Likewise, the **U-01** sample after the sharp weight loss emerges as a white solid foam at least twice the volume of the original sample. Under SEM, an irregular porous 3D network can be seen with crystallites developing on the surface of the material (Figure 4-8). The mass loss plateaued at around 120 °C, while hydrogen is still detected in the exhaust stream up to 140 °C.

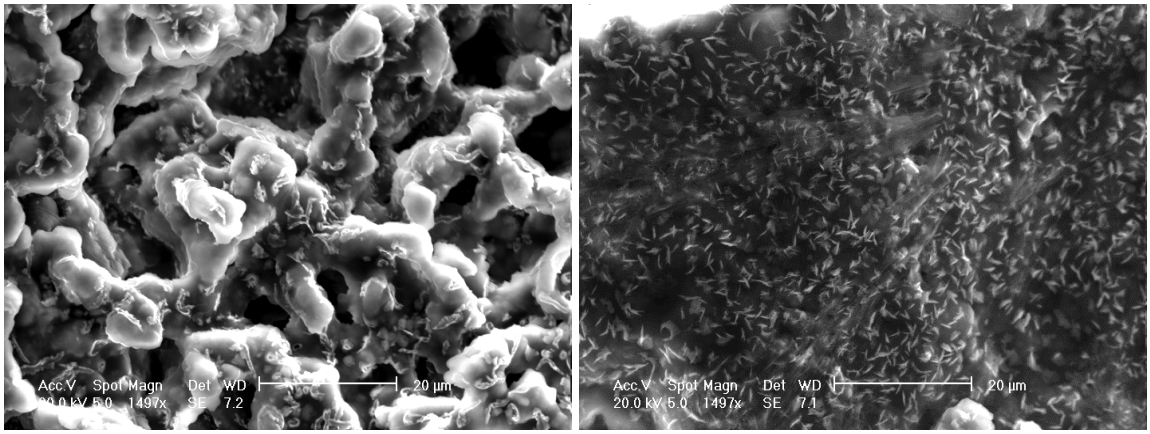

Figure 4-8. SEM image of **U-01** foamed structure extracted at 150 °C

It is worthy to draw attention to the consistency of the DTA and MS responses observed in this region, where the small first DTA peak can be fitted to a classic Gaussian model (Figure 4-9), while the second exotherm has an asymmetric profile with a near vertical edge. DTA peak asymmetry can be a result of changes in the sample dimensions during reaction which is corroborated by the sample foaming during the reaction.[61]

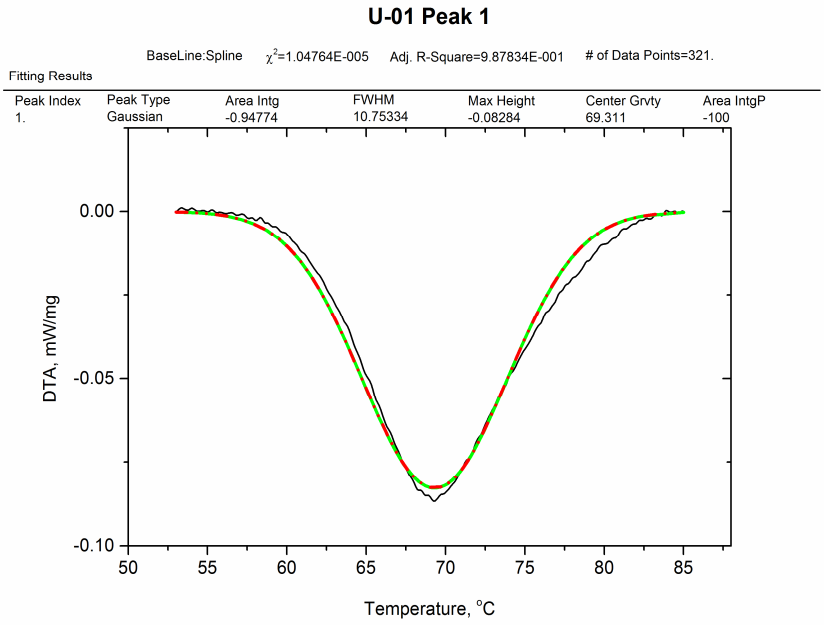

Figure 4-9. **U-01** DTA peak T_{peak}= 69.3 °C

The solid white foam sampled at 150 °C is comprised of LiH and $LiCON_2H_3$ (Figure 4-10). Evidently the LiH-urea dehydrogenation reaction is unlikely to be ammonia mediated as the characteristic product of the LiH:NH_3 reaction (equation 4-13), $LiNH_2$ is absent from the system:[62]

$$LiH_{(s)} + NH_{3\,(g)} \rightarrow LiNH_{2\,(s)} + H_{2\,(g)} \qquad (4\text{-}13)$$

Instead a lithium ureate salt, $LiCON_2H_3$ is formed, probably initiated by a solid-gas interaction between LiH and the low vapour pressure urea at 105 °C (equation 4-14). Note that crystalline urea cannot be observed at this stage.

$$LiH_{(s)} + CO(NH_2)_{2\,(g)} \rightarrow LiCON_2H_{3\,(s)} + H_{2\,(g)} \qquad (4\text{-}14)$$

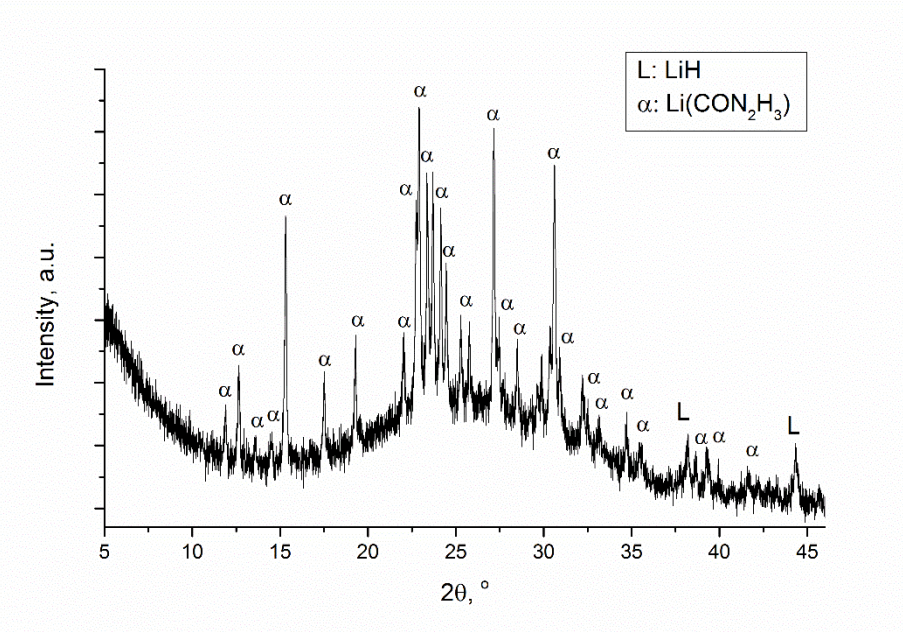

Figure 4-10. PXD of **U-01** heated to 150 °C

In Figure 4-11, the FTIR spectra of the starting material urea (black trace) is compared with the product at 150 °C (red). The consumption of urea can be first and foremost confirmed as it is absent both in the PXD pattern and FTIR spectra of the products. The most apparent discrepancy between the two spectra are that of $\nu(NH_2)$ symmetric and asymmetric stretching modes at 3440 and 3340 cm^{-1}, have diminished after the first reaction step. In fact, all $–NH_x$ modes have either shifted or disappeared. It should be noted that the broad peak between 2000 and 600 cm^{-1} is a feature of pristine LiH that may be the sum of different bands of LiH nanoclusters, which are not resolved. Such features can only be distinguished at very low temperatures when the nanoclusters are embedded in solid H2, Ar, or Ne matrix.[63] The product spectrum closely resembles that reported by Sawinski *et al* except for the *ν*(NH) modes.[41]

If lithium ureate is indeed the reaction product between LiH and urea (1:1), an elimination of a single equivalent of H_2 gas would be expected, accounting for a mass loss of 2.195 wt%; however 5.1% mass was lost during this step. By MS, this additional mass loss is likely a result of ammonia and water being released, detected by trace quantities ($3x10^{-10}$ torr); albeit the stoichiometric

product lithium ureate was formed without by-products by PXD and FTIR analysis. The formation of a dilithium ureate compound could potentially rationalise the excess mass loss however the PXD pattern and FTIR spectrum would be drastically different. One possible explanation is that urea partially sublimes during the highly exothermic formation of lithium ureate (ΔH_{sub}(urea) = 90.9 ± 1.9 kJ mol^{-1} at 381 K[64]), which would further decompose into ammonia and water in the gas state in the reaction chamber as described in scheme 4-3. On the other hand, it could be also be possible that the ammonia desorption and the sample frothing at 104.5 °C are correlated to urea melting. Under the current experimental condition, pristine urea was found to melt at 136.5 °C (TG/DTA profiles in Appendix B) however a partial melting of urea could arise from localised heat generation by the exothermic interaction between urea and LiH particles. As urea melts, the solid state diffusion barrier with LiH will no longer exist and the reaction to form lithium ureate would proceed rapidly. This is reflected in the high reaction kinetics exhibited by the vertical mass loss on the TG profile. In either cases, foaming of the sample material could lead to potential sample mass by physical dislodge from the alumina sample pan.

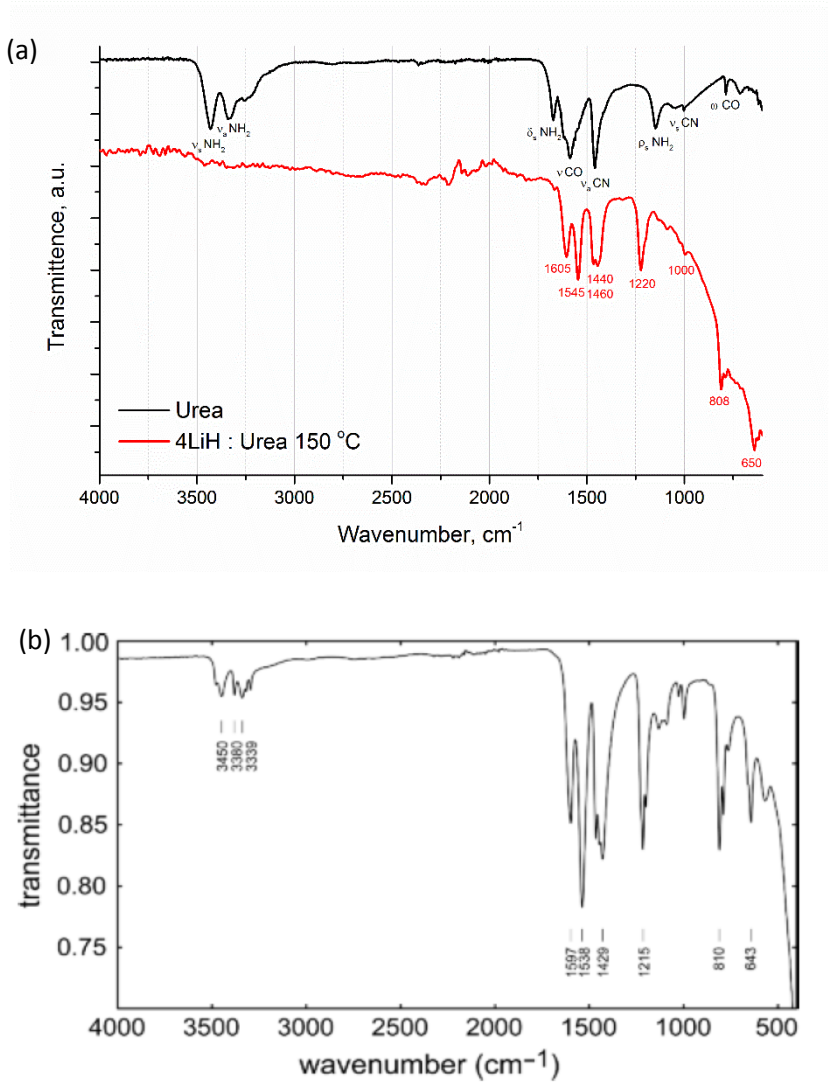

Figure 4-11. FTIR spectra of (a) urea and own work and (b) Li-ureate reported by Sawinski.[41]

4.3.1.2 Region 2 – 160 to 230 °C

The reaction proceeds to release ammonia and small amounts of hydrogen at an onset of 187.3 °C *via* endothermic thermal events. The total mass loss averages to 13.8 wt%. The endothermic DTA profile was deconvoluted showing at least two peaks contribute to the overall shape of the profile (Figure 4-12). The first peak, depicted in green, corresponds to the first ammonia peak on the MS while the second ammonia MS peak is delayed by a few degrees Celsius compared to the DTA signal.

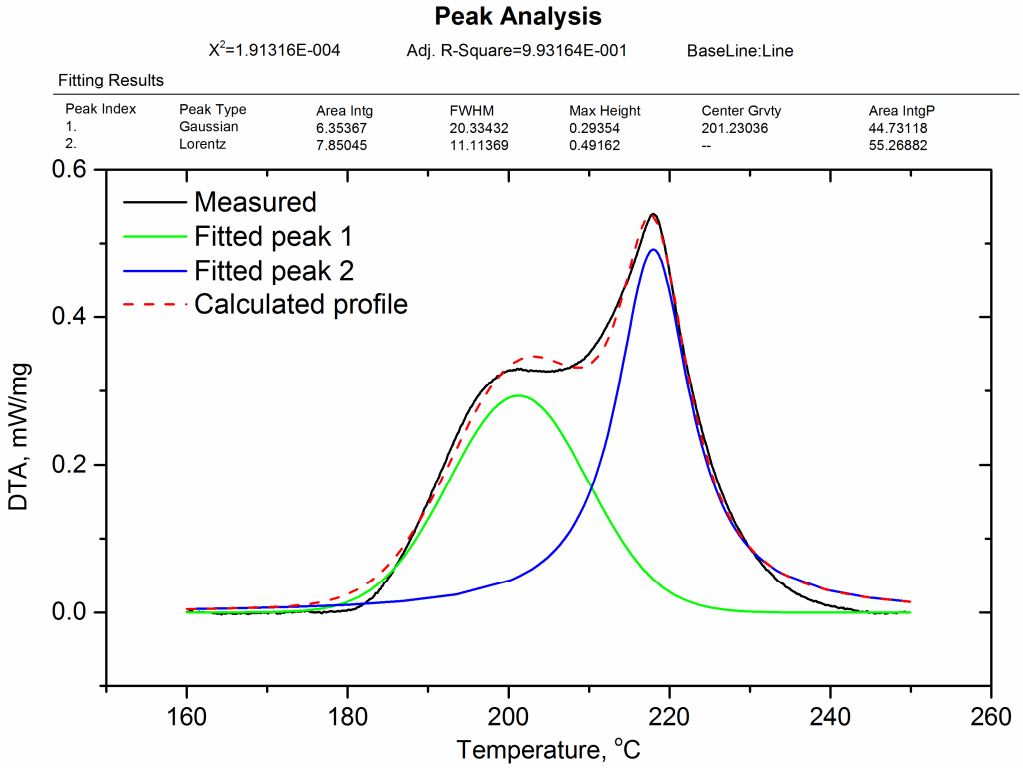

Figure 4-12. Deconvoluted DTA peak corresponding to 13.8% mass loss during the decomposition of **U-01** between 160 and 230 °C.

Trigonal lithium cyanate (LiOCN) and LiH were identified as the crystalline products by diffraction with significant amorphous characteristics showed by the poor signal to noise ratio and heightened background signal between 15 and 35° 2Θ (Figure 4-13). Based on the solid and gas products we propose the thermal decomposition of lithium ureate as:

$$LiCON_2H_{3\,(s)} \rightarrow LiOCN_{\,(s)} + NH_{3\,(g)} \qquad (4\text{-}15)$$

DTA results allude to an intermediate step between the formation of lithium cyanate from the ureate however as the steps overlap significantly, isolation of this intermediate was not possible for sample **U-01**. It should be noted that the theoretical mass loss for the reaction described by equation 4-15 is 25.81 wt%, and even when accounting a maximum of 3 equivalents of LiH as if it

does not participate in deammoniation, the mass loss is 18.96 wt%, higher than the observed 13.8 wt%.

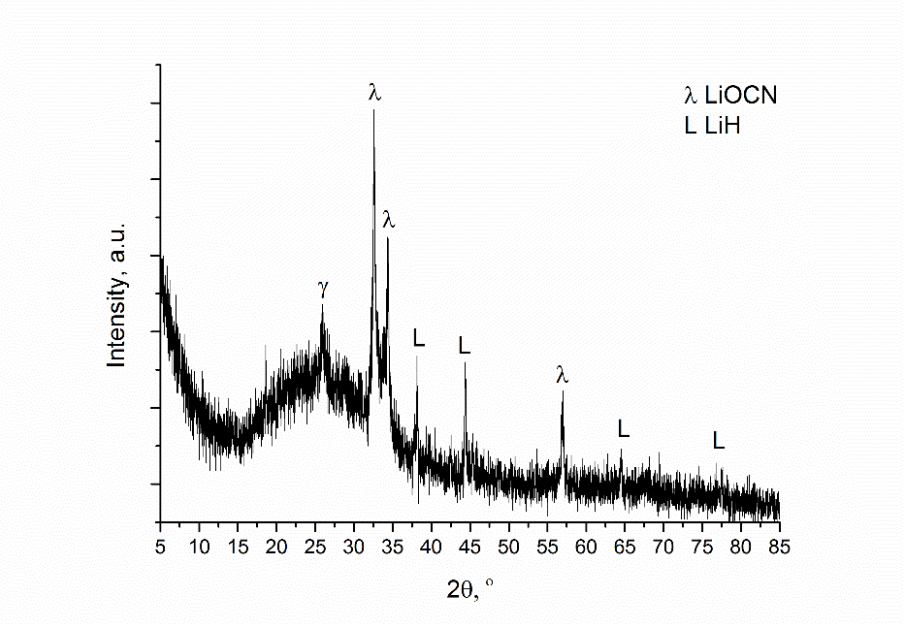

Figure 4- 13. PXD of **U-01** heated to 230 °C

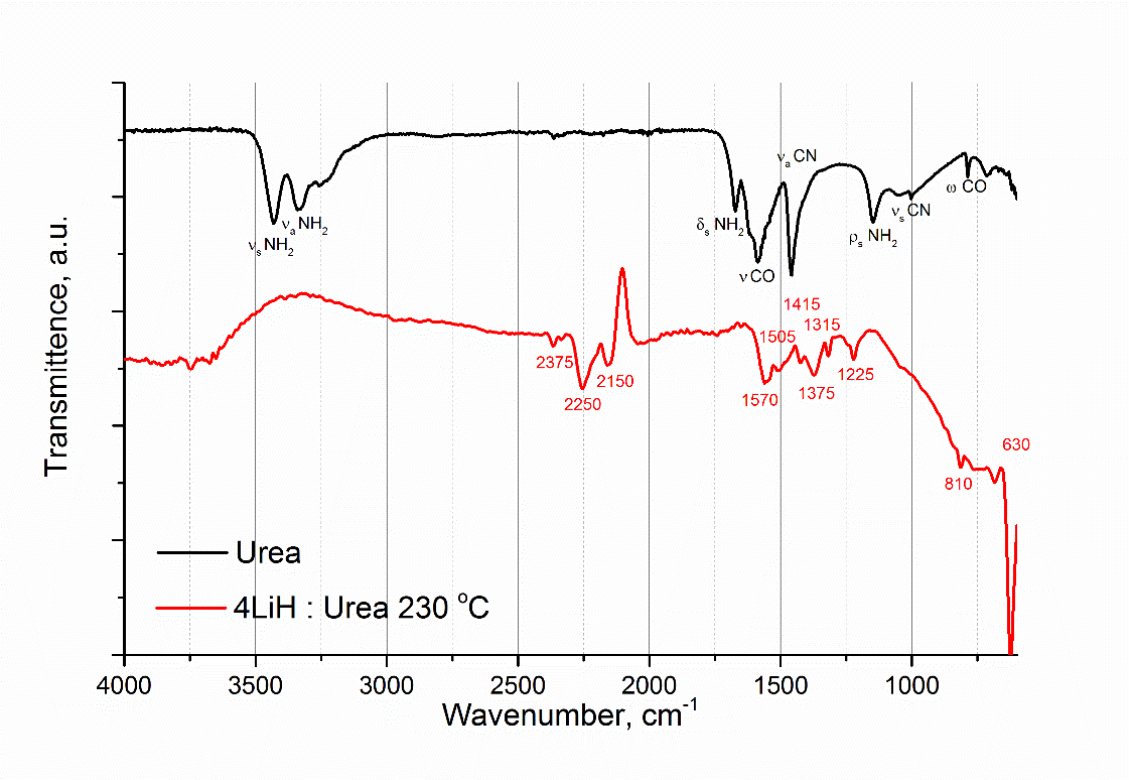

Figure 4-14. FTIR spectra of urea and **U-01** heated to 230 °C

FTIR of the solid product shows some typical features for metal-cyanates (M= Na, K, Rb, Cs, Ag and Ti): $[OCN]^-$ asymmetric stretching vibration at 2250 cm^{-1}, the strong Fermi resonances at 1375 and 1225 cm^{-1} attributed to symmetric stretch and degenerate bending vibrations and finally at 630 cm^{-1} for the second part of the degenerate bending vibrations.[65-66] Hennings *et al.* reported the Raman spectrum of LiOCN which showed features similar to those of its alkali metal counterparts, sodium and potassium cyanate.[67] There is strong evidence that LiOCN and LiH are not the only phases present in **U-01** at 230 °C due to the unassigned bands at 2150, 1570 and 810 cm^{-1}. These bands can be associated to the stretching mode of C≡N similar to that in hydrogen cyanamide, and the stretching and waggling modes in a carbonyl group respectively.

The absence of $LiNH_2$ in any significance by both diffraction and FTIR analysis advocates that the ammonia released at this step either does not interact with any residual LiH, or that the phase reacts immediately with other species in the solid. The first hypothesis can be ascribed to a reduction of free LiH surfaces in the foamed structure, poses a diffusion barrier for NH_3 to react with the residual LiH trapped inside the structure.[68-70] This is demonstrated by a mass loss reduction by 3% during region 2 when the foam solid product obtained after heating to 150 °C is pulverised in the ball mill and again decomposed in the STA to 300 °C (Figure 4-15). Ammonia desorption associated with region 2 is reduced by close to two orders of magnitude while the hydrogen signal halved by mass spectrometry (Figure 4-16). The final product at 300 °C in the diffraction pattern indicate very little long range order but it is still possible to identify Li_2NCN and Li_2O likely as a result of the reaction in equation 4-12 (Figure 4-17). Whether other phases besides LiOCN form cannot be verified due to limited spatial and time resolution of laboratory based techniques.

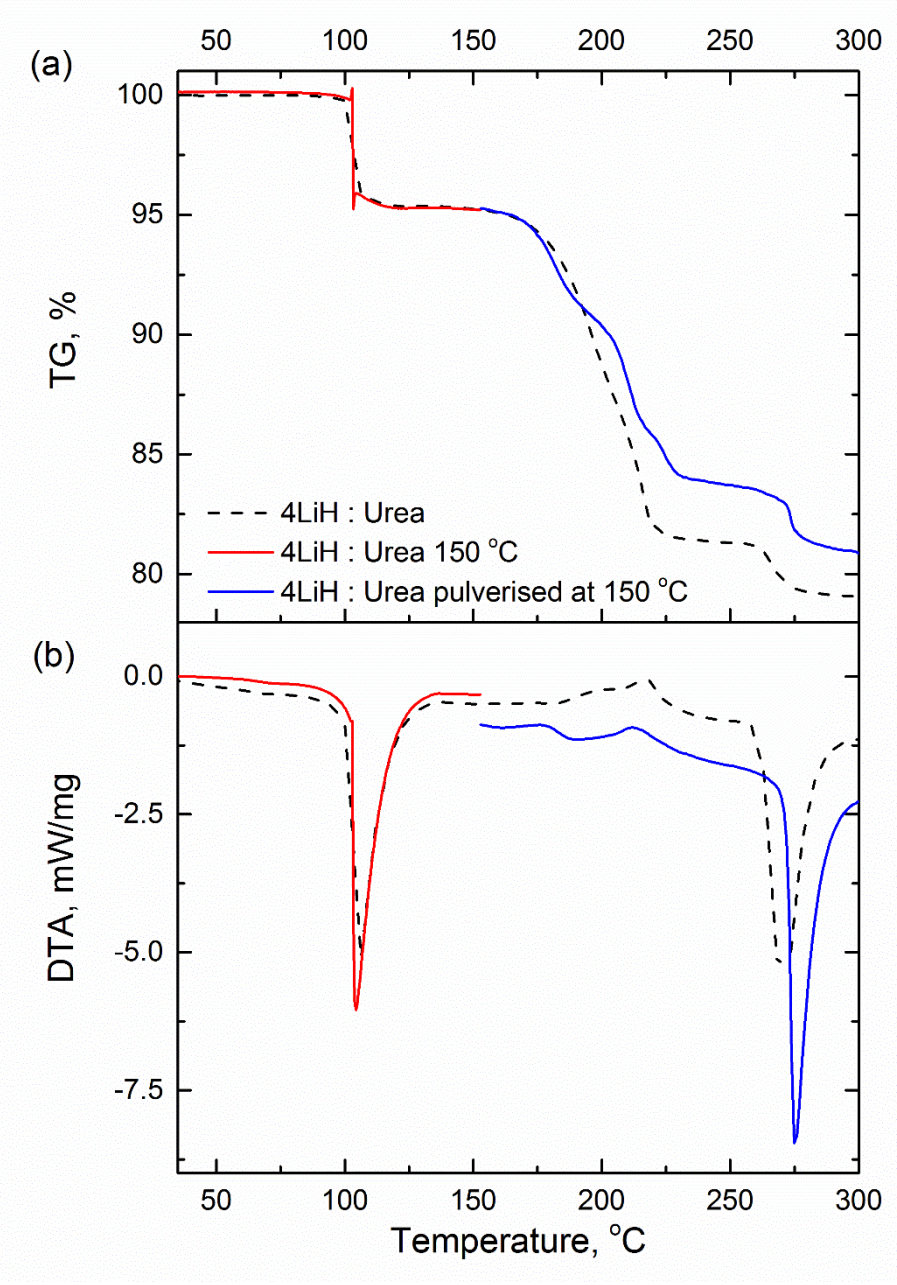

Figure 4-15. Data from (a) TG and (b) DTA comparing the decomposition of **U-01** (dashed trace) to a sample extracted at 150 °C (red trace) which is heated again to 300 °C after being milled (blue trace).

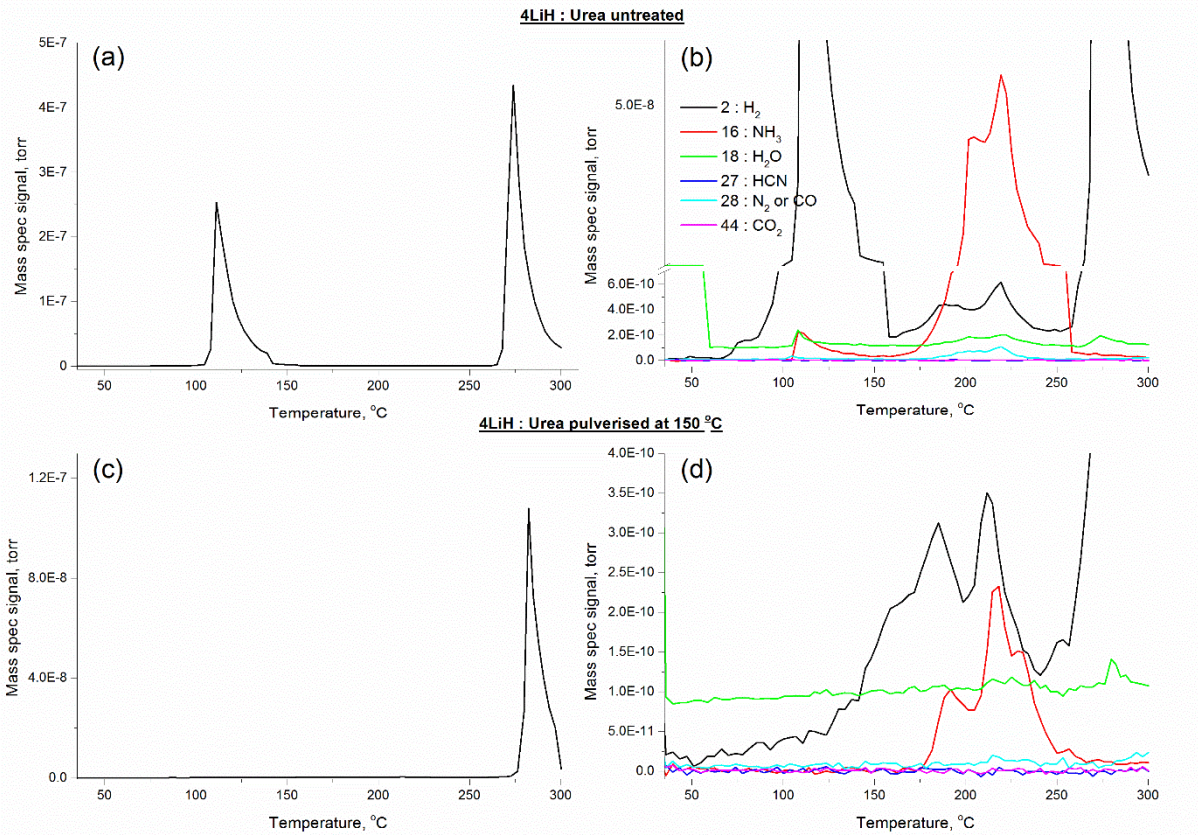

Figure 4-16. Evolved gas MS of **U-01** compared to a sample extracted at 150 °C which is heated again to 300 °C after milling. (a) and (c) show the hydrogen signals, while (b) and (d) show the signals for ammonia, water, HCN, N_2/CO and CO_2 for the respective experiments.

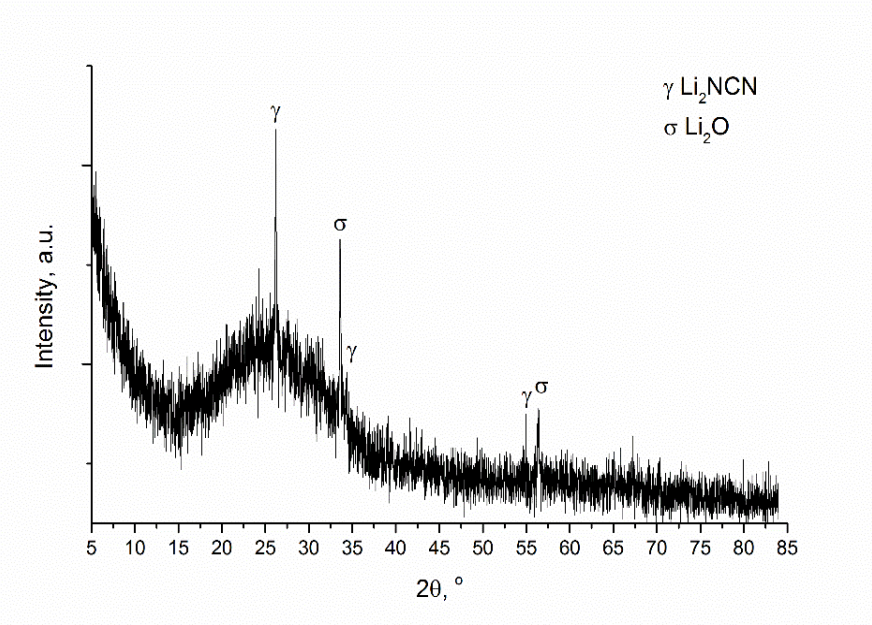

Figure 4-17. PXD of condensed phase products post thermal analysis of the pulverised foam

4.3.1.3 Region 3 – 230 to 300 °C

Finally, pure hydrogen is released from 266 °C in an exothermic event corresponding to a mass loss of 2.26 %, one equivalent of H_2. Examination of the product post-decomposition revealed a white solid residue with patches of black found closer to the bottom of the alumina crucible. This strongly indicates inhomogeneous components and from diffraction, the final crystalline product consists of the reactant, LiH, together with Li_2NCN, Li_2O, LiCN and Li_2CO_3 (Figure 4-18). Since the amorphous phase in the previous region has not yet been identified, it is not possible to propose the dehydrogenation reactions to form Li_2NCN, Li_2O, LiCN and Li_2CO_3. It is notable that all of the LiOCN seen at 230 °C has been apparently consumed at this higher temperature.

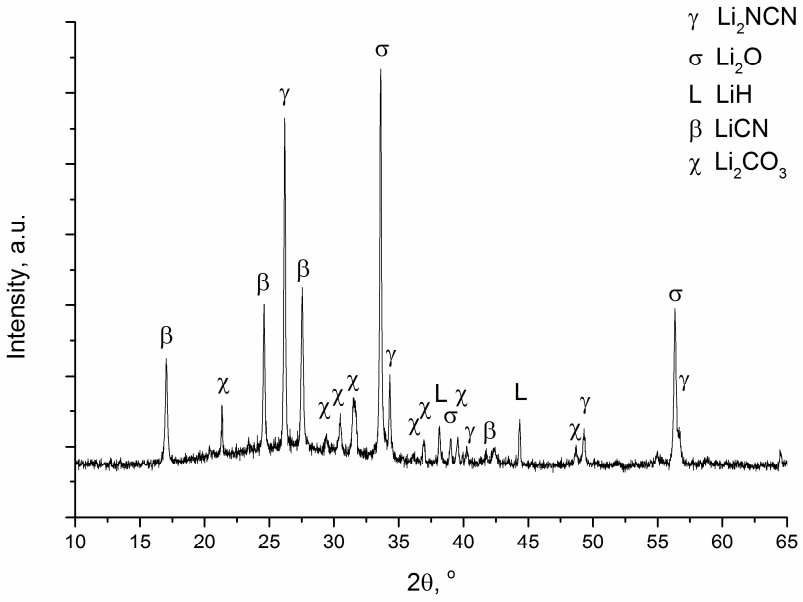

Figure 4-18. PXD of **U-01** heated to 300 °C.

Table 4-3 presents approximate weight fractions of each phase calculated by Rietveld refinement using the GSAS package. The theoretical weight fractions according to equation 4-12 are also presented (table 4-3). To verify the validity of the Rietveld results, it is assumed reasonably that lithium does not form any gaseous species at 300 °C, which allows the mass loss of the system to be calculated from lithium containing species in the product. This is done by calculating the ratio between weight fraction of lithium in the starting material (0.3022) and in the product (0.3907) which estimates the mass loss to be to be 22.64 %. This is slightly higher than the 20.88 % recorded by the STA. Nevertheless a difference might be expected as the diffraction pattern indicates the presence of an amorphous component (non-linear background between 20 and 35° 2Θ) implying that not all products could be accounted for by diffraction (Figure 4-18). Using the refinement

estimation, it was determined that at least 25% of the initial LiH remained unreacted by 300 °C, equivalent to 1.10 wt% of the system.

Table 4-3. Comparison between phase fractions predicted by equation 4-12 and those calculated from PXD data of **U-01** heated to 300 °C using the Rietveld method (background: Shifted Chebyschev, where goodness of fit, X^2 was calculated to 1.094 reliably to a wRp of 0.1173)

	Li_2O	**Li_2NCN**	**LiCN**	**Li_2CO_3**	**LiH**
Theoretical	0.3888	0.6112	-	-	-
Experimental	0.38(7)	0.20(3)	0.21(5)	0.08(4)	0.11(2)

The overall mass spectrum in Figure 4-7 provides further insight into the overall decomposition scheme as signal intensity reflects quantitatively the composition of the gaseous products. By comparing the integrated area underneath the two predominant hydrogen peaks in region 1 (2.588 x 10^{-6} torr) and region 3 (2.908 x 10^{-6} torr) it can be shown that the two steps yielded a similar amount of hydrogen. Since hydrogen is the only gaseous product associated with the 2.26% mass loss in region 3 the overall hydrogen desorbed by sample **U-01** by 300 °C can be estimated to be at least 4.27 wt% (accounting the first and final hydrogen desorption peak on the MS).

In summary the thermolysis of LiH and urea intimately mixed in a 4:1 stoichiometry can be described in terms of 3 distinct regions between RT to 140 °C, 160 to 230 °C and 260 to 300 °C. Whilst the main gaseous products are H_2 and NH_3, the final solid product is comprised of stoichiometric products Li_2NCN and Li_2O, as well as LiCN, Li_2CO_3 and residual starting material LiH.

4.3.2 Reaction stoichiometry studies

Results described above suggest that one equivalent LiH remained unreacted in the 4:1 LiH to urea stoichiometry mixture (**U-01**) probably due to physical diffusion restraints. Given this premise, it was considered whether changing the LiH to urea molar ratio would yield the same solid products without the presence of any residual LiH. This section examines the effects of varying the LiH to urea ratio on the decomposition pathway with the aim of further unravelling the reaction steps that occur for LiH and urea during dehydrogenation.

Indeed when the reactant ratio is reduced sequentially from 4:1 to 1:1 LiH:urea, the amount of residual LiH post thermolysis decreases by half for the 3LiH:urea sample (**U-02**), and is completely absent in the 2LiH (**U-03**) and 1LiH (**U-04**) samples (table 4-4). When considering the product composition alongside the thermolysis profiles and the released gases (TGA/DTA Figure 4-19, MS

Figure 4-20 and 4-21), a number of deductions can be made regarding the effects on the reaction pathway by varying the molar ratio of LiH and urea. These are described below:

Table 4-4. Theoretical weight fraction according equation 4-12, against those derived from Rietveld refinement against PXD data (background function: Shifted Chebyschev) of decomposed samples **U-01** to **U-03** to 300 °C. The refinements are plotted in the Appendix C. Sample **U-04** consists of one phase and the pattern was not refined.

	Theoretical	**U-01** (4LiH)	**U-02** (3LiH)	**U-03** (2LiH)	**U-04** (1LiH)
LiH	0	0.112(0)	0.052(8)	0	0
Li_2NCN	0.6112	0.197(6)	0.302(1)	0.460(9)	0
Li_2O	0.3888	0.389(8)	0.316(5)	0.045(2)	0
LiCN	0	0.215(9)	0.185(9)	0.103(9)	0
Li_2CO_3	0	0.084(0)	0.142(6)	0.390(1)	0
LiOCN	0	0	0	0	1
X^2		1.094	1.042	3.231	-
wRp		0.1173	0.1440	0.0548	-

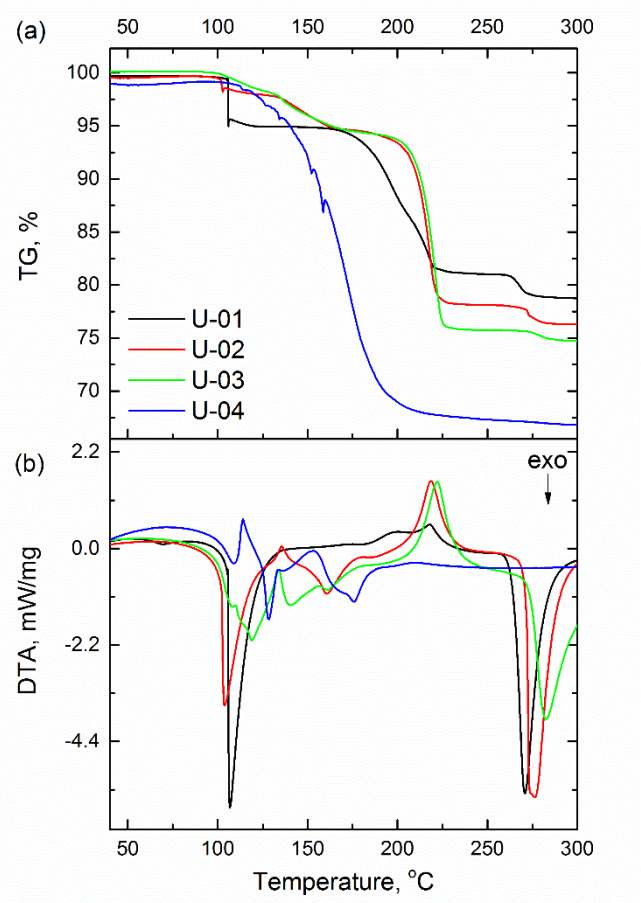

Figure 4-19. (a) TG and (b) DTA profiles of samples **U-01** to **U-04** when heating to 300 °C

Table 4-5. DTA T_{onset}, and mass loss of samples **U-01** to **U-04** when heating to 300 °C.

	U-01		**U-02**		**U-03**		**U-04**
	T_{onset} /°C	*Mass loss /wt%*	*T_{onset} /°C*	*Mass loss /wt%*	*T_{onset} /°C*	*Mass loss /wt%*	*T_{peak} /°C*
Region 1	105	4.8	100	5.4	103	5.6	106
Region 2	190	13.9	208	16.5	212	18.7	128
Region 3	264	2.2	272	1.8	277	1	167 / 175
Total mass loss /wt%	20.9		23.7		25.3		31.3

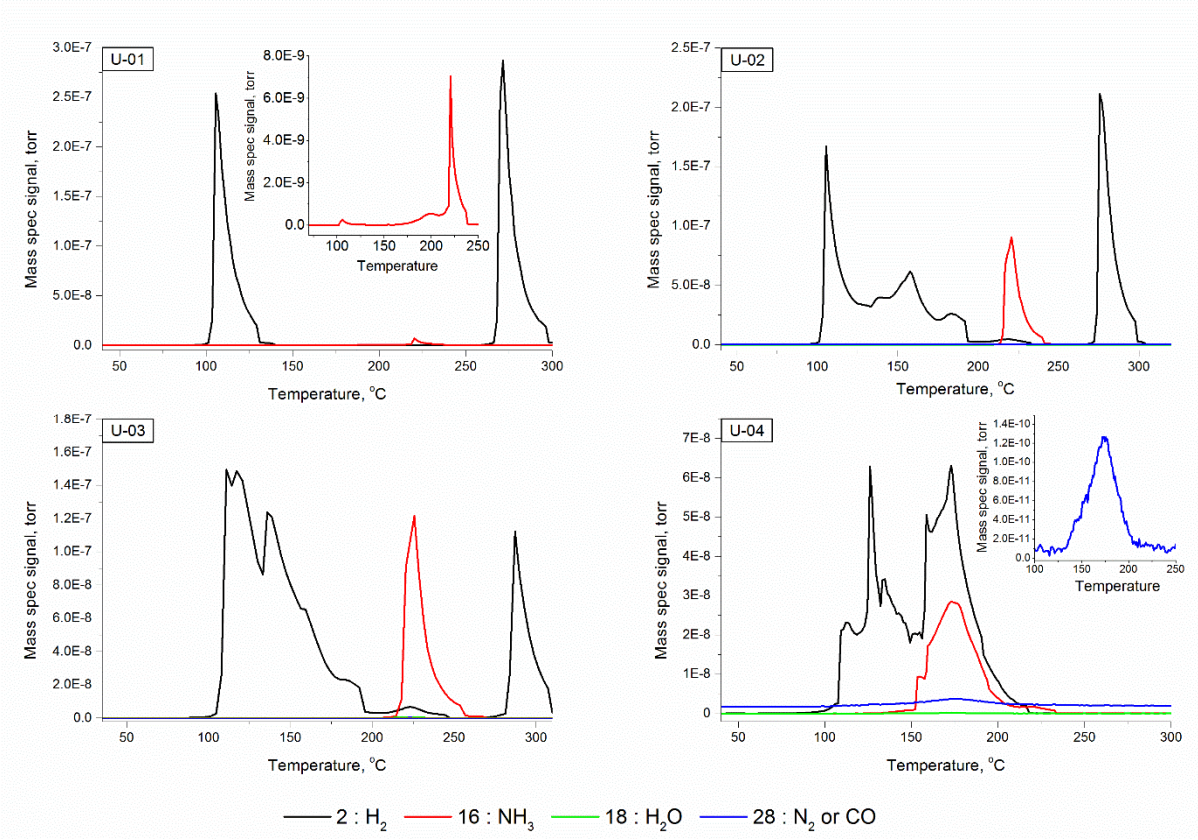

Figure 4-20. Mass spectra of samples **U-01** to **U-04** after heating to 300 °C

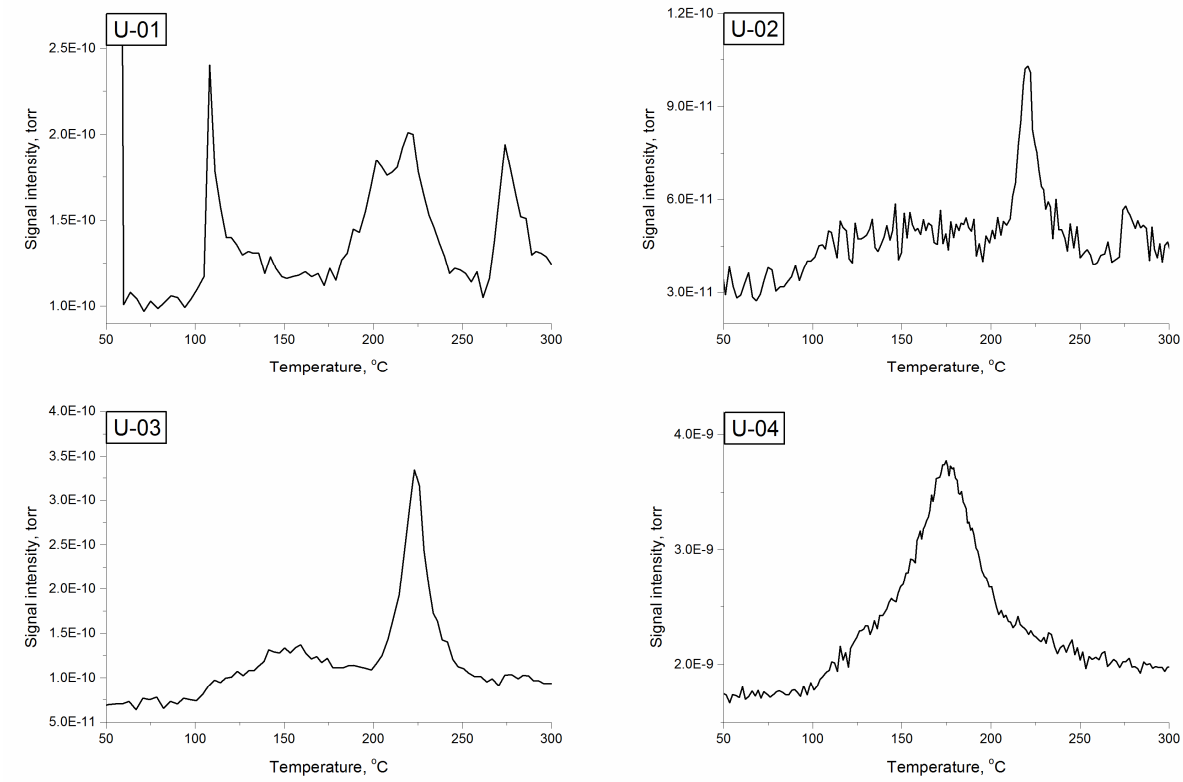

Figure 4-21. H_2O (*m/z*= 18) spectra of samples **U-01** to **U-04** after heating to 300 °C

4.3.2.1 Sample U-04, 1LiH:urea

Sample **U-04** yielded LiOCN as its final decomposition product at 300 °C (figure (4-22)). This suggests that the consumption of LiOCN in the presence of excess LiH is associated to the formation of some, if not all of the products observed in **U-01** to **03** (Li_2NCN, Li_2O, LiCN and Li_2CO_3). The mass loss follows a continuous TG profile adding to 31.3 wt%, which is 3 wt% higher than theoretical estimation. Considering the DTA and MS data, however, the exothermic formation of LiOCN from LiH and urea occurs *via* at least three intermediate reaction steps by DTA: the first step occurs at 106 °C, producing hydrogen; the second step peaks at 128 °C with a shoulder 10 °C higher also releasing hydrogen; and finally two DTA peaks occur at 167 °C and 175 °C, with associated products of ammonia, hydrogen and nitrogen. It should be noted that ammonia signals are only approximately half of those found for hydrogen, rather than a few orders of magnitudes smaller as found in **U-01**. Water, although three orders of magnitude smaller than the ammonia signal, was continuously evolved throughout the decomposition with a maximum release found at 175 °C. The simultaneous release of hydrogen and nitrogen in the presence of ammonia suggest either these processes are competitive, or that ammonia cracking in equation (4-16) occurs at a very low temperature compared to that normally expected (*ca.* 650 °C).[71-72]

$$2\ NH_3 \rightarrow N_2 + 3\ H_2 \qquad (\Delta H = 46\ kJ\ mol^{-1}) \qquad (4\text{-}16)$$

An examination of the solid products at 150 °C revealed the coexistence of LiOCN and the urea starting material in the approximate ratio of 3:2 by Rietveld refinement, with very weak reflections from the expected lithium ureate and reactant LiH (Figure 4-22). This is in contrast to the observations in **U-01**, where urea is completely consumed to form lithium ureate by 150 °C. In the absence of excess LiH, it appears that the lithium ureate formation proceeds more slowly and that the formation of LiOCN occurs almost simultaneously with faster kinetics, resulting in a continuous TG profile but with distinct thermal events detected by DTA. Another possible route to form LiOCN might be through the decomposition of urea into isocyanic acid at, HNCO 133 °C (scheme 3) which would react with LiH to release hydrogen. However the formation of isocyanic acid from urea involves an elimination of ammonia which is not observed on the MS by 150 °C, at which point LiOCN had already been formed. The residual urea observed at 150 °C presumably continues to interact with LiH instead of self-decomposing, as pristine urea decomposition is endothermic whereas all of the thermal events recorded here are exothermic. Moreover, the morphology of the products post-decomposition consists of not the foamed solid as observed for **U-01**, but of solid residues that adhere to the bottom of the alumina sample pan. There is also a noticeable lack of LiH hydrolysis (Li_2O and LiOH) and ammoniated products (Li_2NH and $LiNH_2$) in both the intermediate and final products of **U-04**, despite the proximity of low concentration of water vapour and a more substantial amount of ammonia partial pressure at elevated temperatures.

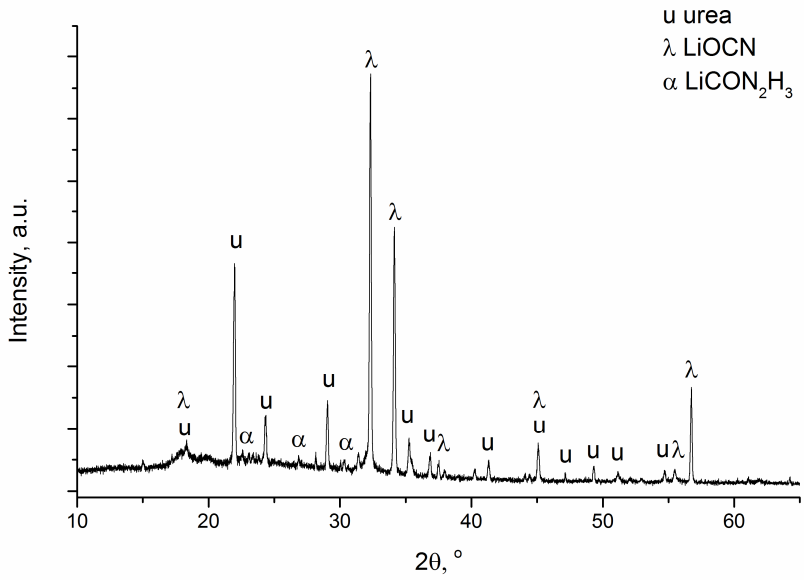

Figure 4-22. PXD of **U-04** after heating to 150 °C. The u symbols denote reflections for urea and λ indicate those of LiOCN.

4.3.2.2 LiH : urea ratio of 2:1, 3:1 and 4:1

Table 4-4 compiles the weight fraction of each phase from Rietveld refinement against PXD data for **U-01** to **U-03**. Sample **U-04** contains only single phase LiOCN and was not refined. It was observed that an increase in LiH reactant stoichiometry from 2:1 to 4:1 versus urea favoured the formation of Li_2O and LiCN over that of Li_2NCN and Li_2CO_3. It appears as though that when the LiH:urea ratio is increased, the formation of Li_2O increases in proportion to how much Li_2CO_3 decreases, whilst there is no obvious trend for the changes for Li_2NCN and LiCN. For **U-01**, the weight fraction of Li_2O approaches that of the theoretical according to equation 4-12, whereas lowering LiH content tends towards the other expected dehydrogenation product, Li_2NCN.

In contrast to **U-04**, **U-02** and **03** share similar three-region TG profiles as previously described for **U-01** in terms of the overall sequence of events. However, the DTA profile shapes, magnitude and positions differ (Figure 4-19). In the broad sense, all three samples produce hydrogen exothermically in region 1, followed by endothermic ammonia release with a trace amount of water and hydrogen in region 2 and a final dehydrogenation exotherm in region 3. It appears that, with a decrease in LiH content, the singular DTA exotherm found in region 1 (**U-01**, onset 105 °C) is replaced by multiple events of smaller magnitude. Ammonia release becomes a one step process, whilst the final dehydrogenation exotherm experiences a 7 °C increase in peak value per LiH equivalent removed. In terms of the TGA profiles, the near vertical mass loss for **U-01** in region 1 became less severe in **U-02**, and much more gradual in **U-03**. In region 2, the TG profile of the deammoniation step is sharper in comparison to that found in **U-01**, followed by similar TG profiles in region 3.

By comparing the overall mass loss between samples **U-01** to **03** (figure 4-19 (a)), it is clear that decreasing LiH stoichiometry has negligible effect on region 1, whereas the increased mass loss in region 2 and the decreased mass loss in region 3 are more pronounced as the LiH:urea ratio is reduced. The above trend loosely ties in with the changes in LiH:urea ratio however the effects are not strictly quantitative. Furthermore, the relative ratios of H_2 and NH_3 emitted by MS during thermolysis in Figure 4-20 suggests that an increase in LiH content promotes dehydrogenation between LiH and urea. It should be noted that the ratio of the gaseous species could be further quantified using appropriate calibration gas mixtures which were unavailable during this project.

Coincidently, according to diffraction, the intermediate compositions observed in the decomposition of **U-03** are very similar to those of **U-01** discussed previously (Figure 4-23). Lithium ureate is formed during the first thermal event with a DTA peak value of 119.3 °C. The phase is present below 200 °C, accompanied by a steady decline of mass and a continuous release of hydrogen. At this point the mass drops by approximately 19 wt% in a window of 30 °C followed by

an endothermic release of ammonia alongside traces of water and hydrogen. The green trace in Figure 4-23 captures the transition composition at 200 °C, consisting of LiOCN and a decreasing amount of lithium ureate. Note that LiH can be found in all of the intermediate diffraction patterns but the final product contains no LiH, alluding to the consumption of LiH in the formation of Li_2NCN, Li_2O, LiCN and Li_2CO_3.

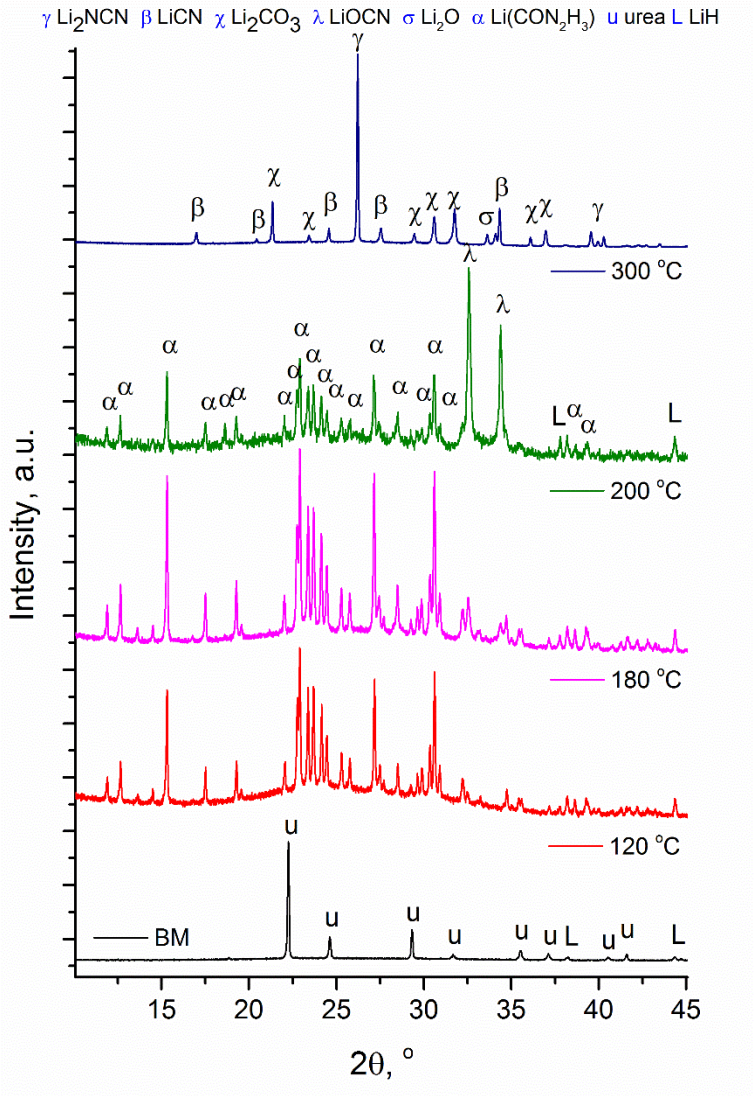

Figure 4-23. PXD of **U-03** at temperatures of 120, 180, 200 and 300 °C. Symbols ϒ denotes the reflections for Li_2NCN, β for LiCN, *X* for Li_2CO_3, λ for LiOCN, σ for Li_2O, α for lithium ureate, u for urea and L for LiH.

In the absence of sufficient LiH, the solid product when heating LiH and urea to 300 °C is LiOCN only. This again suggests that the formation of H_2, Li_2NCN, Li_2O, LiCN and Li_2CO_3 in region 3 is assisted by the presence of LiH. Increasing the LiH:urea ratio above 1:1 favours the release of hydrogen in this system over ammonia, without which the mixture decomposes in a continuous profile releasing H_2, NH_3 and H_2O. When LiH:urea increase lithium ureate is observed which decomposes to LiOCN by

the end of region 2. There was no evidence to suggest either of the thermodynamically favourable reactions between LiH and NH_3 or LiH and H_2O had occurred. In theory, the reaction between LiOCN and LiH to form the observed products could occur *via* the equations below, with increasing LiH content:

$$3\ LiOCN + 2\ LiH \rightarrow Li_2NCN + Li_2CO_3 + LiCN + H_2 \qquad (4\text{-}17)$$

$$4\ LiOCN + 4\ LiH \rightarrow Li_2NCN + Li_2O + 2\ LiCN + Li_2CO_3 + 2\ H_2 \qquad (4\text{-}18)$$

$$LiOCN + 2\ LiH \rightarrow Li_2O + LiCN + H_2 \qquad (4\text{-}19)$$

This would reflect product weight fractions compiled in table 4-6. By comparing tables 4-4 and 4-6, it can be noticed that with varying LiH:LiOCN ratios, Li_2NCN forms in greater quantity than those estimated by equations 4-17 to 4-19. This suggests that the unidentified *v*(CN) containing phase observed in the FTIR of sample **U-01** heated to 230 °C (figure 4-14) is likely involved in the formation of Li_2NCN. On the other hand the equations predicted the observed trend that with greater LiH presence the amount of Li_2O and LiCN increases alongside a decrease in Li_2CO_3.

Table 4-6. Theoretical weight fractions of observed products from the reaction between LiOCN and LiH according to equations 4-17 to 4-19.

Equation	**Li_2NCN**	**Li_2O**	**LiCN**	**Li_2CO_3**
4-17	0.331	-	0.202	0.453
4-18	0.237	0.131	0.290	0.325
4-19	-	0.461	0.508	-

As much as dehydrogenation could be encouraged with a high ratio of LiH, it was evident that the hydrogen rich LiH is not fully utilised when introduced in higher ratios. In addition, a large portion of hydrogen contained within urea is released in the form of ammonia during the decomposition of lithium ureate to LiOCN. Under the thermolysis conditions employed, the LiH – ammonia interaction to form Li_2NH or $LiNH_2$ would be expected to occur, even if there exists a considerable diffusion barrier. In the case of the Li-N-H hydrogen storage system reviewed in chapter 1, the selectivity of dehydrogenation or deammoniation is contingent on the physical conditions of the starting materials, which can be tuned by varying ball milling conditions. It is therefore compelling to study the effects of ball milling on the LiH:urea system with the purpose of improving LiH consumption and enhancing dehydrogenation over deammoniation for the system.

4.3.3 Ball milling experiments

Unlike the case for urea-$LiBH_4$ system, a stable coordination complex has not been found between urea and LiH.[73] When the pair is ball milled at high energy (500 RPM, 60:1 ball to powder ratio for 15 h), a pressure increase is detected with milling time (Figure 4-24). This pressure increases linearly until 300 kPa and then plateaus at 340 kPa. Analysis post milling identified Li_2NCN and Li_2O with broad Bragg reflections in the diffraction pattern due to the size reduction and lattice deformation introduced during milling (Figure 4-25). A broad peak centred at centred at 29.8° 2Θ cannot be assigned to any known phases containing the elements Li, H, O, C and N. The formation of Li_2NCN and Li_2O, which are the reaction products predicted by equation 4-12 indicates that the stoichiometric reaction (equation 4-12) had occurred; and that much of the barrier to successful dehydrogenation between LiH and urea is kinetic. As the milled product contains Li_2NCN and Li_2O, by inference the pressure measured would be due to hydrogen release. It can also be implied that complete dehydrogenation could occur at moderate temperatures when facilitated by appropriate mixing and reaction conditions. Given that over-milling could induce premature hydrogen release, it was the aim of the work described in the following section to investigate how ball milling could facilitate a change in decomposition pathway to promote theoretical hydrogen release and eradicate ammonia evolution.

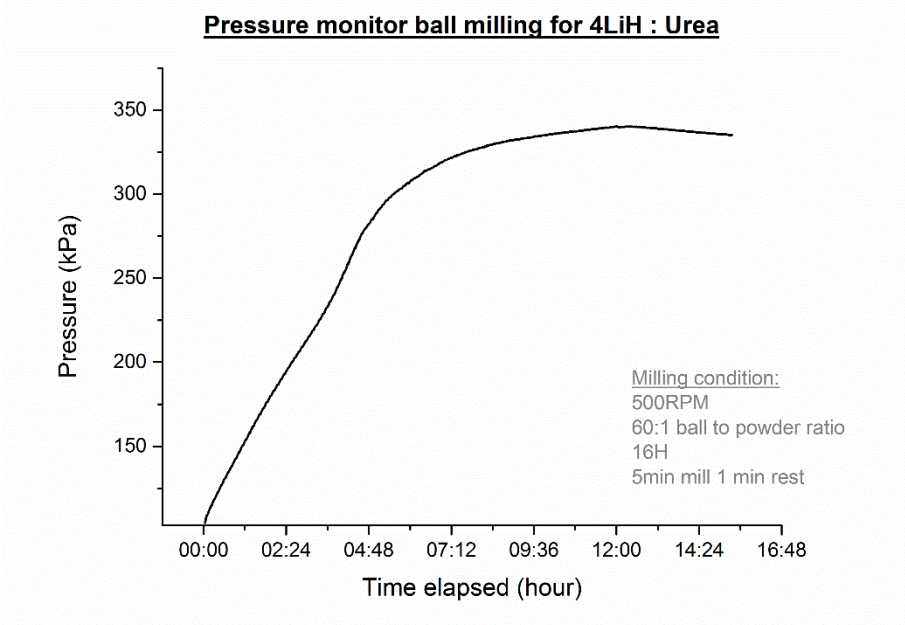

Figure 4-24. Pressure versus time elapsed during a prolonged ball milling experiment between 4 LiH and urea

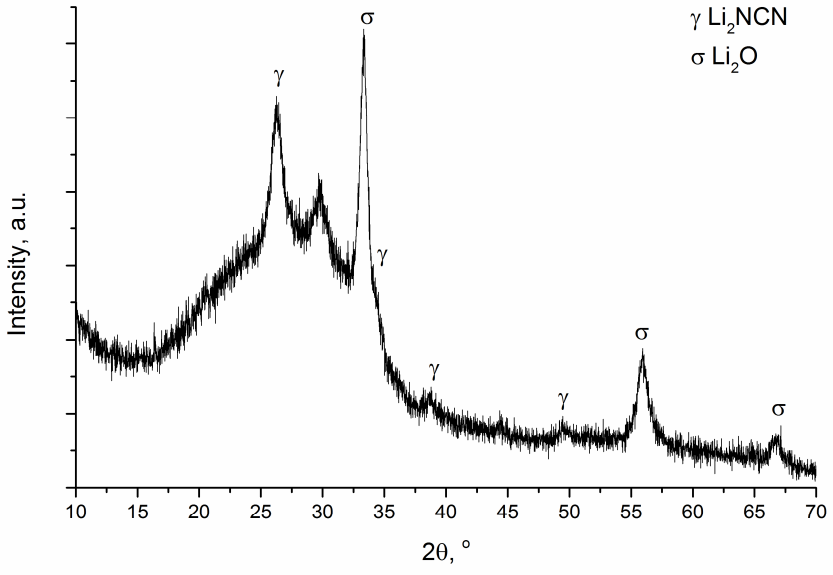

Figure 4-25. Diffraction pattern of the products of the prolonged ball milling experiment, showing main Li_2NCN (ϒ) and Li_2O (σ) phases.

4.3.3.1 Effect of increasing ball milling speed

Mild mixing conditions by ball milling were applied to three 4:1 LiH:urea mixtures: (i) hand grinding for five minutes (**U-06**), (ii) ball milling at 150 RPM (**U-01**) and (iii) ball milling at 200 RPM (**U-07**). Both milled samples used 30:1 ball to powder ratios and were milled for 36 min. The thermolysis of the three mixtures is shown in Figure 4-26. First to note is that as the milling speed increases, the first DTA peak at *ca.* 60 °C diminishes. This is followed by a pronounced decrease in the onset temperature of the second DTA event with the extent of milling:

$$T_{\text{Hand ground}} > T_{150\ \text{RPM}} > T_{200\ \text{RPM}}$$

Whilst region 2 of the TG profile remained similar for the three samples, the final dehydrogenation exotherm in region 3 is lowered by 20 °C as a result of ball milling.

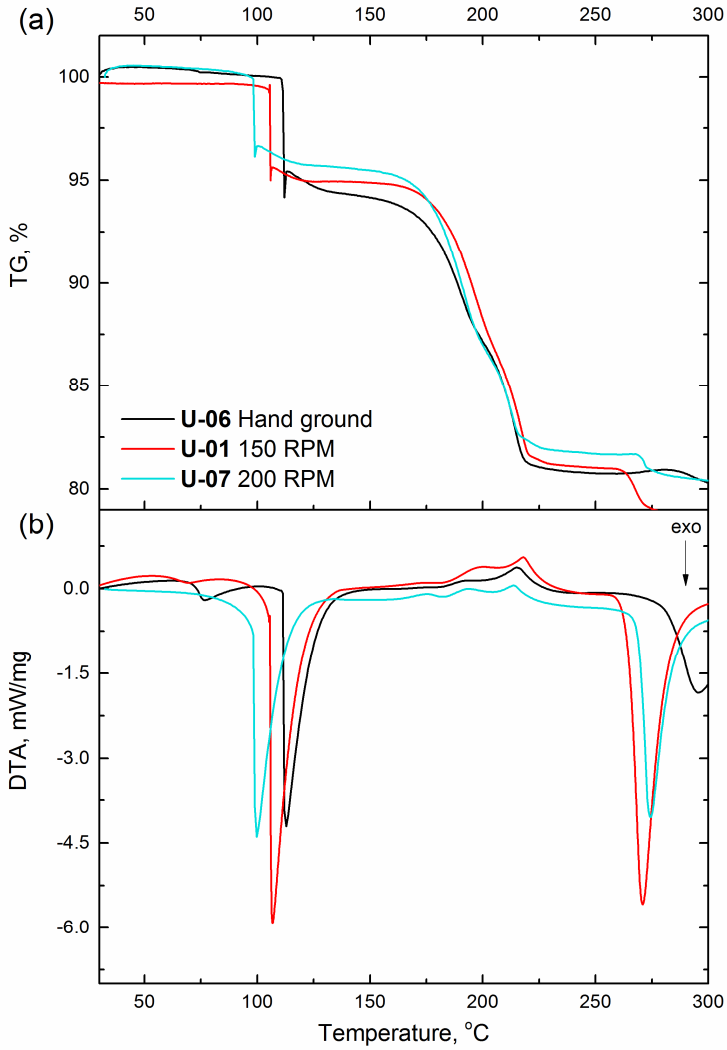

Figure 4-26. (a) TG and (b) DTA profiles for heaingt samples **U-01**, **U-06** and **U-07** to 300 °C

At even higher milling speeds of 300 (**U-08**), 450 (**U-09**) and 600 RPM (**U-10**), the thermolysis profiles change drastically with increasing milling rate (the same 30:1 ball to powder ratio is used, Figure 4-27). **U-08** sees a separation of the two endothermic deammoniation DTA peaks; the vertical mass loss in region 1 becomes gradual in **U-09** as well as losing a smaller mass of 1.3 wt% during the final step in region 3 and a higher DTA onset temperature. The mass loss for **U-10** is the lowest observed in the series at 10.93 wt% over at least 4 main steps (figure 4-27(a)). In addition the DTA peaks in region 2 are exothermic instead of endothermic for **U-10** (figure 4-27 (b)). However noticeable pressure build up was also observed in the milling jar after milling **U-10**, suggesting dehydrogenation had occurred prior to heating.

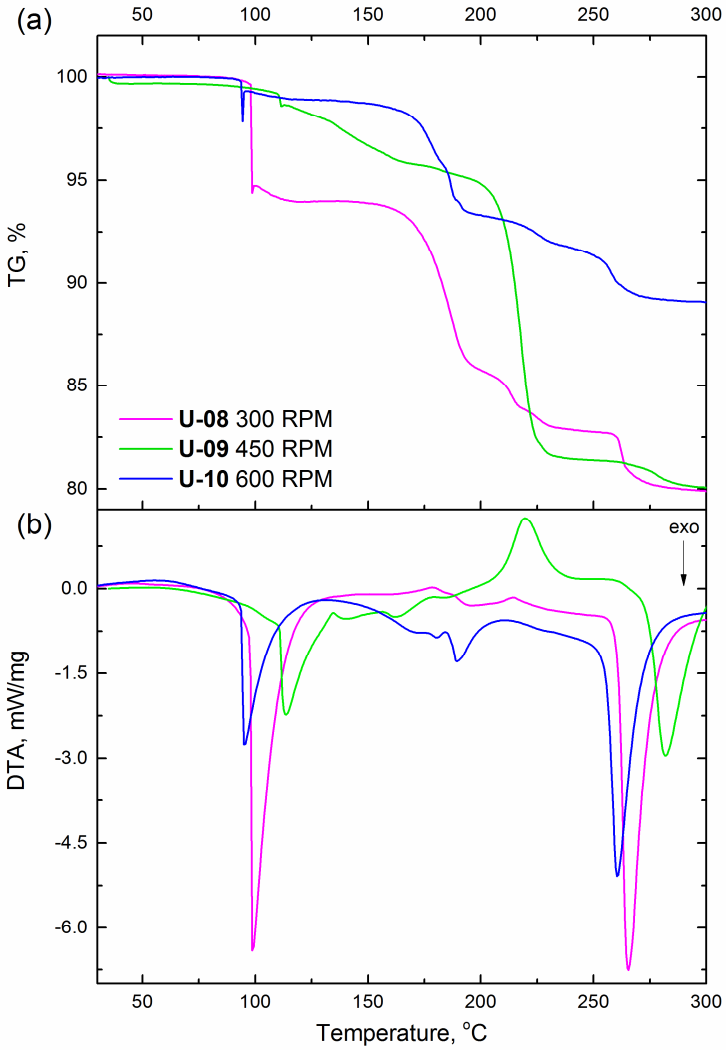

Figure 4-27. (a) TG and (b) DTA profiles for heating samples **U-08** to **U-10** from RT to 300 °C

The breakdown of the product composition post thermolysis by Rietveld refinement is compiled in table 4-7. From the residual LiH content it can be inferred that accelerating ball milling speed has a positive influence on LiH consumption. This is accompanied by a steady increase of the desired reaction product Li_2NCN with a coincident decrease in LiCN. Li_2CO_3 is absent when milling speed at speeds of 300 RPM and above. High milling speed therefore appears to facilitate the ideal dehydrogenation reaction as proposed in equation 4-12. On the other hand less milling leads to deammoniation and the formation of LiCN, given a C=N bond is broken from the reactant urea molecule during the release of ammonia.

Table 4-7. Phase fractions of product of thermal decomposition at 300 °C for 4LiH and urea. The refinement plots are included in the Appendix.

*U-07 data unavailable as the sample was lost during transportation between instruments.

	Expected	U-06	U-01	U-08	U-09	U-10	U-11	U-12
		Hand ground	150 RPM 36m	300 RPM 36m	450 RPM 36m	600 RPM 36m	PreUrea 150R 36m	Pre3HLiH 150R 36m
Li_2NCN	0.6112	0.322(4)	0.197(6)	0.215(1)	0.465(0)	0.543(1)	0.232(7)	0.243(0)
Li_2O	0.3888	0.242(3)	0.389(9)	0.504(5)	0.417(3)	0.408(0)	0.389(5)	0.342(7)
LiCN	0	0.122(6)	0.215(9)	0.212(2)	0.092(9)	0.048(9)	0.201(2)	0.206(5)
Li_2CO_3	0	0.184(2)	0.084(0)	0	0	0	0.056(5)	0.102(5)
LiH	0	0.128(6)	0.112(1)	0.068(2)	0.024(9)	0	0.120(0)	0.105(4)
LiOH	0	0	0	0	0.015(3)	0	0	0
X^2	n/a	1.319	1.094	1.179	1.147	1.265	1.194	1.054
wRp	n/a	0.0877	0.1173	0.0929	0.0472	0.0387	0.0574	0.1167

4.3.3.2 Effects of ball milling on reactant activity

As a means of enhancing solid state activity, defects can be introduced into a solid by vigorous mechanical deformation in the ball mill. This method was proposed as a crucial means of improving dehydrogenation in the Li-N-H system reviewed in Chapter 1 and the LiH-melamine system in Chapter 3. As LiH readily reacts with urea when ball milled at high energy, pre-milling the two components independently at 600 RPM with a 60:1 ball to powder ratio for three hours was adopted with the intention of reducing particle size and introducing defects without inducing premature hydrogen release. The premilled urea and LiH are then intimately mixed with pristine LiH and urea respectively in the ball mill at 150 RPM for 36 min at a ball to powder ratio of 30:1 and a milling programme of 5 min mill 1 min rest. The thermolysis of premilled urea with pristine LiH (**U-11**), and premilled LiH with pristine urea (**U-12**) are presented in the following (Figure 4-28, Table 4-8).

Sample **U-11** produced a similar thermolysis profile to that of **U-09**, where the mass in region 1 decreases gradually accompanied by several exothermic DTA peaks. This is followed by a strong endotherm with a peak value of 217.4 °C. Only a very small difference was observed in the overall mass loss for **U-11** at 20.56 wt% versus 19.42 wt% for **U-09**. The solid composition post thermolysis contains Li_2NCN, Li_2O, LiCN and Li_2CO_3, with a high portion of residual LiH.

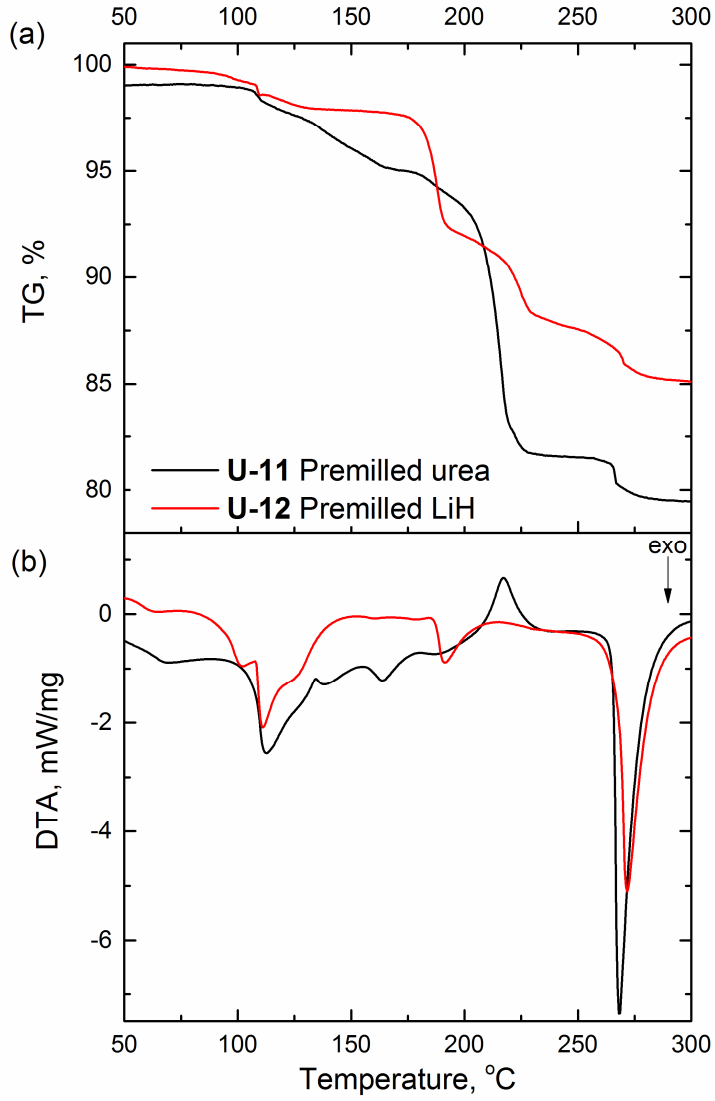

Figure 4-28. (a) TG and (b) DTA profiles for heat samples **U-11** and **U-12** from RT to 300 °C**.**

Table 4-8. TG and DTA peak value data for samples **U-11** and **U-12**

	Region 1		**Region 2**		**Region 3**		**Total**	
	U-11	**U-12**	**U-11**	**U-12**	**U-11**	**U-12**	**U-11**	**U-12**
Mass loss /wt%	6.86	2.20	11.76	10.7	1.94	1.86	20.56	14.76
DTA T_{peak} /°C	70.2 112.6 138.0 163.7 186.7	64.9 102.0 111.1 126.0 160.4 178.8	217.4	191.3	268.3	271.8		

On the other hand, the DTA profile of **U-12** shares the same exothermic peak at 191.3 °C in region 2 with **U-10**; while the single exotherm of **U-10** in region 1 is replaced with multiple peaks smaller in magnitude for **U-12**. Moreover, the **U-12** decomposition product was distinctively powder in comparison to the porous foam solid found in all of the other samples tested which again verified that the vertical mass loss in the other samples can be attributed to frothing. It should be noted that the mass loss during region 1 in the thermolysis of **U-12** (2.20 wt%) is the theoretical mass loss for releasing one equivalent of H_2 by the formation of lithium ureate in equation 4-14.

The two samples also share similar MS profiles showing three intense hydrogen release in regions 1, 2 and 3 with two ammonia peaks in region 2 (Figure 4-29). On further inspection of the TG and MS profiles it can be observed that although the overall mass loss for **U-10** (10.87 wt%) appears to be closer to the theoretical 8.78 wt% (equation 4-12), it is estimated that **U-10** and **U-12** have released similar amounts of hydrogen. This deduction was made by utilising the semi-quantitative nature of the MS with respect to the mass loss step in region 3 which released only hydrogen. By integrating the area under the hydrogen peak in this region and taking the ratio against respective mass losses during this step of the two samples, it was possible to estimate that the overall mass loss due to hydrogen release for both **U-10** and **U-12** to be approximately 5.8 wt% (Table 4-9).

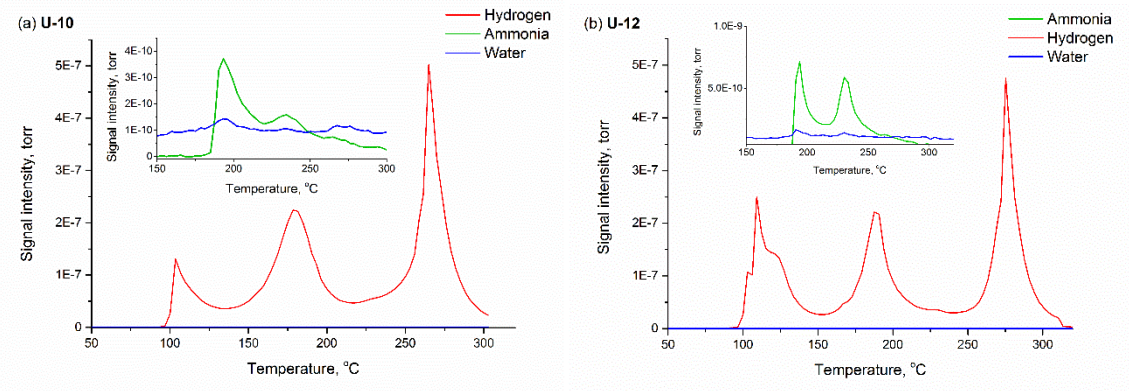

Figure 4-29. Mass spectra showing hydrogen, water and ammonia signals for samples (a) **U-10** and (b) **U-12**

Table 4-9. Estimation of the overall mass loss due to H_2 release during thermal decomposition of samples **U-10** and **U-12**

	Range	**Region 3**			**Overall**	
	(°C)	MS (H_2 area)	TG (wt%)	MS/TG	MS (H_2 area)	TG (wt%)
U-10	250-315	7.93 E-06	2.31	3.43 E-06	1.99E-05	5.80
U-12	230-300	1.20 E-05	3.28	3.66 E-06	2.14E-05	5.85

At this point, it is evident that ball milling can be effectively used to improve LiH consumption while at the same time mitigating ammonia release. Some of the observed characteristics such as shifts in DTA peak temperature may be attributed to particle size variations between samples, but a thermodynamic change from an endothermic to exothermic ammonia release requires further exploration.

Reaction products of **U-12** examined using PXD *ex situ* at plateau temperatures of 150, 190, 230 and 300 °C reveal intermediate compositions previously undetected in **U-01** (Figures 4-30 to 4-33). At 150 °C, the expected lithium ureate phase is formed with a mass loss of 2.2%. Another 5 wt% is lost when heating to 190 °C, corresponding to the exothermic DTA peak with the highest rate of heat release at 189.3 °C. The PXD pattern in Figure 4-31 shows trace of residual of lithium ureate and a combination of a small amount of LiOCN, Li_2NH and a new set of unidentified peaks marked by '?'. The formation of Li_2NH in parallel to a stronger H_2 and weaker NH_3 release detected on the MS in comparison to **U-01** can be ascribed to a reaction between LiH and ammonia (equation 4-13).

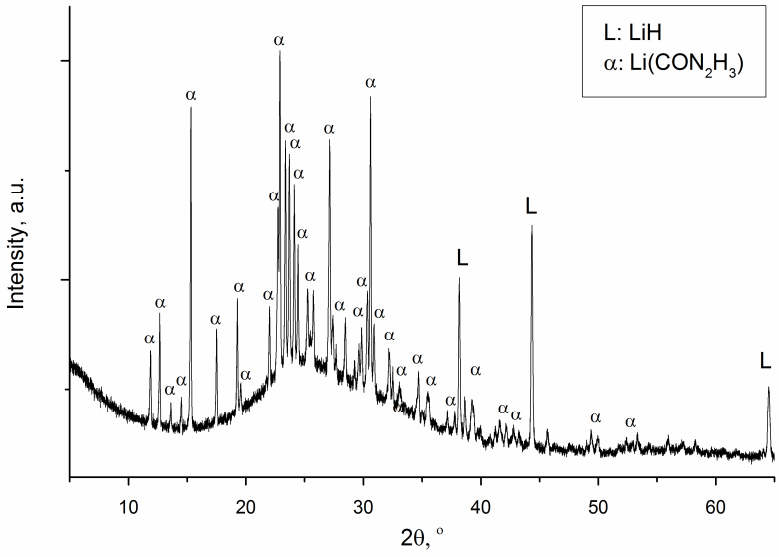

Figure 4-30. PXD of **U-12 after** heating to 150 °C

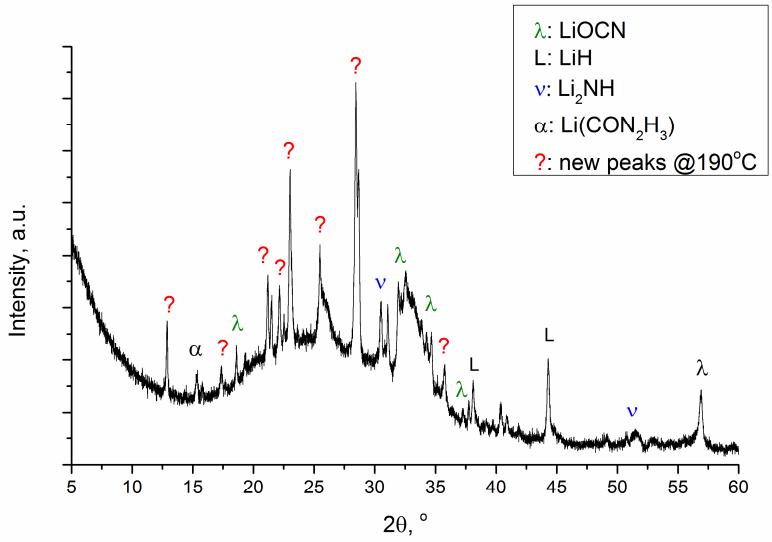

Figure 4-31. PXD of **U-12** after heating to 190 °C

By 230 °C another 4.3 wt% is lost and only NH_3 is released as detected by the MS. There is thus no evidence that the LiH-NH_3 hydrogen production reaction occurred during this second release of NH_3 as LiOCN and two of the newly formed peaks increase in intensity (Figure 4-32). From the PXD patterns at least two new distinct phases appear to have formed, however none of these newly observed peaks could be matched to reference patterns on the ICDD and ICSD databases. At 300 °C the final product is found to contain the same 5 phases seen in other 4:1 LiH:urea samples (table 4-6). LiH remained a high portion in the thermolysis product. (The corresponding FTIR spectra are included in the Appendix)

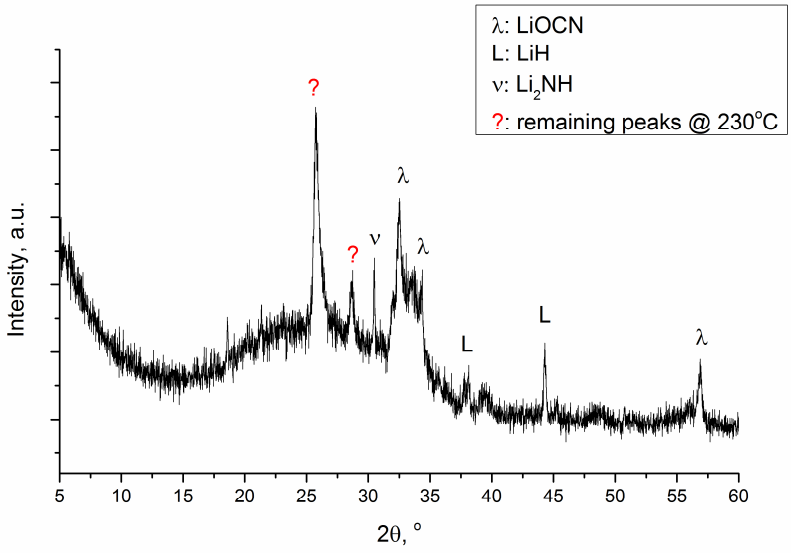

Figure 4-32. PXD of **U-12** after heating to 230 °C

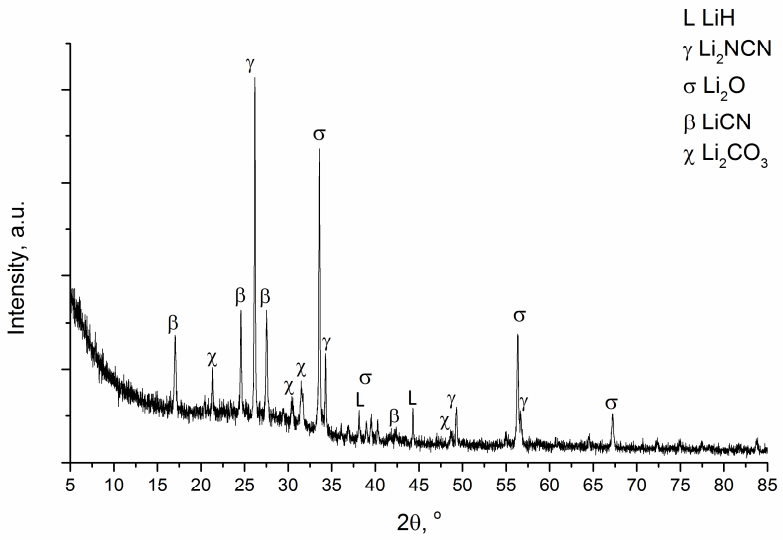

Figure 4-33.PXD of **U-12** after heating to 300 °C

4.3.3.3 Activation energy calculation

An attempt was made to evaluate the kinetic behaviour of reactions at each region of sample **U-12** by characterising the activation energy, E_a, using the Kissinger-Akahira-Sunrose method (equation (4-20)). This is done by using a range of heating rates, β_i for the thermolysis experiment in the STA (1, 2, 5, 8 and 10 °C min^{-1}) and taking the DTA peak temperatures as $T_{a,i}$:[74]

$$\ln \frac{\beta_i}{T_{a,i}^2} = A - \frac{E_a}{RT_a} \qquad (4\text{-}20)$$

The resulting TG and DTA profiles however, shows discrepancy between the thermolysis behaviour discussed previously when **U-12** is heated at different rates. (figure 4-35). The most obvious is that of the gradual mass loss during region 1 is once again replaced by sharp, vertical profile accounting to 10.5 and 10.87 wt% in the 8 and 10 °C min^{-1} experiments respectively. This is succeeded by a single step observed in region 2 and another vertical step observed in region 3 for the two heating rates to yield a significantly frothed sample at the end of the thermolysis experiment. At lower heating rates of 1 and 2 °C min^{-1}, whilst the majority of the thermal events match those of the 5 °C min^{-1} experiment discussed previously, there were only two peaks during region 1 instead of three. It appears, that similar to the thermolysis of pristine urea discussed in scheme 4-3 and those of AB discussed in section 1.3.1.1, the decomposition pathway between LiH and urea is also sensitive to the reaction conditions, and as a consequence of potential physical sample loss during foaming. Given that foaming occurs at higher heating rates (associated with high kinetics), the Kissinger analysis was performed for the lower heating rates: 5, 2 and 1 °C min^{-1}.

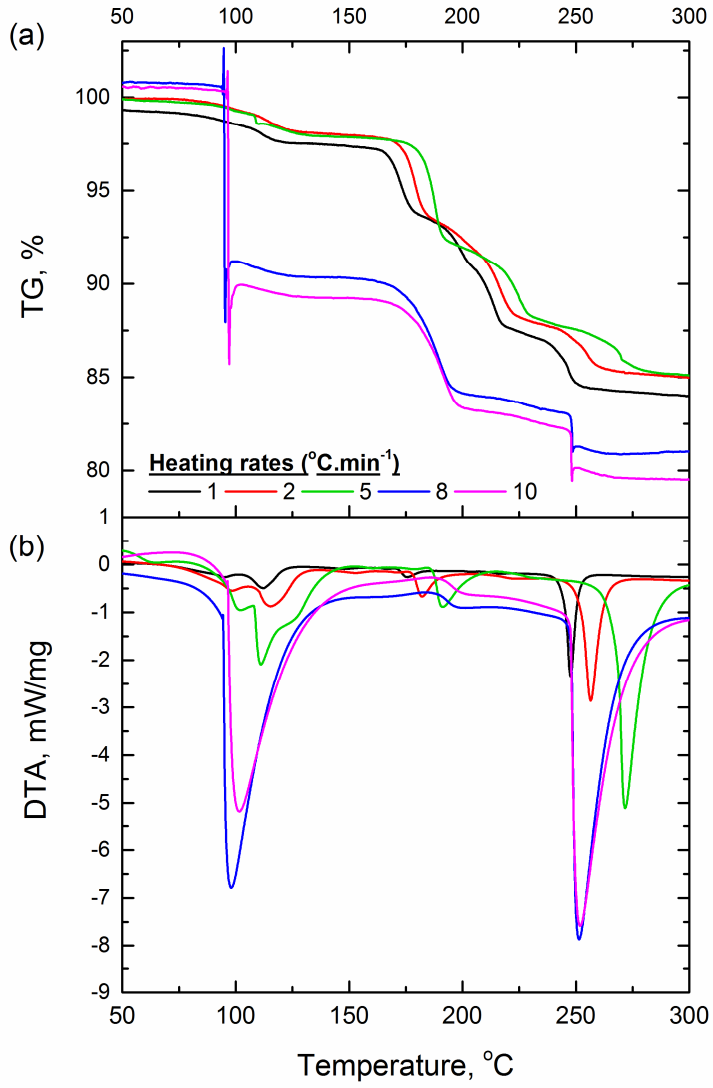

Figure 4-35. (a) TG and (b) DTA profiles when heating sample **U-12** at various heating rates of 1, 2, 5, 8 and 10 °C min^{-1}

The activation energies for the decomposition reactions in region 2 and 3 (figure 4-36), according to the DTA peak temperatures of the 1, 2 and 5 °C min^{-1} experiments were tentatively calculated to be 171.2±0.7 and 146.6±0.6 kJ mol^{-1} respectively. The error, σ_m adopted here is a percentage error of 0.41% calculated using the peak temperature values in region 2 at 5 °C min^{-1} over 4 repeats with sample **U-12** according to the equation:

$$\sigma_m=\sqrt{\frac{1}{n-2}\sum(y_m-y)^2} \qquad (4\text{-}21)$$

Given that the exotherm in region 2 has been associated with the formation of Li_2NH (from LiH and NH_3), an activation energy more than twice than that characterised for ball milled LiH-$LiNH_2$ (83.3

kJ mol^{-1})[75] suggests that a variety of other complex rate limiting processes contribute to the reaction in this region.

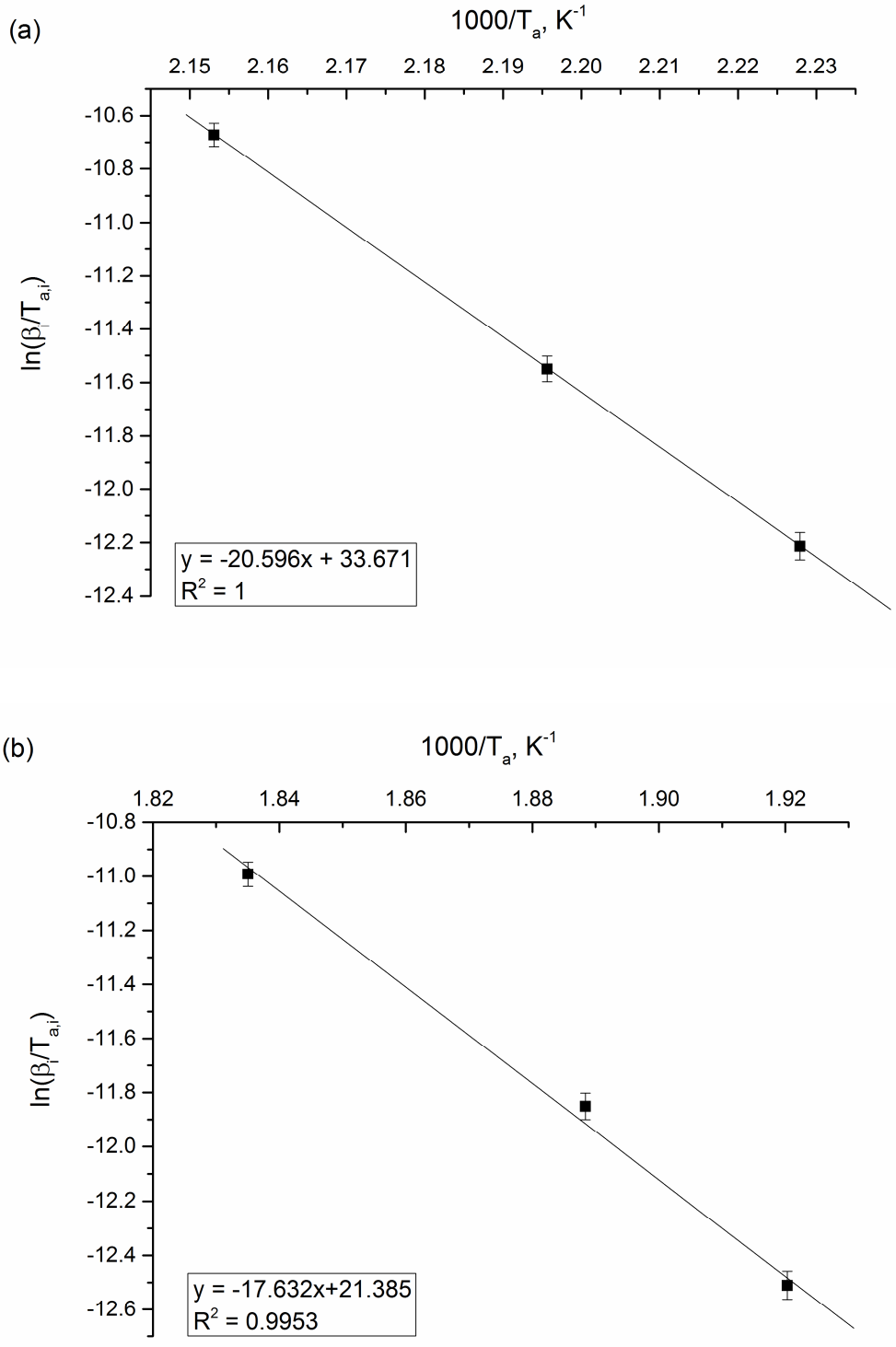

Figure 4-36. Activation determination using the Kissinger-Akahira-Sunrose relation for the gas desorption reactions in sample **U-12** in (a) region 2 and (b) region 3

4.3.3.4 Summary

From the results discussed above it can be concluded that high energy ball milling induces *in situ* hydrogen release in the ball mill according to equation 4-12. The undesirable ammonia release is therefore a result of kinetic barrier between LiH and urea in the solid state. Thus far ball milling has shown a positive effect on the dehydrogenation between LiH and urea by facilitating reactant contact, this likely enhancing kinetics; and in some cases changes the reaction pathway, therefore altering the reaction thermodynamics. Under energetic milling foaming of the sample was not observed during the formation of lithium ureate, and subsequently the expected Li_2NH was observed during the deammoniating region 2 as a product of LiH reacting with ammonia gas. It was also found that the system is prone to *in situ* hydrogen release when milled with sufficiently high energy. By pre-milling urea and LiH separately under such conditions we have identified that creating defects in LiH particles of reduced size was key to promoting dehydrogenation. Despite a noticeable change in the composition at intermediate reaction steps compared to other samples, the premilled LiH sample (**U-12)** yielded multiple products and residual reactant LiH. In contrast a sample (**U-10**) in which both reactants were milled together at high energy formed close to the expected ratio of the desired dehydrogenated products according to equation 4-12. It appears that LiH has been consumed completely during the thermolysis of **U-10** and the solid product composition approaches that described by equation 4-12. By combined MS and TG analysis it was possible to estimate a mass loss due to hydrogen in samples **U-10** and **U-12** to be approximately 5.8 wt%. Activation energies of the decomposition in region 2 and 3 for **U-12** were calculated to be 171.2±0.7 and 146.6±0.6 kJ mol^{-1} respectively. It was also found during the varying heating rate experiments for **U-12** that the decomposition pathway changes drastically when the heating rate is increased above 8 °C min^{-1} accompanied by sample foaming.

4.4 The efficacy of the LiH:urea hydrogen storage system

It has been shown thus far that hydrogen can indeed be generated between LiH and urea. Using the MS and TG data obtained it was estimated that at least 5.8 wt% of the theoretical 8.78 wt% can be released. Once the first equivalent of H_2 is released at 105 °C in the formation of lithium ureate, further dehydrogenation appears to follow an ammonia mediated route and no evidence was found for a dilithium ureate compound as suggested by Coumbarides *et al* albeit under very different experimental conditions. (Scheme 4-1). It is likely that regardless to what extent the reaction surface between LiH and ammonia can be improved, it is inevitable that the ammonia released would gradually poison the fuel cell, as well as leading unwanted loss in hydrogen storage capacity. Perhaps the rigidity in a crystal acts as the kinetic barrier for what appears to be the thermodynamically favourable dehydrogenation between LiH and lithium ureate. This dehydrogenation step would otherwise be expected to occur when considering the high energy ball milling experiment reported in this chapter and Coumbarides' dilithium ureate in scheme 4-1. In the discussion of the lithium ureate crystal structure, Sawinski *et al.* pointed out that the lithium cation is coordinated in three symmetry independent configuration shown in figure 4-37.[41]The molecular geometry and proximity between neighbouring NH and NH_2 groups could lead to complex multiple-step ammonia desorption reactions as observed in region 2. However further work would be necessary to verify the decomposition of pure lithium ureate using the synthesis routes reported by Sawinski *et al.* It was also pointed out that there is no observable dihydrogen bonding network within this structure to facilitate dehydrogenation such as those found in LiAB and LiHB compounds.[41]

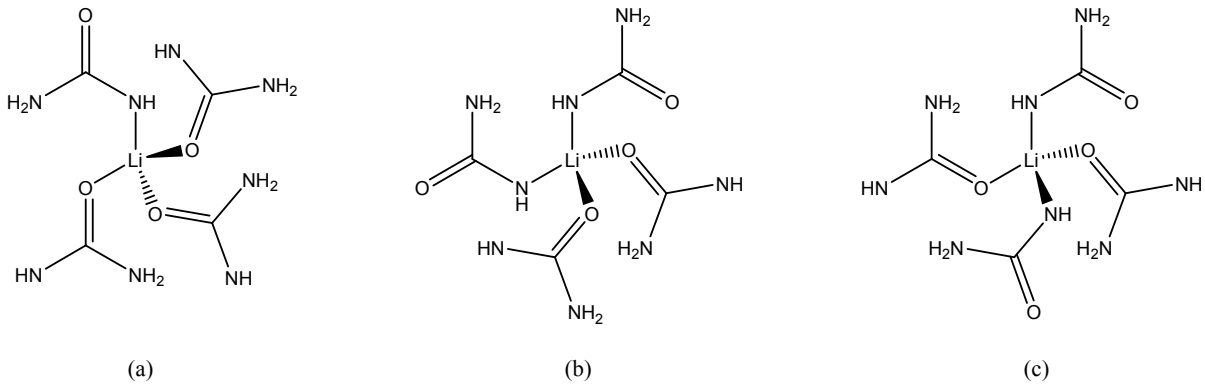

Figure 4-37. Three symmetry-independent Li^+ ions coordinated by distorted tetrahedral ureate ions by single crystal X-ray diffraction experiment[41]

The decomposition pathway between LiH and urea is also contingent on the reaction conditions, as the pathway changed drastically at different heating rates, exemplified by foaming of **U-12** at heating rates above 8 °C min^{-1}. Further study of heat induced hydrogen and ammonia release from

lithium ureate, as synthesised by the methods reported by Sawinski would elucidate the transport mechanism that facilitate gas release. This should allow further manipulation of the system to selectively release hydrogen using strategies such as microstructural alternations (confinements) or metal doping. Furthermore, an attempted rehydrogenation reaction from Li_2NCN to urea using reported acidic condition for analogues CaNCN was unsuccessful (Appendix F).[76] The analysis of the reaction products has been inconclusive and further experiments will be required.

4.5 Conclusions and future work

The dehydrogenation reaction between LiH and urea has been examined in this chapter. Hydrogen release was found to occur in three steps: it is first released during the formation of lithium ureate at 104.5 °C; the second step appears intimately connected to a reaction between LiH and the ammonia released during the decomposition of lithium ureate to form LiOCN, which yields Li_2NH between 150 and 230 °C; and the last step involves the reaction between LiH, LiOCN and unidentified amorphous material from 250 to 270 °C. Ammonia and water were the other gas products during the decomposition of lithium ureate, while the solid product at 300 °C consists of Li_2NCN, Li_2O, LiCN and Li_2CO_3. It was identified that the barrier to full dehydrogenation at moderate temperatures is kinetic as the desired products Li_2NCN and Li_2O were formed during a high energy ball milling experiment. It was also found that under appropriate ball milling preparation, approximately 5.8 wt% of hydrogen was released thermally from the 8.78 wt% available from the 4:1 LiH:urea system. Activation energies associated with the gas desorption reactions associated with the decomposition of lithium ureate from 150 °C and the final dehydrogenation between 250 and 270 °C were calculated to be 171.2±0.7 and 146.6±0.06 kJ mol^{-1}. It was observed that similar to the thermal decomposition of urea, the LiH:urea system is sensitive to the conditions under which the thermolysis is performed.

Future investigations of this system should focus on interpreting the decomposition of pure lithium ureate in order to propose the full reaction scheme between LiH and urea. Moreover the theoretical viable rehydrogenation of Li_2NCN through hydrolysis in acidic or basic conditions would enhance the sustainability of the system.

4.6 References

1. Cadogan, J. I. G.; Ley, S. V.; Pattenden, G.; Raphael, R. A.; Rees, C. W. Urea. *Dictionary of Organic Compounds*; Chapman and Hall: London, 1996; Sixth Edition, Vol. 6, pp 6455
2. Kruzer, F.; Sanderson, P. M. *J. Chem. Educ.* **1956**, *33*, 452-459
3. Wöhler, F. *Annalen der Physik*. **1828**, *88,* 253-256
4. Meessen, J. *Chem. Ing. Tech.* **2014**, *86*, 2180-2189
5. Tsipis, C.; Karipidis, P. A. *J. Phys. Chem.* **2005**, 109, 8560-8567
6. Merchant Research and Consulting Limited Market Reports: Urea. https://mcgroup.co.uk/researches/urea [Online] (accessed 1st August 2016)
7. De Jong, J. I.; De Jonge, J. *Recueil* **1952***, 71*, 643-660
8. Web of Science™ Core Collection search result, keyword 'urea'. http://webofknowledge.com.ezproxy.lib.gla.ac.uk/WOS [Online] (accessed 1st August 2016)
9. Bandyopadhyay, D.; Mohan, S.; Ghosh, S. K.; Choudhury, N. *J. Phys. Chem. B.* **2014**, *118*, 11757-11768
10. Grdadolnik, J.; Maréchal, Y. *J. Molecular Structure* **2002**, *615*, 177-189
11. Finer, E. G.; Franks, F.; Tait, M. J. *J. Am. Chem. Soc.* **1972***, 94*, 4424-4429
12. Frank, H. S.; Franks, F. *J. Chem.Phys.* **1968***,48*, 4746-4757
13. Keuleers, R.; Desseyn, H. O. *J. Phys. Chem. A* **1999,** *103,* 4621-4630
14. Docherty, R.; Roberts, K. J.; Saunders, V.; Black, S. and Davey, R. J. *Faraday Dosscuss.* **1993**, *95,* 11-25
15. Stumpe, M. C.; Grubmüller, H. *J. Am. Chem. Soc.* **2007***, 129*, 16126-16131
16. Bull, H. B.; Bresse, K.; Ferguso, G. L.; Swenson, C. A. *Archives of Biochemistry and Biophysics* **1964***, 104*, 297-304
17. Theophandides, T. *Coord. Chem. Rev.* **1987***,76,* 237-264
18. Kryatov, S. V.; Nazarenko, A. Y.; Roninson, P. D.; Rybak-Akimova, E. V. *Chem. Commun.*, **2000**, 921–922
19. Sagatys, D. S.; Bott, R. C.; Smith, G. *Polyhedron* **1992**, *11*, 49-52
20. Lundström, A.; Andersson, B.; Olsson, L. *Chem. Eng. J.* **2009***, 150*, 544-550
21. Koebel, M.; Elsener, M.; Klemann, M. *Catalysis Today* **2000**, *59*, 335-345
22. Sebelius, S.; Le, T. T.; Pettersson, L. J.; Lind, H. *Chem. Eng. J.* **2013***, 231,* 220-226
23. Fang, H. L.; DaCosta, H. F. M. *App. Catalysis. B: Enviro.* **2003***, 46,* 17-34
24. Hutchby, M. Novel Synthetic Chemistry of Ureas and Amides. PhD thesis, University of Bristol, UK, 2013
25. Stowell, J. C.; Padegimas, S. J. *J. Org. Chem.* **1974**, *39*, 2448-2449
26. Godfrey, P. D.; Brown, R. D.; Hunter, A. N. *J. Molecular Structure* **1997***, 413-414,* 405-414
27. Vaughan, P.l Donohue, J. *Acta Cryst.* **1952***, 5*, 530-535
28. Swaminathan, S.; Craven, B. M. *Acta Cryst.* **1984**, *B40*, 300-306
29. Birkedal, H.; Madsen, D.; Mathiesen, R. H.; Kundsen, K; Weber, H.; Pattison, P.; Scharzenbach, D. *Acta Cryst.* **2004***, A60*, 371-381
30. Bonin, M.; Marshall, W. G.; Weber, H. P. and Toledano, P. *The ISIS Facility Annual Report 1998-1999* **1999**, ISIS Neutron Facility, Rutherford Appleton Laboratory, Chilton, Didcot, Oxford, England.
31. Gora, R. W.l Bartkowiak, W.; Roszak. S.; Leszczynski, J. *J. Chem. Phys.* **2002***, 117*, 1031-1039
32. Liao, H.; Chu, S. *New J. Chem*. **2003**, *27*, 421-424
33. Krajewska, B. *J. Molecular Catalysis B: Enzymatic* **2009***, 59*, 9-21
34. Bouchoux, G. *Mass Spectrometry Reviews* **2015**, *34*, 493-534
35. Tokmakov, I. V.; Alavi, S.; Thompson, D. L. *J. Phys. Chem. A* **2006***, 110*, 2759-2770

36. Boiocchi, M.; Boca, L. D.; Esteban-Gómez, D.; Fabbrizzi, L.; Licchelli, M.; Monzani, E. *Chem. Eur. J.* **2005**, *11*, 3097-3104
37. Amendola, V.; Esteban-Gómez, D. Fabbrizzi, L.; Licchelli, M. *Acc. Chem. Res.* **2006,** *39,* 343-353
38. Franklin, E. C.; Stafford, O. F. *Am. Chem. J*. **1902**, *28*, 83
39. Jacobson, R. A. *J. Am. Chem. Soc.* **1936***, 58,* 1984-1986
40. Coumbarides, G. S.; Eames, J.; Suggate, M. J.; Weerasooriya, N. *J Label Compd Radiopharm* **2006**, *49,* 641-652.
41. Sawinski, H.; Dronskowski, R. *Z. Naturforsch.* **2014**, *69b*, 651-654
42. Sawinski, H.; Dronskowski, R. *Z. Anorg. Allg. Chem.* **2014**, *640,* 846-850
43. Estiu, G.; Merz, Jr. K. M. *J. Am. Chem. Soc.* **2004***, 126*, 6932-6944
44. Benini, S.; Rypniewski, W. R.; Wilson, K. S.; Miletti, S.; Cirurli, S.; Mangani, S. *Structure* **1999***, 7,* 205-216
45. Karplus, P. A.; Pearson, M. A. *Acc. Chem. Res*. **1997,** *30*, 330-337
46. Kaminskaia NV, Kostic NM (1997) Inorg Chem 36:5917–5926
47. Wang J, Li Q, Dong W, Kang M, Wang X, Peng S (2004) Appl Catal A-Gen 261:191–197
48. Shivarkar AB, Gupte SP, Chaudhari RVJ (2004) Mol Catal A-Chem 223:85–92
49. Brack, W.; Heine, B.; Birkhold, F.; Lruse, M.; Schoch, G.; Tischer, S.; Deutschmann, O. *Chemical Engineering Science* **2014**, *106*, 1–8
50. Schaber, P. M.; Colson, J.; Higgins, S.; Thielen, D.; Anspach, B.; Brauer, J. *Thermochimica Acta* **2004**, *424*, 131-142
51. Lundström, A.; Waldheim, B.; Ström, H.; Westerberg, B. *J. Automobile Engineering* **2011***, 225*, 1392-1398
52. Liu, J.; Zhang, T.; Wang, Z.; Dawson, G.; Chen, W. *J. Mater. Chem.* **2011**, *21*, 14398-14401
53. Xu, J.; Li, Y.; Peng, S.; Lu, G.; Li, S. *Phys.Chem. Chem. Phys.* **2013**, *15*, 7657-7655
54. Eichelbaum, M.; Farrauto, R. J.; Castaldi, M. J. *Applied Catalysis B: Environmental* **2010**, *97*, 90-97
55. Stradell, L.; Argentero, M. *Thermochimica Acta* **1993***, 219*, 315-323
56. Zamfirecu, C.; Dincer, I. *Int. J. Hydrogen Energy* **2011***, 36*, 11425-11432
57. Rollinson, A. N.; Rickett, G. L.; Lea-Langton, A.; Dupont, V.; Twigg, M. V. *Applied Catalysis B: Environmental* **2011**, *106,* 304-315
58. Wang, G.; Ling, Y.; Lu, X.; Wang, H.; Qian, F.; Tong, Y.; Li, Y. *Energy Environ. Sci.* **2012**, *5*, 8215-8129
59. Lan, R.; Tao, S.; Irvine, J. T. S. *Energy Environ. Sci.* **2010**, *3*, 438-441
60. Moury, R.; Moussa, G.; Demirci, U.; Hannauer, J.; Bernard, S.; Petit, E.; van der Lee, A.; Miele, P. *Chem. Chem. Phys.* **2012**, *14*, 1768-1777
61. Melling, R.; Wilburn, F. W.; McIntosh, R. M.; *Analytical Chem.* **1969***, 41*, 1275-1286
62. Chen, P.; Xiong, Z.; Luo, J.; Lin, J.; Tan, K. L. *Nature* **2002**, *420*, 302-304
63. Ferro, D.; Barone, G.; Della Gatta, D.; Piacente, V. *J. Chem. Thermodynamics* **1987**, *19*, 915-923
64. Wang, X.; Andrews, L. *J. Phys. Chem. A.* **2007***, 111*, 6008-6019
65. Moreno, M. A.; Maté, B.; Rodriguez-Lazcao, Y.; Gálvez, O.; Gómez, P. C., Herrero, V. J.; Escribano, R. *J. Phys. Chem. A* **2013**, *117*, 9564-9573
66. Waddington, T. C. *J. Chem. Soc.* **1959**, 2499-2502
67. Hennings, E.; Schmidt, H.; Voigt, W. *Z. Anorg. Allg. Chem.* **2011**, *637*, 1199-1202
68. Miyaoka, H.; Tange, K.; Yamamoto, H.; Hino, S.; Ichikawa, T.; Kojima, Y. *Int. J. Hydrogen Energy* **2015***, 40*, 14911-14915
69. Hu, Y. H.; Ruckenstein, E. *J. Phys. Chem. A* **2003**, *107*, 9737-9739
70. David, W. I. F.; Jones, M. O.; Gregory, D. H.; Jewell, C. M.; Johnson, S. R.; Walton, A.; Edwards, P. P. *J. Am. Chem. Soc.* **2007**, *129*, 1594-1601

71. Choudhary, T. V.; sivadinarayana, C,l Goodman, D. W. *Catalysis Letters* **2001**, *72,* 197-201
72. Metkemeije, R.; Achard, P. *J. Power Sources* **1994***, 49*, 271-282
73. Liu, L.; Hu, D.; He, T.; Zhang, Y.; Wu, G.; Chu, H.; Wang, P.; Xiong, Z.; Chen, P. *J. Alloy. Compounds* **2013**, *552*, 98-101
74. Vyazovkin, S.; Burnham, A. K.; Criado, J. M.; Pérez-Maqueda, L. A.; Popescu, C.; Sbirrazzuoli, N. *Thermochimica Acta* **2011**, *520*, 1-19
75. Cao, H.; Wang, H.; He, T.; Wu, G.; Xiong, Z.; Qiu, J.; Chen, P. *RSC Adv.* **2014**, *4*, 32555-32561
76. Hetherington, H. C.; Braham, J. M. *J. Am. Chem. Soc.* **1923***, 45*, 824-829

5.0 Dehydrogenation between LiH and dicyandiamide

5.1 Introduction

The final chapter of this thesis will discuss the preliminary investigation of the solid state dehydrogenation reaction between LiH and dicyandiamide ($H_4N_4C_2$) according to the equation:

$$4\ LiH + H_4N_4C_2 \rightarrow 2\ Li_2NCN + 4\ H_2 \qquad \Delta H^o_r = -335.18\ kJ\ mol^{-1} \quad (5\text{-}1)$$

The proposed 4LiH : $H_4N_4C_2$ system has a theoretical gravimetric hydrogen capacity of 6.98 wt%. Due to the presence of protic ligands in dicyandiamide, the system is expected to release hydrogen driven by, at least in the first stages of dehydrogenation, the $N\text{-}H^{\delta+}\ldots{}^{\delta-}HLi$ interaction as demonstrated by the melamine and urea systems reported in this thesis. In principle this system can be rehydrogenated using the same method reported in chapter 3.5; through the hydrolysis of Li_2NCN while controlling the pH of the solution between 6 and 9 at room temperature.[1-2]

5.1.1 Properties of dicyadiamide

Otherwise known as 2-cyanoguanidine, dicyandiamide is a colourless solid with a neutral pH (figure 5-1).[3-4] It is a zwitterionic compound with an electronegative cyano group and two electron-donating primary amine groups (charge of -0.29 and 0.1 eV respectively[5]). Ergo the molecule is widely applied in coordination chemistry research as it acts both as a monodentate ligand which donates electrons strongly towards a variety of metal centres (Mg, Al, Cr, Fe, Co, Ni, Cu, Zn, Mo, Pd, Cd, Pt, Hg, Pb) *via* the terminal nitrogen on the cyano- group, and as a bidentate ligand when the guanidine amino groups are also involved in the coordination.[6] Commercially it is produced as a fertiliser and curing agent in resins.[7]

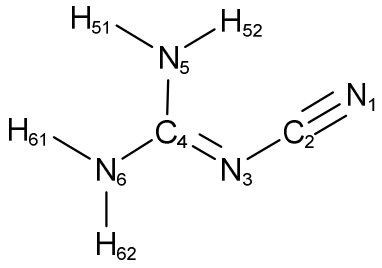

Figure 5-1. The molecular structure of dicyandiamide

Hughes determined the structure of the compound by X-ray diffraction using Cu and Mo Kα X-ray sources. Dicyandiamide crystallises in monoclinic space group $C12/c_1$ containing eight molecules of dicyandiamide per unit cell, with unit cell parameters of a = 15.0(0) Å, b = 4.44 Å, c= 13.12 Å and β = 115.2° (figure 5-2).[8] All the atoms in the unit cell occupy general 8*f* positions.[9] Single crystal

neutron diffraction confirmed the extensive network of hydrogen bonding using deuterated dicyandiamide with a shortest distance between the cyano terminal nitrogen and guanidine amino deuterium found to be 2.02 Å.[9] A total of 4 amino hydrogens was reported to participate in 5 hydrogen bonds, where bifurcated hydrogen bonding was found with one of the hydrogens on N5 while the other hydrogen participates in a normal hydrogen bond.[8] The amino group (N5) is rotated out of the plane from the guanidine skeleton while the amino group (N6) lies in plane. All three of the trigonal hybridized C-N bonds in the guanidine residue have double bond characteristics however the contributions are not equal from the two amino nitrogens due to the N5 rotation. It was found that the π-electrons are delocalised not only in the guanidine moiety but over the six-atom skeleton as the cyanimino group was proposed to resonate between the triple bond (25%) and double bond (75%) structures (figure 5-3) due to hydrogen bonding from the terminal nitrogen to neighbouring guanidine amino moieties.[8] Moreover the terminal nitrogen has an asymmetric electron cloud associated with the lone pair electrons.[9] This was further confirmed by full electron charge density mapping using X-ray diffraction data.[5] The cyano residue is found to tilt away from the guanidine molecular plane slightly, by 3° for the C2-N3 bond and a further 5° for the C2-N1 bond.[5, 8] Overall, dicyandiamide in the solid state is stabilised by the resonances structures in figure 5-3 and the extensive network of hydrogen bonding to result in a relatively high melting point of 209.5 °C. Thermolysis of dicyandiamide follows scheme 3-1 to form melamine approximately 20 °C after melting, releasing ammonia gas in the process; it otherwise forms cyanamide at 130 °C under ammonia pressure.[10]

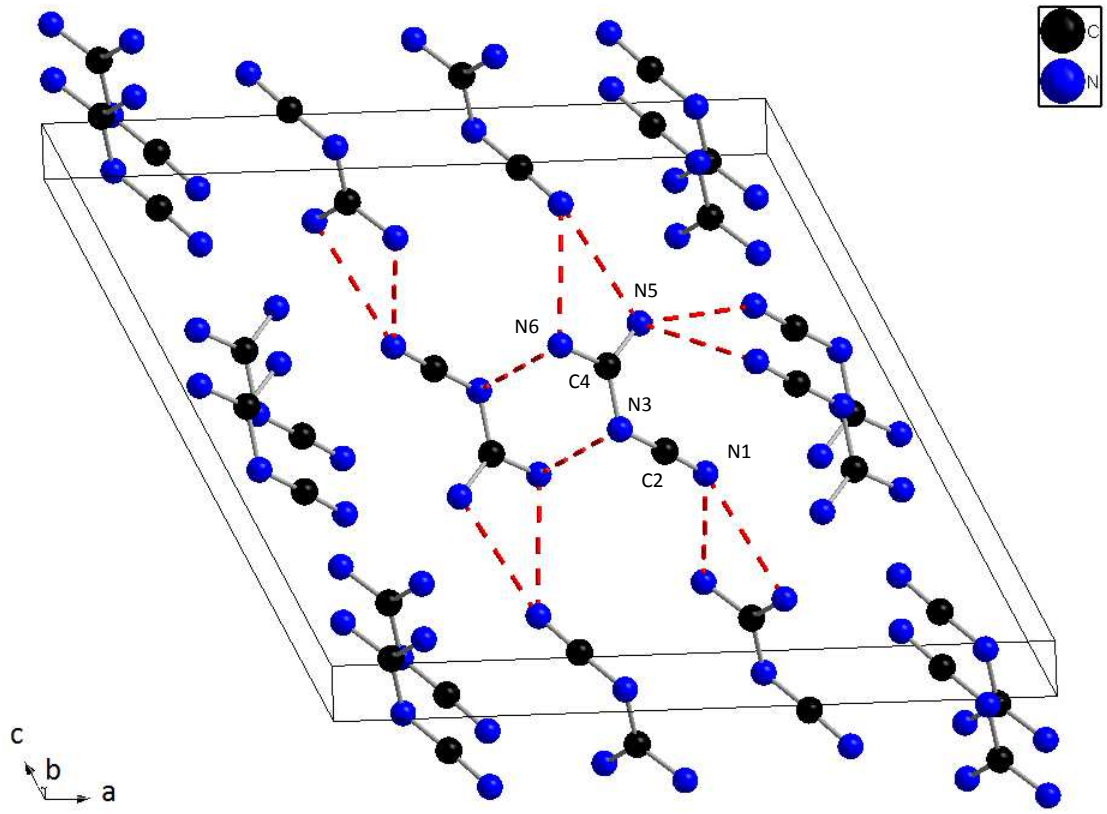

Figure 5-2. Crystal structure of dicyandiamide, red dash line showing hydrogen bond

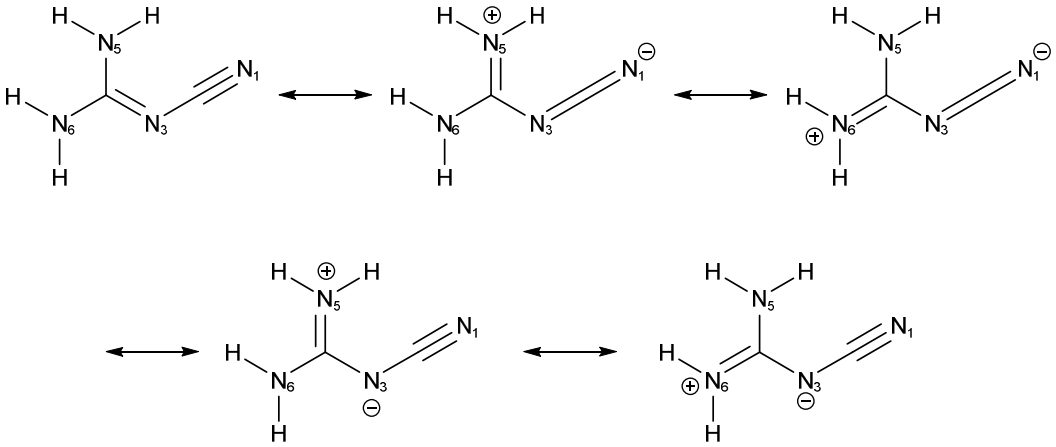

Figure 5-3. Resonances of dicyandiamide[5, 8]

Dicyandiamide has a stable tautomer, cyanoamine (figure 5-4 (a)) and several isomers, of which ammonium dicyanamide (figure 5-4 (b)) is the most important as it undergoes a solid state transition at *ca.* 120 °C to form dicyandiamide.[11-12] The presence of the amino tautomer has been the subject of much debate in the literature, primarily due to conflicting evidence between diffraction and spectroscopy data, especially on the assignment of the bands between 2100 and 2250 cm^{-1}. Whilst there is no evidence of the tautomeric cyanoamine form by diffraction, Sheludyakova *et al.* have published a series of FTIR and Raman investigations and theoretical

calculations to propose that the two tautomers co-exist in the solid state by observation of a doublet at *ca.* 2200 cm^{-1} approximately 45 cm^{-1} apart.[13] Alia *et al.* reported the observation of both imino and amino tautomers in aprotic solutions with DMF, DMSO and HMPA. It appears that with increasing solvent polarity the imino tautomer band signal increases.[14] On the other hand, the pH of dicyandiamide and theoretical calculations based on the stability of the isomers all point to a predominant presence of the cyanoimine tautomer.[3, 15]

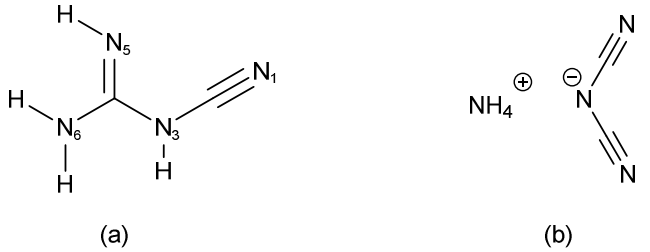

Figure 5-4. Molecular structure of (a) the cyanoamine tautomer of dicyandiamide and (b) the ammonium dicyanamide isomer

5.1.2 Guanidine in hydrogen storage

The guanidine residue has been paired with borohydride moieties to form a new class of B-N hydrogen storage material. One of the first examples is guanidinium borohydride (GBH, $[C(NH_2)_3]^+[BH_4]^-$) which has a theoretical hydrogen capacity of 10.8 wt%. This compound, however suffers from an imbalanced $N\text{-}H^{\delta+}\ldots{}^{\delta-}H\text{-}B$ redox pair which leads to the unfavourable release of ammonia during dehydrogenation up to 450 °C.[16] Various modifications to the original GBH by addition of light metal additives (Li, Na, Mg, Ca[17-19]) and conjugate pair substitution (methyl guandinium ion[20] and octahydrotriborate[21]) have been reported to reduce dehydrogenation to between 75 and 400 °C with a variety of hydrogen purities. Again the main product gas contaminant is ammonia which was attributed to the imbalanced $N\text{-}H^{\delta+}\ldots{}^{\delta-}H\text{-}B$ redox pairing. To date, rehydrogenation of GBH based B-N hydrogen storage material has never been reported presumably due to the stability of the B-N bonds in the reaction products.

The proposed system in equation (5-1) is the first instance of the direct use of dicyandiamide as a hydrogen storage material. The sections below describe the dehydrogenation reaction between LiH and dicyandiamide *via* a variety of mechanical preparations. Through the results discussed in this chapter it can be confirmed that hydrogen can be released from the combination of LiH with dicyandiamide, by analogy to other hydride-amine systems, quantity and purity of the related hydrogen is substantially related to the mechanical preparations involved.

5.2 Experimental

Commercially available LiH (95% pure) was sourced from Sigma Aldrich, whilst dicyandiamide (99%) was purchased from Alfa Aesar.

Standard procedures described for ball milling in chapter 2.2.1 was applied for the experiments in this chapter unless otherwise stated. The list of samples discussed in the results section is compiled in table 5-1 in terms of the milling conditions applied.

Table 5-1. Samples used to investigate the dehydrogenation reaction between 4 LiH and $H_4N_4C_2$

Sample	RPM	Ball : powder	Milling time	Programme	Balls used
D-01	150	30:1	36 min	5 min, rest 1 min	10
D-02	450	30:1	12 h	5 min, rest 1 min	10
D-03	450	30:1	6 h	5 min, rest 1 min	10
D-04	450	30:1	4 h	5 min, rest 1 min	10
D-05	450	30:1	3 h	5 min, rest 1 min	10
D-06	450	30:1	1 h	5 min, rest 1 min	10
D-07	400	30:1	6 h	5 min, rest 5 min	10
D-08	450	20:1	6 h	5 min, rest 5 min	10
D-09	450	15:1	6 h	5 min, rest 5 min	10

5.3 Results and discussion

It was reviewed in chapter 1 and demonstrated by the results discussed in chapters 3 and 4 that ball milling is a reproducible means to improve material contact, reduce particle size and in some cases alter the reaction pathway to facilitate solid state dehydrogenation. It was the purpose of this preliminary investigation of the interaction between LiH and dicyandiamide to devise an appropriate preparation that would facilitate hydrogen desorption by subsequent heating.

First, the interaction between intimately mixed LiH and dicyandiamide was examined. 4 equivalents of LiH were mixed with dicyandiamide (**D-01**) in a 50 ml stainless steel jar with ten 10 mm stainless steel balls. The mixture was milled at 150 RPM for 36 mins in a ball to powder ratio of 30:1 and a milling programme of 5 mins mill and 1 min rest. The PXD pattern of the **D-01** mixture (figure 5-5) resembles the starting materials, which when refined *via* the Rietveld method using GSAS yielded only LiH and dicyandiamide (monoclinic space group $C12/c_1$, a= 14.97(3) Å, b= 4.49(4) Å, c= 13.10(8) Å and β=115.3(8) Å). The resulting cell parameters and atomic bond angle and distances are presented in tables 5-2 and 5-3 which showed slight discrepancy those reported in literature. This

is likely an effect of the ball milling preparation which could disrupt the long range order of the samples involved hence a worsen signal to noise ratio. A shifted Chebyschev polynominal background function was adopted.

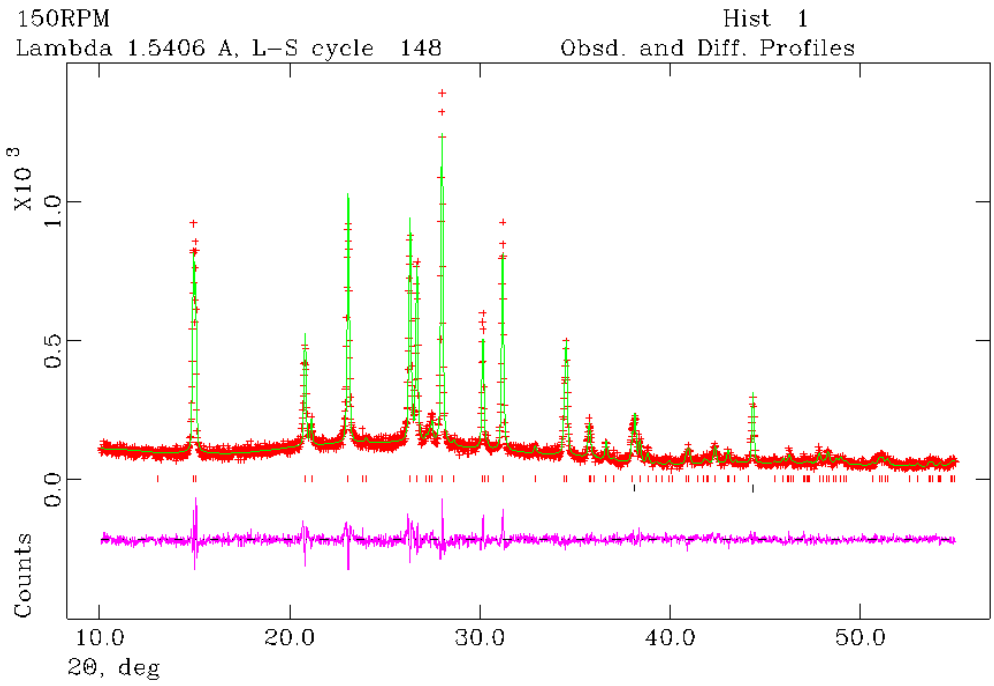

Figure 5-5. Profile plot from the Rietveld refinement against PXD data for of sample **D-01**. Red data points are the experimental profile, green profile is the calculated magenta profile is the difference plot.

Table 5-2. Refinement data for sample **D-01**

	LiH	**$H_4N_4C_2$**
Crystal system	Cubic	Monoclinic
Space group	$Fm\bar{3}m$	C12/c1
Z	4	8
a / Å	4.082(0)	14.972(9)
b		4.493(8)
c		13.107(6)
V / Å^3	68.01(8)	668.85(3)
Formula mass, g mol^{-1}	7.949	84.08
Calculated density / g cm^{-3}	0.82	1.405
weight fraction	0.203(5)	0.796(5)
Number of observations	2718	
Number of variables	37	
R_p / %	8.85	
R_{wp} / %	5.7	
X^2	1.677	

Table 5-3. Selected bond angle and distances of the $H_4N_4C_2$ phase in sample **D-01**

Refinement results		Literature values / Å	
Bond distance / Å		X-ray	Neutron
N1-C2	1.204(1)	1.19(2)	1.15(1)
N3-C2	1.435(1)	1.29(2)	1.29(9)
N3-C4	1.494(8)	1.33(0)	1.33(1)
N5-C4	1.481(9)	1.33(5)	1.30(5)
N6-C4	1.313(1)	-	-
Bond angle / °		X-ray	Neutron
N1-C2-N3	165.1(1)	180	175
N3-C4-N5	114.0(8)	123	124
N3-C4-N6	120.0(9)	117	118
N5-C4-N6	126.0(9)		
C2-N3-C4	115.7(8)	119	119

Sample **D-01** was heated to 400 °C in the STA at 5 °C min^{-1} under He purge which produced the TGA, DTA and MS profiles with two main steps at 150.3 °C and 279.5 °C and yielded an overall mass loss of *ca.* 16.3% (Figure 5-6). From the TGA and MS profiles, it is possible to identify that the mass loss corresponds to hydrogen release, however it is evident that the total mass loss is much higher than the system H_2 content of 6.98 wt%. Moreover, it was not possible to identify the solid products after decomposition as the sample appeared to melt onto the alumina pan during heating and could not be retrieved. Despite the lack of product characterisation some inferences could be made since the resulting TG/DTA profiles resemble closely the behaviour indicative of the direct thermolysis of H_2NCN to form dicyandiamide and melamine (Appendix G).

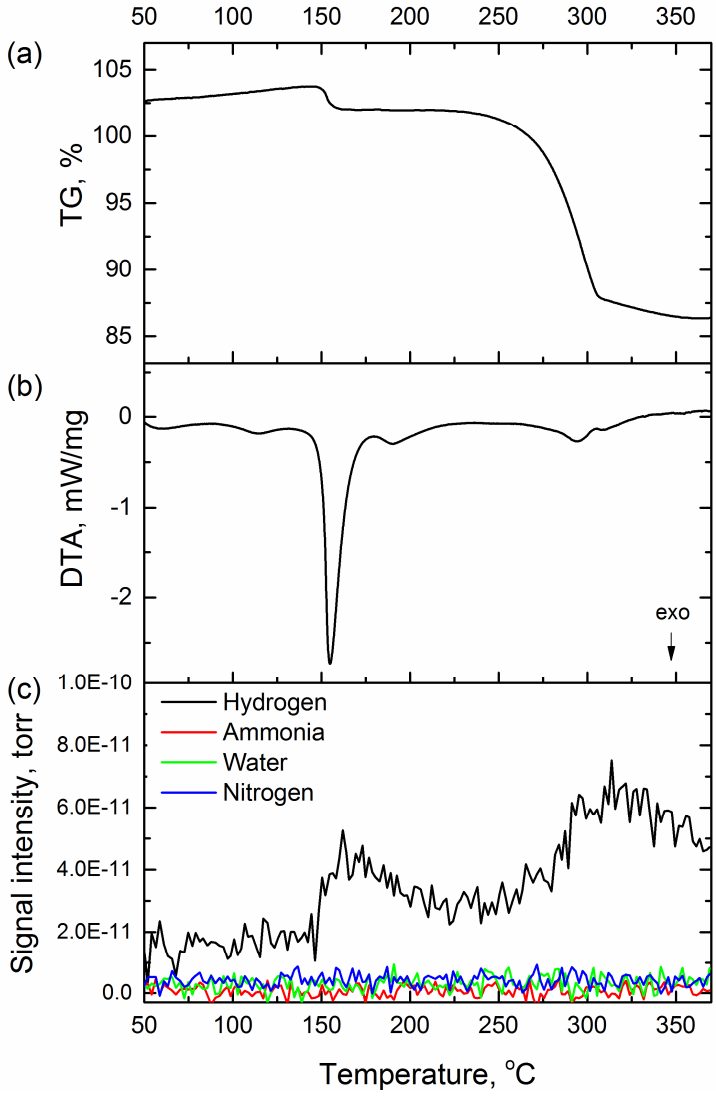

Figure 5-6. (a) TG, (b) DTA and (c) MS profiles of **D-01**

At the other extreme, a prolonged high energy ball milling experiment was carried out using the pressure monitoring GrindControl apparatus in a larger 250 ml jar at a speed of 450 RPM with ten 10 mm balls and a 30:1 ball to powder ratio for 12 h (5 min, rest 5 min programme, sample **D-02**). The resulting plot of pressure increase against time reveals that the 4 LiH : dicyandiamide system is sensitive to the level of mechanical treatment (Figure 5-7). A gradual pressure increase of approximately 9 kPa h^{-1} was observed during the first eight hours of milling, at which point a sudden pressure increase was detected which peaked at just over 900 kPa. As the apparatus has a built in over pressure vent with a threshold of 500 kPa the excess pressure was released. The product of the milling experiment was identified by PXD as lithium cyanamide, Li_2NCN and an unidentified phase with three broad reflections centred at 29.7, 36.3 and 51.6° 2Θ (Figure 5-8). The internal temperature of the jar remained approximately constant throughout the experiment, although one would expect that the local temperature at the powder-ball interface could be higher.

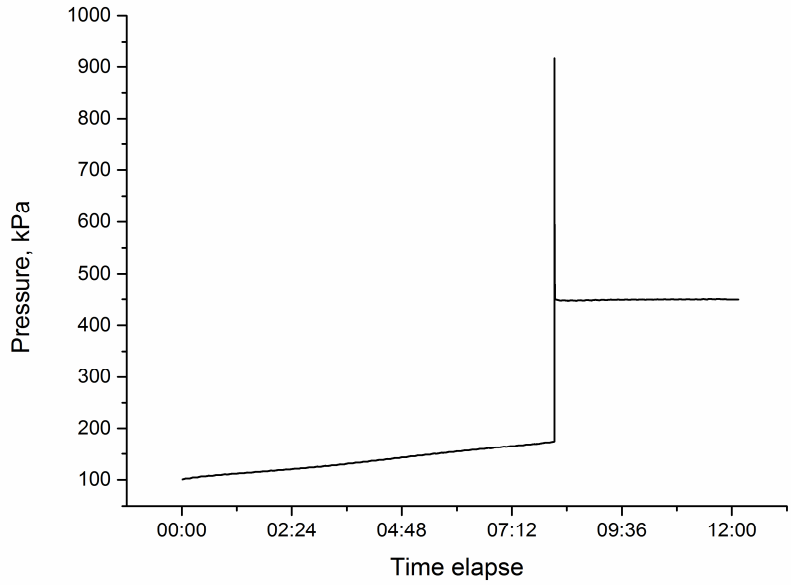

Figure 5-7. Pressure monitored ball milling experiment for sample **D-02**

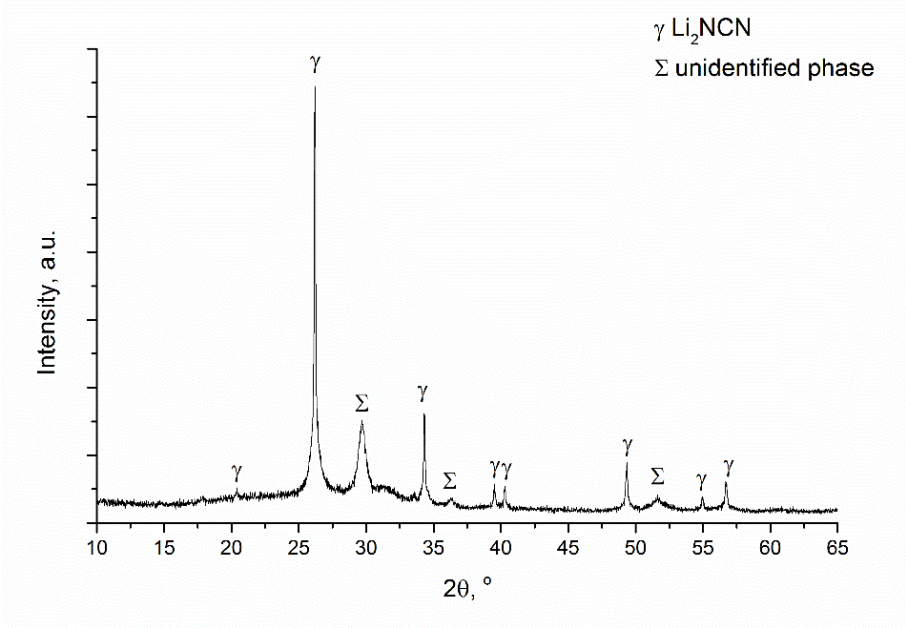

Figure 5-8. PXD pattern of sample **D-02** after milling

To investigate the milled sample up to the point of the sharp hydrogen release shown in figure 5-7, a sample of the same 4:1 ratio of LiH : dicyandiamide was milled using similar conditions to **D-02** in a smaller 50 ml jar (**D-03**, 450 RPM, 30:1, 10 10 ml balls, 5 min, rest 5 min, 6 h). The PXD pattern of this milled sample revealed the presence of product Li_2NCN which indicates that hydrogen has already been released prior to heating (figure 5-9). Indeed, when **D-03** is heated to 400 °C only a 3% mass loss was recorded, corresponding to remaining hydrogen release (figure 5-10 (a, profile (i))). This suggests that over half of the available hydrogen (6.98 wt%) has already been released. A similar thermal response was recorded for the 4 h and 3 h milled samples (**D-04** and **D-05**) with

reduced cooling time (figure 5-10 (ii) and (iii)). On further reduction in the milling time to 1 h (sample **D-06**), the decomposition profile changes (figure 5-11), where a total of 10.6 wt% was lost over several steps releasing hydrogen. Beyond 350 °C, trace amounts of ammonia evolution was observed (figure 5-11 (c, insert)). Hydrogen release was accompanied by four sharp and one broad exothermic DTA signals. This broad DTA signal itself appears to be constituted of several exothermic events. The reaction product at 400 °C consists of Li_2NCN and trace amounts of LiCN by PXD (figure (5-12 (g)). To investigate the mechanism of hydrogen release further, phases at intermediate reaction stages were examined using PXD (Figure 5-12) and FTIR (Figures 5-13 and 5-14). Data were taken from samples heated to five intermediate temperatures, 120 °C, 155 °C, 210 °C, 270 °C and 350 °C.

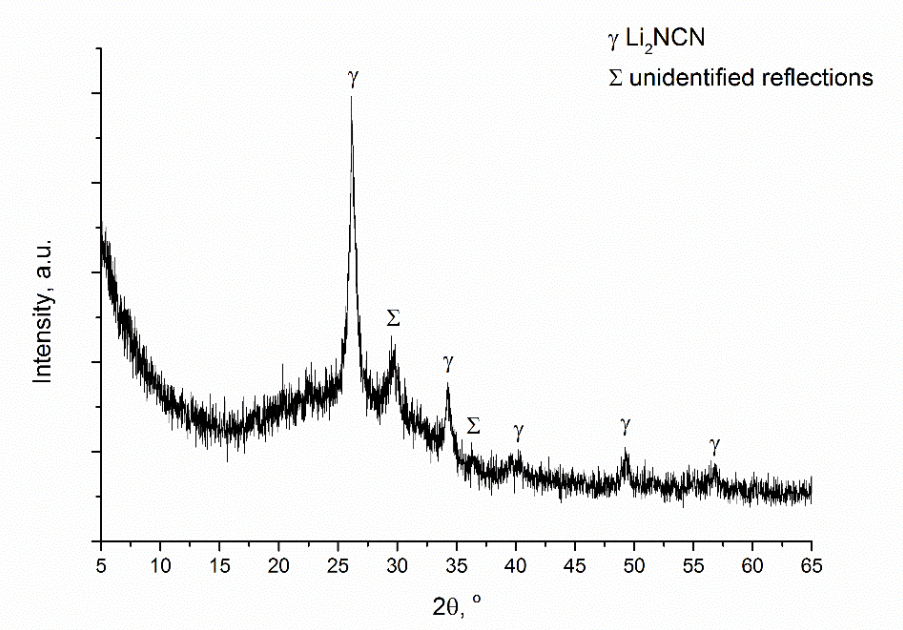

Figure 5-9. PXD of sample **D-03** after milling

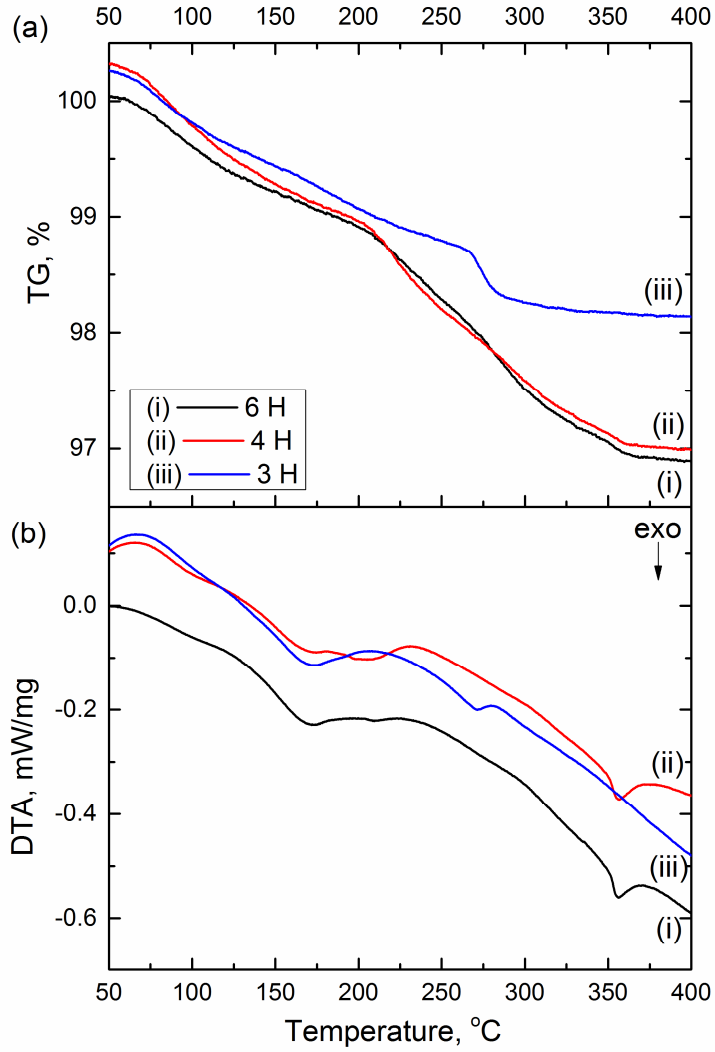

Figure 5-10. (a) TG and (d) DTA profiles of 4LiH : $H_4N_4C_2$ ball milled at 450 RPM for (i) 6 h (**D-03**), (ii) 4 h (**D-04**) and (iii) 3 h (**D-05**).

The PXD pattern of sample **D-06** after milling (figure 5-12 (a)) contains features different to that of **D-01**. Instead of a narrow peak shape the reflections are broadened significantly which is characteristic of the more energetic mechanical treatment of the sample. Ball milling under these conditions would be expected to reduce particle size and introduce defects that disrupt the long range order of the crystallites. An amorphous component is indicated by high background signals between 15 - 35° 2Θ. When **D-06** is heated to 120 °C, corresponding to a mass loss of *ca*. 1% and hydrogen evolution as detected by MS (figure 5-11 (c)), the diffraction pattern in figure 5-12 (b) shows an improved signal to noise ratio compared to (a). It consists of better defined narrow peaks for LiH and dicyandiamide, however a new reflection centred around 28.3° 2Θ can be identified as a shoulder to the most intense peak belonging to the dicyandiamide (310) reflection at 27.94° 2Θ. By 155 °C approximately 1.3% of mass is lost coinciding with hydrogen evolution as detected by MS.

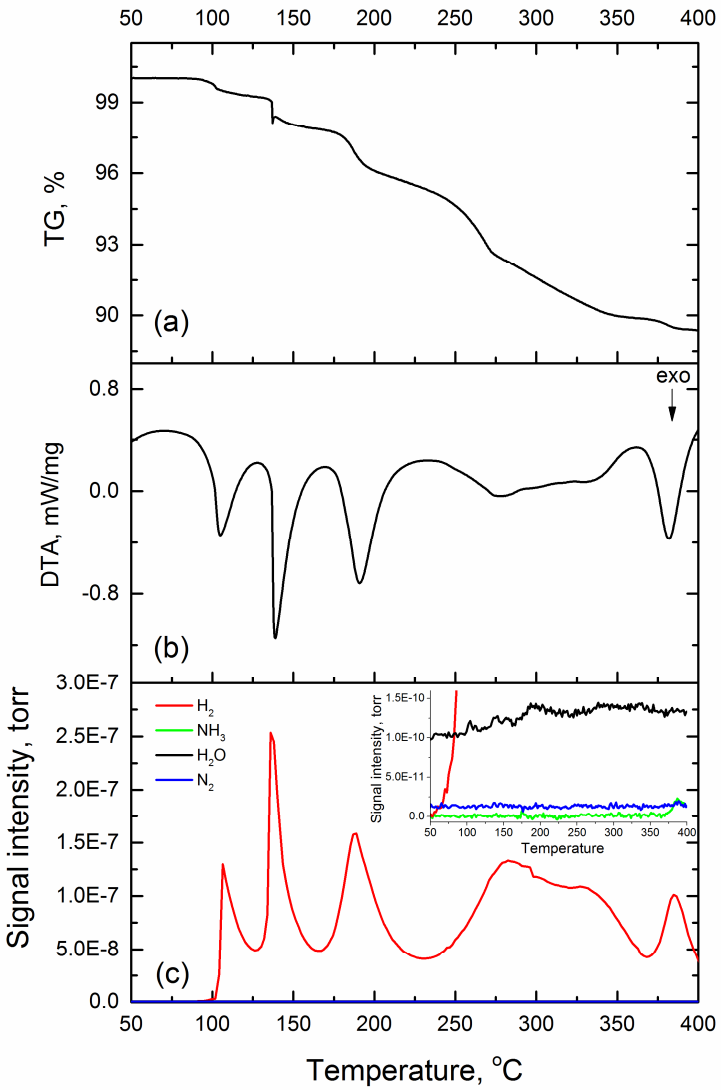

Figure 5-11. (a) TG, (b) DTA and (c) MS spectrum of sample **D-06**.

The corresponding diffraction pattern in figure 5-12 (c) bears little resemblance to the milled material before heating. The dicyandiamide (111) peak at 23° 2Θ has diminished dramatically. Four new peaks at 16.9, 17.67, 21.6 and 22° 2Θ appeared as the peak at 28.3° 2Θ intensified. Further heating to 210 °C resulted in further dehydrogenation and a 2.4% mass loss. According to the diffraction pattern, the sample at this temperature is composed mainly of Li_2NCN, LiH and some minor unidentified reflections present between 15 - 35° 2Θ. This is followed by two equal mass loss steps of 2.94 wt% each between 210, 270 and 350 °C coinciding with two overlapping H_2 peaks in the MS. As the sample is heated to these temperatures the Li_2NCN reflections become more narrow and intense, while the lesser unassigned reflections diminish and disappear (Figure 5-12 (e) and (f)). Finally, at 400 °C Li_2NCN and LiCN can be observed and LiH is no longer discernible in the diffraction pattern (Figure 5-12 (g)).

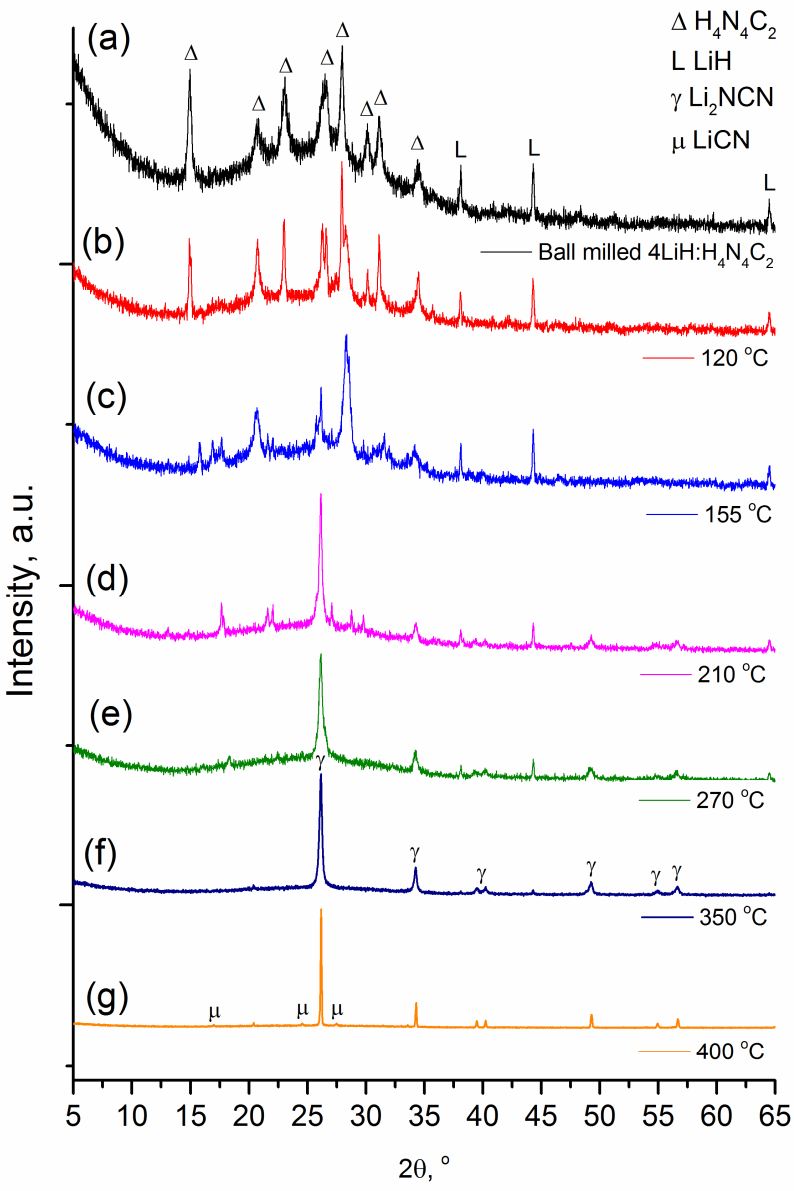

Figure 5-12. PXD patterns of (a) sample **D-06**, **D-06** heated to (b) 120 °C, (c) 155 °C, (d) 210 °C, (e) 270 °C, (f) 350 °C and (g) 400 °C

There is evidence of other phases at intermediate temperatures from the PXD patterns in figure 5-12, however the observed peaks cannot be matched to any pre-existing reference patterns (including that of the lithium dicyandiamide salt, for example), and due the overlaps with the reactant dicyandiamide reflections it has not been possible to identify the cells or crystal systems for these phases. FTIR has provided bonding information pertaining to the sample at each temperature which alludes to ring formation from dicyandiamide during dehydrogenation.

The corresponding FTIR spectra are split and presented in figure 5-13 (up to 2200 cm^{-1}), 5-14 (3700 to 2300 cm^{-1}) and the abruption bands summarised in table 5-2. The spectrum of the as-received dicyandiamide in figures 5-13 (a) and 5-14 (a) matches closely with those reported and assigned by Jones *et al.*[22] It consists of intermolecular NH_2 modes between 3300 and 3100 cm^{-1}, the cyano residue vibrations in the 2200 cm^{-1} and 1250 cm^{-1} regions and the guanidine residue vibrations in

the 1500 cm^{-1} region and at 928 and 719 cm^{-1}. The ball milled sample in figures 5-13 and 14 (b) has comparable features and characteristic LiH vibrations between 1200 cm^{-1} and 600 cm^{-1}. When the sample is heated to 120 °C a strong absorption band at 1421 cm^{-1} with a shoulder at 1443 cm^{-1} can be identified. Further heating to 155 °C sees these bands intensify in the 1400 cm^{-1} region and a band at 811 cm^{-1} can be identified. Absorption bands around 810 cm^{-1} are typically assigned to ring bending which suggests that ring formation has occurred. The bands in the 1400 cm^{-1} region can thus be assigned to the ring-N stretching vibrations similar to those found in the natural condensation product of dicyandiamide, that is melamine.[23-25] The intermolecular NH_2 modes decrease in intensity with an increase in temperature.

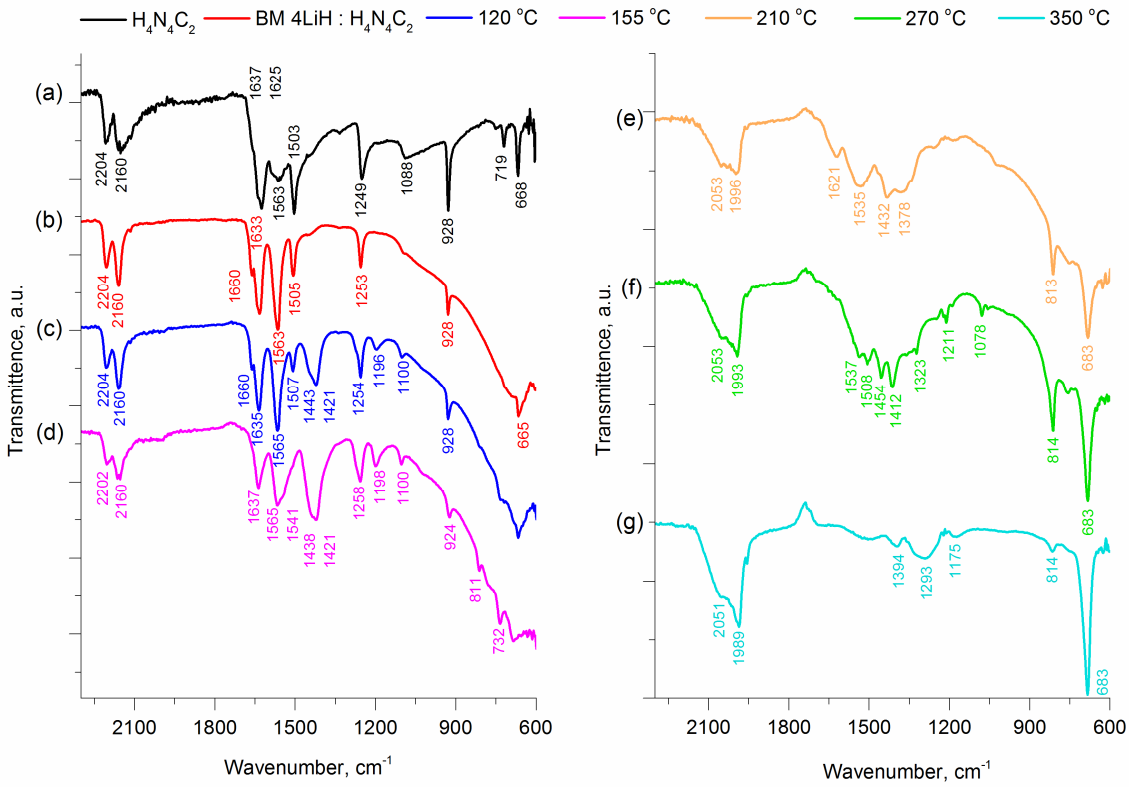

Figure 5-13. FTIR spectra between 2300 and 600 cm^{-1} of (a) commercial $H_4N_4C_2$, (b) sample **D-06**, **D-06** heated to (c) 120 °C, (d) 155 °C, (e) 210 °C, (f) 270 °C and (g) 350 °C

By 210 °C it is no longer possible to observe any bands relevant to the dicyandiamide skeleton as the two 2200 cm^{-1} region absorption bands are replaced with intense N=C=N bands from Li_2NCN. This is consistent with the observations from PXD analysis. Ring bending and Ring-N stretching modes persist until 350 °C as dehydrogenation proceeds. The final hydrogen and trace amount of ammonia detected on the MS above 350 °C is likely a result of NH_2 group remnant in sample **D-06** as manifested by the weak band at 3255 cm^{-1} in Figure 5-14 (g).

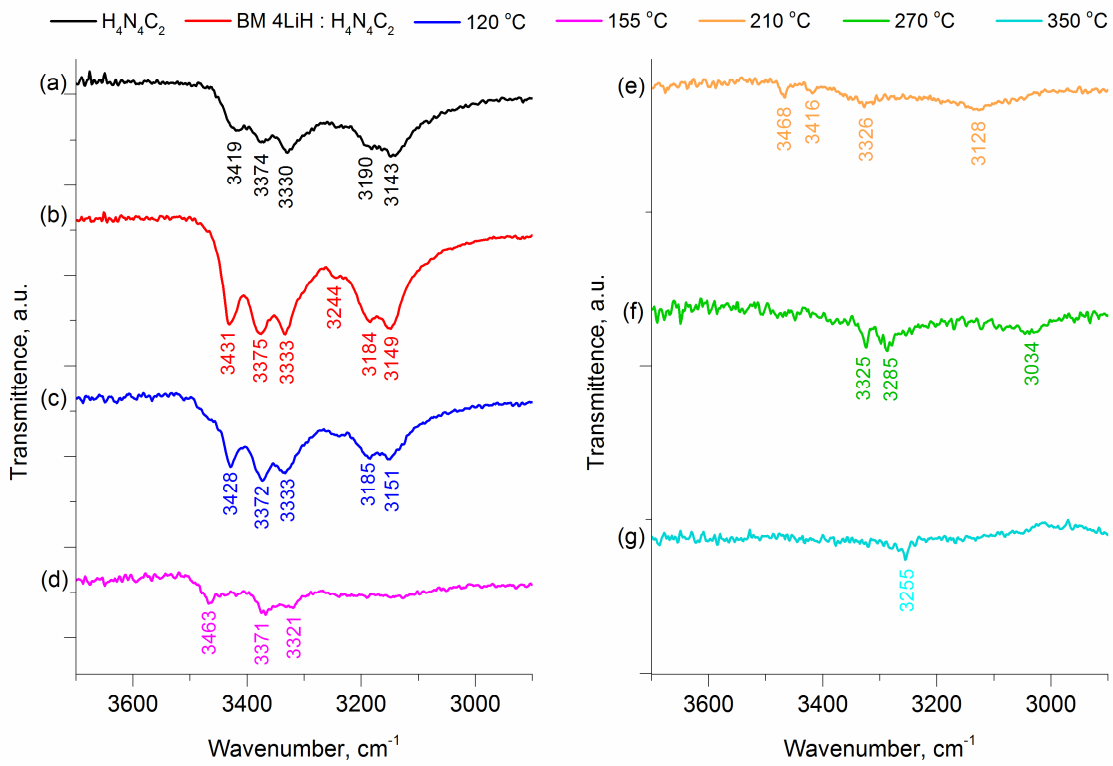

Figure 5-14. FTIR spectra between 3700 and 2300 cm^{-1} of (a) commercial $H_4N_4C_2$, (b) sample **D-06**, **D-06** heated to (c) 120 °C, (d) 155 °C, (e) 210 °C, (f) 270 °C and (g) 350 °C

It can be proposed that ball milling LiH with dicyandiamide in a 4:1 ratio at 450 RPM for 1 h has facilitated a change in the reaction path between the two reactants such that dehydrogenation of the system proceeded alongside ring formation of dicyandiamide. In contrast to pristine dicyandiamide, the observed ring formation in the presence of LiH occurred without melting. The subsequent breakdown of the ring into Li_2NCN implied by STA, PXD and FTIR analysis is dissimilar to that observed in the LiH:melamine system described in chapter 3. One would expect the dehydrogenation process with LiH for dicyandiamide to be similar to that of urea as the two molecules have similar geometry, resonance structure, neutrality and are capable hydrogen bond donors and acceptors. On the contrary, the dehydrogenation of LiH:dicyandiamide proceeds without much ammonia release, unlike that observed in the LiH:urea system in chapter 4. Rather than forming a metal salt such as lithium ureate, the dicyandiamide skeleton oligomerised upon dehydrogenation. This appears to mitigate the formation of ammonia. It has not been possible yet to rationalise fully the excess mass loss during heating of the system as ammonia was only observed in the final step between 350 - 400 °C with a mass loss of 0.5 wt%. No other gases were observed.

Table 5-4. FTIR bands (in cm^{-1}) and assignments of dicyandiamide, sample **D-06** and **D-06** heated to 120, 155, 210, 270 and 350 °C

Literature[22]		**Experimental spectra for D-06**							
$H_2N_4C_2$	**Assignment**	**$H_4N_4C_2$**	**Milled only**	**120 °C**	**155 °C**	**210 °C**	**270 °C**	**350 °C**	**Assignment**
3401 (m, sh)		3419	3431	3428	3463	3468	3325		
3365 (s)	$v_a(NH_2)$	3374	3375	3372	3371	3416	3285	3255	
3323 (s)		3330	3333	3333	3321	3326	3032		
3170 (s)	$v_s(NH_2)$	3190	3184	3185					
3147 (s)		3142	3149	3151		3128			
2203 (s)	v_a(N1C2N3)	2204	2204	2204	2202				
2163 (s)		2160	2160	2160	2160				
						2053 (vs)	2053 (vs)	2051 (vs)	v(NCN)
						1996 (vs)	1993 (vs)	1989 (vs)	
1657 (sh)	$d(NH_2)$	1637	1660						
1639 (vs)		1625	1633	1635	1637	1621 (m)			
1587 (ms)	v_a(N5C4N6)	1563	1563	1565	1565		1537 (m)		
1502 (s)	v_s(N3C4N5)	1503	1505	1507	1541	1535 (s)	1508 (m)		
							1454 (s)		
				1443	1438	1432 (s)	1412 (s)	1394 (w)	v(ringC-N)
				1421	1421	1378 (s)	1323 (m)	1293 (m)	
1252 (m)	v_s(N1C2N3)	1249	1253	1254	1258				
				1196	1198		1211 (w)	1175 (vw)	
1081 (mw)	$\rho(NH_2)$	1088		1100	1100		1078 (w)		
928 (ms)	v_s(N3C4N5)	928	928	928	924				
						813 (s)	814 (s)	814 (vw)	ring bending
718 (w)	w(N5C4N6)	719							
						683 (vs)	683 (vs)	683 (vs)	v(NCN)
		668	665	665					

Finally, a fourth decomposition pathway was identified by considering further similar milling protocols:

1. 400 RPM, 6 h, 30:1 ball to powder ratio, 5 min mill 5 min rest (**D-07**)
2. 450 RPM, 6 h, 20:1 ball to powder ratio, 5 min mill 5 min rest (**D-08**)
3. 450 RPM, 6 h, 15:1 ball to powder ratio, 5 min mill 5 min rest (**D-09**)

The thermal response of these three samples is broadly similar (figure 5-15) and follows a dramatic mass loss with temperature which begins at 85, 87.3 and 91.2 °C for samples **D-07**, **D-08** and **D-09** respectively. The mass loss is accompanied by a large exotherm and the release of hydrogen, ammonia and water in the evolved gas MS (figure 5-15 (c)). The sample expanded and frothed during this step where some of the foamed solid materials were expelled from the reaction pan and found on the radiation shield of the STA instrument. This indicates that the mass loss recorded does not reflect the true change in mass as a consequence of gas desorption. Unlike the decomposition of hydrazine borane reported by Hügle *et al.*,[26] foaming of samples **D-07** to **D-09** was not preceded by the samples melting. A similar observation was made on the heating of intimately mixed 4 LiH and urea in chapter 4.3.1.

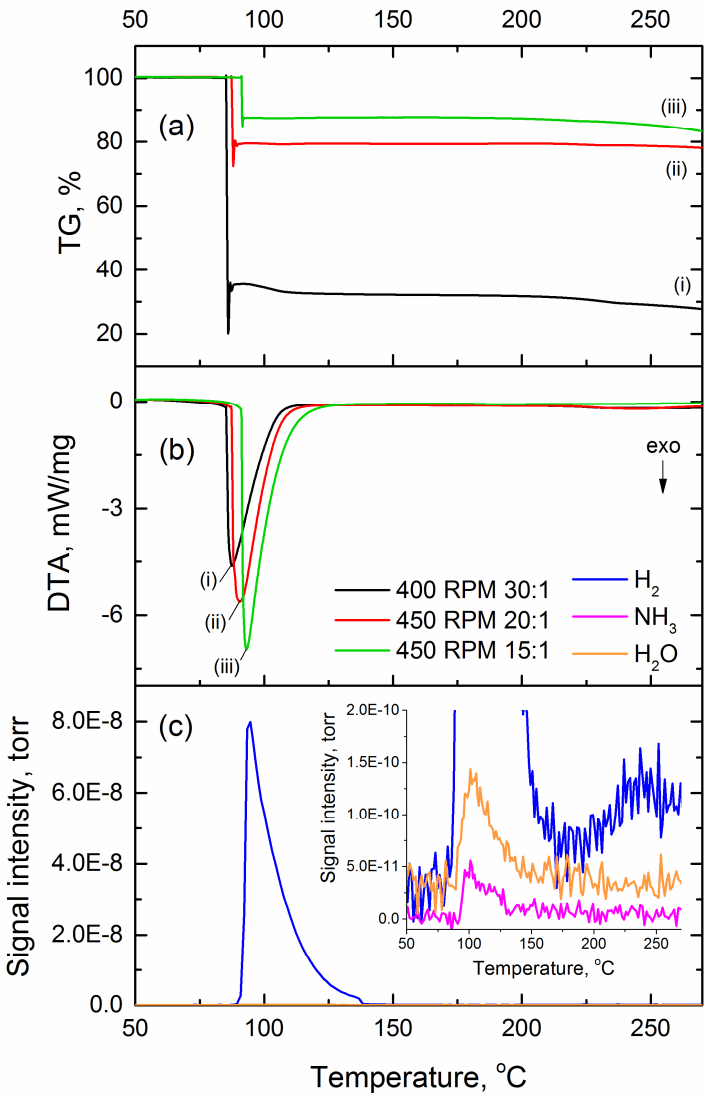

Figure 5-15. (a) TG profile of (i) **D-07**, (ii) **D-08** and (iii) **D-09** and their complementary DTA profiles (b). (c) shows the evolved gas MS from the thermolysis of sample **D-07** showing plots for m/z = 2 (blue), 16 (magenta) and 18 (orange).

PXD of the milled sample **D-07** (figure 5-16) revealed a new set of reflections (denoted by τ) in addition to the reactant dicyandiamide denoted by Δ. The other reactant LiH is not visible in the powder pattern of this sample. The new phase (or phases) τ, is likely to be a contributor to the rapid gas evolution observed during the thermolysis of these samples. Examination of the phases at 130 °C revealed that Li_2NCN has already formed after the initial reaction step. There was however several minor unidentified reflections (denoted as ϕ, figure 5-17) found at 33.58, 38.1, 44.3 and 56.3° 2Θ. These are different from the set of unidentified reflections identified during the thermolysis of **D-06**. Furthermore there is no notable amorphous content in the sample given the background in the diffraction pattern. It is possible that the unidentified phase(s) decompose(s) further when heating to 400 °C as the diffraction pattern contains relatively less intense ϕ reflections than those in the 130 °C pattern (figure 5-18).

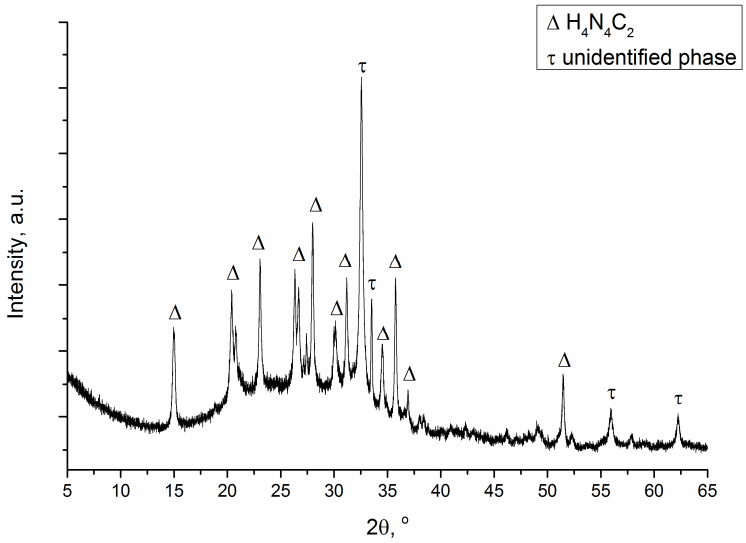

Figure 5-16. PXD pattern of **D-07**

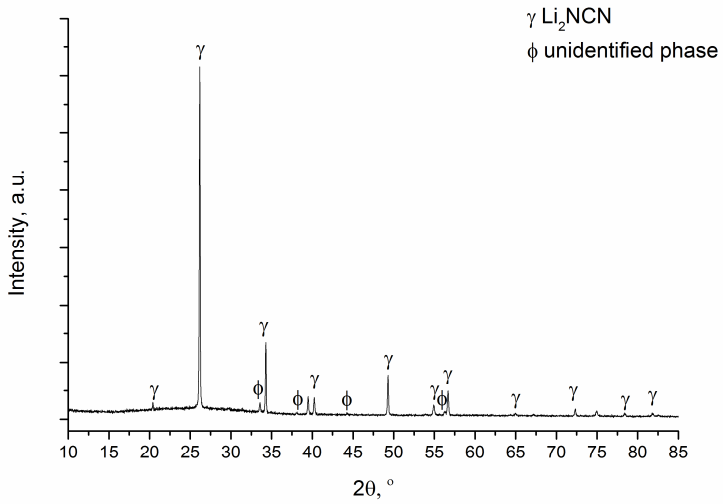

Figure 5-17. PXD of **D-07** heated to 130 °C

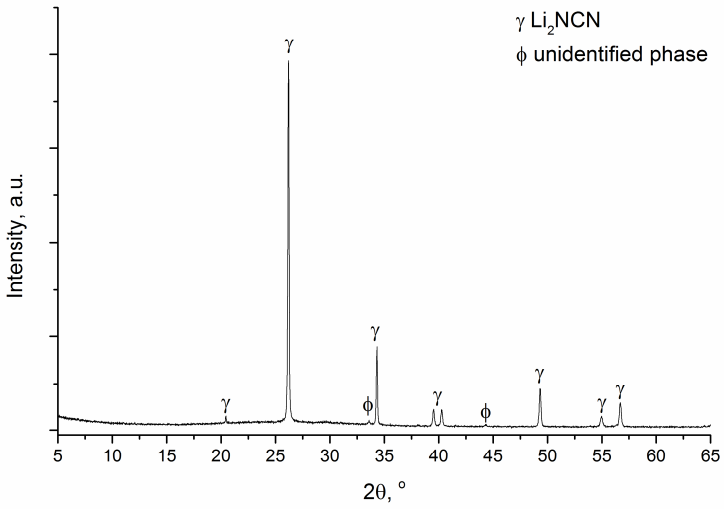

Figure 5-18. PXD pattern of **D-07** heated to 400 °C.

The FTIR spectrum of **D-07** after milling contains resembles many of the features found in the spectrum for pristine $H_4N_4C_2$ and **D-06** (figure 5-19 (b)). However the absorption bands at 2003 and 1439 cm^{-1} are particular to this sample. The band at 2003 cm^{-1} lies in the common *ν*(C=N) region, and it is unlikely related to Li_2NCN as the associated N=C=N bending mode at 683 cm^{-1} is absent. The band at 1439 cm^{-1} could not be identified. After heating to 130 °C, the IR spectrum corroborates the PXD observation that Li_2NCN constitutes the majority of the sample (figure 5-19 (c)). Among the minor absorption bands a familiar ring deformation mode at 812 cm^{-1} can be identified, yet the positions of remaining bands are different from those found spectra materials of **D-06** once heated **(**figure 5-13 (c)-(g)) and cannot be easily assigned. A very weak *ν*(NH) band can be identified at 3253 cm^{-1} which indicates hydrogen retention in the form of N-H groups. Further heating to 400 °C sees a further diminution of bands from the secondary phase (figure 5-19 (d)), though it appears that the N-H containing phase is stable below 400 °C.

It can be deduced from the evidence presented that with adequate ball milling, LiH and dicyandiamide in the ratio of 4:1 can react to form Li_2NCN in one step beginning at 85 °C. The reaction is accompanied mainly by H_2 desorption with trace amounts of undesirable ammonia. No other gases could be detected. Phase analysis revealed a stable phase containing a C=N moiety had formed as a result of ball milling, which is likely to have facilitated the change in reaction pathway observed. Further work to clarify the phase is necessary for a full deduction of the decomposition mechanism. This should also elucidate whether it is possible to control the observed material foaming and thereby improve the performance of the system to approach the specifications outlined in table 1-1.

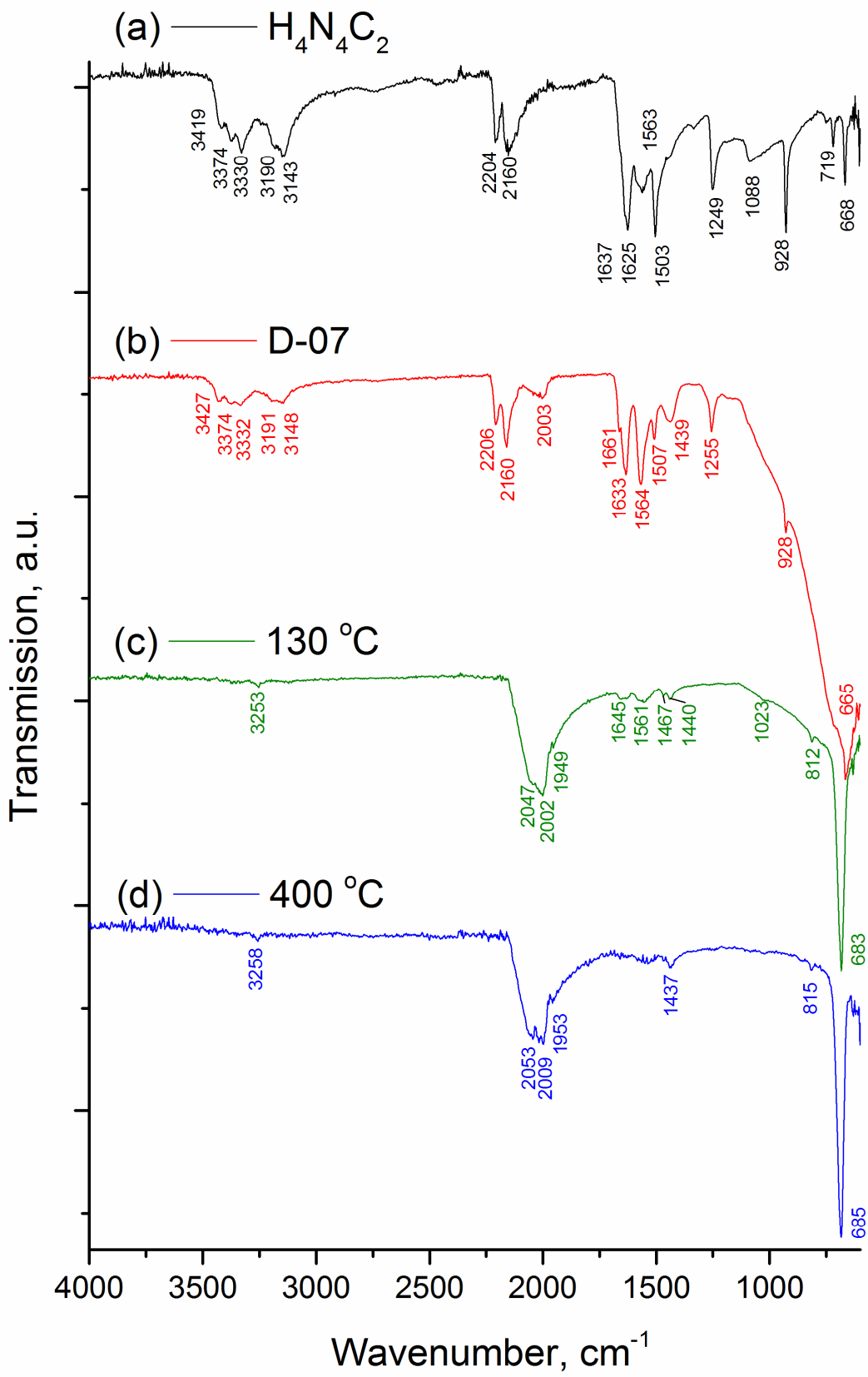

Figure 5-19. FTIR spectra of (a) $H_4N_4C_2$, (b) **D-07**, **D-07** heated to (c) 130 °C and (d) 400 °C

5.4 Conclusion

From the results presented in this chapter it can be confirmed that the proposed 4 LiH: dicyandiamide system releases hydrogen on heating. The interaction between these two compounds are highly dependent on the mechanical preparation through ball milling. It has been shown that two distinct potential pathways to hydrogen desorption can occur in the hydride-dicyandiamide system, one of which involves ring formation of dicyandiamide, likely similar to the natural condensation of dicyandiamide to melamine below 400 °C. The other pathway involves a rapid release of hydrogen and traces of water and ammonia at approximately 85 °C accompanied by foaming of the reaction mixture. In both instances the stoichiometric solid product Li_2NCN is formed following desorption. Considering that Li_2NCN can be rehydrogenated to dicyandiamide by simple hydrolysis, the proposed hydrogen storage system has high potential applicability. Further investigation of this system should focus on identifying the intermediate milling products and how to control foaming of the mixture during heating.

5.5 References

1. Buchanan, G. H.; Barsky, G. *J. Am. Chem. Soc*. **1930**, 52, 195-206
2. Pinck, L. A. *Inorganic Syntheses*; McGraw-Hill Book Company, Inc: New York Toronto London, **1950**; Vol. 3, 43-44
3. Kumler, W. D. *J. Org. Chem.* **1955***, 20*, 700-706
4. Franklin, E. C. *J. Am. Chem. Soc.* **1922***, 44*, 486-509
5. Hirshfeld, F. L.; Hope, H. *Acta Cryst.* **1980,** *B36*, 406-415
6. Bailey, P. J.; Pace, S. *Coord. Chem. Rev.* **2001***, 214,* 91-141
7. Saunders, T. F.; Levy, M. F.; Serino, J. F. *J. Poly. Sci. A*. **1967***, 5*, 1609-1617
8. Hughes, E. W. *J. Am. Chem. Soc.* **1940***, 62,* 1258-1267
9. Rannev, N. V.; Ozerov, R. P.; Datt, I. D.; Kshnyakina, A. N. *Soviet Physics Crystallography* **1966***, 11*, 177-181
10. May, H. *J. Appl. Chem.* **1959**, *9*, 340-344
11. Jürgen, B.; Höppe, H. A.; Irran, E.; Schnick, W. *Inorg. Chem.* **2002***, 41,* 4849-4851
12. Lotsch, B. V.; Jürgen, S.; Schnick, W. *Inorg. Chem.* **2004***, 43,* 895-904
13. Sheludyakova, L. A.; Sobolev, E. V.; Arbuznikov, A. V.; Burgina, E. B.; Kozhevina, L. I. *J. Chem. Soc. Faraday. Trans.* **1997**, *93*, 1357-1360
14. Alía, J. M.; Edwards, H. G. M.; García Navarro, F. J. *J. Molecular Struct.* **2001***, 597*, 49-55
15. Moffat, J. B. *J. Molecular Struct.* ***1981****, 86,* 119-122

16. Groshens, T. J.; Hollins, R. A. *Chem. Commun.* **2009**, 3089–3091
17. Wu, H.; Zhou, X.; Rodriguez, E. E.; Zhou, W.; Udovic, T. J.; Yildirim, T.; Rush, J. J. *J. Solid State Chem.* **2016***, 242*, 186-192
18. Guo, Y.; Gu, Q.; Guo, Z.; Mao, J.; Liu, H.; Dou, S.; Yu. X. *J. Mater. Chem.* **2011***, 21*, 7138-7144
19. Tang, Z.; Guo, Y.; Li, S.; Yu, X. *J. Phys. Chem. C* **2011**, *115*, 3188-3193
20. Doroodian, A.; Dengler, J. E.; Genest, A.; Rösch, N.; Rieger, B. *Angew. Chem. Int. Ed.* **2010**, *49*, 1871-1873
21. Chen, W.; Huang, Z.; Wu, G.; He, T.; Li, Z.; Chen. J.; Guo. Z.; Liu. H.; Chen, P. *J. Mater. Chem. A* **2015**, *3*, 11411-11416
22. Jones, W. J.; Orville-Thomas, W. J. *Trans. Faraday Soc.* **1959***, 55*, 193-202
23. Wang,Y.; Mebel, A. M.; Wu, C.; Chen, Y.; Lin, C.; Jiang, J. *J. Chem. Soc. Faraday Trans.* **1997**, *93,* 3445-3451
24. Mircescu, N. E.; Oltean, M.; Chiş, V.; Leopold, N. *Vibrational Spectroscopy,* **2012**, *62*, 165-171
25. Jones, W. J.; Orville-Thomas, W. J. *Trans. Faraday Soc.*, **1959**, *55*, 203-210
26. Hügle, T.; Kühnel, M. F.; Lentz, D. *J. Am. Chem. Soc.* **2009**, *131*, 7444-7446

6.0 Concluding remarks

In this thesis, the hydrogen desorption reactions between LiH and three organic amines: melamine, urea and dicyandiamide, were investigated as potential chemical hydrogen storage systems. Dehydrogenation was found to be facilitated by the thermodynamically favourable $HN^{\delta+}\ldots{}^{\delta-}HLi$ interactions in the solid state, which was found to be contingent on mechanical treatment of the mixture in terms of varying extent of ball milling. Through the thermal analysis, and structural analysis by diffraction as well as a variety of spectroscopic techniques, the reaction pathways of the three proposed systems were postulated and are summarised below.

Chapter 3 reported the dehydrogenation between 6 equivalents of LiH and melamine by heating to 320 °C. The full theoretical capacity of 6.98 wt% of hydrogen was released in three steps assisted by energetic ball milling. It was observed that ball milling not only provided means of particle size control while mixing the reactants intimately, but also induced structural changes in the reactant melamine without premature hydrogen release. It was proposed that melamine condensation occurs during the release of the first equivalent of hydrogen, and that the triazine skeleton remains intact after desorption of the first three equivalents of hydrogen. Although stable phases exist during dehydrogenation, it has not yet been possible to confirm the mechanistic details, which should form the subject for subsequent investigation on this system by means of 2D solid state ^{2}H and ^{15}N NMR spectroscopy. It was also confirmed that $HN^{\delta+}\ldots{}^{\delta-}HLi$ is indeed the dominant pathway of hydrogen release between LiH and melamine.

The dehydrogenation reaction between LiH and urea was examined in chapter 4. It demonstrated that approximately 5.8 wt% of hydrogen was released accompanied by undesirable ammonia by 270 °C in association with three processes: first involving the formation of lithium ureate, followed by the decomposition of lithium ureate to lithium cyanate and finally during the consumption of lithium cyanate. Ball milling again plays a crucial role in the selectivity of dehydrogenation over deammoniation in this system. It can also be concluded that the dehydrogenation products Li_2NCN and Li_2O are indeed thermodynamically favourable and that a kinetic barrier obstructs full dehydrogenation between LiH and urea.

In chapter 5 the preliminary examination of the LiH and dicyandiamide hydrogen storage system was described. It revealed that two distinct dehydrogenation pathways exist under varying extent of ball milling. Whilst both pathways yield the product Li_2NCN, one proceeds through the condensation of the dicyandiamide molecule followed by ring rupturing by 350 °C. Whereas the other pathway involves sample foaming to yield the final product at 85 °C.

From the proposed mechanisms it can be inferred that perhaps the selectivity on hydrogen desorption over ammonia release for these naturally deammoniating organic amines with LiH is a

function of kinetics. Whereby the molecular geometries of the initial dehydrogenation products dictate the subsequent interactions, or lack of, between the remaining N-H moieties in the material to result in deammoniation or dehydrogenation respectively.

Regarding systems sustainability, it was demonstrated that the common product Li_2NCN to the three proposed systems can be hydrogenated to melamine by hydrolysis, with dicyandiamide as an intermediate product. However, despite being theoretically probable, the rehydration of Li_2NCN to urea under acidic conditions has not been successful. This could be further explored as the cyanamide ion is known to hydrolyse to urea in both high and low pH.

Appendix A

Contour profiles of in situ neutron diffraction experiments conducted on ball milled LiD and $H_6N_6C_3$.

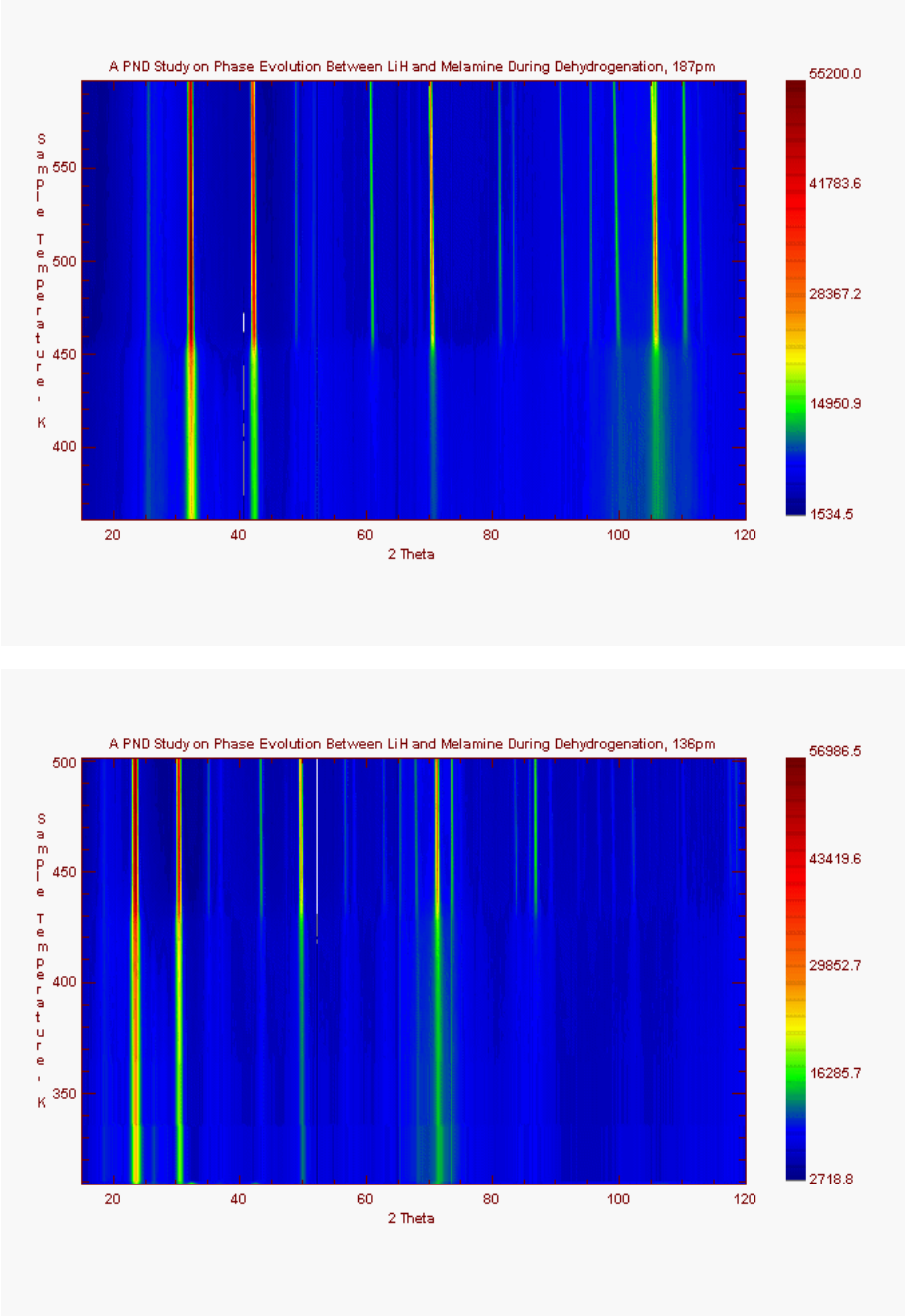

Figure A-1. *In situ* powder neutron diffraction experiments data for 6 LiD : $D_6N_6C_3$ collected on D20 with (a) λ = 1.87 Å and (b) λ = 1.36 Å, each profile shows sample profile against 2Θ. Diffraction intensities are coded according to the respective colour contour bars legend on the right of each plot.

Appendix B

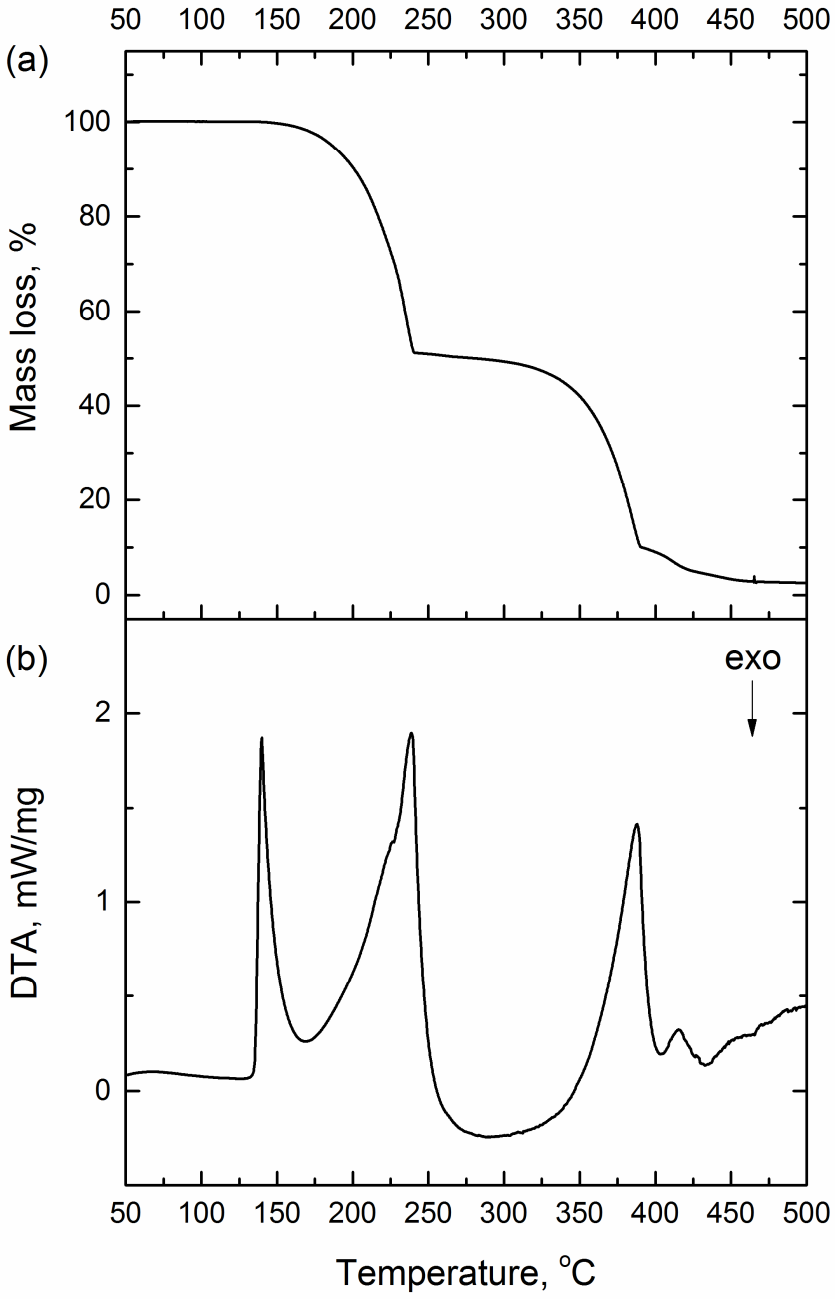

Figure B-1. Thermolysis of pristine urea at 5 °C min^{-1} in flowing Ar in the STA showing (a) TG and (b) DTA profiles.

Appendix C

Rietveld refinement plots used in chapter 4

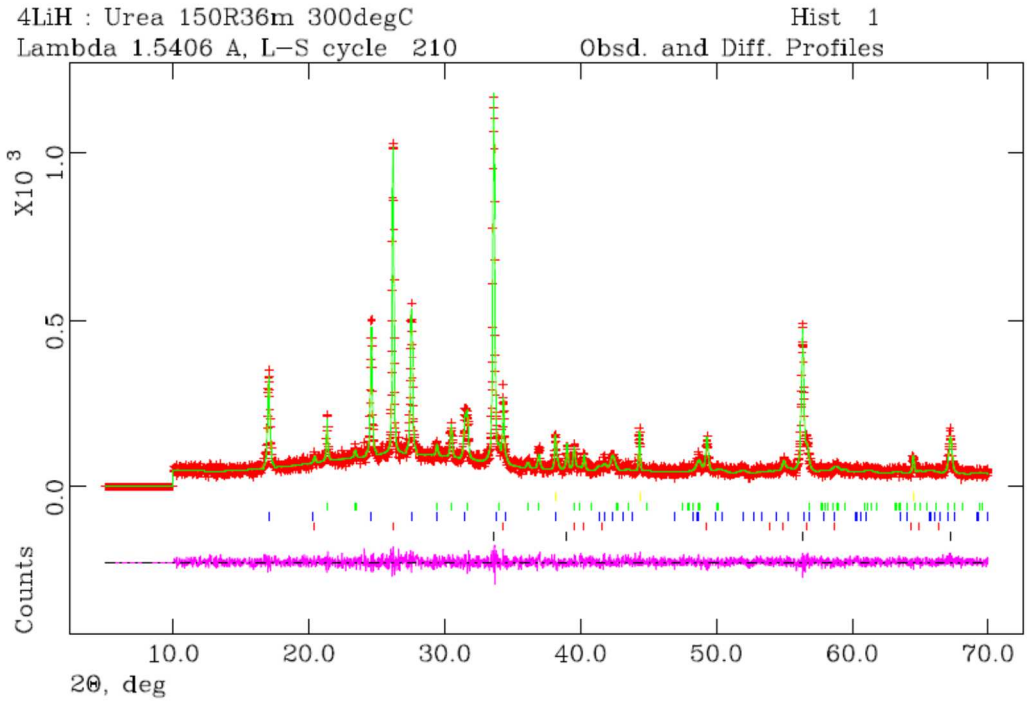

Figure C-1. Rietveld refinement plot for sample **U-01.** Tick marks represent LiH (orange), Li_2CO_3 (green), LiCN (blue), Li_2NCN (red) and Li_2O (black). The refinement converged at $X^2 = 1.094$ and $R_{wp} = 0.1173$

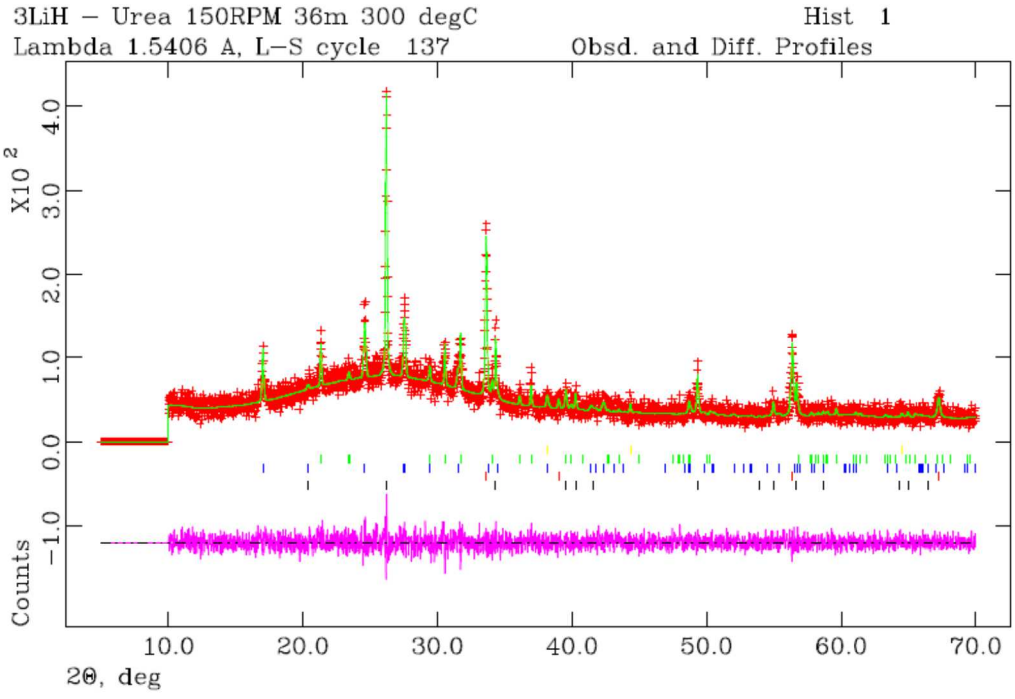

Figure C-2. Rietveld refinement plot for sample **U-02.** Tick marks represent LiH (orange), Li_2CO_3 (green), LiCN (blue), Li_2NCN (black) and Li_2O (red). The refinement converged at $X^2 = 1.042$ and $R_{wp} = 0.1440$

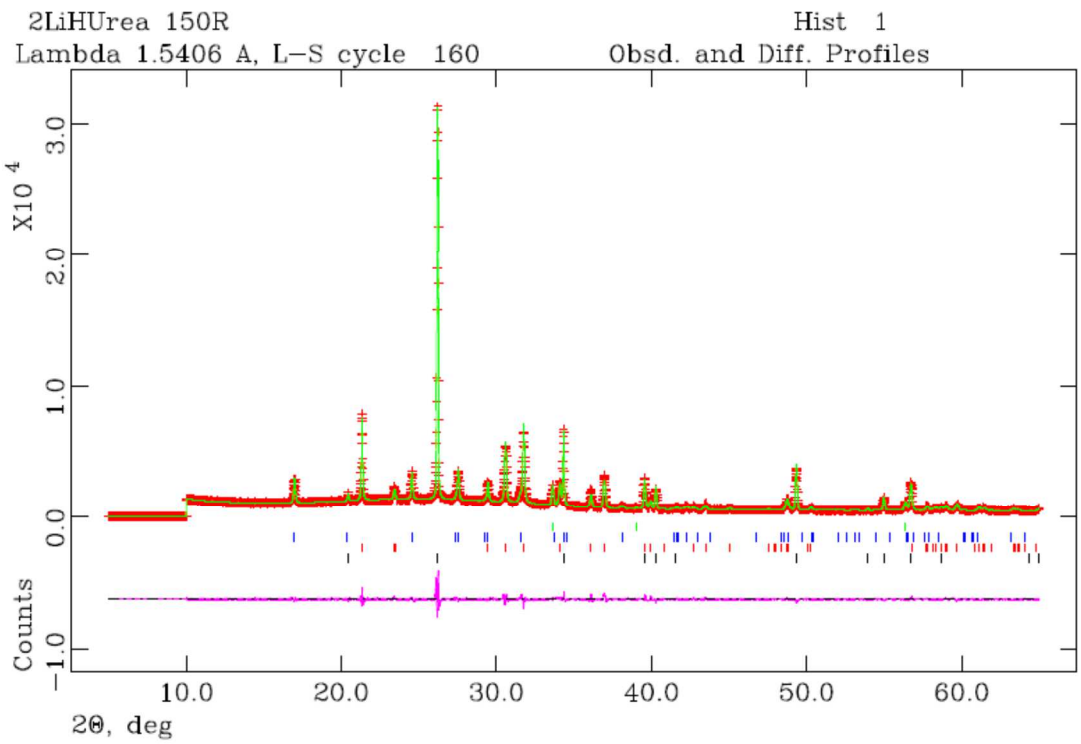

Figure C-3. Rietveld refinement plot for sample **U-03.** Tick marks represent Li_2CO_3 (red), LiCN (blue), Li_2NCN (black) and Li_2O (green). The refinement converged at $X^2 = 3.231$ and $R_{wp} = 0.0548$

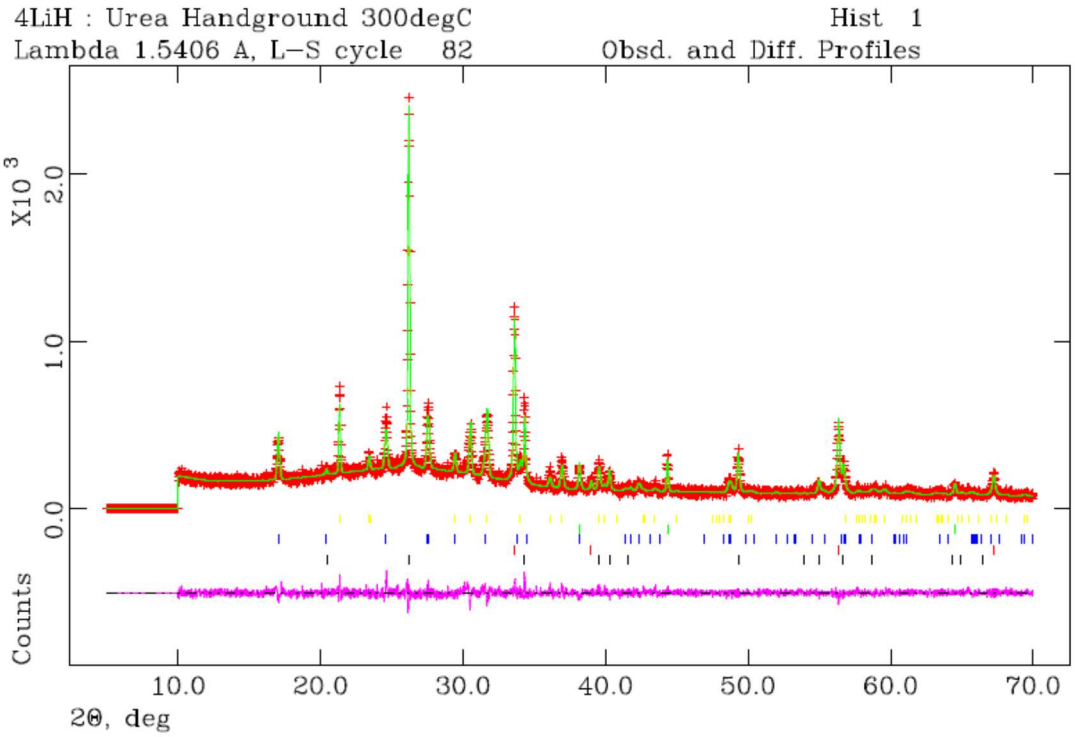

Figure C-4. Rietveld refinement plot for sample **U-06.** Tick marks represent LiH (green), Li_2CO_3 (yellow), LiCN (blue), Li_2NCN (black) and Li_2O (red). The refinement converged at $X^2 = 1.319$ and $R_{wp} = 0.0877$

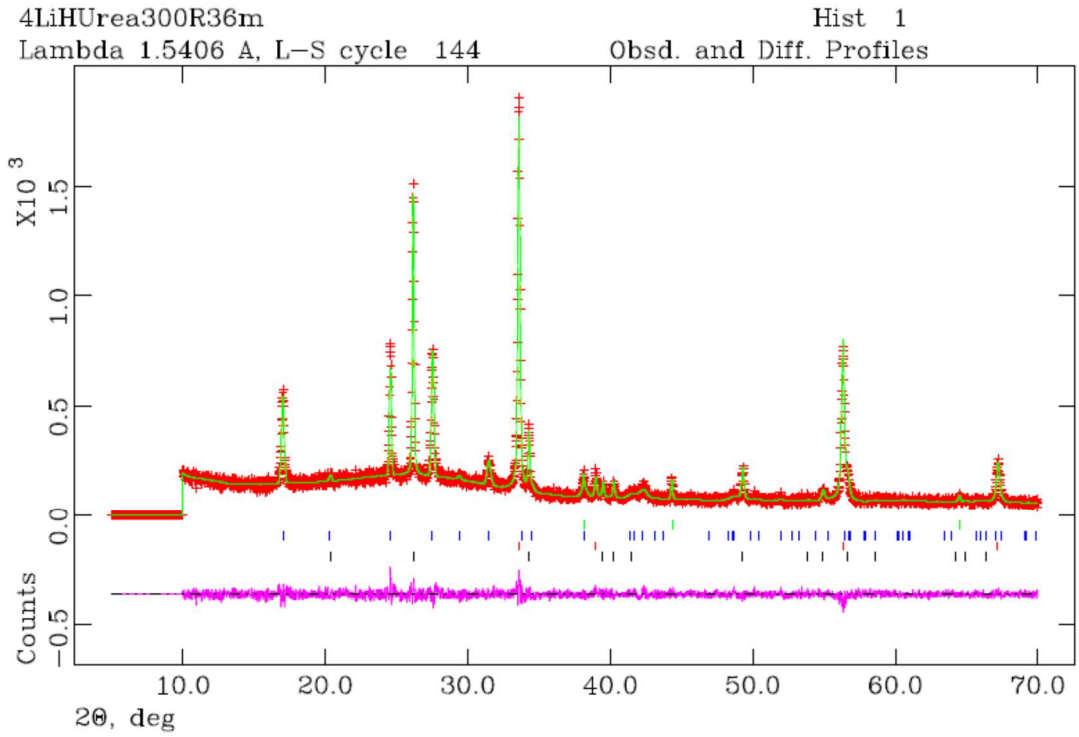

Figure C-5. Rietveld refinement plot for sample **U-08.** Tick marks represent LiH (green), LiCN (blue), Li_2NCN (black) and Li_2O (red). The refinement converged at $X^2 = 1.179$ and $R_{wp} = 0.0929$

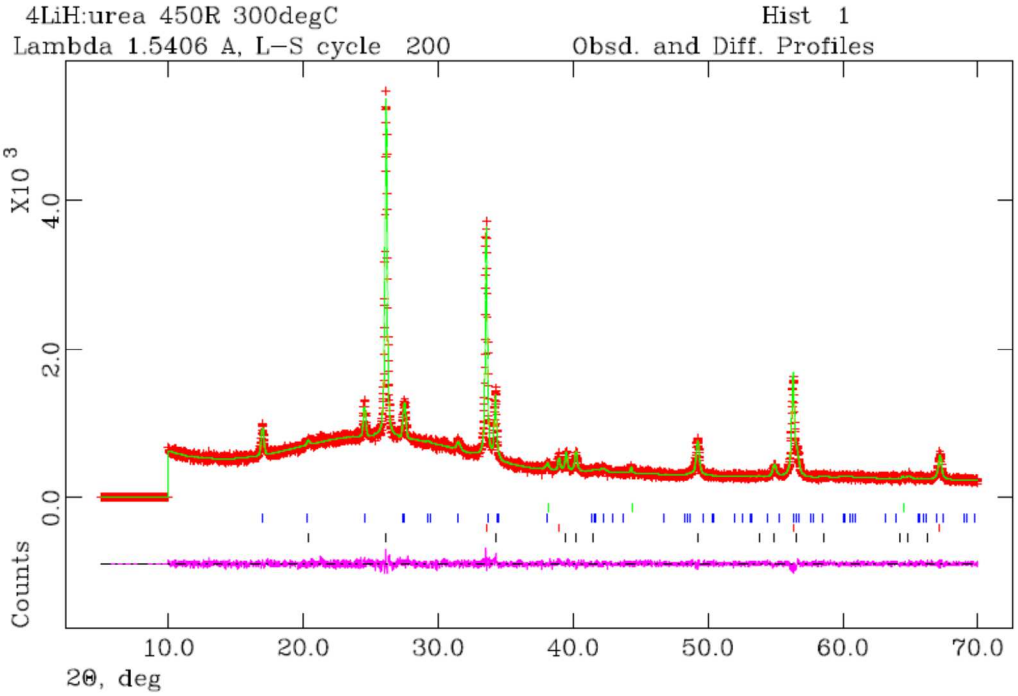

Figure C-6. Rietveld refinement plot for sample **U-09.** Tick marks represent LiH (green), LiCN (blue), Li_2NCN (black) and Li_2O (red). The refinement converged at $X^2 = 1.147$ and $R_{wp} = 0.0472$

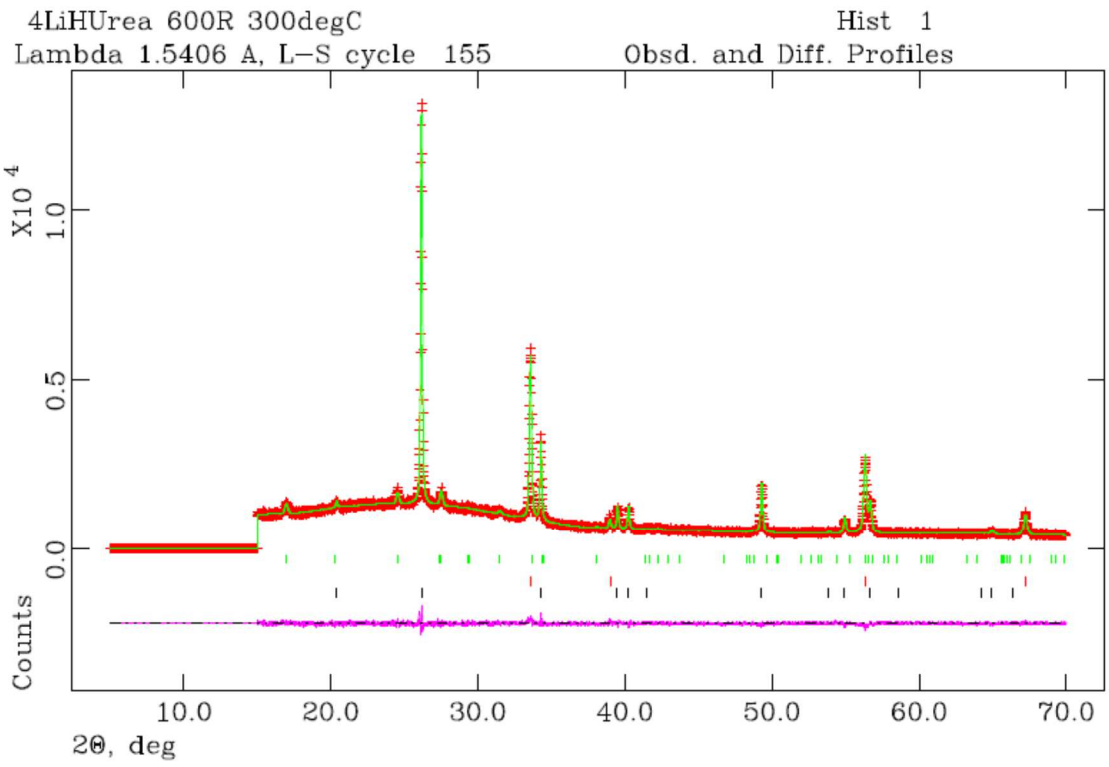

Figure C-7. Rietveld refinement plot for sample **U-10.** Tick marks represent LiCN (green), Li_2NCN (black) and Li_2O (red). The refinement converged at $X^2 = 1.265$ and $R_{wp} = 0.0387$

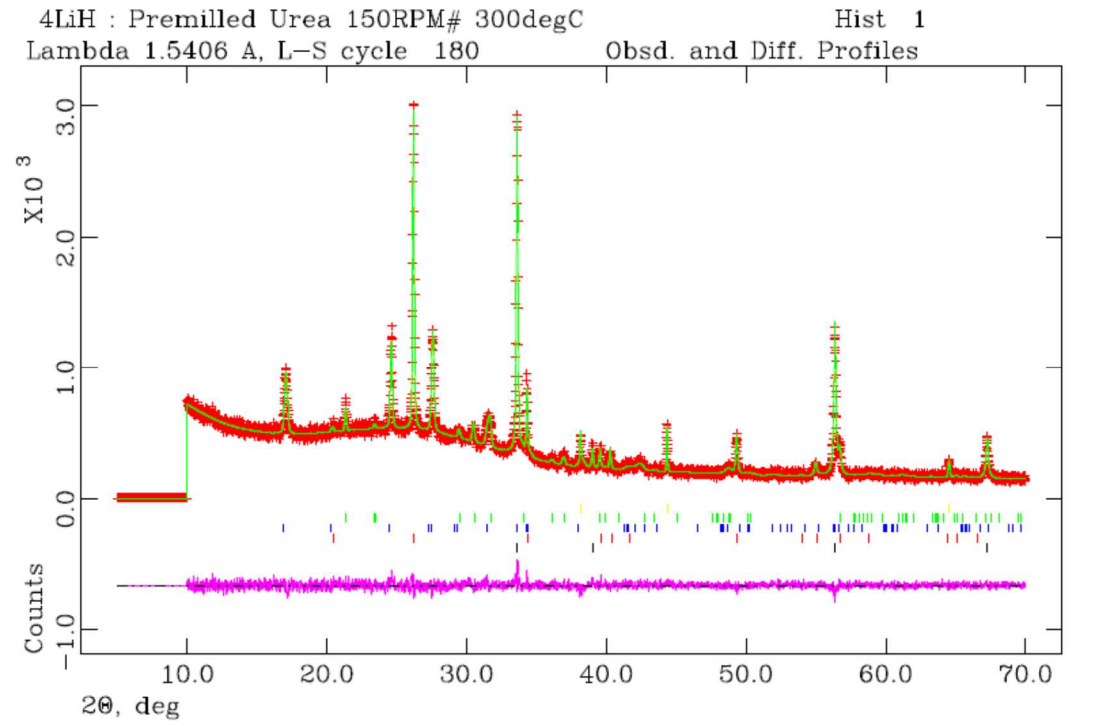

Figure C-8. Rietveld refinement plot for sample **U-11.** Tick marks represent LiH (orange), Li_2CO_3 (green), LiCN (blue), Li_2NCN (red) and Li_2O (black). The refinement converged at $X^2 = 1.194$ and $R_{wp} = 0.0574$

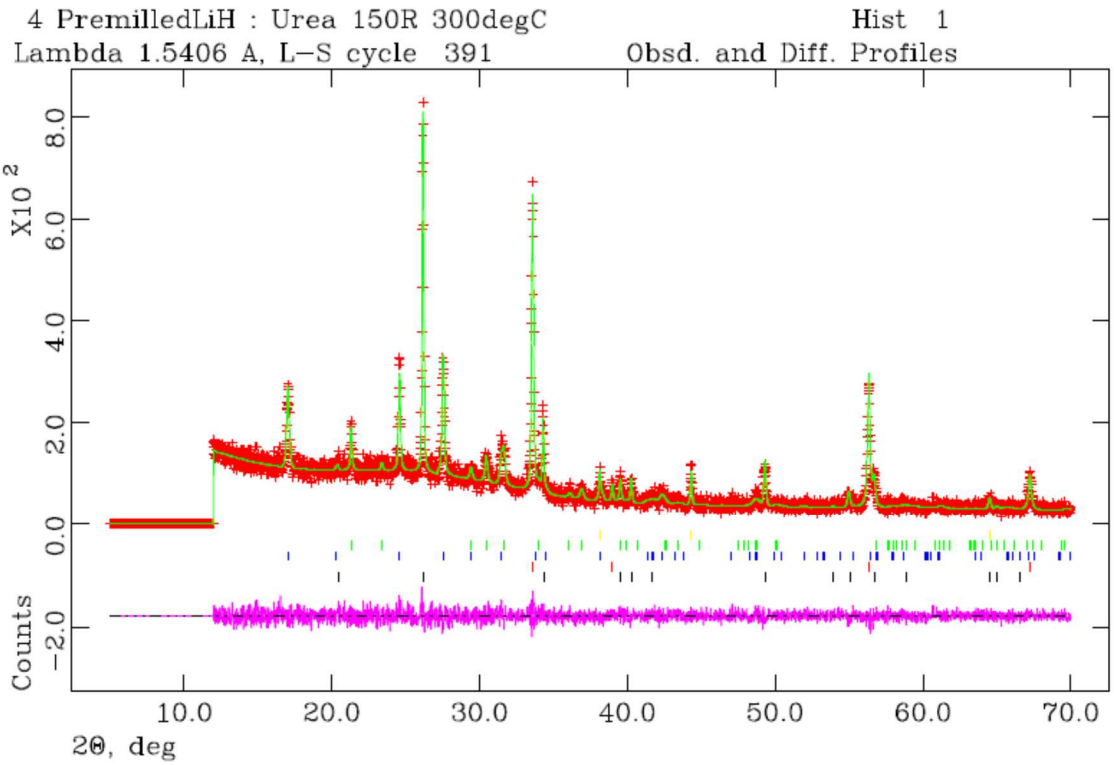

Figure C-9. Rietveld refinement plot for sample **U-12.** Tick marks represent LiH (orange), Li_2CO_3 (green), LiCN (blue), Li_2NCN (black) and Li_2O (red). The refinement converged at $X^2 = 1.054$ and $R_{wp} = 0.1167$

Appendix D

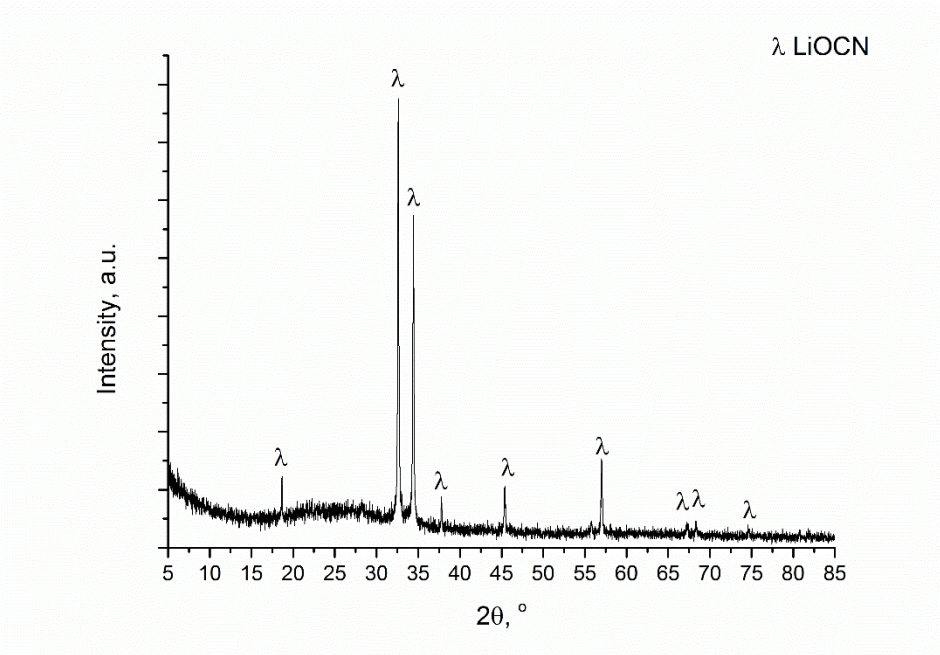

Figure D-1. PXD pattern of sample **U-04** heated to 300 °C showing LiOCN is the sole crystalline product.

Appendix E

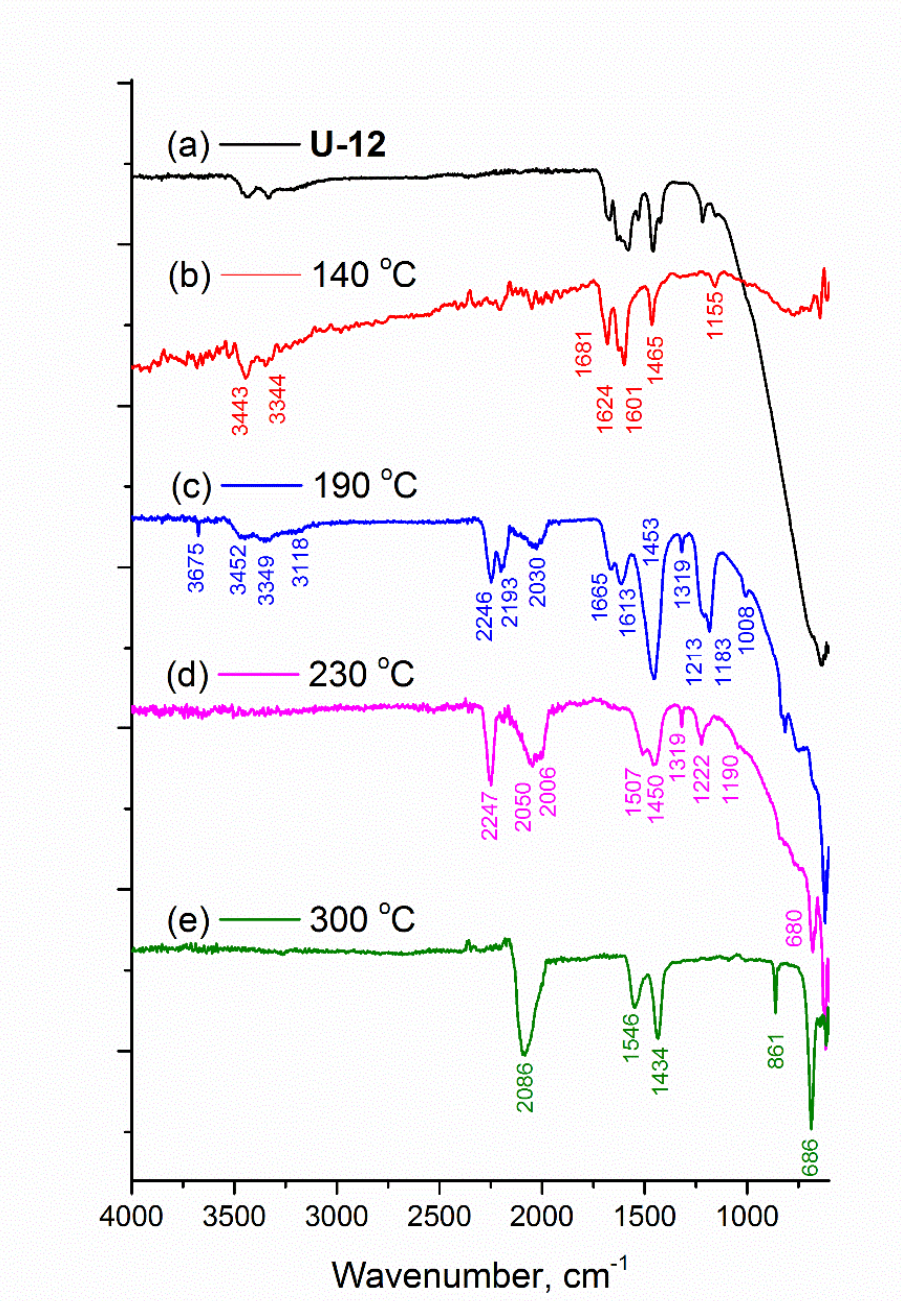

Figure E-1. FTIR spectra of (a) sample **U-12** heated to (b) 140 °C, (c) 190 °C, (d) 230 °C and (e) 300 °C.

Table E-1. FTIR absorption band values and assignments for pristine urea, sample **U-01** and **U-12** heated to various intermediate temperatures.

Urea		U-01				U-12					
RT	**Assignment**	**150 °C**	**Assignment**	**230 °C**	**Assignment**	**140 °C**	**190 °C**	**230 °C**	**Assignment**	**300 °C**	**Assignment**
3429	$v_a(NH_2)$					3443	3452		$v(NH_2)$		
3333	$v_s(NH_2)$					3344	3349				
3228							3118		v(NH)		
				2375	v(C≡N)						
				2250	v(C=N)		2246	2247	v(C=N)		
				2150			2193				
							2030	2050		2086	v(NCN)
								2006			
1670	$\delta_s(NH_2)$					1681	1665				
						1624					
1612	$\delta_a(NH_2)$	1605	$\delta_a(NH_2)$			1601	1613				
1586	v(CO)	1545	v(CO)	1570				1507		1546	$v(CO_3)$
		1460		1505		1465	1453	1450			
1459	v_a(CN)	1440	v_a(CN)							1434	$v(CO_3)$
				1415							
				1315			1319	1319			
		1220	$\rho_s(NH_2)$	1225		1155	1213	1222			
1146	$\rho_s(NH_2)$						1183	1190			
1000	v_s(CN)	1000	v_s(CN)				1008				
786	ω(CO)	808	ω(CO)	810			815			861	$v(CO_3)$
714	$\tau_a(NH_2)$										
		650		630			620	680		686	v(NCN)

Appendix F

An attempt to hydrolyse Li_2NCN to urea was conucted using dilute H_2SO_4 (10%). Li_2NCN was dissolved in DI water and stirred for 10 min before dilute H_2SO_4 was added in drop-wise until the pH of the solution reached 2.6. When the water was dried off using the Schlenk line a white solid remained. A white precipitate was observed when adding ethanol to the solid, which was filtered off. After further drying of the solvent on the Schlenk line a white solid was obtained to afford an unidentifiable PXD pattern shown in figure F-1. ^{13}C NMR was conducted for the solid in D_2O (figure F-2) which yielded a chemical shift at 162.7 ppm, consistent with a carbonyl moiety found in the urea molecule. Residual ethanol peaks are also present.

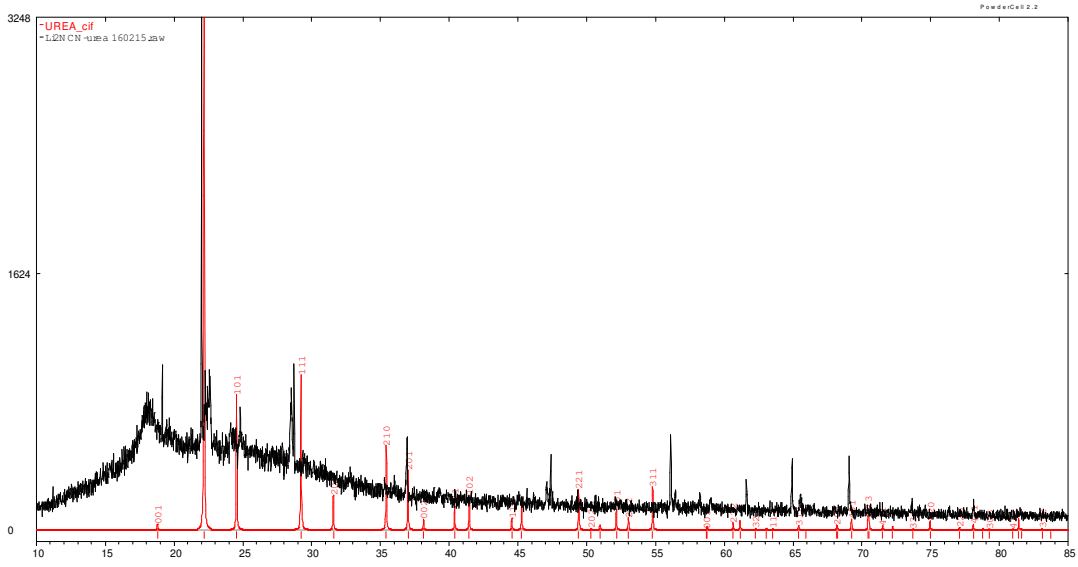

Figure F-1. PXD pattern of solids afforded from the acidic hydrolysis of Li_2NCN. The urea reference pattern is overlaid on the pattern to show where the urea reflections should lie.

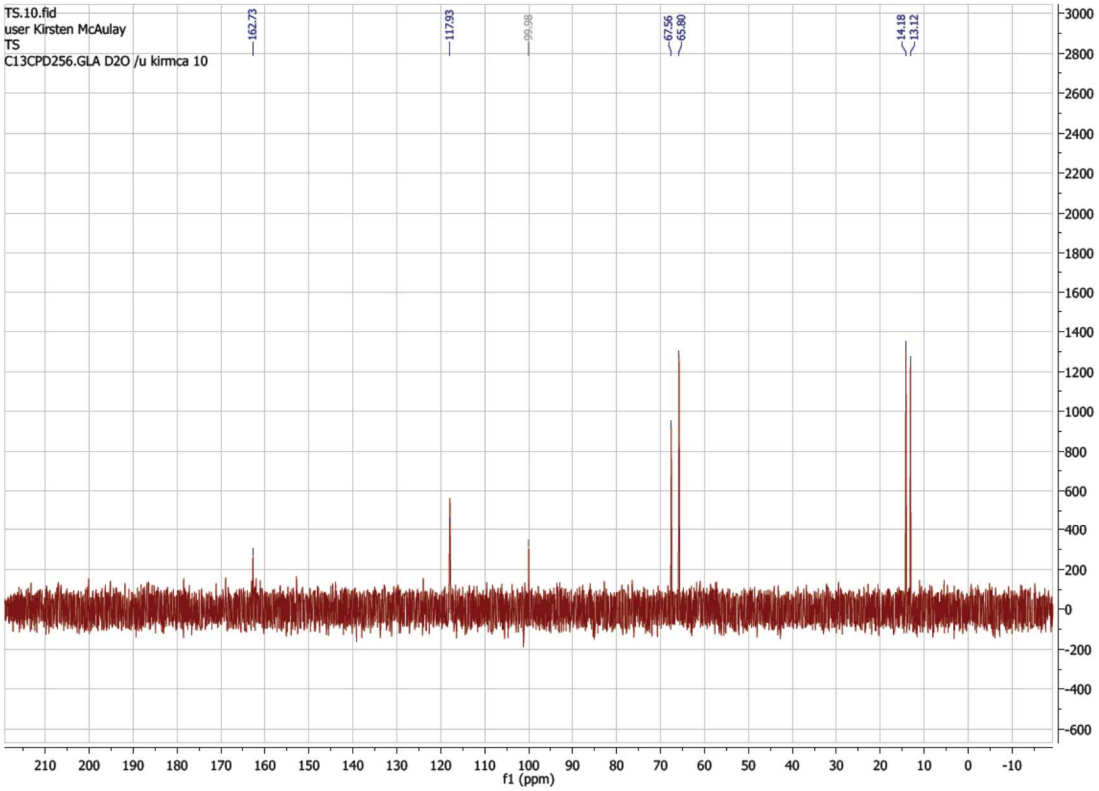

Figure F-2. ^{13}C NMR of solid afforded from the acidic hydrolysis of Li_2NCN in D_2O.

Appendix G

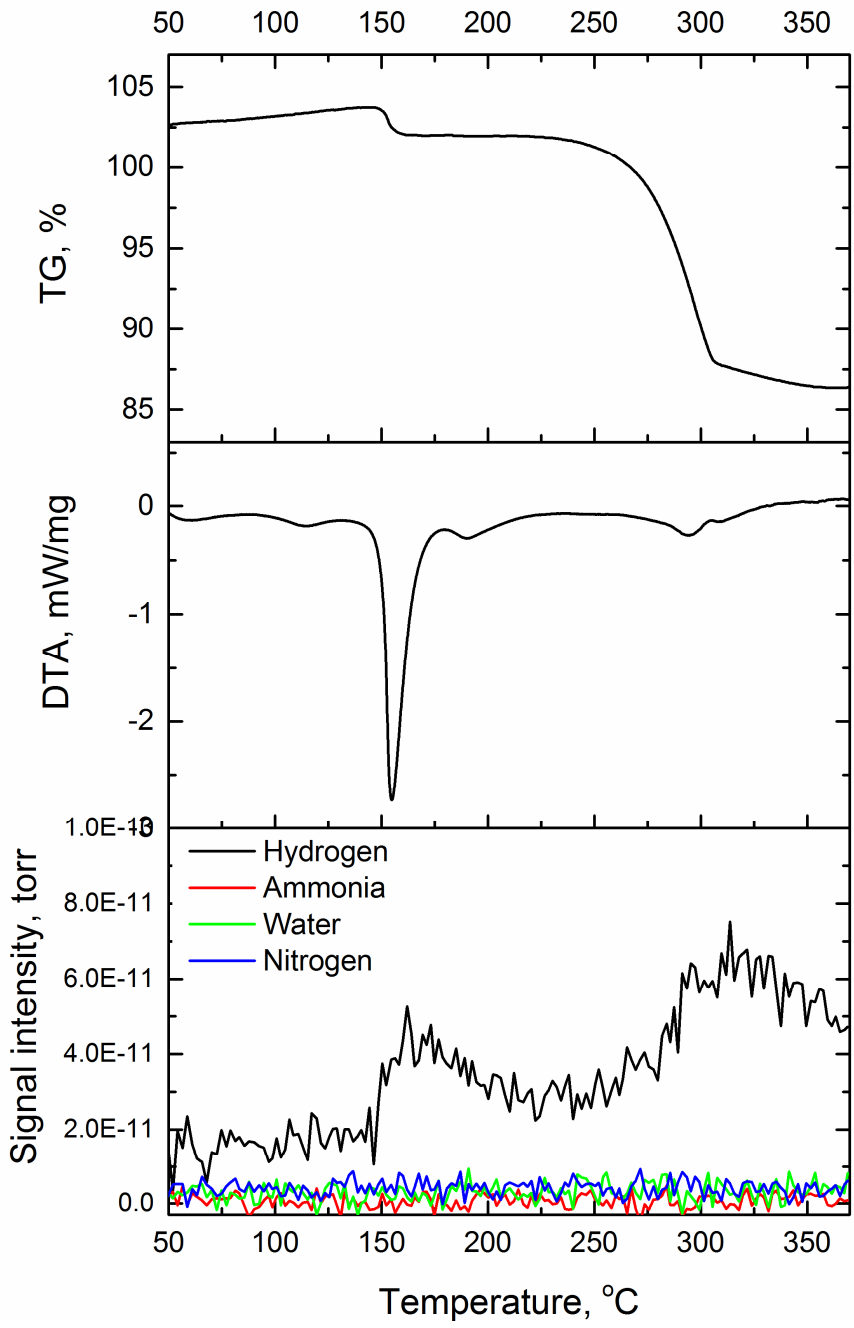

Appendix G-1 TG, DTA and MS of intimately mixed 4LiH : dicyandiamide powder heated to 400°C. An initial weight gain of approximately 2% prior to 50 °C was observed due to a buoyancy effect as a product of using He purge gas in an Ar filled glovebox.

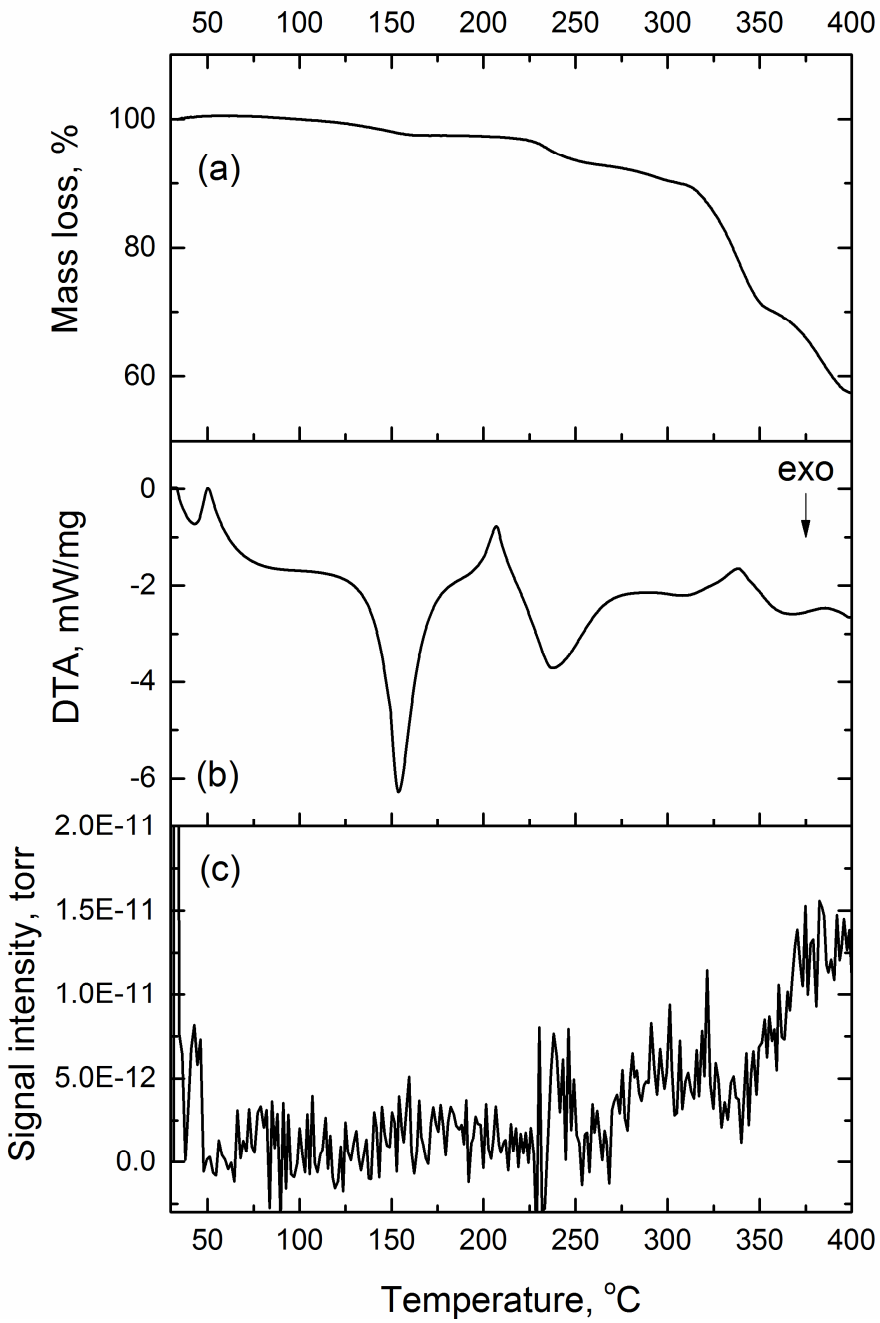

Figure G-2. (a) TG, (b) DTA and (c) NH_3 MS profiles of heating pristine H_2NCN to 400 °C.